Elaboration of plasmonic nano-composites and study of their specific catalytic activities

Olga Ishchenko

UNIVERSITÉ DE STRASBOURG

ÉCOLE DOCTORALE DES SCIENCES CHIMIQUES (ED222)

Institut de Chimie et Procédés pour l'Energie, l'Environnement et la Santé ICPEES (Strasbourg)

THÈSE présentée par :

Olga ISHCHENKO

soutenue le : **30 septembre 2016**

pour obtenir le grade de : **Docteur de l'université de Strasbourg**

Discipline/ Spécialité: Chimie

Elaboration of Plasmonic Nano-Composites and Study of their Specific Catalytic Activities

PRESEDENT DU JURY:

Mr GARIN François	Université de Strasbourg

THÈSE dirigée par :

Mr LENOBLE Damien	Luxembourg Institute of Science and Technology
Mme FECHETE Ioana	Université de Strasbourg
Mr TUREK Phillipe	Université de Strasbourg

RAPPORTEURS :

Mr ZAHRAA Orfan	Université de Lorraine
Mr MARCEAU Eric	Université de Lille

EXAMINATEURS :

Mr Da COSTA Patrick	Université Pierre et Marie Curie, Sorbonne, Paris
Mr MARCU Ioan-Cezar	Université de Bucarest

Acknowledgements

I would like to express my gratitude to Mr. Jens Kreisel, head of the Materials Research and Technology (MRT) department of the Luxembourg Institute of Sciences and Technology, for hosting me during these three and a half years within the department.

I express my sincere gratitude to Mr. Damien Lenoble, head of the Nanomaterials Unit, for offering me the opportunity to accomplish this work and being my supervisor along the way. I would like to thank him for his continuous support of my study and research, his patience, availability, professionalism and knowledge that led me to the right direction.

I would like to thank my director and co-directors from the University of Strasbourg Ioana Fechete, François Garin, and Philippe Turek for their co-supervision, experience, scientific discussions and helpful advice.

I also want to express my gratitude to all the members of the PhD jury: reporters Mr. Orfan Zahraa, Mr. Eric Marceau and examinations Mr. Partick Da Costa and Mr. Ioan-Cezar Marcu to accept to evaluate my work in a very restricted time. I am very thankful to them for their insightful comments, questions and also their different perspective on my research.

I express my most sincere acknowledgement to my close colleagues with whom I have sheared the every day laboratory life. First of all is the ex-UGN team, Bianca Rita, Didier, Kevin, Guillaume, Naoufal, Noureddine, Jean-Sébastien, Vincent, Moustapha, Manuel, Siva, César, Petru, Renaud. Your welcoming was especially memorable with the Christmas dinner. I would like to thank all the current Nanomaterials Unit team which I see growing, thank you all for nice insightful discussions and the nice time during the coffee breaks.

I would like to address a particular acknowledgement to Siva, Naoufal and Guillaume who have invested a lot of their time helping me with my research. Thank you for all MRT characterization team, especially, Gérôme Gillot, Nathalie Valle, Patrick Grysan, Yves Flemming, Stéphanie Girod for their help to understand the complex methods subtilities and especially for “urgent” requests, without forgetting the MRT-support support team.

Thanks to the PhD student F1.14 office-colleagues, the “Lippmann” version, Vincent, Mousthapha, Rodolphe, Céderic, Simon, Giuseppe, Nohora, Jonathan, Florian, for the unforgettable atmosphere; and the new “LIST” version, David, Alex, Sunil, Hamida, Catarina,

Divya, Serena to sharing with me the most difficult moments. Thanks to all others PhDs students and good luck for their defenses.

I would like to thank my family and my friends, even being faraway, I could feel their love, support and belief. The moments together were very rechargeable giving me new forces and motivation. I would like to thank my husband for his inestimable every-day support, his love and understanding.

Synthèse en français

La dépollution environnementale est devenue un des défis majeurs de la société contemporaine. Les activités économiques et industrielles des pays développés ainsi que des pays en forte croissance, sont des sources principales de contamination des eaux et de l'air. Les eaux usées des grandes villes et les activités agricoles ont également un impact important sur l'environnement. Il devient évident que la purification de l'eau est un enjeu vital de nos sociétés modernes.

Actuellement, les principes d'épuration de l'eau sont basés sur des procédés physicochimiques assez complexes et coûteux, tels que décantation, flottation, coagulation, floculation, sédimentation, filtration avec macro-, micro- et nano-filtres et désinfection par utilisation du chlore, d'un traitement ozone ou UV. L'efficacité de ces techniques de traitement des eaux ainsi que leur coût sont aujourd'hui discutées notamment pour la dégradation de nouvelles molécules comme les résidus médicamenteux. La dégradation photocatalytique a été proposée il y a plusieurs décennies comme un concept potentiellement efficace et écologique permettant la dégradation efficace des polluants organiques complexes sous irradiation UV dans les milieux aqueux et gazeux. Sous irradiation, les matériaux photocatalytiques sont capables de générer des porteurs de charge (paires électron/trou) qui initient les réactions d'oxydo-réduction, jusqu'à la minéralisation des molécules organiques. Les matériaux photocatalytiques efficaces doivent démontrer plusieurs propriétés, telles que stabilité chimique, biocompatibilité, non-toxicité et faible coût. Une quantité significative des travaux réalisés sur le développement et la compréhension des propriétés photocatalytiques des matériaux tels que TiO_2, ZnO, SnO_2, Fe_2O_3, CdS, ZnS etc, a été publiée [1–6]; TiO_2 reste aujourd'hui le matériau de référence dans les communautés scientifiques et technologiques.

Toutefois, les matériaux photocatalytiques usuels (TiO_2, ZnO ou SnO_2) présentent encore de nombreux facteurs limitant leur efficacité. Premièrement, la valeur de la bande interdite des niveaux d'énergie électronique limite l'absorption de la lumière au rayonnement UV. Les porteurs photo-générés ont également tendance à se recombiner rapidement dans le matériau. Actuellement plusieurs approches ont déjà été proposées pour améliorer l'activité photocatalytique de ces matériaux. Par exemple, le dopage [7–10] ou l'assemblage des oxydes métalliques avec des nanoparticules plasmoniques permet de promouvoir l'absorption de la lumière visible. Le problème de la recombinaison des porteurs photo-générés peut être résolu

par l'ingénierie d'hétéro-structures semi-conductrices. Le décalage des niveaux énergétiques de la structure des bandes de conduction et de valence des matériaux favorise la création de champ électrique interne à la structure augmentant ainsi la durée de vie des porteurs photo-générés.

L'amélioration de l'activité photocatalytique reste un grand défi pour la communauté scientifique. Ainsi, l'objectif principal de la thèse est d'atteindre une dégradation photocatalytique sous la lumière visible et d'améliorer celle sous UV sur les systèmes à base de TiO_2.

Il est nécessaire d'étudier les problématiques majeures telles que la recombinaison des porteurs (paires électron/trou) par assemblage avec des pièges de porteurs (nanoparticules plasmoniques, les hétérostructures etc.) et l'amélioration d'absorption de la lumière en utilisant des nanostructures périodiquement organisées (approche photonique).
Afin d'améliorer l'absorption de la lumière dans l'UV, nous proposons de fabriquer un réseau de nanofils de TiO_2 organisés périodiquement et nous étudierons l'absorption de la lumière visible sur les films de TiO_2 assemblés avec des nanoparticules plasmoniques.
Dans ce travail de thèse, nous développons des nanostructures de TiO_2 organisées périodiquement ainsi que des films des TiO_2 couplées à des systèmes plasmoniques auto-organisés.
Afin d'obtenir des nanofils de TiO_2 périodiquement organisés, deux approches de fabrication ont été étudiées (Figure 1).

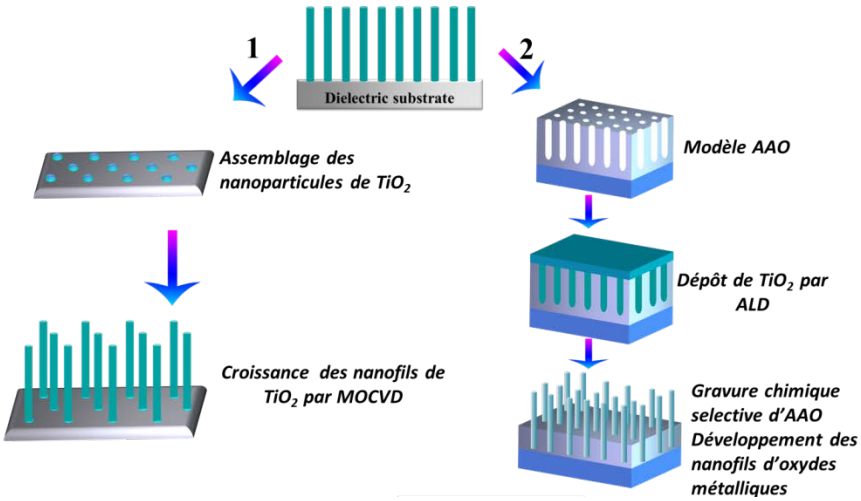

Figure 1 Représentations schématiques des deux approches de la fabrication des nanofils.

La première approche repose sur la fabrication de nanoparticules TiO_2 auto-organisées sur la surface afin de catalyser la croissance sélective de nanofils TiO_2 par MOCVD (Metal Organic Chemical Vapour Deposition). La seconde approche se base sur la fabrication de nanofils en utilisant un « moule » auto-organisé de « pores » tel que les membranes poreuses d'aluminium anodisé (AAO). Pour la réalisation expérimentale de cette dernière approche, une optimisation des dépôts conformes des oxydes métalliques par ALD (Atomic Layer Deposition) est réalisée. Nous verrons, dans la première partie, les étapes d'optimisation de fabrication des nanofils périodiques en utilisant ces deux approches.

Fabrication des nanoparticules de TiO_2 auto-organisées

La technique d'auto-organisation de nanoparticules catalyseurs de croissance repose sur la formation de micelles de « block copolymère » polystyrène-b-poly-2-vinylpyridine (PS-b-P2VP) dans des solvants adéquats (type toluène). Les micelles inverses sont déposées sur le substrat de Si/SiO_2 par « spin-coating ». Le précurseur est introduit au centre de la micelle par diffusion assistée par gradient de concentration chimique dans la micelle. Un post-traitement par plasma oxygène permet de graver le polymère résiduel et de révéler des nanoparticules d'oxydes métalliques sur le substrat [11–13].

Des résultats particulièrement intéressants ont été obtenus lors du développement des nanoparticules de TiO_2 (Figure 2). Nous avons contribué significativement à la compréhension des mécanismes de formation des nanoparticules de TiO_2 par cette technique. L'exposition des micelles à la vapeur du précurseur $TiCl_4$ a été réalisée par ALD en utilisant deux modes d'exposition : (I) avec l'injection supplémentaire de vapeurs d'H_2O et (II) exposition uniquement au $TiCl_4$. Le contrôle des tailles des nanoparticules après l'exposition et le traitement de plasma oxygène a permis de conclure que le mode (II) limite la croissance des nanoparticules par l'humidité piégée dans la micelle permettant de confiner la réaction. Le mode (I) conduit à une croissance continue, qui n'est pas limitée par la micelle. Le mode (I) peut également donner une croissance de film oxyde-métallique sur la micelle en formant une coquille. Une étude approfondie par l'ensemble des méthodes de caractérisations telles que SEM, AFM, XPS, SIMS et TEM a permis de conclure sur les mécanismes réactionnels régissant la synthèse des nanoparticules.

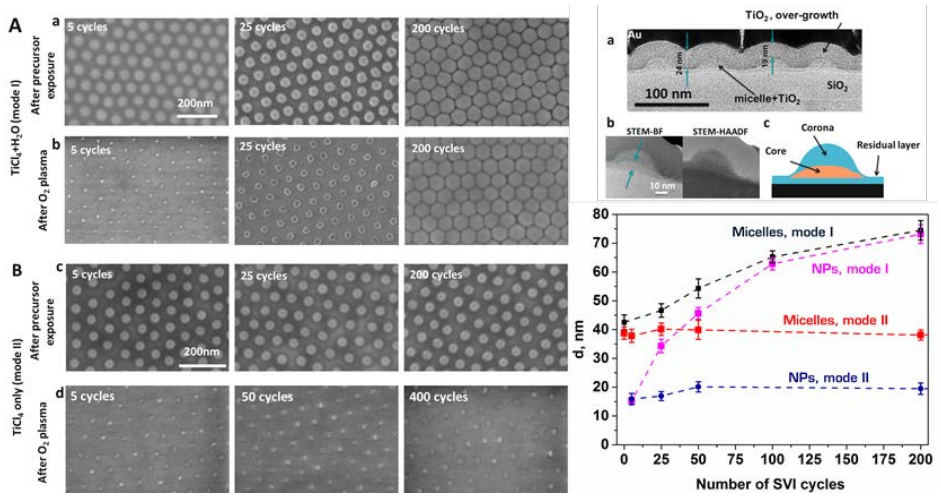

Figure 2 Images MEB de nanoparticules auto-organisées de TiO_2.

La meilleure reproductibilité de la taille de nanoparticules est obtenue en utilisant le mode d'exposition II ($TiCl_4$ uniquement).

Synthèse des nanofils de TiO_2 par MOCVD

La technique de MOCVD a été étudiée afin de favoriser la croissance préférentielle sur les nanoparticules de TiO_2 précédemment développées. L'isopropoxide de titane (TTIP) a été sélectionné, étant un précurseur classique pour la croissance de TiO_2 par MOCVD. Une large gamme de conditions de dépôts a été testée. La pression totale a varié dans la gamme de 0.94 à 15 mbar et la température dans la gamme 200 - 750°C ; ce sont ajoutées les fréquences d'injection des précurseurs.

La Figure 3 résume les différents types de morphologies obtenus en fonction des paramètres de dépôt. On peut distinguer une croissance granulaire de film mince continue et une croissance colonnaire compacte. Néanmoins, nous n'avons pas pu obtenir la croissance sélective des nanofils sur les nanoparticules de TiO_2. Nous en avons conclu que la taille des nanoparticules pré-déposées est inférieure du rayon critique nécessaire pour assurer la croissance sélective de type Volmer-Weber sur les ilots de TiO_2.

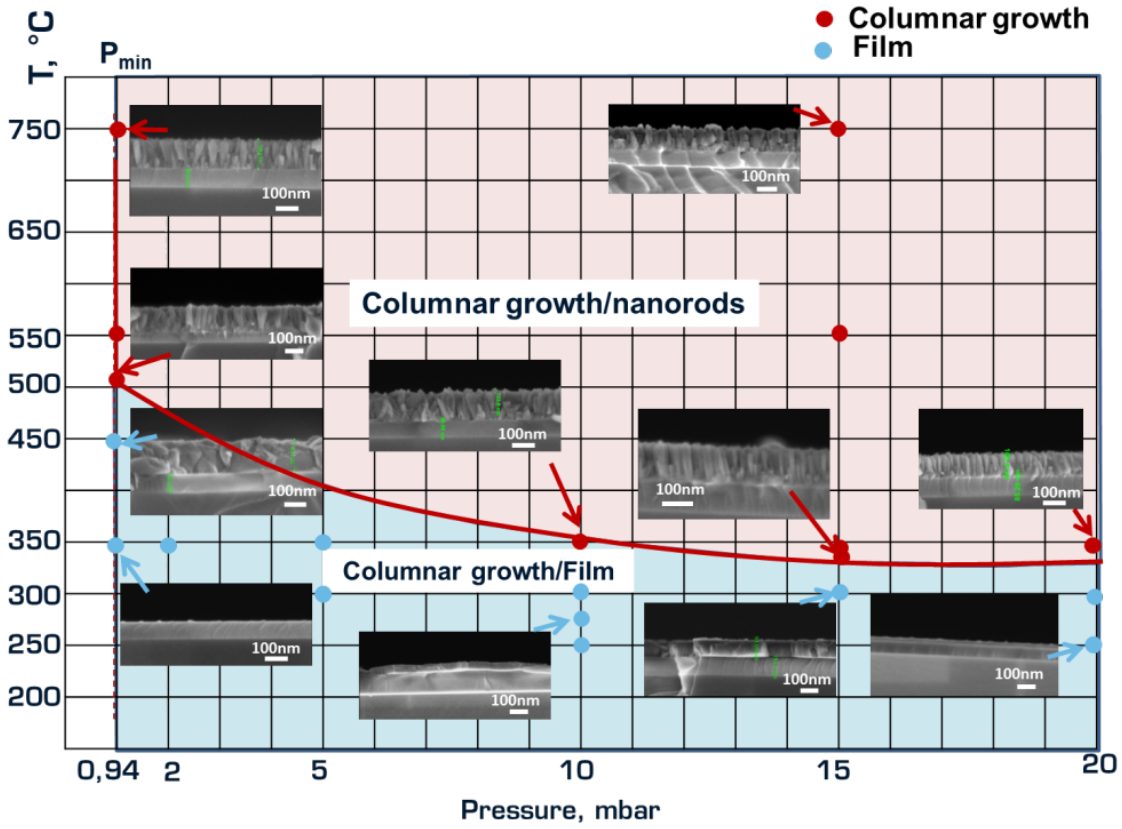

Figure 3 Schéma des différentes morphologies de croissance en fonction de la température et de la pression.

Optimisation des dépôts conformes de TiO_2 par ALD pour le traitement des membranes AAO

Le développement des films de TiO_2 par ALD est nécessaire pour réaliser la synthèse des nanofils périodiques dans les membranes AAO avec des pores de diamètre 40 nm. La synthèse des films de TiO_2 par ALD, en utilisant $TiCl_4$ et H_2O comme précurseurs, est largement étudiée dans la littérature. Néanmoins, le problème majeur de ces dépôts est la forte rugosité de surface de ces films cristallins [14]. Dès lors, nous avons choisi d'étudier la croissance des films dans une large gamme de températures 20 - 400°C. L'analyse DRX a montré que les films obtenus jusqu'à 250°C sont amorphes. La cristallinité, ainsi que la rugosité des films, progressent avec l'augmentation de la température du procédé tandis que la vitesse de croissance diminue. La croissance de films lisses de TiO_2 est obtenue dans la gamme de températures 20 - 200°C.

La température de recristallisation de TiO_2 amorphe en phase anatase a été déterminée par des mesures *in-situ* DRX à température variable. D'après les diffractogrammes, la température de

recristallisation de TiO_2 en phase anatase doit être supérieure à 500°C. Le recuit des films amorphes a été donc réalisé à 600°C à la pression atmosphérique.

Les films de TiO_2 déposés à basse température recristallisent en phase anatase avec deux morphologies différentes. Les films déposés à 20°C forment un revêtement très poreux. Les morphologies des films déposés à 100 et 200°C ont une recristallisation de type « explosive » et forment des grains de taille supérieure à 1 µm.

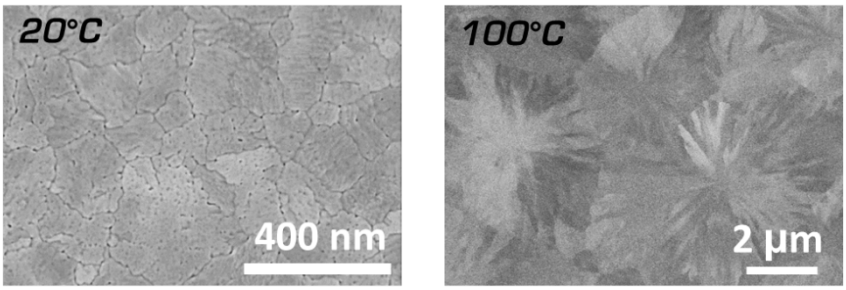

Figure 4 Les films de TiO_2 déposés à 20 et 100°C après le recuit.

Il est aussi important de noter que les paramètres de dépôt ALD tels que le temps de purge entre les pulses des précurseurs ont un impact significatif sur la morphologie des films déposés à 100 et 200°C. Les dépôts réalisés avec le temps de purge plus long (30 s), après le recuit ne forment pas des larges grains comme c'est le cas pour les dépôts avec le court temps de purge (5s). L'analyse chimique par XPS des échantillons avant et après le recuit a démontré que la présence de chlore ou composé chlorure résiduels dans le film amorphe est a priori une signature intrinsèque des différences morphologiques. Après le recuit, le film déposé à 20°C ne montre plus de présence de composés chlorés. Les sous-produits de la réaction et les précurseurs non-réagis, piégés dans le volume du film forment des espèces volatiles qui dégazent durant le recuit et conduisent à la porosification du film. Dans le cas du dépôt à 100 et 200°C, un faible pourcentage des précurseurs peut être piégé dans le film. Le recuit initie la réaction exothermique locale d'hydrolyse du $TiCl_4$ résiduel dont la chaleur latente associée est caractéristique du mécanisme de recristallisation «explosive». Les films de TiO_2 à larges grains ont été caractérisés par l'EBSD qui a montré que le recuit initiant la recristallisation « explosive » du TiO_2 permet de stabiliser les orientations cristallines à forte énergie de surface.

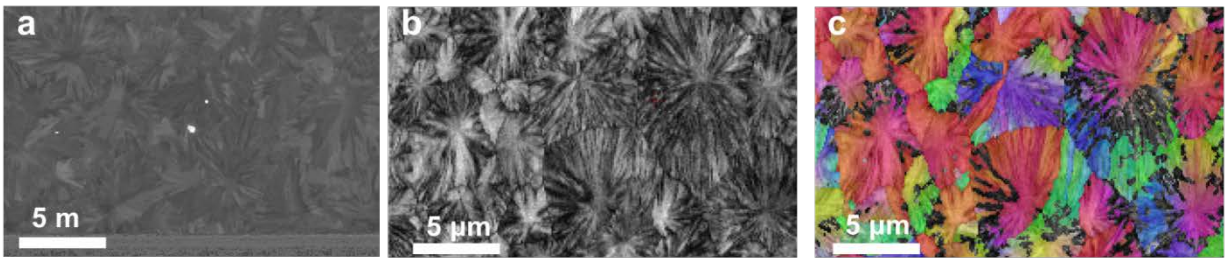

d

Orientation cristalline	Energie de surface, γ J/m²
{111}	1.61
{110}	1.09
{001}	0.90
{010}	0.53
{101}	0.44

Figure 5 Film de TiO_2 de 35 nm après le recuit : image MEB (a); band contrast (b) et cartographie EBSD (c); table récapitulative des énergies de surface en fonction de l'orientation des facettes d'anatase (d).

Etant donné que les films déposés à la température de 100 et 200°C sont les plus lisses après le recuit, ces régimes de dépôt sont sélectionnés pour le dépôt des films de TiO_2 dans les membranes AAO pour la fabrication des nanofils.

Réalisation des nanofils périodiques dans les membranes auto-organisées AAO

La croissance par ALD de films peu rugueux d'oxydes-métalliques nous a permis de réaliser des dépôts conformes dans les membranes AAO, nécessaires à la fabrication des nanostructures périodiques. Les nanostructures typiquement réalisées dans la littérature [15,16] en utilisant une approche similaire ont un rapport longueur des pores/diamètre très important (~4000) ; cependant la valeur élevée de ce rapport complique significativement la libération stable des nanostructures. Nous avons contourné ce problème en contrôlant la vitesse de gravure sélective de la matrice de l'alumine.

Les dépôts conformes réalisés par ALD forment toujours un film résiduel sur la surface de la membrane qui doit être retiré pour pouvoir graver la matrice d'AAO. Nous avons choisi d'appliquer une gravure sélective par voie sèche (Reactive Ion Etching - RIE) afin d'éliminer le film résiduel. Par la suite, une gravure chimique a été développée dans le but de retirer sélectivement la membrane tout en préservant le pied de celle-ci permettant le maintien mécanique des nanostructures en organisation verticale sans agrégation (Figure 6).

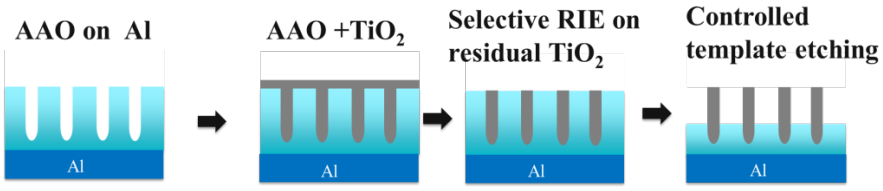

Figure 6 Schéma de la stratégie pour la fabrication des nanofils périodiques.

Le protocole de la gravure chimique est développé pour pouvoir retirer la matrice d'Al_2O_3 partiellement et pouvoir contrôler la longueur des nanofils et donc leur stabilité mécanique. Le réseau des nanofils développé présente un faible nombre de défauts à grande échelle (Figure 7). Apres le recuit à 600°C les nanofils cristallisent en phase anatase.

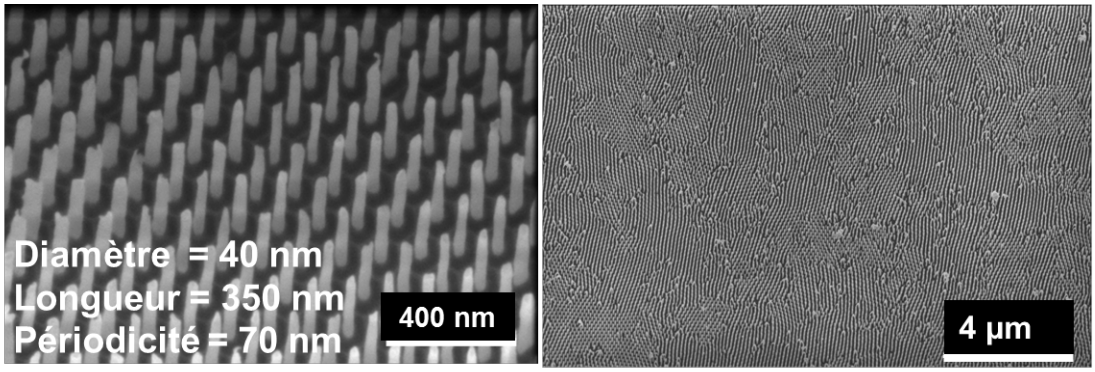

Figure 7 Images MEB du réseau des nanofils de TiO_2.

Optimisation des dépôts de SnO_2 par ALD

La synthèse des films de SnO_2 par ALD a été effectuée à partir de $SnCl_4$ et H_2O. Le défi de cette étude est similaire à celui du développement de films de TiO_2. Il est connu [17,18] que les films de SnO_2 synthétisés par ALD ont une rugosité très importante et donc *a priori* incompatible avec des pores nanométriques d'AAO. Néanmoins nous avons étudié les paramètres de synthèse afin d'améliorer la conformité de dépôt dans les substrats poreux. Dans un premier temps nous avons optimisé la croissance sur les surfaces planes d'alumine et également dans des membranes AAO commerciales de diamètre de pores de 200 nm. Nous avons déterminé les conditions optimales de dépôt à 350°C avec des temps de « pulse » de 0.2 s et des temps de « purge » de 5 s, et ce pour les deux précurseurs. Cependant les films obtenus dans les substrats poreux ne sont pas continus. Ce type de croissance peut être expliqué par deux mécanismes : (i) le HCl formé lors de la réaction peut graver le film, et (ii) à hautes températures le phénomène de désorption des espèces réactives, notamment

deshydroxylation ne permet pas de former une monocouche « continue » mais favoriserait plutôt la formation d'agrégats. Nous avons modifié l'état de surface d'AAO et de substrat Si en déposant un film de 20 nm de TiO_2 à basse température, recuit par la suite. Le TiO_2 est connu pour sa capacité hygroscopique même à hautes températures qui peut permettre d'améliorer la hydroxylation de la surface.

Le dépôt de SnO_2 réalisé sur ce film d'accroche (TiO_2 - anatase) montre un changement significatif de morphologie et de conformité des films dans les substrats poreux (AAO). Cette approche nous a permis de former directement des hétérostuctures SnO_2/TiO_2 (Figure 8).

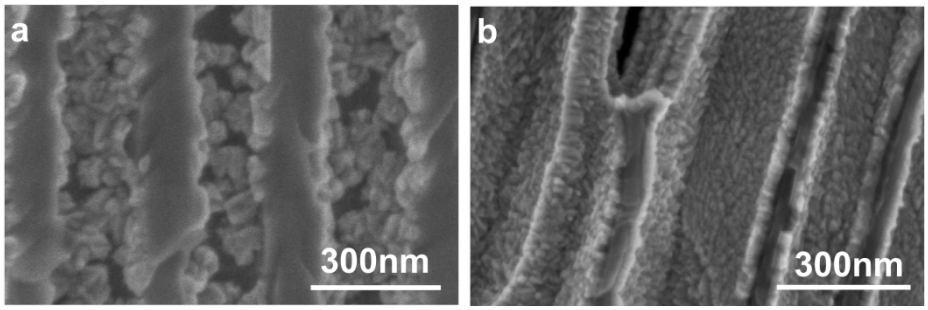

Figure 8 Images MEB en coupe transverse : (a) dépôt de SnO_2 dans AAO, (b) dépôt de SnO_2 dans AAO avec un film d'accroche de TiO_2 anatase.

Le dépôt sur les substrats planaires de Si (100) en utilisant le film d'accroche de TiO_2 à large grains montre également une différence significative de croissance de SnO_2 en fonction de l'orientation des grains de TiO_2 (Figure 9). On attribue une croissance très lisse aux grains à haute énergie de surfaces tels que (111), (110) et (001).

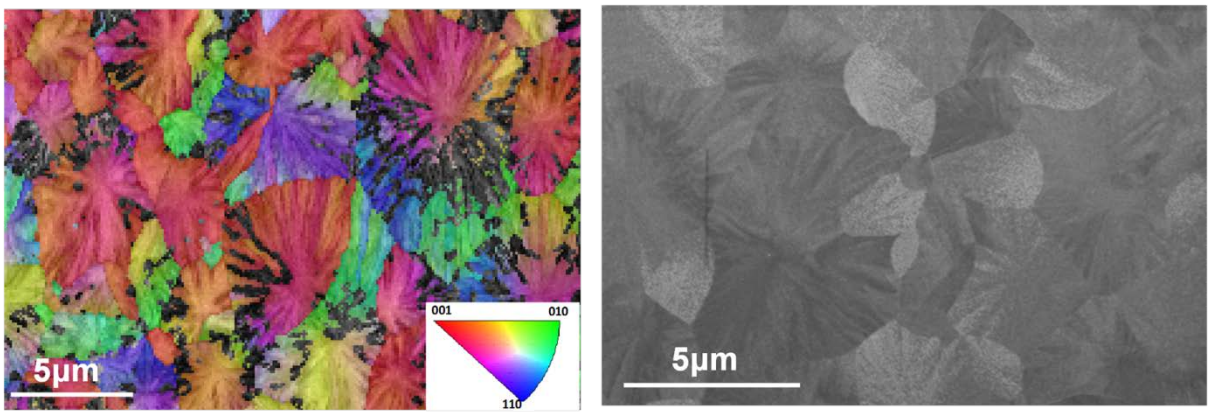

Figure 9 Cartographie EBSD du film d'accroche de TiO_2 (gauche) et image MEB après le dépôt de SnO_2 (droit).

L'application des protocoles développés de la gravure ionique et chimique a permis de développer les hétérostructures SnO_2/TiO_2 organisées périodiquement (Figure 10).

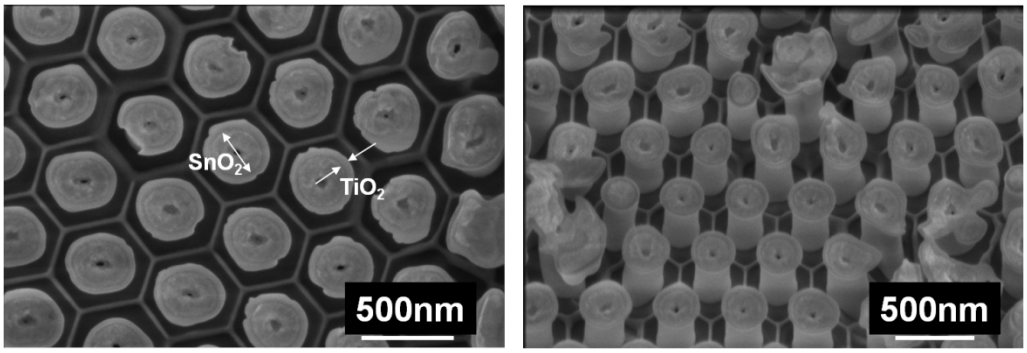

Figure 10 Nanostructures SnO_2/TiO_2 périodiquement organisées.

Fabrication des nanoparticules plasmoniques

Une approche similaire à celle utilisée pour la fabrication des nanoparticules de TiO_2 permet également de fabriquer des nanoparticules avec différents matériaux, notamment les nanoparticules métalliques. Nous avons réalisé la fabrication de nanoparticules d'or auto-organisées sur la surface. Les micelles ont été imprégnées dans une solution aqueuse de précurseur d'or ($HAuCl_4*3H_2O$). Par la suite, un traitement de plasma oxygène permet de retirer le polymère et un recuit à 500°C favorise la réduction du précurseur (Figure 11).

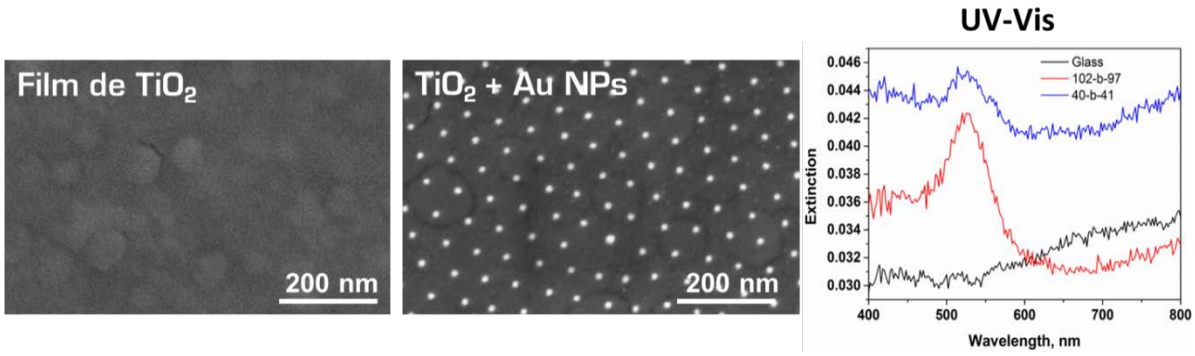

Figure 11 Image MEB des films de TiO_2 (gauche), films de TiO_2 avec les nanoparticules d'or (centre) et leur spectre UV-VIS (droit)

En résumé le travail de thèse a abouti à la fabrication de six architectures différentes de TiO_2 :

- Films colonnaires et continus (MOCVD) ;
- Films poreux (ALD) ;
- Films à larges grains (ALD) ;
- Nanofils de TiO_2 organisés périodiquement ;
- Hétérostructures SnO_2/TiO_2 ;
- Films de TiO_2 fonctionnalisés avec des nanoparticules plasmoniques d'or.

Les propriétés photocatalytiques sous irradiations UV et Visible des différentes architectures sont caractérisées.

Tests photocatalytiques

Les performances photocatalytiques des systèmes fabriqués ont été évaluées principalement sur la molécule modèle du bleu de méthylène (BM) mais aussi sur la rhodamine B (RhB) et l'acide salicylique (SA). Les tests de la dégradation photocatalytique ont été réalisés sur une installation développée au laboratoire. Chaque échantillon fut testé dans un système fermé, en quartz, afin de minimiser l'erreur de la mesure due à l'évaporation de la solution.

Les films déposés par MOCVD montrent une activité photocatalytique sous UV proche à la dégradation photocatalytique du TiO_2 classique. Néanmoins, les films continus déposés à 15 mbar et 300°C montrent la meilleure activité photocatalytique que les films colonnaires. Ceci est attribué aux défauts structuraux comme les lacunes d'oxygène.

Pour les films de TiO_2 déposés par ALD, le meilleur taux de dégradation est déterminé pour les films poreux déposés à la température ambiante (Figure 12). Il est important de noter que la constante de dégradation, normalisée par la surface géométrique de l'échantillon est de $57.6 \cdot 10^{-4}$ $min^{-1}cm^{-2}$, ce qui est 3 fois plus rapide que les valeurs rapportées dans la littérature pour des conditions de tests photocatalytiques similaires sur le TiO_2 macro-mesoporeux ($20.5 \cdot 10^{-4}$ $min^{-1}cm^{-2}$) [20].

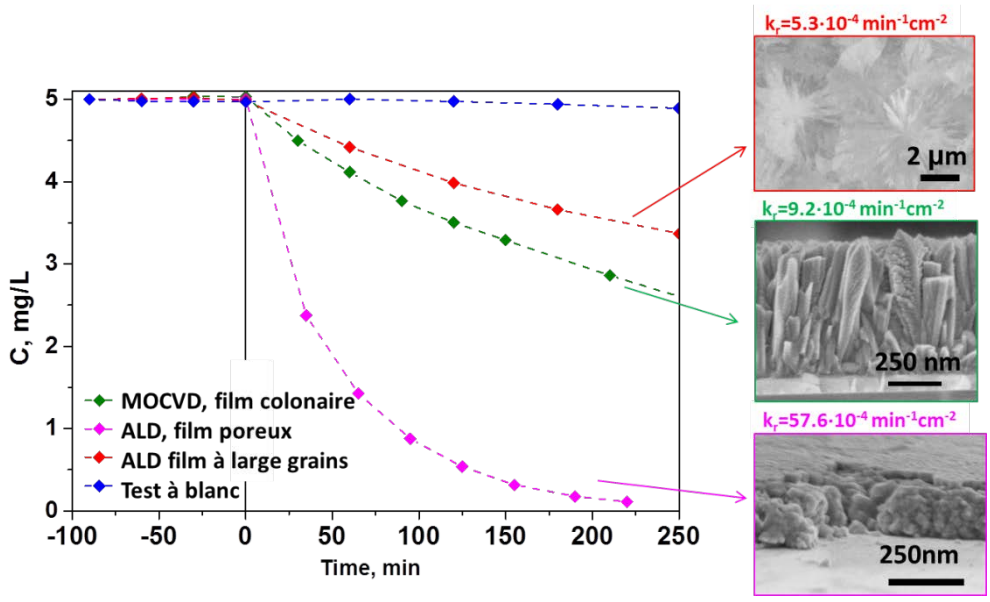

Figure 12 Courbes de la dégradation photocatalytique sur les films de TiO_2 synthétisés par MOCVD et ALD.

Les mêmes films ont été testés sous irradiation visible (400-700 nm) et ont montré une dégradation photocatalytique (Figure 13). La vitesse de la dégradation normalisée par la surface géométrique est du même ordre de grandeur que le TiO_2 classique sous UV (~$8 \cdot 10^{-4}$ $min^{-1}cm^{-2}$).

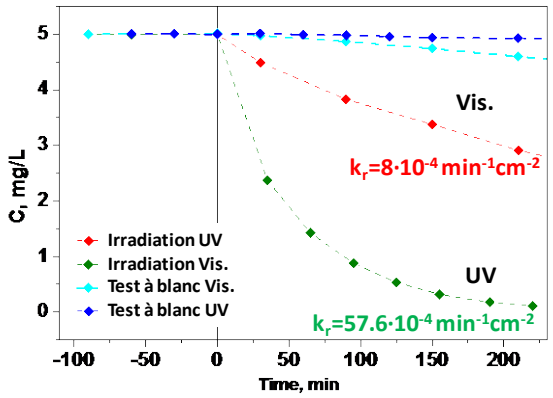

Figure 13 Courbes de la dégradation photocatalytique sur les films de TiO_2 mésoporeux sous irradiation UV et Visible.

La dégradation photocatalytique sur les échantillons méso-poreux de TiO_2 sous irradiation UV est un résultat remarquable qui nécessite une étude détaillée. Les propriétés optiques des films ont été étudiées par spectroscopie UV-Visible en transmission et par photoluminescence (PL) (Figure 14).

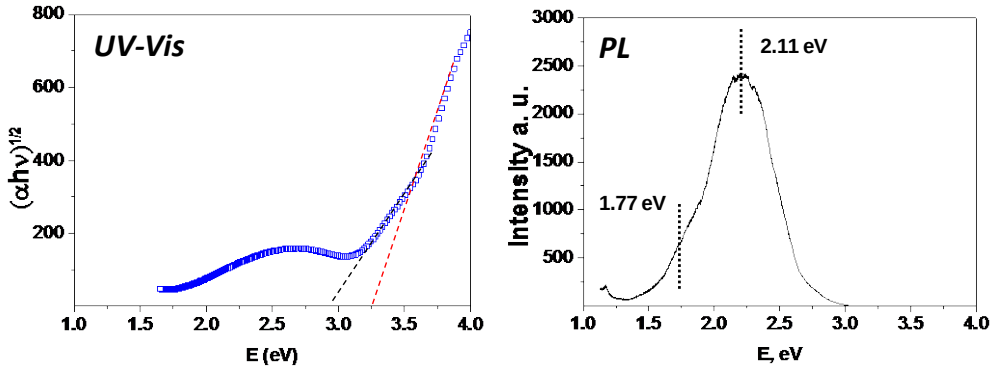

Figure 14 Propriétés optiques de film de TiO_2 mésoporeux : Tauc plot (à gauche); spectre de la photoluminescence (à droite).

La spectroscopie UV-VIS montre la présence de « bandgaps » optiques distincts à 3.2 eV et 2.9 eV ainsi qu'un pic d'absorbance dans la gamme visible à ~ 2.5 eV. Le spectre de la PL montre la présence de deux niveaux de luminescence dans la bande interdite à 2.11 et 1.77 eV. Ces résultats sont relativement en accord avec la littérature pour le TiO_2 traité par hydrogène. Notamment le niveau à 2.11 eV est attribué aux lacunes d'oxygène, tandis que l'épaulement à 1.7 eV n'est pas encore défini. Il a été démontré que le traitement de TiO_2 par

hydrogène (H-TiO_2) apporte une certaine désorganisation structurale de la maille cristalline de TiO_2 anatase et induit des niveaux « mid-gap » à l'origine de l'absorption de la lumière dans le visible. Cela peut expliquer l'activité photocatalytique des films mésoporeux sous la lumière visible.

Les différents polluants modèles (BM, RhB, SA) ont été testés sur les films mésoporeux sous irradiations UV et VIS. La dégradation photocatalytique sous UV présente la même vitesse de dégradation pour les trois molécules modèles. Sous irradiation visible, les mêmes molécules sont également dégradées avec des cinétiques différentes dans l'ordre MB, SA > RhB (Figure 15).

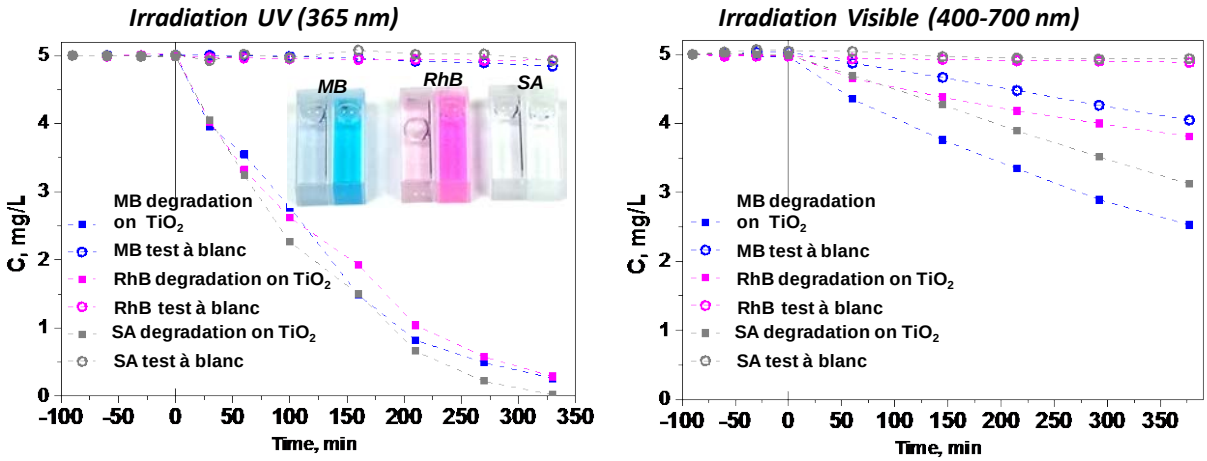

Figure 15 Courbes de la dégradation photocatalytique sur les films de TiO_2 mésoporeux sous irradiation UV et Visible sur MB, RhB et SA.

Les activités photocatalytiques des nanofils de TiO_2 organisés périodiquement ont également été étudiées. Le réseau des nanofils développé n'a pas apporté d'amélioration de l'activité photocatalytique par rapport aux films planaires. Cela est premièrement associé aux recombinaisons des paires électron/trou sur les défauts structuraux des nanofils. Deuxièmement, les films planaires présentent des larges grains à forte énergie de surface élevée. L'étude plus approfondie de la microstructure des nanofils est prévue en perspective.

Les hétérostructures SnO_2/TiO_2 n'ont pas démontré une amélioration de l'activité photocatalytique. En effet, ces hétérostructures augmentent significativement l'hydrophobicité des nanostructures organisées périodiquement.

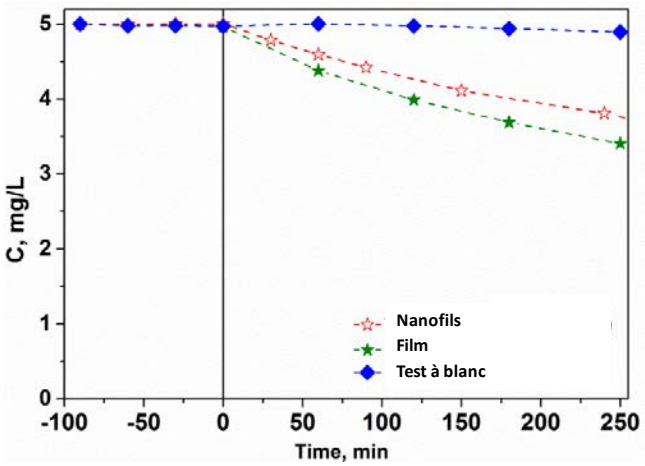

Figure 16 Courbes de la dégradation photocatalytique du MB sur les nanofils de TiO_2 et le film planaire (déposé dans les mêmes conditions) sous irradiation UV.

Nous avons également réalisé un assemblage des films de TiO_2 mésoporeux avec des nanoparticules plasmoniques d'or. Deux types d'assemblage des nanoparticules/film sont réalisés suivant les protocoles de fabrication:

1. Film de TiO_2 (recuit à 600°C) → dépôt des nanoparticules → recuit (600°C)
2. Film de TiO_2 (amorphe) → dépôt des nanoparticules → recuit (600°C)

L'assemblage de type 1 n'a pas apporté une amélioration de l'activité photocatalytique, potentiellement due au mauvais contact électronique entre le film et les nanoparticules. Dans le cas d'assemblage selon le deuxième protocole, l'activité photocatalytique est améliorée sous irradiation UV mais les nanoparticules tendent à se désactiver au fur et à mesure de la réaction photocatalytique (Figure 17). Sous irradiation visible, les films de TiO_2 mésoporeux sans l'assemblage avec les nanoparticules montrent une meilleure activité photocatalytique.

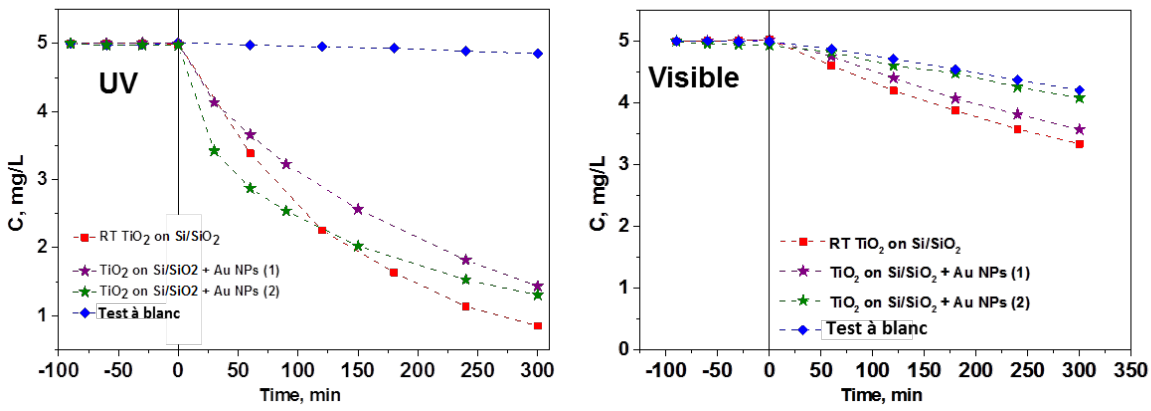

Figure 17 Courbes de la dégradation photocatalytique du MB sur films de TiO_2 sans et avec les nanoparticules d'or assemblées selon les deux protocoles.

Conclusion

Deux stratégies de fabrication de nanofils de TiO_2 organisés périodiquement sont étudiées lors de cette thèse. La première approche en utilisant les nanoparticules auto-organisées de TiO_2 et la croissance en phase vapeur n'a pas abouti en croissance sélective des nanofils de TiO_2. La taille des ilots de TiO_2 est potentiellement inferieure au rayon critique nécessaire pour induire une croissance sélective.

La deuxième approche de fabrication consiste en l'utilisation des membranes d'alumine poreuses (AAO) et le développement des films de TiO_2 par ALD, compatibles avec la taille des pores d'AAO (40 nm). Les films lisses de TiO_2 ont été démontrés ainsi que les protocoles de gravure chimique permettant de fabriquer le réseau de nanofils de TiO_2 organisés périodiquement à grande échelle et avec un faible nombre de défauts morphologiques. Ce résultat est un accomplissement technologique majeur de cette thèse.

Le développement des films de TiO_2 par ALD a aussi abouti à la fabrication des films mésoporeux de TiO_2, potentiellement hydrogénés qui montrent une activité photocatalytique importante dans l'UV mais aussi dans le Visible avec des constantes de dégradation proches de celles de TiO_2 classique sous UV. La dégradation photocatalytique est stable et la vitesse de dégradation est indifférente de la nature de molécules à dégrader (BM, RhB, SA). Ce type de TiO_2 montre un potentiel très important pour la dégradation photocatalytique sous irradiation visible et sans dopage, sans éléments toxiques et sans assemblage avec des nanoparticules plasmoniques. L'étude plus approfondie des propriétés des films mesoporeux est prévue en perspective.

Références

1. Grätzel M. Solar energy conversion by dye-sensitized photovoltaic cells. Inorg Chem [Internet]. 2005 Oct 3;44(20):6841–51. Available from: http://www.ncbi.nlm.nih.gov/pubmed/16180840

2. Pelaez M, Nolan NT, Pillai SC, Seery MK, Falaras P, Kontos AG, et al. A review on the visible light active titanium dioxide photocatalysts for environmental applications. Appl Catal B Environ [Internet]. Elsevier B.V.; 2012 Aug [cited 2014 Jul 15];125:331–49. Available from: http://linkinghub.elsevier.com/retrieve/pii/S0926337312002391

3. Chen Y, Liu B, Chen J, Tian L, Huang L, Tu M, et al. Structure design and photocatalytic properties of one-dimensional SnO2-TiO2 composites. Nanoscale Res Lett [Internet]. 2015;10(1):0–5. Available from: http://www.nanoscalereslett.com/content/10/1/200

4. Wu JM, Chen Y. Ultraviolet-Light-Assisted Formation of ZnO Nanowires in Ambient Air : Comparison of Photoresponsive and Photocatalytic Activities in Zinc Hydroxide. 2011;2235–43.

5. Kumar Challa K, Goswami SK, Oh E, Kim E-T. Effect of CdS film thickness on the photoexcited carrier lifetime of TiO2/CdS core-shell nanowires. Appl Phys Lett [Internet]. 2011 [cited 2014 Feb 18];99(15):153111. Available from: http://link.aip.org/link/APPLAB/v99/i15/p153111/s1&Agg=doi

6. Sfaelou S, Kontos AG, Falaras P, Lianos P. Micro-Raman, photoluminescence and photocurrent studies on the

photostability of quantum dot sensitized photoanodes. J Photochem Photobiol A Chem [Internet]. Elsevier B.V.; 2014 Feb [cited 2014 Feb 5];275:127–33. Available from: http://linkinghub.elsevier.com/retrieve/pii/S1010603013004851

7. Zaleska A. Doped-TiO2: A Review. Recent Patents Eng [Internet]. 2008;2(3):157–64. Available from: http://www.eurekaselect.com/openurl/content.php?genre=article&issn=1872-2121&volume=2&issue=3&spage=157

8. Dozzi MV, Selli E. Doping TiO2 with p-block elements: Effects on photocatalytic activity. J Photochem Photobiol C Photochem Rev [Internet]. Elsevier B.V.; 2013;14(1):13–28. Available from: http://dx.doi.org/10.1016/j.jphotochemrev.2012.09.002

9. Carmichael P, Hazafy D, Bhachu DS, Mills A, Darr J a, Parkin IP. Atmospheric pressure chemical vapour deposition of boron doped titanium dioxide for photocatalytic water reduction and oxidation. Phys Chem Chem Phys [Internet]. 2013;15(39):16788–94. Available from: http://www.ncbi.nlm.nih.gov/pubmed/23999866

10. Dunnill CW, Parkin IP. Nitrogen-doped TiO2 thin films: photocatalytic applications for healthcare environments. Dalton Trans. 2011;40(8):1635–40.

11. Krishnamoorthy S, Pugin R, Brugger J, Heinzelmann H, Hinderling C. Nanopatterned Self-Assembled Monolayers by Using Diblock Copolymer Micelles as Nanometer-Scale Adsorption and Etch Masks. Adv Mater [Internet]. 2008 May 19 [cited 2014 Mar 28];20(10):1962–5. Available from: http://doi.wiley.com/10.1002/adma.200702005

12. Kumar MK, Krishnamoorthy S, Tan LK, Chiam SY, Tripathy S, Gao H. Field Effects in Plasmonic Photocatalyst by Precise SiO 2 Thickness Control Using Atomic Layer Deposition. ACS Catal [Internet]. 2011;1(4):300–8. Available from: http://dx.doi.org/10.1021/cs100117v

13. Yin J, Xu Q, Wang Z, Yao X, Wang Y. Highly ordered TiO2 nanostructures by sequential vapour infiltration of block copolymer micellar films in an atomic layer deposition reactor. J Mater Chem C [Internet]. 2013 [cited 2014 May 19];1(5):1029–36. Available from: http://xlink.rsc.org/?DOI=c2tc00306f

14. Cheng H-E, Chen C-C. Morphological and Photoelectrochemical Properties of ALD TiO2 Films. J Electrochem Soc. 2008;155(9):D604.

15. Liu S, Huang K. Straightforward fabrication of highly ordered TiO 2 nanowire arrays in AAM on aluminum substrate. Sol Energy Mater Sol Cells. 2005;85:125–31.

16. Yao Z, Wang C, Li Y, Kim N-Y. AAO-assisted synthesis of highly ordered, large-scale TiO2 nanowire arrays via sputtering and atomic layer deposition. Nanoscale Res Lett [Internet]. 2015;10(1):166. Available from: http://www.nanoscalereslett.com/content/10/1/166

17. Roge V, Georgantzopoulou A, Mehennaoui K, Fechete I, Garin F, Dinia A, et al. Tailoring the optical properties of ZnO nano-layers and their e ff ect on in vitro biocompatibility. RSC Adv. 2015;5:97635–47.

18. Meng X, Zhang Y, Sun S, Li R, Sun X. Three growth modes and mechanisms for highly structure-tunable SnO2 nanotube arrays of template-directed atomic layer deposition. J Mater Chem [Internet]. 2011 [cited 2015 Jul 30];21(33):12321. Available from: http://xlink.rsc.org/?DOI=c1jm11511a

19. Selloni A. Crystal growth: Anatase shows its reactive side. Nat Mater. 2008;7(8):613–5.

20. Du J, Lai X, Yang N, Zhai J, Kisailus D, Su F, et al. Hierarchically ordered macro-mesoporous TiO2-graphene composite films: Improved mass transfer, reduced charge recombination, and their enhanced photocatalytic activities. ACS Nano. 2011;5(1):590–6.

Contents

List of Tables

List of Figures

List of Abbreviations

AAO: Anodized Aluminium Oxide

AFM: Atomic Force Microscope

ALD: Atomic Layer Deposition

AR: Anti-reflection

ARC: Anti-reflective Coating

BCP: Block Copolymer

BF: Bright Field

BSE: Backscattered Electrons

CB: Conduction Band

CBO: Conduction Band Offset

CCD: Charge-Coupled Device

CPD: Contact Potential Difference

CVD: Chemical Vapour Deposition

DF: Dark Field

DRX: X-ray Diffraction

EBSD: Electron Back Scatter Diffraction

EDX: Energy Dispersive X-ray spectroscopy

FdM: Frank van der Merwe

FIB: Focuced Ion Beam

FTIR: Fourier Transform Infrared spectroscopy

GPC: Growth Per Cycle,

HBA: Hydroxybenzoic Acid

JCPDS: Joint Committee on Powder Diffraction Standards

KPFM: Kelvin Probe Force Microscope

LC/MS: Liquid Chromatography–Mass Spectrometry

LSPR: Localized Surface Plasmon Resonance

MB: Methylene Blue

MBE: Molecular Beam Epitaxy

MOCVD: Metal - Organic Chemical Vapour Deposition

NHE: Normal Hydrogen Electrode

PDF: Powder Diffraction File

PL: Photoluminescence

PLD: Pulsed Laser Deposition

PMMA: Poly(methyl methacrylate)

PS-b-P2VP: Polystyrene-b-poly-2-vinylpyridine

PS-b-PEO: Polystyrene-b-poly(ethylene oxide)

PVD: Physical Vapour Deposition

PVP: Poly-vinylpyridine

QCM: Quartz Crystal Microbalance

RhB: Rhodamine B

RIE: Reactive Ion Etching

RT: Room Temperature

SE: Secondary Electrons

SEM: Scanning Electron Microscope

SG: Staggered Gap

SIMS: Secondary Ion Mass Spectrometry

SK: Stranski–Krastanov

SPR: Surface Plasmon Resonnance

STEM-HAADF: Scanning Transmission Electron Microscopy - High-Angle Annular Dark-Field imaging

SVI: Sequential Vapour Infiltration

SVIS: Sequential Vapour Infiltration Synthesis

TBOT: Tetrabutyltitanate,

TDMATi: Tetrakis (dimethylamido) Titanium

TEM: Transmission Electron Microscope

TMA: Trimethylaluminium

TTIP: Titanium-tetraisopropoxide

UN WWAP: United Nations World Water Assessment Programme

UNICEF: United Nations International Children's Emergency Fund

UV: Ultraviolet

VB: Valence Band

VBO : Valence Band offset

VLS: Vapour Liquid Solid

VW: Volmer–Weber

WCA: Water Contact Angle

WHO: World Health Organisation

XPS: X-ray Photoelectron Spectroscopy

XRD: X-ray Diffraction

Introduction

Context

The issue of environmental pollution is one of the most discussed modern challenges. The pollution due to the economic activities of developed and developing countries have important impacts on water or air quality. Industrial activities are clearly the source of pollution. However, organic waste such as sewage or farming activities waste also has an important environmental impact. Every day, 2 million tonnes of sewage and industrial and agricultural waste are discharged into the world's water (UN WWAP 2003), the equivalent of the weight of the entire human population of 6.8 billion people. This is critical, knowing that only 2.5 % of the total volume of available water on Earth is fresh. What is more, according to WHO and UNICEF, approximately 894 million people globally do not have access to improved water sources. On an average, 250 million people worldwide succumb to diseases related to water pollution [1]. Water purification in modern societies has become a critical need. In general, water purification consists of complex physicochemical processes such as coagulation and flocculation into insoluble phase, sedimentation, several filtration steps, and disinfection. Several types of disinfection exist, such as the use of chlorine, ozone or UV radiation. However, the purified water introduced to the rivers still contains chemical substances, such as antibiotics or pesticides. This means there is a need to improve the efficiency of water purification to increase the accessibility of purified water and to prevent the release of pollutants into the ecosystem.

Research problem

The photocatalytic approach was proposed several decades ago as an eco-friendly solution for water and air pollution by the degradation of pollutants in the aqueous or gas phases. The possibility of degradation of complex organic compounds into simple CO_2 and H_2O seems very attractive and promising for environmental remediation. A range of semiconductor materials can initiate the redox degradation mechanism due to their electronic band structures. The first water splitting property was shown by Honda-Fujishima on titanium dioxide initiated by the irradiation lower than 400 nm, that corresponds to the TiO_2 band gap at 3.0 eV [2]. Since then, a large number of investigations has been published over the last four decades. However, the high potential of this approach still attracts interest from the scientific community.

The existing photocatalytic materials that meet the criteria, namely, to be chemically stable, biocompatible, non-toxic and low-cost, are TiO_2, ZnO, and SnO_2 [3][4]. A significant amount of work has been dedicated to understanding and improving the performances of photocatalysis, where TiO_2 remains the leading material for environmental remediation.

The main problem of basic photocatalysis is the wide band gap that limits the light absorption. In fact, the activation of photocatalytic materials is only allowed for light with lower wavelengths (higher frequencies) than the band gap energy; this means that only 3-4% of the solar spectrum could be involved in the photocatalytic reaction. The activation of the photocatalytic material under visible light became a major challenge for the scientific community. However, it is not only the limited range of light frequencies but also a short carrier lifetime due to recombination that reduces its efficiency.

Objectives and approaches

Currently, the major research efforts to improve the efficiency of the photocatalytic reaction are based on band gap tuning via the doping of known metal oxides (with C, P, N, etc.) or the introduction of other lattice defects, fabrication of heterostructures with overlapping band-gap levels (ZnO/SnO_2), and coupling the metal oxides with plasmonic nanoparticles. This last approach is very promising regarding the spectral shift in the light absorption. The plasmonic nanoparticles are acting to improve carrier trapping by reducing the electron-hole recombination in the UV range, but they also allow activation by visible light. Under visible light, the metal nanoparticles produce the phenomenon of surface electron oscillations known as the surface plasmon resonance (SPR). The downside to this plasmonic approach is the possible overlapping of the photocatalytic surface by the metal nanoparticles, which could reduce the specific surface area of metal oxides.

Another potential approach is the improvement of the light absorption for more efficient light to carrier conversion is in the use of periodically organised nanostructures. It was also shown in the literature that the nanostructuration of films increases the efficient light absorption by increasing the light path, reducing reflection [5]–[7].

In the present work, we examine the fabrication of highly organised TiO_2 nanostructures and their assembly with plasmonic nanoparticles. The fabrication of periodically organised TiO_2 free-standing nanowires is a true technological challenge. The development of the fabrication approaches for such nanostructure fabrication is expected from principally vapour-phase

deposition techniques as ALD and MOCVD assisted with growth limitations as the controlled deposition of nanoparticle seeds or templating.

Thesis structure

Although the objective is the development of periodically organised TiO_2 nanowires, we intend to achieve a more general goal, namely, the improvement of the photo-response basic photocatalysts without using hazardous materials. Therefore, in the first chapter of this thesis an analysis of the current technological state of basic photocatalyst systems is presented. Furthermore, the existing and potential approaches to the improvement of the basis photocatalyst principles are discussed to define the research strategy better. To achieve the technological objective fabricating of freestanding TiO_2 nanowires, a review of the current technological state of the existing TiO_2 nanowire methods is presented in the *Materials and Methods* chapter. The literature overview will allow us to define our technological strategy. To that end, the fabrication techniques, as well as the optimisation procedures, are presented in this chapter. The results of the nanostructure fabrication and development are presented in the *Results and Discussion* chapter. The first part of this chapter discusses aspects of the fabrication, and the second part presents the functional application of the developed materials to photocatalysis. The materials development is divided into three categories according to the fabrication approaches. The first one presents the development of the well organised TiO_2 seed nanoparticles by the block-copolymer method. This chapter is followed by the vapour-phase deposition of TiO_2 by MOCVD to find the selective growth regime that the nanoparticles require. The second approach that is addressed in this thesis is the templated fabrication of periodic metal-oxide nanostructures. Therefore, the optimisation of the smooth thin film of TiO_2 and SnO_2 grown by ALD, being compatible with the membrane architecture, is presented.

The valorisation of the developed materials is dependent on their photocatalytic performances in both UV and visible ranges. The results of the photocatalytic test correlated with physicochemical properties of the materials allow us drawing the conclusions and future perspectives of this work in the final chapter.

1 State of the art

1.1 Principle of photocatalysis

A catalyst is a substance that allows the acceleration of a chemical reaction by lowering its free activation energy while the catalyst itself does not undergo any permanent modification [8]. A photocatalyst is a photo-sensitive substance that manifests its catalytic properties via a photon absorption. One can draw a simplistic analogy with photosynthesis in green plants in which chlorophyll plays the role of a photosensitive catalyst to transform CO_2 and water into energy and O_2 (Figure 1-1). A photocatalyst is typically a semiconductor material that under light irradiation and in the presence of water and/or oxygen forms highly reactive species, i.e. radicals. These radicals have a strong ability to oxidise organic molecules and enable their degradation.

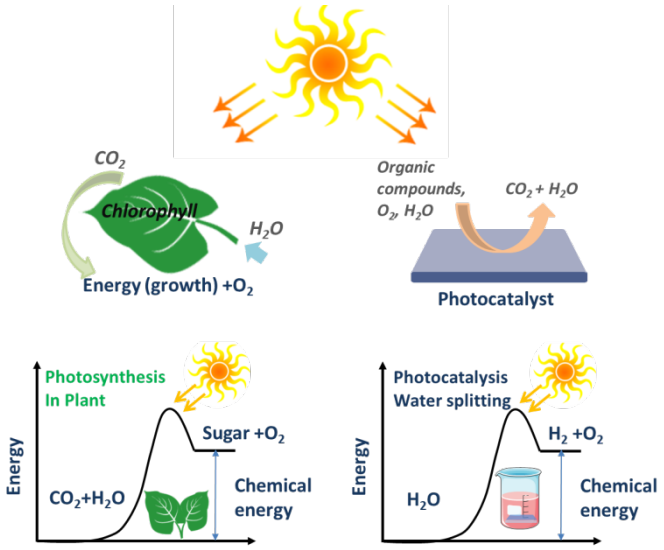

Figure 1-1 Simplistic comparison between photosynthesis and photocatalysis.

Since Honda-Fujishima [2] first reported on water-splitting into O_2 and H_2 under UV irradiation at 400 nm on titanium dioxide electrode, the domain of photocatalysis has undergone significant development. Various photocatalytic materials have already been reported in the literature. They are classified among the families of metal-oxides, metal-sulfides, metal nitrides as well as metal free compounds such as polymers or graphene [9][10]. Metal oxides such as TiO_2, ZnO, Fe_2O_3, ZrO_2, SnO_2, MgO, GeO_2, Sb_2O_3, V_2O_5, WO_3, In_2O_3 and Nb_2O_5 as well as perovskite materials are among the most investigated materials for photocatalysis today. The particular interest in classically photocatalytic materials such as TiO_2 and in a lesser extent ZnO and SnO_2 is due to their high photocatalytic activity, good chemical stability, non- or low-toxicity, and low cost.

One of the key elements characterising photocatalytic materials is the interaction with light and in particular the photon absorption. A photon with an energy higher than the semiconductor band gap energy can be absorbed by the photocatalytic material. A photon absorption will excite electrons from the valence band (VB) and promote them to the conduction band (CB) (e_{CB}^-), generating holes in the VB (h_{VB}^+). These generated carriers (e^-, h^+) may migrate to the material surface and since they are in contact with water and/or oxygen molecules, they induce the formation of $OH^\bullet$ and $O_2^{\bullet-}$ radicals (Figure 1-2) [11].

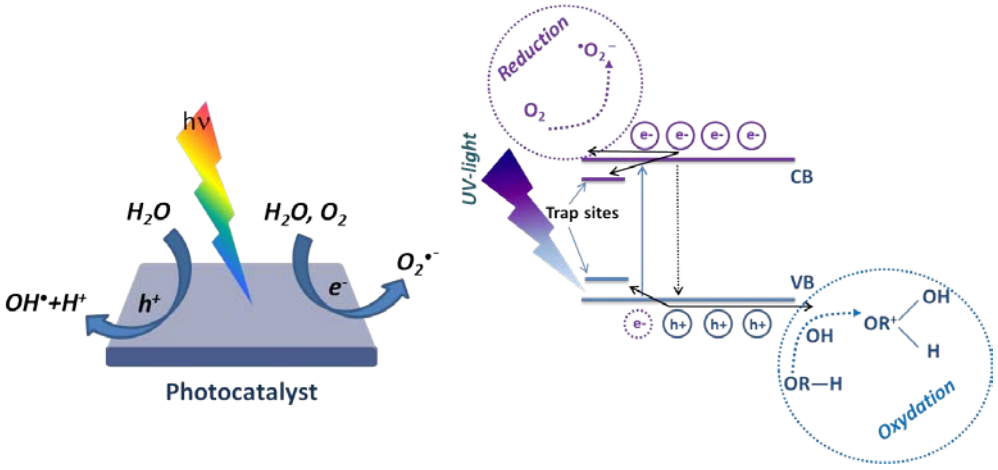

Figure 1-2 Scheme of the photocatalysis principle.

On the surface and depending on the photocatalyst, holes have a typical oxidative potential from +1 to +3.5 V compared to the Normal Hydrogen Electrode (NHE), and electrons have a reduction potential from +0.5 to -1.5 V [3]. The redox potential value of the semiconductor is determined by its electronic band structure. The main condition of $OH^\bullet$ radicals generation is that the potential of valence band should be higher than the potential of hydroxyl radical formation. Figure 1-3 represents the positioning of the band gap energy compared to the potential of radicals formation. The redox potential of $OH^\bullet$, H^+/H_2O is 2,31 V vs NHE [12]. The formation of superoxide radicals $O_2^{\bullet-}$ by e_{CB}^- requires a potential of 0.92 V vs NHE. Superoxide radicals formation is typically induced when the semiconductor's CB energy is higher than this threshold potential.

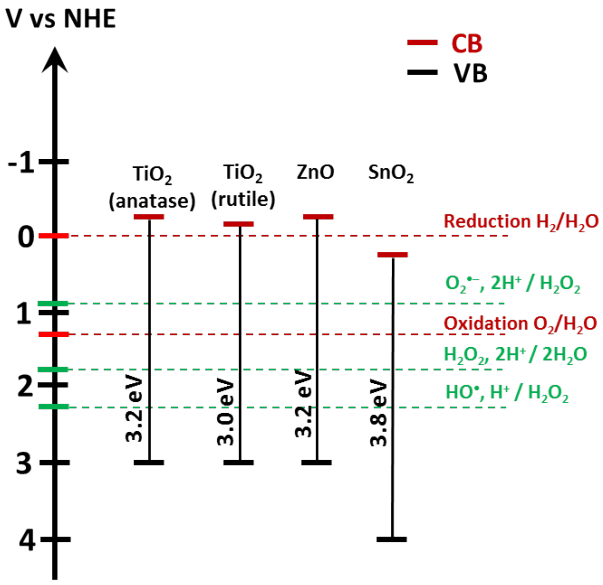

Figure 1-3 Band gap energy for TiO_2, ZnO and SnO_2 on a potential scale (V) versus the normal hydrogen electrode (NHE).

The degradation of organic molecules mainly relies on high oxidative potential of $OH^{\bullet}$ radicals, which enables the breaking of C-C bonds. A typical photocatalytic degradation reaction of organic molecules has been reported with TiO_2 as photocatalyst [3],[11],[13]:

first, the carriers are photo-generated under photon absorption within a few femto-second range:

$$TiO_2 + hv \rightarrow e^- + h^+ \quad (1\text{-}1)$$

The electrons in contact with the adsorbed oxygen molecules demonstrate their reductive potential and form superoxide radicals:

$$(O_2)_{ads} + e^- \rightarrow O_2^{\bullet -} \quad (1\text{-}2)$$

The interaction between holes and water molecules produces hydroxyl radicals $OH^{\bullet}$

$$(H_2O \leftrightarrow H^+ + OH^-)_{ads} + h^+ \rightarrow H^+ + OH^{\bullet}$$

The superoxide radicals being very reactive (non-stable), they can react with H^+ and undergo a fast transformation in $OH^{\bullet}$ radicals

$$O_2^{\bullet -} + H^+ \rightarrow HO_2^{\bullet} \quad (1\text{-}3)$$

$$2HO_2^{\bullet -} \rightarrow H_2O_2 + O_2 \quad (1\text{-}4)$$

$$H_2O_2 + e^- \rightarrow OH^{\bullet} + OH^- \quad (1\text{-}5)$$

Hydroxyl radicals enables the organic molecule oxidation:

$$R + OH^{\bullet} \rightarrow R'^{\bullet} + H_2O \quad (1\text{-}6)$$

$$R + h^+ \rightarrow R^{+\bullet} \rightarrow degradation\ products$$

1.2 Basic photocatalytic systems

Typically, photocatalytic systems belong to the family of binary metal oxides such as TiO_2, ZnO or SnO_2. These materials can be characterised as wide band gap semiconductors having a light absorption in the UV range. Historically, TiO_2 was the first commercialised and mainly used material for its photocatalytic properties. Tin oxide having particular electronic and optical properties, it is also successfully applied in photocatalytic degradation, but requires deeper UV irradiation [14].

This work mainly relied on advanced TiO_2 and SnO_2 nanostructures, therefore, their physical and chemical properties are hereafter summarised.

1.2.1 Titanium dioxide

The improvement of the photocatalytic degradation process requires a clear understanding of photocatalytic materials properties. Although TiO_2 is the most studied photocatalyst, it continues to attract attention from the scientific community [15].

The various TiO_2 applications are principally based on UV-light absorption, such as UV light protection, photocatalysis, hydrogen production and solar cells. TiO_2 is also applied in gas sensors, varistor and as anti-corrosive coatings.

Crystallographic structure

TiO_2 exists in three main crystallographic phases: anatase, rutile and brookite [16]. Rutile is the thermodynamically stable phase while anatase and brookite are metastable. Both anatase and rutile modifications have tetragonal structures; brookite possesses orthorhombic structure. For all polymorphic TiO_2 structures, TiO_6 octahedrons represent basic blocks, where the Ti atom is bonded with 6 oxygen atoms, and each oxygen atom is bonded with three Ti atoms. In the anatase structure, each TiO_6 octahedron has 4 shared edges and 4 shared corners with 8 neighbours. The edge shared octahedra are aligned along [100] or [010] direction, forming zigzag chains perpendicular to *c* axis. In the rutile structure, each TiO_6 octahedron is connected with 10 neighbour octahedrons having 2 shared edges and 8 shared corners. The edge shared octahedrons are aligned along the [001] direction [17]. The unit cell parameters for anatase, rutile and brookite is illustrated in Figure 1-4.

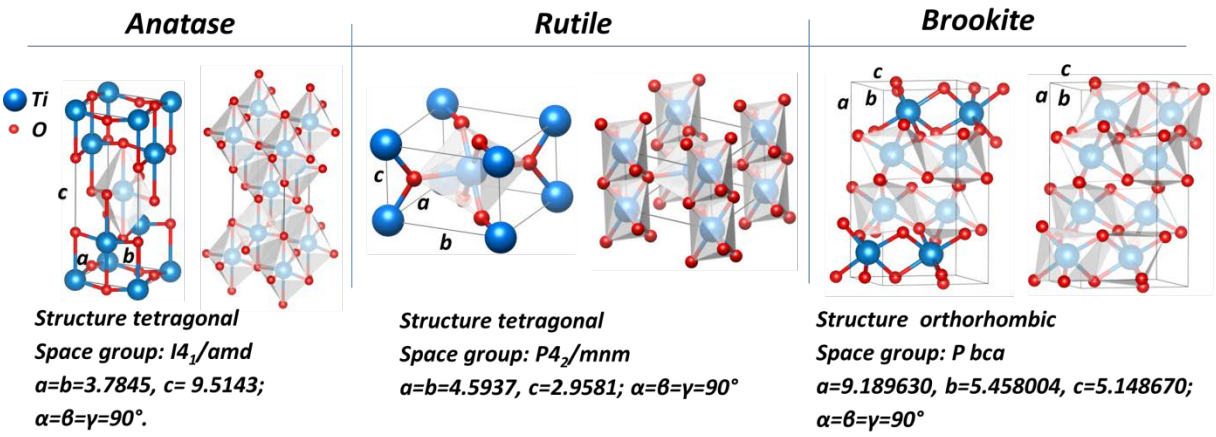

Figure 1-4 Crystalline structures of anatase, rutile and brookite.

Electronic properties

TiO_2 is a wide band gap semiconductor with a band gap value of 3.2 eV for anatase and 3 eV for rutile. The anatase phase has electrons mobility higher than rutile phase due to the lower electrons effective mass ($1m_0$ for anatase and $9\text{-}13m_0$ for rutile) [17], [18].

In the TiO_2 electronic band gap structure, the maximum of the VB principally gets the contribution of O 2p orbitals and the CB minimum is mainly due to Ti 3d orbitals.

It is generally reported that anatase has an indirect, and rutile a direct electronic band gap. However, numerous studies on this topic are still controversial regarding the electronic structure of the band gap. The experimental (spectroscopic) methods of band gap measurements indicate for anatase and rutile that there is a dependence of the band gap nature on the electric field orientation. If the electric field is perpendicular to c axis ($E \perp c$), the optical band gap is found to be direct, and indirect if the applied electrical field is parallel to *c* axis ($E \parallel c$). [4], [17]–[20]. Another opinion is about the crystallites size dependency on direct-indirect band gap transition [11], [21]. It was shown by Reddy et al. [21] that anatase nanoparticles with grain size of 5-10 nm exhibit a direct band gap transition.

The photocatalytic activity of anatase is known to be more important than for rutile, even despite of the wider band gap [22], [23]. The investigation realised by Zhang et al. [23] demonstrates that in anatase, in case of the indirect band gap the life time of photo-generated carriers is increased due to the phonons assisted recombination (Figure 1-5).

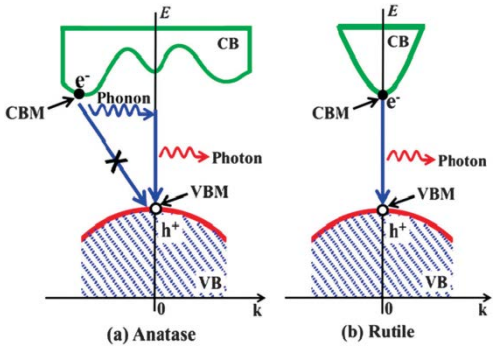

Figure 1-5 Schematic illustration of possible recombination processes of photogenerated electrons and holes in (a) anatase (indirect gap) and (b) rutile (direct gap) [23].

Concerning the brookite phase, being less investigated, the literature overview gives contradictory information about the band gap energy. According to the theoretical predictions and reported experimental measurements, the brookite band gap values vary in the range between 3.1 and 3.4 eV [24]. This lack of information could be justified by the difficulty to obtain pure brookite phase. However, the recent advances on hydrothermal synthesis of pure brookite nanostructures raise the interest in this phase, but the film deposition of pure brookite phase remains an open challenge.

Table 1-1 Summary of anatase and rutile physical properties (reproduced from ref. [17]).

	Anatase	**Rutile**
Lattice parameter a(Å) c (Å)	 3.7874 9.5147	 4.5937 2.9587
Density (g/cm^3)	3.894	4.250
TiO_6 coordination number	8	10
Dielectric constant ⊥ //	 31 48	 89 173
Electron effective mass	$1m_0$	$9\text{-}13m_0$
Hall mobility (cm^2/Vs) (300-10K)	15-550(crystal) 4(thin film)	0.1-10(crystal) 0.1(thin film)
Non-metal-metal transition by a shallow donor band	Yes	No
Excitons	Self-trapped	Free
Luminescence	Visible broad band cantered at 2.3eV	Sharp peak at 3.031eV
Optical absorption edge: Eg(eV) ⊥ (direct) // (indirect)	 3.420 3.460	 3.035 3.051

It is worth noticing that TiO_2 anatase demonstrates a different photocatalytic activity as a function of the dominant crystallographic orientation. It was found that among

crystallographic orientations, the facet (001) is the most reactive. This is under intense investigating.

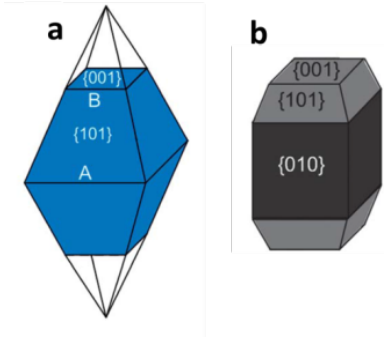

Figure 1-6 Illustration of anatase crystal facets (a) normal anatase crystal, (b) elongated anatase crystal.

However, being the most energetic facet, it is difficult to obtain, mostly due to the principle of the minimization surface energy during a growth process. The anatase synthesised by conventional methods like CVD or hydrothermal synthesis, contains more than 94% of thermodynamically stable and low-surface-energy (101) facets (Figure 1-6 a). The average surface energy (γ) given by theoretical predictions for principal TiO_2 anatase facets are: γ (001) 0.90 $J.m^{-2}$ > γ (100) 0.53 $J.m^{-2}$ > γ (101) 0.44 $J.m^{-2}$ [16] [25]. Currently, hydrothermal synthesis is the most appropriated method to obtain a significant percentage of (001) facets using a shape controlling agent, mainly HF [26]. The thin films deposition of (001) facets could be achieved by epitaxial growth on Si (001) substrate with buffer layer $SrTiO_3$/TiN or on $SrTiO_3$(100) single crystal [27]. It is worth mentioning that the development of new methods tailoring the crystalline orientations and its stability is one of the emerging routes in the research on TiO_2. Therefore the crystalline structure of TiO_2 and thus potential tailoring of the surface energy has to be taken under consideration as a potential way of enhancing the photocatalytic activity. Nevertheless the photocatalytic activity remains in the UV range.

1.2.2 Tin oxide

Tin oxide is another wide band gap semiconductor which is already used in numerous application areas. SnO_2 is used as transparent electrodes, gas sensors etc. [28]–[30]. The combination of optical transparency and high conductivity makes SnO_2 very attractive for optoelectronic and photovoltaic applications [31]–[35].

Crystallographic structure

SnO_2 - cassiterite (or rutile phase) has a tetragonal crystallographic structure with space group P42/mnm and lattice parameters a = b = 4.731 Å and c = 3.189 Å. A schematic illustration of

the casseterite unit cell is represented on Figure 1-7. Cassiterite's crystallographic parameters are very close to TiO_2 rutile. As with the TiO_2 rutile structure, SnO_2 has SnO_6 octahedron building blocks, were each cation (Sn) is connected to 6 anions (oxygen).

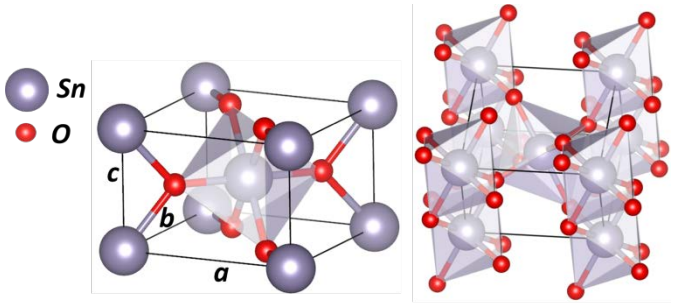

Figure 1-7 SnO_2 cassiterite unit cell.

Electronic properties

Tin oxide has a direct band gap with an energy value between 3.6 and 3.8 eV and an n-type conductivity [36]. The electronic band gap structure along high symmetry directions is represented on Figure 1-8.

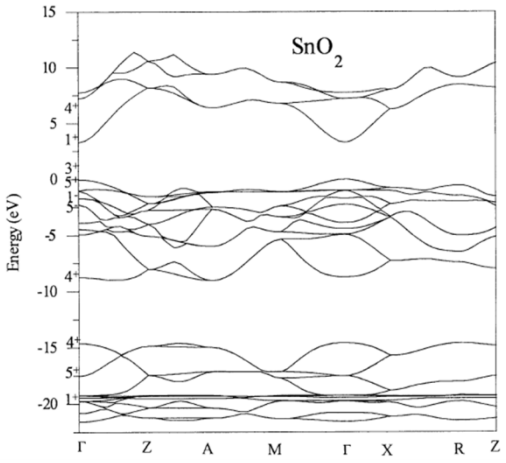

Figure 1-8 The electronic band gap structure of Tin oxide [31].

In the SnO_2 electronic bands structure the maximum of the valence band (VB) principally get the contribution from oxygen 2p orbitals while the minimum of conduction band (CB) is mainly due to tin 4s orbitals.

Tin oxide shows a possibility to change a stoichiometry on the surface and become SnO, where Sn^{4+} can be reduced to Sn^{2+}. This modification has an important effect on the surface electronic structure, leading to the formation of Sn 5s derived surface states, and reduces the work function of the materials. This property is largely used in gas-sensitive applications.

1.3 Limitations of basic photocatalytic systems and solutions

The three main metal oxides TiO_2, ZnO and SnO_2 are fundamental in the photocatalytic approach. However, their electronic and optical properties have few important drawbacks that limit its photocatalytic potential. The wide band gap of metal-oxide semiconductors represents the first important limitation. The light absorption allowed only for photons with higher energy than the respective band gap energy restricts the use of classical photocatalysts in the UV range of sun light. It means that only 3% of the solar spectrum is involved in a photocatalytic degradation reaction. Therefore, one of the current challenges is to push forward the light absorption to the visible range.

The second issue is the low stability of the photo-generated carriers; in particular, their fast recombination (few nanoseconds) represents one of main issues in photocatalysis. This phenomenon could be avoided by the addition of electron and hole scavengers, which could be various metastable surface states, electron donors or electron acceptors adsorbed on the semiconductor's surface [3]. Consequently, the increase of photocatalytic system efficiencies could be reached by acting principally on the band gap structure, in order to increase the range of absorption and reduce the carrier recombination. Therefore, in this section we will discuss the various approaches that have been already proposed such as the doping, the heterostructure fabrication and the use of plasmonic materials.

1.3.1 Doping

In the semiconductor industry, doping is one of the main approaches to tune the Fermi level. In photocatalysts, the doping approach consists of a direct modification of the band gap structure by creating additional energetic levels, in order to extend the light absorption and also create trap sites of carriers to prevent the fast recombination [37]; n-type doping of TiO_2 by C, N, P, S, B has shown a significant improvement of the visible range light absorption in the photocatalytic material.

The nitrogen incorporation within TiO_2 lattice has demonstrated the photocatalytic activity in the visible range that opened a potential way for the improvement of photocatalytic systems. The visible range absorption may be induced by the substitutional or interstitial nitrogen incorporation. The impurity incorporation in the metal-oxide lattice may create oxygen

vacancies which may also be responsible of the photocatalytic efficiency enhancement [38] [39].

The theoretical prediction through DFT calculations showed that, in the case of substitutional N-doping, the occupied N 2p localised states are slightly above the valence band edge (Figure 1-9). While for the interstitial incorporation of nitrogen, the unpaired electron is shared between the N and O atoms and formed NO bond. That generates π-type localised states which are higher than the valence band edge of 0.73 eV [40] [38].

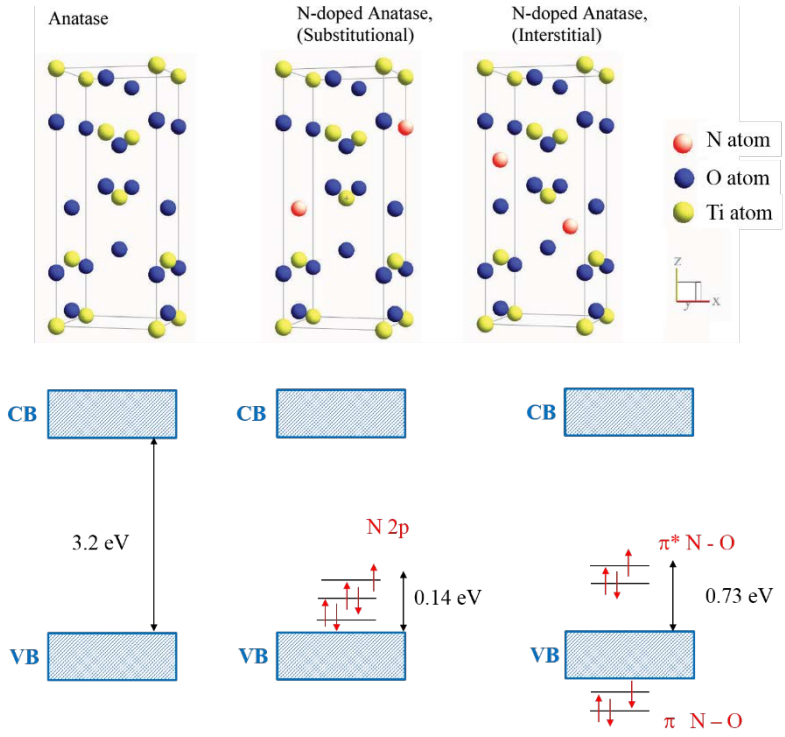

Figure 1-9 Schematic of possible N-doped TiO_2 crystalline structure [38], [40].

Besides the N-doped TiO_2, doping with Boron- Carbon- and Fluorine are extensively studied in the literature and appear as also attractive candidates for the significant improvement of the photocatalytic activity [39], [41].

However the bang gap tailoring trough the impurity incorporation in the metal-oxide lattice may also have a reverse effect and promote the undesirable fast recombination of carriers.

1.3.2 Stoichiometry

Oxygen vacancies (V_O) are particular defects of the crystalline lattice, which could be present either in bulk or on the surface and results in reducing of Ti^{4+} to Ti^{3+} [39]. The presence of Ti^{3+} defects, also called a self-doping significantly enhance the light absorption of TiO_2 in the

visible range creating the inter-band gap states. Therefore, the attention to non-stoichiometric TiO_2 has been increased recent years [42]–[45].

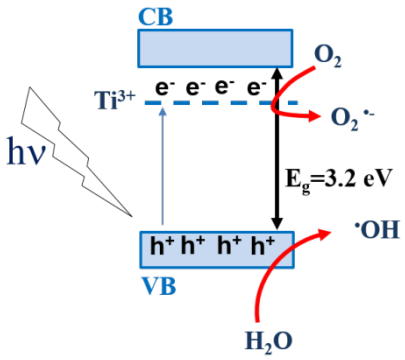

Figure 1-10 Schematic diagram for TiO_2 band gap engineering by Ti^{3+} self-doping.

The oxygen vacancies in the TiO_2 lattice can be created by the high vacuum annealing or the use of a reduction agent. However, the important drawbacks of these methods are high cost and critical experimental conditions [45]. Last years an important number of publications report on the hydrothermal approach offering better control on the Ti^{3+} generation [42], [44]–[46]. The Ti^{3+} self-doped TiO_2 powder synthesised by the hydrothermal approach confirms the significant enhancement of TiO_2 photocatalytic performances in the visible range.

Recently, Sasinska and co-workers achieved a highly Ti^{3+} doped film by realising the hydrogen plasma post-treatment of amorphous TiO_2 films deposited by ALD [47]. The H_2 modified TiO_2 films demonstrated significant improvement of the photocurrent density and the light absorption in the visible range.

1.3.3 Heterostructures

The fabrication of heterostructures does not imply the band gap modification of each material participating in the heterostructure as in the doping approach. Instead, it involves the combination of materials with different band gap energy levels and the formation of heterojunction.

As mentioned previously, to prevent the fast recombination of photogenerated electrons and holes, they have to be separated. The band gap engineering via the heterostructures fabrication acts principally to improve the carriers separation and thus increases their lifetime, and consequently the photocatalytic efficiency.

We wish to draw here a particular attention to the semiconductor/semiconductor heterostructures.

The staggered gap (SG) (Figure 1-11) is formed when the semiconductor interface forms an energy gradient that promotes the carriers separation. The electrons will intend to migrate into the semiconductor with the lowest energy position of conduction band (CB_1), contrary to the holes that would migrate to the semiconductor with the highest position of the valence band (VB_2). A typical example of SG heterostructures is an assembly of SnO_2 and TiO_2 (Figure 1-12).

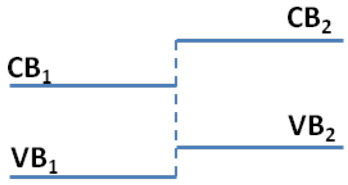

Figure 1-11. Schematic of the staggered gap. CB_1 and VB_1 represent the conduction band and the valence band respectively of the semi-conductor 1. CB_2 and VB_2 represent the conduction band and the valence band respectively of the semi-conductor 2.

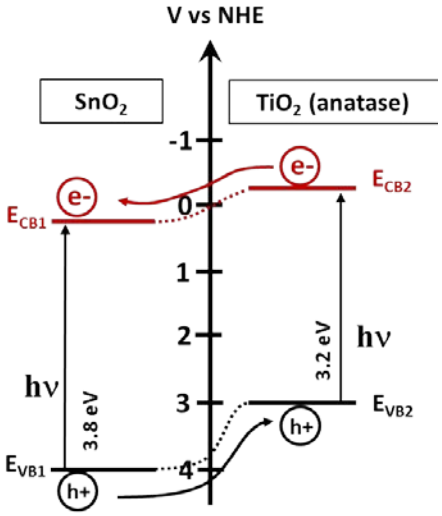

Figure 1-12 Representation of the SG heterostructure present in a SnO_2/TiO_2 heterostructure.

The SG heterostructure formation can be demonstrated with the characterisation of the band gap alignment through an XPS analysis. A similar assembly type was investigated on SnO_2/ZnO heterostructures [48], [49]. The authors calculated the valence band and the conduction band offsets ((VBO (ΔEv), CBO (ΔEc)) in the heterostructure, using the following equations:

$$\Delta Ev = (E_{Zn2p} - E_{v_{ZnO}})_{ZnO\ bulk} - \left(E_{Sn3d} - E_{v_{SnO_2}}\right)_{SnO_2\ bulk} - \Delta E_{CL} \quad (1\text{-}7)$$

Where E_{Zn2p} corresponds to the binding energy of the Zn 2p peak in bulk ZnO; Ev_{ZnO} to the valence band maximum of bulk ZnO; E_{Sn3d} to the binding energy of the Sn 3d peak in bulk SnO_2; and Ev_{SnO2} to the valence band maximum in bulk SnO_2. The ΔE_{CL} term can be determined from:

$$\Delta E_{CL} = (E_{Zn2p} - E_{Sn3d})_{heterostructure} \quad (1\text{-}8)$$

Where E_{Zn2p} corresponds to the position of the Zn 2p peak in the heterostructure of ZnO/SnO_2 and E_{Sn3d} to the position of the Sn 3d peak in the heterostructure of ZnO/SnO_2.
The conduction band offset (ΔEc) can be calculated using:

$$\Delta E_c = \Delta E_v + E_{g_{ZnO}} - E_{g_{SnO_2}} \quad (1\text{-}9)$$

Where ΔEv is the valence band offset previously calculated, Eg_{ZnO} is the optical band gap of ZnO and Eg_{SnO2} is the optical band gap of SnO_2.

As a conclusion, the presence of a SG type heterostructure on the ZnO/SnO_2 interface was confirmed with 0.67 eV valence band offset and 0.24 eV conduction band offset on the ZnO/SnO_2 interface.
The heterostructure fabrication approach can be divided into two strategies of semiconductors assembly: core/shell, and Janus type structures (Figure 1-13). The core/shell type involves a complete covering of one semiconductor by another. Such assembly type considers the activity of only one type of carrier because the carriers migrated to the core would not participate in the formation of radicals. In the second assembly type – Janus structure, both materials are exposed to the environment. It enables the participation to the photocatalytic reaction of both carriers (e^-, h^+) separated by the heterojunction. Therefore, the Janus-type of heterostructures seems to be more advantageous for enhancing the photocatalytic efficiency.

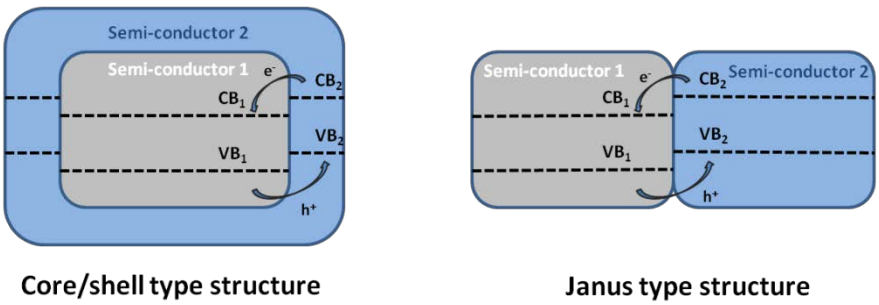

Figure 1-13 Representation of a core/shell (on the left) and a Janus type (on the right) heterostructure.

The assembly of various metal-oxide or metal-sulphide semiconductors are known to form a SG type heterostructure. However, ZnO- and TiO_2-based heterostructures are still commonly investigated: ZnO/SnO_2 [50]–[53], TiO_2/SnO_2 [54]–[56], TiO_2/ZnO [57]–[60], TiO_2/WO_3 [61] or ZnO/CuS [62].

TiO_2 and ZnO have very similar electronic properties, such as a band gap value of 3.2 eV, or similar valence and conduction band positions. In contrast, tin oxide has a larger band gap value, which limits its absorption to the deep UV range. The assembly of SnO_2 with TiO_2 or ZnO in heterostructures creates favourable conditions for charge separation and the enhancement of photocatalytic activity, unsurprisingly, they attract considerable attention and appear in numerous scientific publications.

The increase of the photocatalytic efficiency has been reported in the literature in the case of using Janus type ZnO/SnO_2 and TiO_2/SnO_2 heterostructures compared to basic metal-oxide systems. Uddin et al. [51] demonstrated twice faster rate of photocatalytic degradation of methylene blue (UV at 365 nm - 125 W) on SnO_2/ZnO nanoparticles compared to ZnO only. Similar heterostructure systems show a 100% enhancement on the decolourisation of methyl orange solution [52]. The assembly of TiO_2/SnO_2 nanoparticles exhibits a 50% increase in the rate of photocatalytic degradation of Rhodamine B compared to commercial TiO_2 nanoparticles [56].

A high number of publications discuss the heterostructure assembly of nanaowires/nanoparticles, which allows us to draw a conclusion about the efficiency of this approach. The decoration of metal-oxide nanowires grown by various methods with metal-oxide nanoparticles also demonstrates the efficiency of the heterostructure approach [53],[63]. Zhu et al. [63] demonstrated by photocurrent measurements that the efficient carriers separation promotes photocatalytic degradation. As it was shown the semiconductor heterostructures can solve the problem of the carriers recombination, however the photocatalytic activity still be limited to the UV range. Moreover, the semiconductor-semiconductor interface should not have any parasitical contamination, otherwise the carriers separation will not occur.

1.3.4 Plasmonic approach for the enhancement of the photocatalytic activity

Assembly of basic photocatalytic metal-oxides with plasmonic nanoparticles have also been considered as heterostructures [64], [65]. Similar to semiconductor heterostructures, nanoparticles of noble metals could act as electron traps. In such metals, the Fermi level is lower than in semiconductors; this allows the migration of photo-generated electrons into the metal, thus such assembly improves the charges separation and the carriers scavenging. However, the main asset of plasmonic nanoparticles is their ability to extend the light absorption into the visible range.

Principles of the plasmonic approach for improvement of light absorption

Plasmonics address the core idea of a coherent oscillation of electrons in metals induced by the interaction of incident electromagnetic radiation with metallic nanostructures. The principle of this phenomenon can be explained by drawing an analogy with a mechanical oscillator [66]. The displacement of a simple harmonic oscillator from equilibrium results in a continuous sinusoidal motion. An external periodic force applied to the system with an identical frequency (“in phase”) fulfils the resonance conditions and can therefore increase the amplitude of the harmonic oscillator. Similarly, in plasmonics, the incident electromagnetic radiation acts as the external force on the delocalised electrons (electron clouds) of the conduction band and enhances their displacement. Coulombic forces induced between the delocalised electrons cloud and the nucleus of the metal atoms are opposed to this displacement. The plasmon resonance corresponds to the conditions where the resultant of those two opposite phenomena leads to the collective oscillation of the delocalised electrons (Figure 1-14 a).

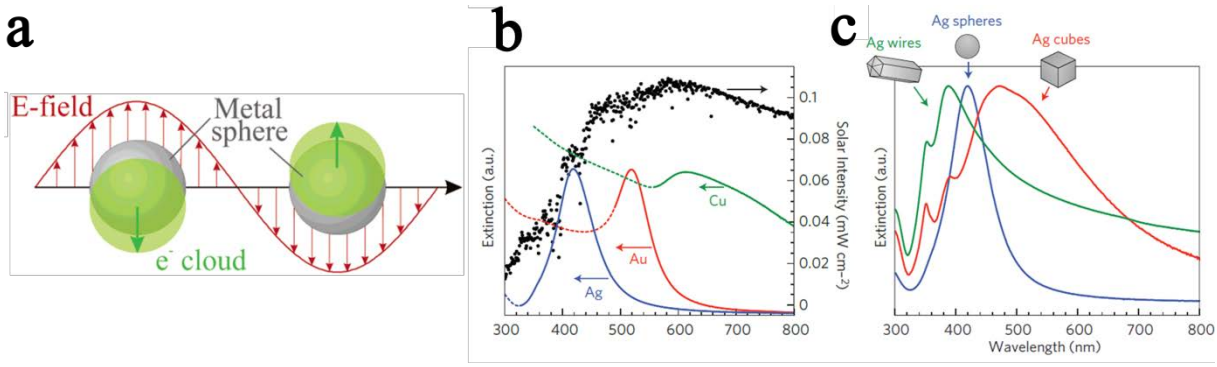

Figure 1-14 (a) Schematic illustration of surface plasmon resonance, (b), (c) Illustration for plasmon resonance dependency on nanoparticles material an shape [67] [68].

In the case of metal nanoparticles, where the size is significantly lower than the light wavelength, the resulting collective oscillation of electrons is called Localized Surface Plasmon Resonance (LSPR). The oscillation frequency mainly depends on the electron properties, such as their density and effective mass, and also on the nanoparticles size, shape and charge distribution [67], [68]. Among the numerous metals showing LSPR, the noble metals are gaining popularity for their stability at the nanometer scale and the strong LSPR in the visible range of the electromagnetic spectrum (Figure 1-14 b and c).

The combination of plasmonics with metal-oxide photocatalysts is particularly interesting since it can improve the charge separation and expand the allowed absorption to the visible range.

In the UV-visible range, nanoparticles act as small light collectors and result in the increased absorbance of the electromagnetic field incident on the semiconductor surface due to the LSPR. Earlier publications reporting on the enhancement of the photocatalytic activity using plasmonic nanoparticles coupled with semiconductor materials, focused on the ability of nanoparticles to promote the carriers separation. The proposed mechanism considers the interface between the photocatalytic semiconductor and the metallic nanoparticle as a Schottky barrier [69]–[74]. Under a visible range irradiation, the electrons could be injected from the photo-excited metal to the semiconductor (Figure 1-15). As an example described in Figure 1-15, this electron transfer modifies the gold atom into an oxidised state. According to a mechanism proposed by Tian and Tatsuma [71], the oxidized gold could be immediately reduced by an electron donor present in the solution. Furube et al. [72] demonstrated in 2007, with a femtosecond IR probe, that this electron injection occurs within a few hundreds femtoseconds.

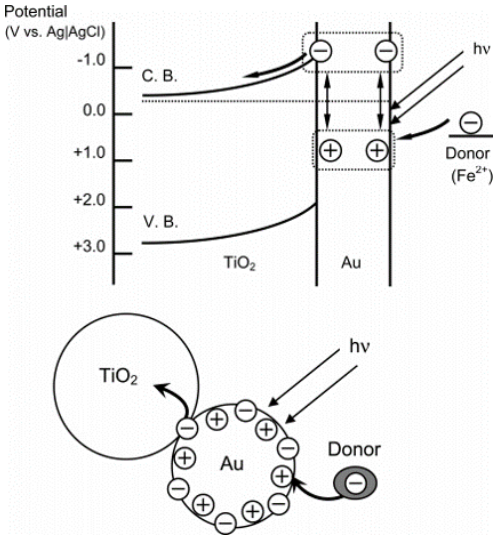

Figure 1-15 Possible mechanism of charge separation (direct charge transfer mechanism) [71].

However, the mechanisms leading to this enhancement are not fully understood. The mechanism related to the direct charge injection gained important support through theoretical and experimental investigations [75], [76].

Another important factor to be taken into account is the effect of local heating on the plasmonic nanoparticles. This phenomenon happens because of the local electromagnetic field induced by the plasmonic phenomena. This effect has already been used in photothermal therapy in medicine [77] and photoassisted synthesis [78] [79]. Fasciani and co-workers [80] have estimated that the local temperature increase on the surface of gold nanoparticles exposed to a laser pulse (8 ns at 532 nm, 50 mJ/pulse) could reach 500 ± 100°C.

Assemblies of various combinations of conventional photocatalyst materials (TiO_2, ZnO, CeO, Fe_2O_3, CdS etc.) with plasmonic nanoparticles, typically silver, gold, platinum or mixed alloys are reported in the literature [65]. The assembly of plasmonic nanoparticles on photocatalytic materials has different geometries like the once detailed for semiconductor heterostructures assembly. Two assembly types - core/shell and Janus structures were investigated in the literature [64], [81]. Various calculations as well as the experimental results indicate that the Janus assembly type allows nearly maximal near field enhancement and consequently increase the light absorption (Figure 1-16).

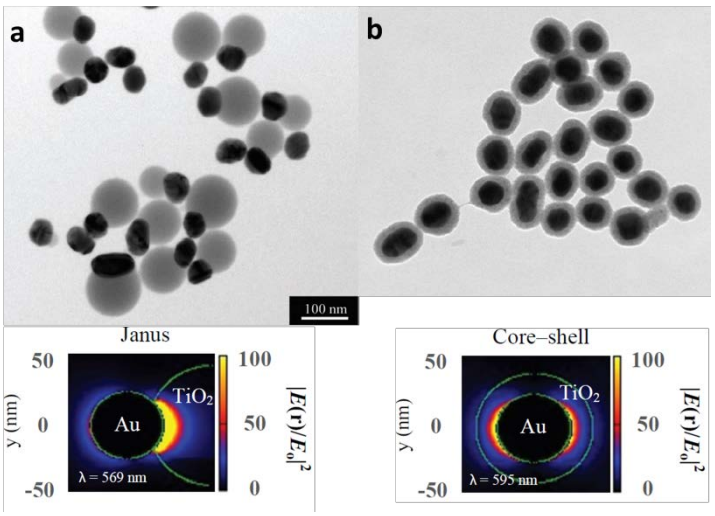

Figure 1-16 Illustration for Janus (a) and core-shell (b) Au 50 nm-TiO_2 nanostructures and their plasmonic near-field maps obtained by DDA simulation [64].

It was demonstrated by Seh et al. [64] that in the case of using the Janus configuration, the light absorption and thus the photocatalytic efficiency were increased by 1.7 times compared to the core/shell configuration. The plasmonic approach is a relatively simple approach compared to doping, which also allows the activation of wide band gap semiconductors in the visible range. The metal-oxide nanostructures decorated with plasmonic nanoparticles enable us to engineer a photocatalyst which is active under visible light. However, it is important to underline a significant drawback of this approach. The percentage of the photocatalytic surface covered by plasmonic nanoparticles should be well controlled, otherwise the predominant coverage by metallic nanoparticles reduces the specific surface area of the photocatalyst and make it inaccessible for the radicals generation. It was demonstrated that the coverage of more than 15% of the photocatalytic surface inhibits the effect of plasmonic enhancement [74] [82] [83].

1.3.5 Light management approaches

The light management approaches attract considerable attention in photovoltaics. This strategy mainly targets two goals: antireflection (AR) and absorption enhancement. Given that, the increase of light absorption would be also relevant for the photocatalysis.

Fundamental studies on the antireflection principles were already well investigated on bulk materials. The maximum of achievable absorption on solar cells was determined to be $4n^2$, known as Yablonovitch or Lambertian limit (where n is refractive index of the semiconductor material). This limit was determined by Yablonovitch and Cody based on Lambertian scatter.

[84], [85]. Various studies intend to reach this limit and photonic structures have been considered to go beyond this theoretical limit. It was shown that the use of periodic structures could increase the density of optical modes [5], [86]–[89]. Therefore, the key parameters determining the interaction light/material are spacing, spatial arrangement and optical properties of materials [5]. Some publications even underlined the importance of geometry that may predominate intrinsic material properties [90]. This phenomenon is based on the light scattering and reflection on periodic nanostructures which increases the optical path. The sharp nanostructures such as nanocones, nanoneedles with dimensions below the light wavelength act as an anti-reflective coating (ARC) [90] [5], whereas the nanostructures with uniform diameters such as nanowires show fundamental photonic resonant modes and could lead to the light confinement and absorption [90]. Figure 1-17 represents the basic periodic nanostructures types that allow improve light absorption.

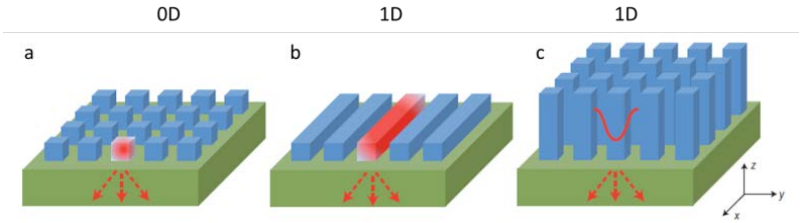

Figure 1-17 Examples of field distribution of optical modes on zero-dimensional nanoparticles (a) one-dimensional horizontal nanowires (b), one-dimensional vertical nanowires (b) [5].

The nanostructures spacing also determines the light interaction: if the spacing is typically on deep sub-wavelenght scale ($\lambda/15$), such structures have ARC behaviour, while if the spacing is on the wavelength scale, the effective light resonance modes can be achieved [5]. A spectacular result was demonstrated by Seo and co-workers on periodic array of silicon nanowires [7]. By creating a 100 μm x 100 μm array of silicon nanowires with 1 μm of periodic spacing, 45-70 nm diameters and 1 μm of length, the authors proved the ability to tune the absorbed light wavelength as a function of nanowires diameter through the variation of diameter of freestanding Si-nanowires (Figure 1-18). The nanowires arrays demonstrate the colour change with 5 nm of nanowires diameter variation (Figure 1-18 b,c).

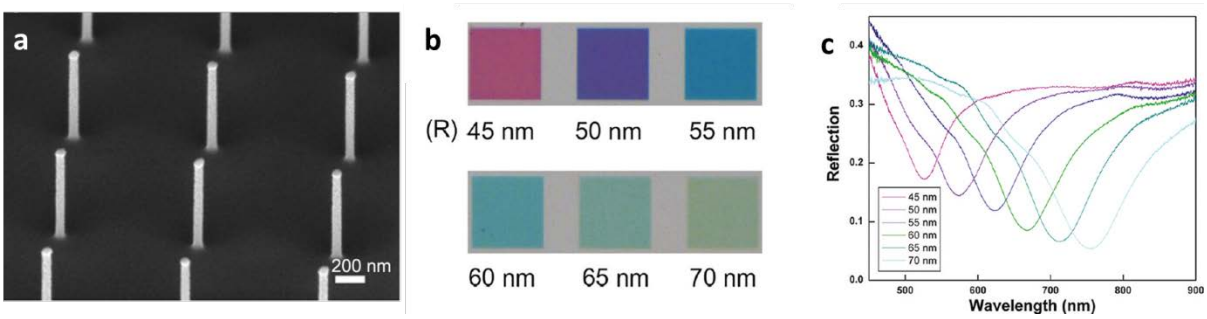

Figure 1-18 (a) Tilted SEM image of vertical Silicon nanowires, (b) bright field optical image of nanowires array, (c) reflection spectra of nanowires [7].

Another example of the light management approach is the periodic assembly of plasmonic nanoparticles on the semiconductor surface [91]. The well-controlled nanoparticles deposition with precise size and spacing can induce an advantageous optical effect for light management. For instance, placing nanoparticles in a close proximity (1 nm) has an important effect on their scattering performance and their near-field, due to the local coupling effect [92]. If the inter-particles distance could be well-controlled, it would offer the possibility of tuning the light scattering and the light absorption on the semiconductor [92]. The deposited nanoparticles (n_s) and active layer (n_2) should have a high refractive index $n_s=n_2 > n_1$ and a mirror (n_3). Figure 1-19 represents a schematic for four common modes that could improve the light absorption: (1) Fabry–Perot resonance, (2) guided resonance, (3) grating coupling, and (4) whispering gallery modes (Figure 1-19). Fabry–Perot resonance, guided resonance and grating coupling modes are of particular interest for the broadband light absorption [91]. This promising approach attracts a strong interest for the photovoltaic application as a light absorber and could also be considered for photocatalytic devices.

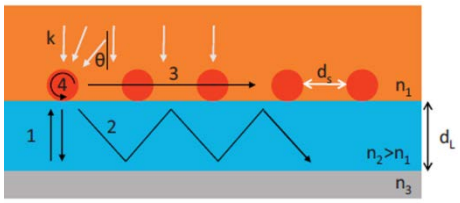

Figure 1-19 Representation of four common modes for increasing of light absorption: Fabry–Perot resonance (1), guided resonance (2), grating coupling (3), and Whispering gallery modes (4) [91].

1.3.6 Summary on photocatalysis enhancement approaches

The overview of the current state of photocatalytic materials and devices summarises possible paths to enhance the degradation efficiency of photocatalysts. In addition to the photo-generation and transport of carriers, photocatalysis is a surface-dependant approach.

Therefore, it is also obvious that the increase of specific surface area would increase the photocatalytic activity. Thus, two kinds of nanoscale photocatalysts can be distinguished: suspensions of nanostructures in solutions or nanomaterials supported on appropriated templates. The main advantages of dispersed nanostructures are the simplicity of use and their low cost. Nevertheless, nanomaterials dispersed in solution tend to agglomerate, lowering their exposed specific surface area. Moreover, due to the toxicity of the nano-objects, they have to be removed after the pollutants degradation cycle, thus an additional filtration step is needed. For this reason, there is a growing interest in supported nanomaterials. To increase the exposed specific surface area of nanotextured photocatalysts, their synthesis at the surface of porous supports like membranes has been envisioned for water treatment [93] [94] or water splitting [95]. The conventional photocatalytic approach, which uses basic metal oxides such as TiO_2, ZnO, SnO_2, is far from reaching the required efficiency. Light absorption limited to the UV range and fast recombination of photo-generated carriers are the main bottlenecks.

Various solutions were proposed to overcome these limitations. Among these solutions, the most commonly used have been previously discussed. The direct band gap engineering via doping intends to lower the band gap energy by creation of additional energy levels. It will extend the light absorption in the visible range. The assembly of metal-oxides with plasmonic nanoparticles also allows the activation of conventional photocatalysts in the visible range. Moreover, this approach improves the photocatalytic activity in the UV range by electrons trapping. The semiconductor/semiconductor heterostructures approach acts on the carrier separation. The light management approach is already applied in the field of photovoltaics; it would be also interesting for the photocatalytic applications as a way of light absorption improvement. The periodic organisation of metal oxide nanostructures with a high refractive index offers myriad possibilities of light manipulation. Nevertheless, the methods allowing the metal oxide structuration in the periodic arrays at deep sub-wavelength scale are expensive, especially for TiO_2 and SnO_2. Therefore, it is an open challenge to develop large-scale and low-cost methods of periodic doped metal-oxides nanostructures over highly reflective substrate and to combine them with well- and periodically organised plasmonic nanoparticles.

1.4 Presentation of the research project and strategy

The strategy of the present research is to combine several already proposed ways of photocatalytic activity enhancement in one device. The first goal of this work is the control of

tailored growth of TiO_2 films with industrially scalable techniques. The second goal is to translate such thin film into high-surface area periodic 1D TiO_2 nanostructures. We concentrate our effort on the development of TiO_2, as a material with essential properties required for photocatalysis, such as stability, non-toxicity, low-cost etc.

Further photocatalytic device architecture is based on periodic 1D TiO_2 vertically standing nanostructures assembled with plasmonic nanoparticles. The well-organised TiO_2 nanostructures should increase the specific surface area and enhance the light/material interaction. The ultimate device architecture would be the assembly of the periodic vertical nanostructures (TiO_2) or heterostructures (SnO_2/TiO_2) with plasmonic nanoparticles as it is depicted in Figure 1-20.

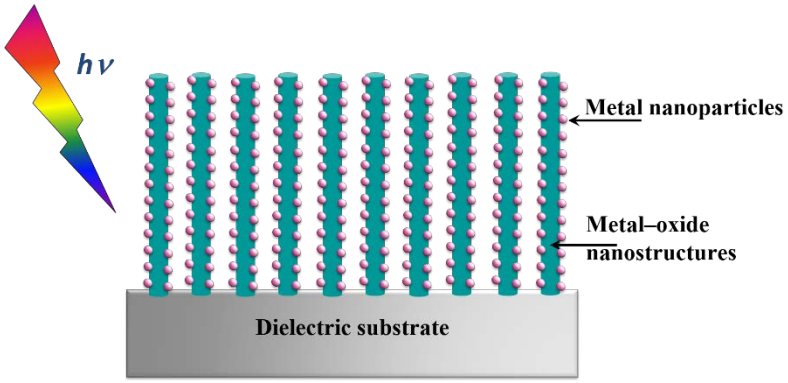

Figure 1-20 Schematic diagram of nanocomposite photocatalyst.

A schematic diagram of the device band alignment is represented on Figure 1-21. The fabrication of periodically well-organised 1D vertically standing TiO_2 nanostructures is not well investigated in the literature. Therefore, the development of such arrays and the investigation of their properties constitute one of the main goals of this thesis.

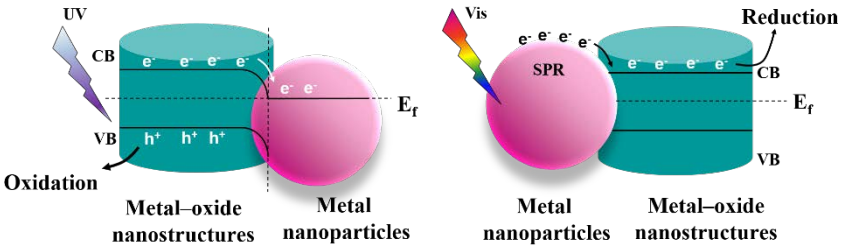

Figure 1-21 Schematic diagram of energy levels of nanocomposite photocatalysis and working principle under UV and visible light.

2 Materials and methods

The objective of this chapter is to give an overview on fabrication techniques, experimental setups and processes used along the thesis to achieve the determined goals of the thesis. Therefore, we start with the literature overview on the existing nanowires fabrication methods in order to determine our experimental strategy.

2.1 State of the art of TiO_2 nanowires synthesis

Nanostructure fabrication methods are divided in two main approaches: "Top-down" and "Bottom-up" approaches (Figure 2-1).

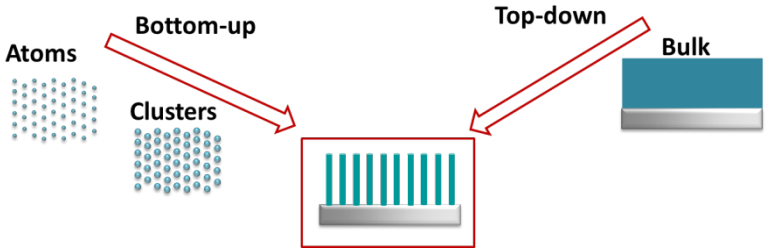

Figure 2-1 Schematic of Bottom-up and Top-down approaches.

The "Top-down" approach consists of the bulk materials nanostructuration via various lithographic techniques. This approach is widely adopted by the industry especially in microelectronics. The main advantages are the large-scale production and its relatively low cost. However, the cost significantly increases with resolution going down to the sub-50 nm scale and fabrication methods impose several limitations. The "Bottom-up" approach consists in the fabrication of nanostructures by precisely controlling the deposition of building blocks (atom, molecules). Theoretically, this approach does not have any limitation (in terms of size features). However, it is not yet fully adopted by the industry due to a lack of mature applications. This section provides an overview on the existing techniques for the TiO_2 nanowires synthesis principally using the bottom-up approach or a combination of top-down/bottom-up approaches. The existing nanowires synthesis processes are divided into two main categories: vapour phase and liquid phase approaches.

2.1.1 Nanowires synthesis by vapour-phase approach

The vapour phase growth represents an important variety of methods based on chemical or physical interactions of atoms/clusters/molecules with surface. The physical vapour deposition (PVD) techniques are methods based on different ways of the materials

evaporation and the vapour condensation on substrates. PVD includes techniques as Pulsed Laser Deposition (PLD), magnetron sputtering, cathodic arc deposition, Molecular Beam Epitaxy (MBE) etc. Among these techniques, PLD and MBE allow obtaining a very high-quality coating or nanostructures, but their integration into industrial production line would significantly increase the cost. Therefore, we focus on the chemical approaches of vapour phase deposition, such as Chemical Vapour Deposition (CVD) and its variations: Metal – Organic Chemical Vapour Deposition (MOCVD) and Atomic Layer Deposition (ALD).

2.1.1.1 Metal –Organic Chemical Vapour Deposition

MOCVD deposition, compared to classical CVD process (reported in Appendix 1 for further detailes), uses metal-organic precursors. The TiO_2 deposition by MOCVD mostly uses titanium-tetraisopropoxide (TTIP), tetrabutyltitanate (TBOT), titanium acetyl-acetonate as precursors [96]–[101]. MOCVD deposition consists of vaporising the precursor diluted or not in inert organic solvent. The goal is to control the reaction of the precursors on the surface (and not in the gas phase). Therefore, several parameters such as temperature, pressure, and concentration trigger the deposition properties (roughness, chemistry, thickness, impurity etc.).

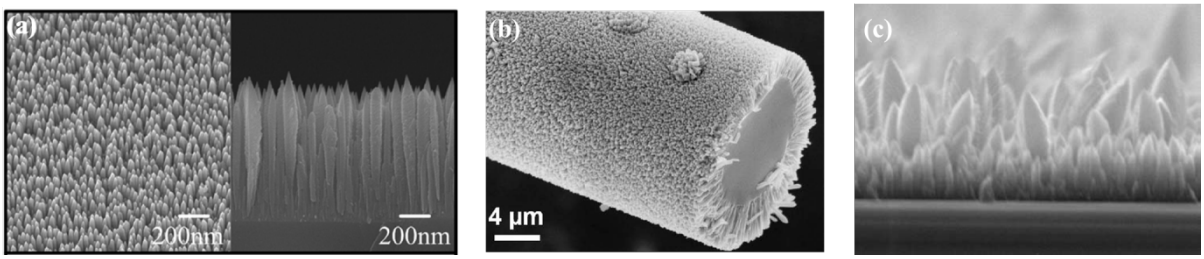

Figure 2-2 SEM images of TiO_2 columnar growth my MOCVD (a) from reference [96], (b) from reference [99], (c) APCVD [98].

Chen and co-workers investigated the growth of well-aligned TiO_2 nanocrystals by MOCVD [96], [97]. The authors used a cold-wall and vertical flow MOCVD reactor. The chamber pressure was maintained at 1.5 - 5 mbar and the substrate temperature at 550°C. The authors demonstrated a strong influence of the substrate orientation on the crystalline structure of grown TiO_2. Rutile nanorods with orientations (001) and (101), were obtained on the sapphire substrate with (100) and (012) orientations respectively [96] (Figure 2-2). However, such a substrate is too expensive in our application scope. In the case of using fused silica as a substrate, well-aligned anatase nanocrystals were grown [97]. Sarantopoulos et al. [99] performed the columnar growth of TiO_2 on glass fiber substrates and achieved similar

nanowire-like morphology at 400°C. Sarantopoulos and co-workers also demonstrated the morphology dependency on the process temperature and precursors concentration [99] [102] [103]. Similar TiO_2 growth was demonstrated by Duminica and co-workers [98]. The authors investigated the atmospheric pressure MOCVD deposition in the temperature range 350-700°C using TTIP, water vapour and oxygen as precursors with various mole fractions. A strong dependency of morphology on the temperature and concentration was also shown. At low temperature (350°C), the increase of a mole fraction demonstrates a morphology transition from a compact film to a columnar growth.

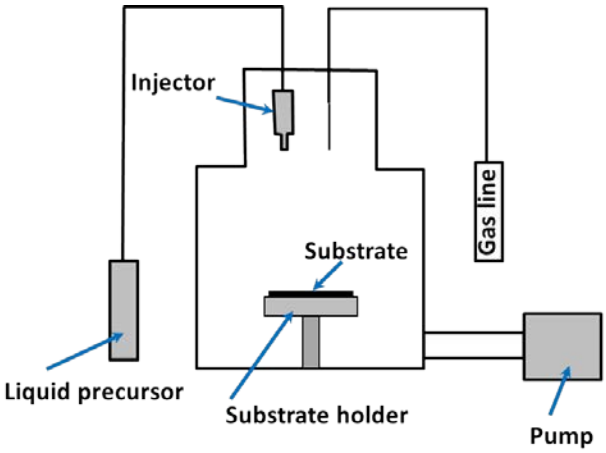

Figure 2-3 Schematic of MOCVD MC200 ANNEALSYS reactor.

In our case we use the MOCVD equipment MC200 from the ANNEALSYS Company (France) (Figure 2-3) was used to develop TiO_2 films and nanowires. This deposition setup enables large scale production on substrates up to 200 mm in diameter. The temperature range allowed by the equipment is between room temperature and 850°C. The sample is heated from the backside by the sample holder and the reactor walls kept cold. The substrate holder is installed on the spinning platform for the homogeneous precursor dispersion (distribution). These principles promote a homogeneous reaction on the substrate surface and not in the gas phase. The precursor injection, which can be defined as a direct liquid injection, enables immediate vaporization of the injected liquid in the reactor. The vaporisation is ensured by important a pressure gradient between the canister pressure (5 bars) and the reactor pressure (~0.1 mbar). The advantage of a direct liquid injection is the possibility of using various metal-organic precursors diluted or dissolved in the inert organic solvents, which significantly increases the spectrum of possible materials chemistry that do not rely on volatile precursors.

Four injection heads enable the deposition of complex metal-oxides. The precursor condensations along the injection line or injector head could be prevented by heating lines and injectors to a temperature significantly lower than the decomposition temperature of the used precursors. The injection rate is controlled by the frequency and the duration of the injection pulses. Four gas sources are available during the deposition: nitrogen, oxygen, hydrogen and ammoniac for which flows are controlled by digital mass flow controllers (MFC). A security interlock prohibits the simultaneous use of incompatible gases. The injection head is installed perpendicular to the substrate holder to ensure direct injection on the heated substrate. A primary pump ensures the vacuum level in the reactor, which is generally ~ 0.1 mbar. The pump exhaust placed below the reaction zone avoids any gas perturbation on the substrate surface.

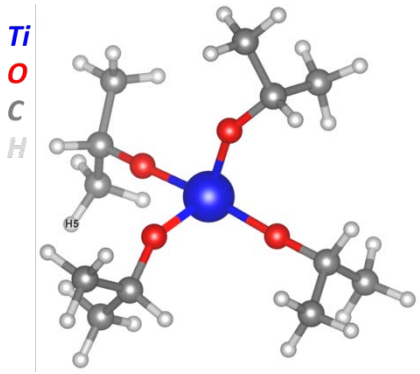

Figure 2-4 Molecule of titanium (IV) isopropoxide.

The development of TiO_2 deposition was performed using TTIP as a Ti-precursor diluted in anhydrous heptane. The TTIP molecule is represented in Figure 2-4. The thermal decomposition of TTIP occurs at 250°C and stoichiometrically forms TiO_2 without supplemental oxygen source [104]–[106]. The TTIP with purity >97% for MOCVD deposition was supplied by Sigma Aldrich.

Various conditions (temperature, pressure) are investigated to determine the conditions of preferential (selective) growth of TiO_2. No additional gas is used during the deposition

2.1.1.2 Atomic Layer Deposition (ALD)

The ALD technique could be also considered as one variation of the CVD process. The self-limiting reaction on the surface is the main ALD principle underlying the uniqueness of this approach. The sequential injection of precursors and nitrogen flow purge between pulses enables the control of the chemical reaction of precursors chemisorbed on the surface. The

advantage of the ALD technique is the conformal thin films growth. TiO_2 films grown by ALD are typically carried out using Ti-halides, principally $TiCl_4$ and water as oxidative precursor.

The ALD of conformal films is also characterised by a temperature window where the growth rate becomes independent on the temperature. It means that one monolayer is formed by one cycle. Above or below this window (Figure 2-5), the precursor reactivity is not sufficient or its condensation, desorption or pyrolysis occur. Numerous studies determine this window for TiO_2 growth in the temperature range 200-600°C [107], [108].

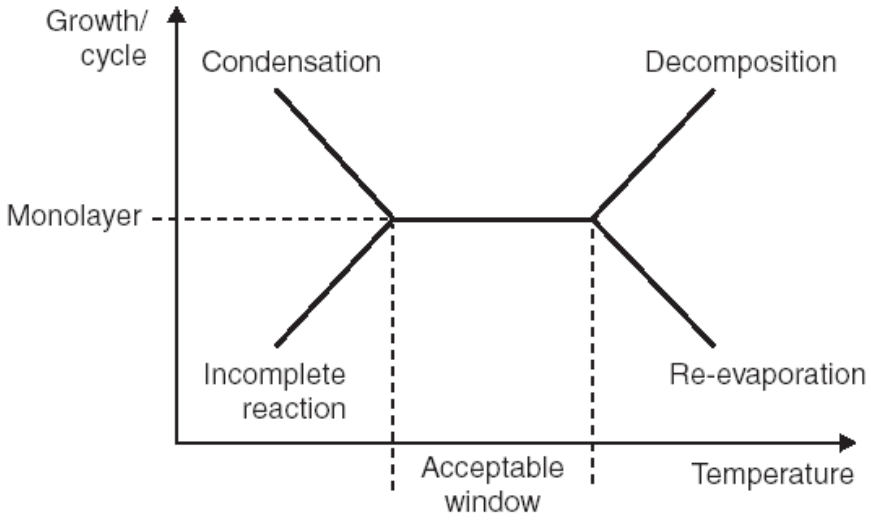

Figure 2-5 ALD growth rate dependency on temperature [109].

Recently, an ALD-derived technique, the Surface-reaction-limited Pulsed Chemical Vapour Deposition (SPCVD) was successfully applied for the TiO_2 nanowires growth [110]–[113]. Using classical precursors $TiCl_4$, H_2O and operating at low pressure 300-400 mTorr at high temperature 600 - 650°C, the authors realised TiO_2 nanowires grown in confined space of AAO porous membranes and also on flat Si surfaces and on nanofibres (Figure 2-6). This approach seems to be very interesting, however does not allow the growth of periodically organized nanowires.

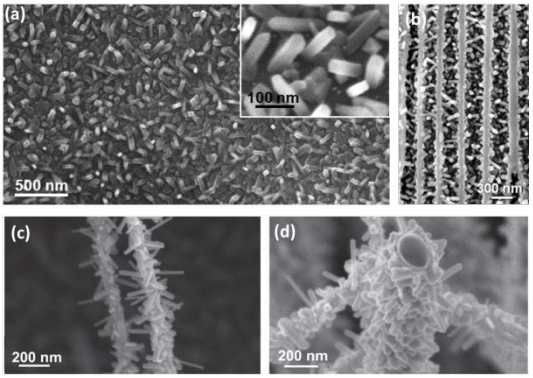

Figure 2-6 SEM images of TiO_2 nanorods grown by SPCVD on Si substrate (a), in AAO (b), on cellulose nanofibre (c,d) [113], [114].

The conventional ALD approach enables a fabrication of templated nanostructures formation due to its high conformity. The deposition of TiO_2 or SnO_2 by ALD allows a precise control on deposited thickness and filling of confined space of the template. Chang and co-workers [115] realised TiO_2 nanotubes fabrication by ALD using $TiCl_4$ and water at 400°C. At high temperature, the film roughness is important and hinders a uniform filling of pores [49] [116]. SnO_2 nanotubes fabricated using $SnCl_4$ and H_2O at temperature range 200-400°C demonstrates also an important film roughness (Figure 2-7A) [116]. Therefore, the fabrication of TiO_2 and SnO_2 nanowires via AAO template approach is currently limited to use of membranes with large pore diameters (≥100 nm).

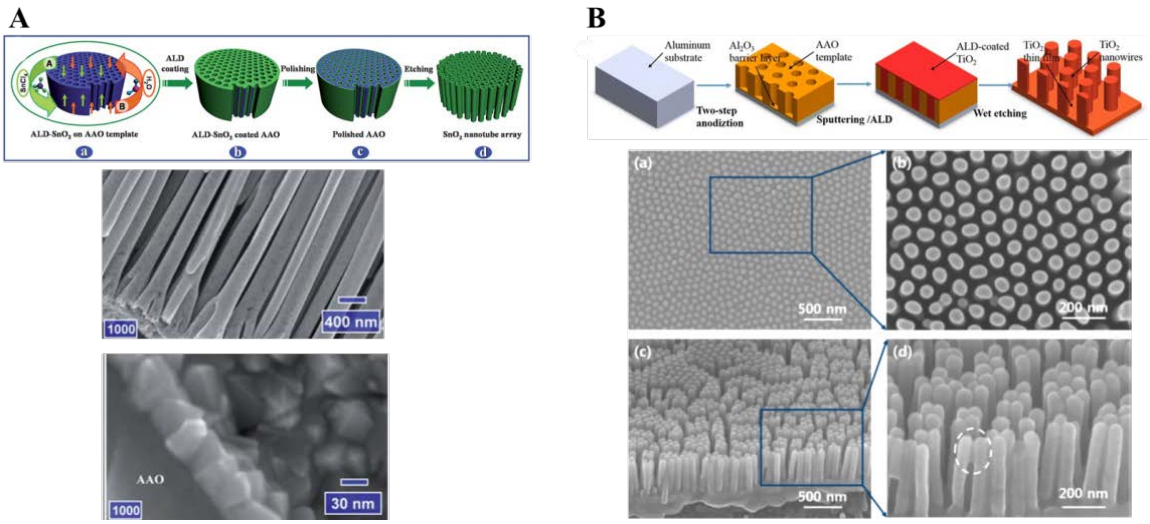

Figure 2-7 Schematic diagram of AAO templated approach of TiO_2 nanowires fabrication (A) and SnO_2 nanotubes fabrication (B) and SEM images obtained TiO_2 and SnO_2 nanostructures [117] [116].

The most used precursors for TiO_2 films grown by ALD are $TiCl_4$, TTIP or tetrakis(dimethylamido) titanium (TDMATi). However, $TiCl_4$ is still largely used as a precursor, combining at the same time high reactivity at low temperature, and high vapour

pressure. However, its important drawback is its corrosive behaviour that may damage reactors or vacuum pumps. TTIP requires additional heating in order to increase the vapour pressure. Recently, non-halide metal oxide precursors such as tetrakis(dimethylamino)tin and tetrakis(dimethylamino)titanium have attracted an important attention in the ALD domain. These precursors have a low temperature window and relatively low surface roughness. Nevertheless, in the case of tin oxide at low deposition temperature, using water as an oxidative source, amorphous films are formed, which need to be annealed at high temperature [118] and they are very expensive on the market.

In our case we use a commercial Atomic Layer Deposition (ALD) equipment, TFS 200 from Beneq (Finland) to grow TiO_2 and SnO_2 thin film deposition.

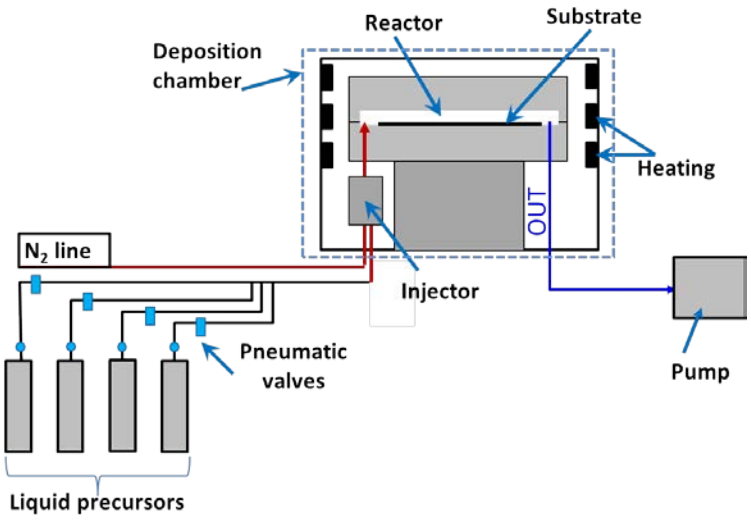

Figure 2-8 Schematic of ALD TFS 200 from Beneq.

According to the substrate geometry or process required, the ALD reactor can be transformed into four possible configurations: flat thermal configuration, flat configuration assisted with plasma RF head, internal or external fluidized-bed configurations. All of the internal configurations are heated by the resistance placed on the reactor wall with a temperature limit 450°C (Figure 2-8). ALD is generally a vacuum-based process; therefore a pump is connected to the reactor exhaust in order to reach a typical pressure of ~ 1-2 mbar.

Various precursors could be used in ALD, however the most common precursors are liquids with high vapour pressure at room temperature. These precursors easily form a vapour phase, which is transported and injected into the reactor chamber by the flow of an inert gas (nitrogen). Some liquid precursors with low vapour pressure could also be used via the increase of their vapour pressure by heating in dedicated hot sources with temperature limits

at 250 and 300°C. A hot source for solid precursors is also available in the TFS200 with a temperature limit of 500°C. Thus, an appropriate heating enables precursor evaporation, and the formed vapour is transported by inert gas into the reaction chamber. The quantity of injected precursor is controlled by pneumatic valves with a shortest aperture time of 50 ms. Therefore, it offers a possibility to have a precise control of the quantity of injected precursors and also on the pulse/purge sequences.

The standard planar configuration was used to develop TiO_2 and SnO_2 films on flat and porous substrates. The deposition conditions such as the temperature and purge time are varied to determine the best balance between roughness and films crystallinity (quality).

We use $TiCl_4$ as a classical precursor for ALD TiO_2 depositions (purity ≥99.995% from Sigma-Aldrich).

Tin tetrachloride ($SnCl_4$) is used for the SnO_2 deposition by ALD. Similar to $TiCl_4$, $SnCl_4$ has corrosive behaviour. Among the existing tin precursors that are currently used in ALD, $SnCl_4$ allows the formation of crystalline structures without further annealing, and is relatively low-cost. Other commercially available precursors are either more hazardous such as dimethyltin or diethyltin, either form amorphous film that requires further high temperature annealing at 600-700°C.

2.1.2 Liquid phase approach via hydrothermal synthesis

The liquid phase approach for nanostructures synthesis generally consists of the hydrothermal or solvothermal process. This technique depends on the minerals solubility in water (hydrothermal) or organic solvent (solvothermal) under high pressure and high temperature. The solvent evaporation increases the pressure of the thermodynamic system and makes the ionic solution supersaturated. This causes the precipitation of the first nuclei. The gradual oxidation or reduction leads the growth of crystals. The hydrothermal approach enables the fabrication of various morphologies both in the solution (further powders) and on the substrates. We focus our attention principally on the vertical nanowires fabrication with the positioning control of crystal growth.

Generally, TiO_2 nanostructures are grown using titanium (IV) organic precursors such as titanium isopropoxide (TTIP) [119] or titanium butoxide [30], [120], [121] mixed with aqueous solution of HCl. The growth can be controlled through the concentration, pressure, temperature and synthesis duration. The main advantage of a hydrothermal approach is the ability to grow crystalline phases, such as rutile, at significantly low temperatures (100-200°C). The classical hydrothermal method uses autoclaves and requires long synthesis

duration (ten hours scale). This drawback could be avoided by the use of microwave assisted hydrothermal approach. An extremely fast temperature ramp-up allows to significantly decrease the reaction time [122]. However, the nanowires length still depends on the synthesis duration [30] (Figure 2-9).

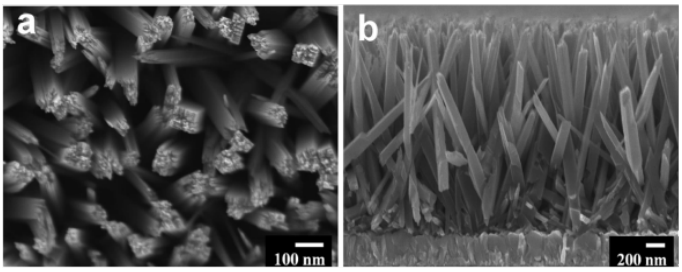

Figure 2-9 TiO_2 nanowires grown by hydrothermal method [30].

It was shown in the literature that the pre-deposition of a seed layer on the substrate allows to decrease the synthesis temperature, and also obtain a high temperature phase rutile at 120°C [123]. However, there is no information on the fabrication of periodic TiO_2 nanowires. In contrast, ZnO periodic nanowires can be fabricated through the seed layer assisted hydrothermal synthesis [124].

We have rapidly investigated the selective growth of TiO_2 nanowires via hydrothermal process on TiO_2 seed nanoparticles. The detailed fabrication of TiO_2 seed nanoparticles will be described in details in Sections 2.2.1 and 3.1.1.

The hydrothermal synthesis was performed in the microwave reactor which functionality is presented further detailed in appendix 2. The main objective of this study is to verify the ability of TiO_2 nanoparticles to act as seeds. The microwave approach is hardly scalable and is used only as prove of concept for the selective growth of nanowires from seed nanoparticles. The investigation on the influence of precursor concentration, temperature is realised.

The effect of the concentration is investigated using 28 mmol/L and 56 mmol/L aqueous solution of TTIP in HCl medium. After 1 h we only observe the nanowires growth on samples with seeds. The increase of concentration leads to more important nanowires growth rate, while density of nanowires seems to be very similar. According to SEM characterisations, the growth seems to be initiated by nanoparticles. For higher concentration, the nanowires width is significantly higher than the nanoparticles diameter. The increase of the synthesis temperature from 110 to 130°C results in higher nanowires growth rates (Figure 2-10). The

increase of the synthesis duration (from 1 to 3 h) forms wider nanowires. However, nanowires grow randomly without any defined geometric orientation. Moreover, only few nanoparticles seem to initiate the nanowires growth. Therefore, we do not further consider this synthesis method to grow well-ordered TiO_2 nanowires.

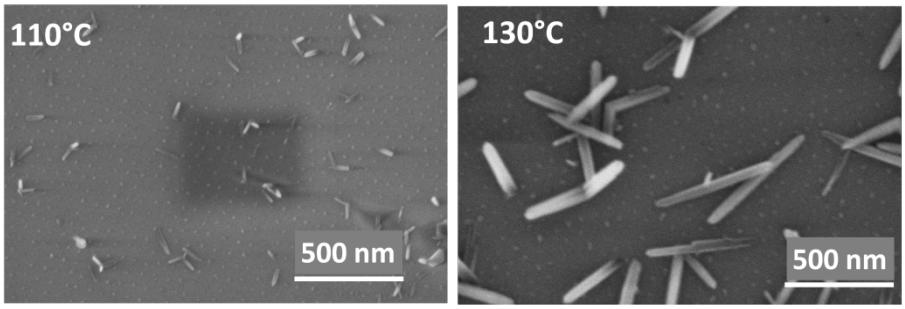

Figure 2-10 Temperature effect using TTIP concentration of 56 mmol/L.

2.1.3 Summary

Our strategy for the fabrication of free-standing periodic metal-oxide nanowires with up-scalable methods is restricted to the use of vapor phase processes as schematically summarized in Figure 2-11.

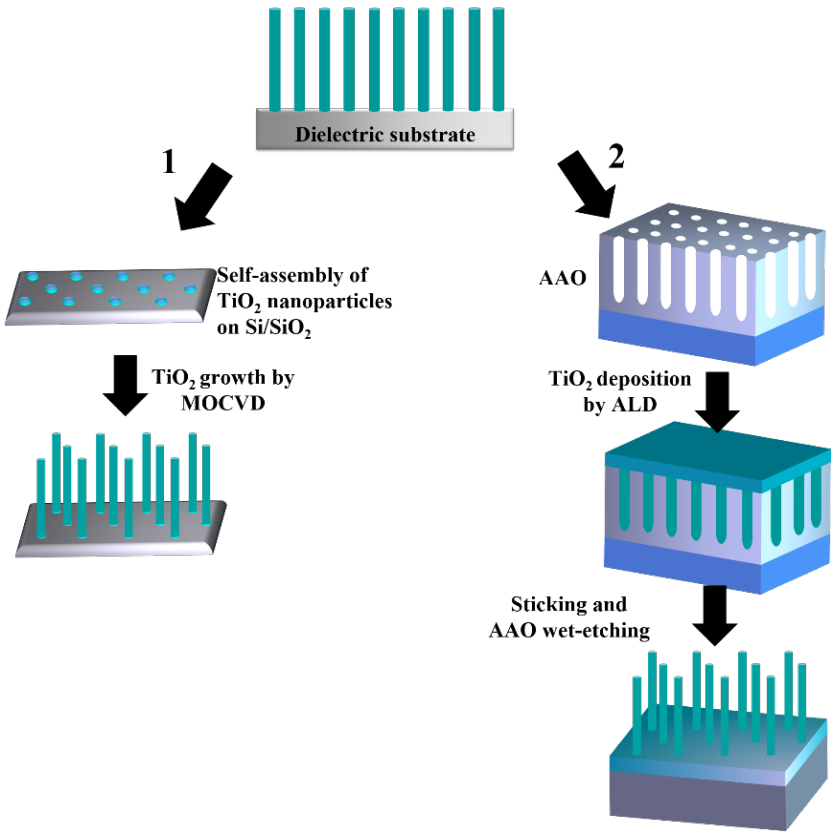

Figure 2-11 Schematic of periodic TiO_2 nanowires fabrication by two approaches investigated in this work.

We focus on two approaches:

The selective growth of TiO_2 nanowires over ordered seed nanoparticles. The first approach consists of synthesising well-controlled TiO_2 nanoparticles by direct block-copolymer assembly. In this approach the seed nanoparticles are foreseen to act either as a catalyst of the selective precursor decomposition, either as a germ for the growth initiation on TiO_2 nanowires.

The templated crystal growth. The second and alternative approach consists of TiO_2 films deposition by ALD into porous template. Various kinds of template are largely used for the control of the nanostructures shape. They could be realised using a polymer or inorganic matrix. However, the use of a polymeric template for the fabrication of free standing metal-oxide nanostructures restricts the temperature and chemistry process window. In contrast, the inorganic matrix such as Anodized Aluminium Oxide membrane (AAO), presents a good thermal and chemical stability. Therefore the AAO is the template that we selected in our case.

2.2 Fabrication methods

2.2.1 Fabrication of nanoparticles via the block-copolymer method

The first approach that we choose for the selective nanowires growth is based on a combination of the seed nanoparticles and vapour phase/liquid phase growths.

We aimed at depositing nanoparticles (seeds) on the substrate with a precise control of the size and spacing. Various lithographic methods allow the fabrication of such kind of seed nanoparticles. However, the block-copolymer method has a very high potential as a low cost and a scalable lithographic technique.

The typical steps involved in the fabrication of micellar arrays on surface is depicted on Figure 2-12.

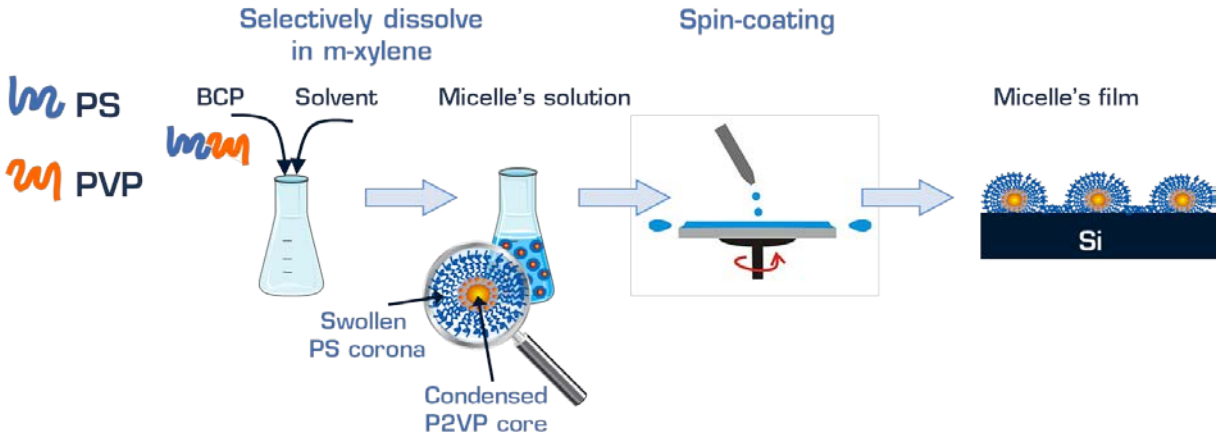

Figure 2-12. Schematic illustration of the micellar array deposition on the surface.

Two block copolymer systems composed of polystyrene-b-poly-2vinylpyridine (PS-b-P2VP) with a block molecular weight of 40500-b-41000 $gmol^{-1}$ (further labelled 40.5-b-41) and 102000-b-97000 $gmol^{-1}$ (102-b-97) respectively, are used in this work. The PS-b-PVP block-copolymer is dissolved in anhydrous m-xylene in order to obtain 0.3-1.5%wt concentration. The micelle solution is obtained after 24 h of vigorous stirring and then spin-coated on the Si substrates with thermal oxide layer. All substrates are cleaned and functionalised by UV-ozone cleaner (UVO-Cleaner® 42, Jelight Company, USA) before the spin-coating. The reversed micellar arrays were obtained by spin-coating with a rotation speed of 8000 rpm for 30 seconds.

2.2.1.1 Fabrication of TiO_2 nanoparticles

The ordered micelle arrays are exposed to $TiCl_4$ vapour using ALD reactor (TFS-200, Beneq, Finland). The ALD reactor was conditioned by heating at 400°C for 3 hours to remove any residual moisture within the chamber. The parameters of ALD deposition are chosen according to an initial study of TiO_2 films deposited on planar substrates: 200 ms pulses for $TiCl_4$ and H_2O, followed by 30 s of purging with nitrogen between pulses of precursors at a reactor pressure of 1-2 mbar. The growth rate of titania on silicon, as determined by ellipsometry and SEM cross-sections, is found to be ~ 0.125 nm/cycle. $TiCl_4$ exposures without additional water pulses are realized by sequential pulses of $TiCl_4$ (200 ms) and nitrogen purge (30 s). The exposure to the precursors vapours is performed at 20°C. Before exposure to the precursors, the samples are degassed by purging the ALD reactor with nitrogen for 30 min. Two exposure modes are studies in order to investigate the formation

mechanism of TiO_2 nanoparticles using BCP templated. The first mode (mode I) consists in the sequential exposure to $TiCl_4$ and water pulses. The second mode (mode II) consists in the exposure to only $TiCl_4$ without additional water pulses during the exposure process.

The TiO_2 nanoparticle arrays are subsequently obtained by oxygen plasma treatment (0.4 mbar, 200 W, 30 min) in order to strip the polymer template. The nanoparticles synthetised at low temperature are supposed to be amorphous, therefore an annealing step is performed at 600°C under O_2 atmosphere for 1 h to ensure the crystallisation of nanoparticles, before their further use.

2.2.1.2 Fabrication of plasmonic nanoparticles

The fabrication of plasmonic nanoparticles and in particular gold, is performed by spin-coating the micellar solution as described previously. Both BCP systems were used. The gold nanoparticles rely on using the impregnation of 5 mmol aqueous solution of Gold(III)chloride trihydrate ($HAuCl_4 \cdot 3H_2O$). After exposure to the precursor, the samples are washed with DI water and dried with nitrogen flow. The polymer stripping is performed using O_2 plasma (Reactive Ion Etching (RIE) 50 W, 60 mTorr, 10 min). An annealing step (500°C, in ambient air atmosphere) is performed in order to promote the reduction of Au^+ to Au^0.

2.2.2 Template assisted fabrication of periodic nanostructures

The template assisted growth of nanowires is chosen as an alternative to the selective MOCVD growth over seed nanoparticles. The template assisted approach consists of the following steps: (i) the fabrication of well-ordered porous substrates (AAO in our case); (ii) deposition of conformal metal-oxide thin films by ALD on porous surfaces; (iii) the removal of AAO template using wet-etching process in basic or acid solution. Such fabrication procedure is already well known and widely reported in the literature [117], [125], [126]. However, an important drawback of this approach is the poor control of nanostructures organisation, which tends to aggregate due to their high aspect ratio. To avoid this problem, anodization the Al-film deposited directly on the surface could be done. Chang et al. [115] realised AAO directly on Si and quartz substrates for the fabrication of TiO_2 nanotubes. However, the authors did not mention how to remove the alumina matrix and did not report on the final organisation of the nanotubes. Yao and co-workers [117] researched TiO_2 deposition into 500-nm-thick AAO with approximately 170 nm of over-deposition on top of

the membrane. The authors demonstrated the well-organised nanowires, which tended to aggregate. Moreover, the authors did not report on the nanowires functionalities. A sticking with the sample-holder is required in order to manipulate the nanowires network. The fabrication steps generally presented in the literature (Figure 2-13 (I)) face the manipulation difficulties described above. Sticking layer which must provide excellent thermal and chemical stability was not found. To overcome this issue, we develop a new fabrication protocol. After the deposition of metal-oxide into the porous template, we propose using dry-etching, to remove the residual oxide layer and then applying a wet-etching of the controllable removal of alumina. These modifications will allow controlling the height of formed nanowires, and be applied in large-scale fabrication (Figure 2-13(II)). In the scope of our applications, it brings also the benefit of having highly reflective aluminium underlayer.

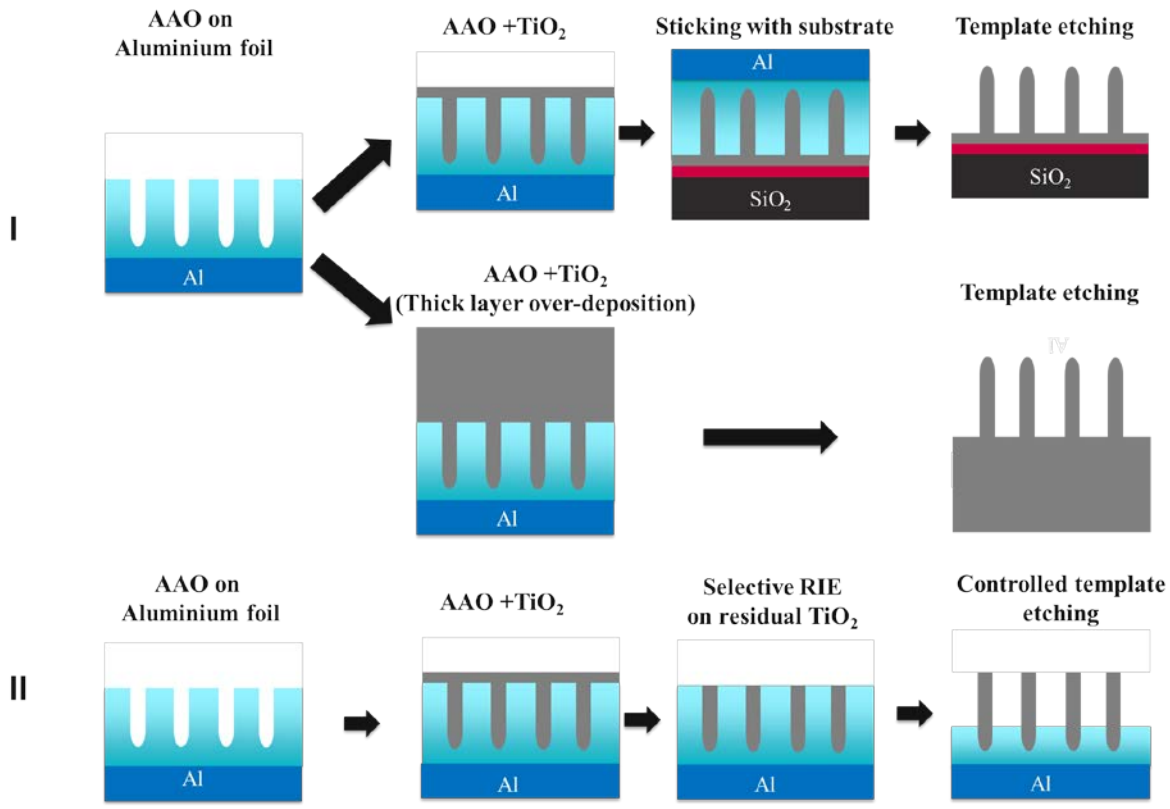

Figure 2-13 Nanowires fabrication using AAO template assisted process: (I) from literature overview, (II) our approach.

2.2.2.1 AAO template fabrication

The development of AAO membranes with specific parameters is required for the tuning of the nanowires aspect ratio. The fabrication of AAO is a well-known process, which consists in two anodizing steps. The Al foil is initially electrochemically polished in a solution of

perchloric acid and absolute ethanol (25 mL/100 mL). In order to avoid over-heating, the electrochemical cell is chilled at -4°C. The solution temperature is additionally controlled by an external thermometer. Therefore, the electro-polishing is performed by applying a voltage of 35 V and a current of 4 A. When the electrolyte temperature reached 12°C, the anodizing process is turned off until the decrease of the solution temperature to -1°C. The sequence of the electro-polishing and cooling steps is performed to achieve a mirror Al surface and to avoid the over-heating of the perchloric acid solution.

The anodizing process is performed in oxalic acid (0.3 mol) at 1°C in two steps. In the first anodising step, applying a voltage of 50 V during 2 h leads to the formation of porous alumina film. This film needs to be removed in order to obtain a void-like Al surface. Typically, the mixture of chromic and phosphoric acids (80 ml H_2O, 1.47 g CrO_3 and 2.76 ml H_3PO_4) heated at 80°C for 30 min is used for the selective alumina etching. The second anodising step is performed in similar conditions as the first one, on pre-structured Al surface, and forms the well-organised porous materials. Consequently, the pore depth is triggered by the anodizing time. In our case, to achieve a pore depth of 1-2 µm, the duration of the second anodising step is 15-30 min.

2.2.2.2 Optimisation of the nanowires fabrication protocol

Following the fabrication approach presented on Figure 2-13 (II), the deposition of the metal-oxide thin films into porous AAO membranes is performed by ALD. A conformal ALD deposition on porous surface inevitably forms a residual film on top of the membrane, thus needs to be removed.

Reactive Ion Etching

Reactive Ion Etching (RIE) is a powerful tool for the large scale nanostructuration. Plasma etching has significant advantages for the pattern transfer of nanoscale features compared to wet-etching. RIE ensures an anisotropic etching; moreover it is a relatively clean process and does not produce chemical waste. Typically, various types of masks, almost insensitive to the etching agent, are used for the features fabrication. The RIE mechanism depends on the etching agent (reactive gas) and its interaction with the treated material. Gases such as nitrogen or argon are often used for sputtering, rather than a selective etching.

In the literature, the typical metal-oxide etching process is performed using halide gases such as Cl_2 or Br_2, which demonstrate a high etching efficiency [127]. The fluorine-based gases

such as CF_4, C_4F_8, CHF_3, SF_6 etc. are appropriate for the SiO_2 etching, and they present lower ability for the metal-oxides (type TiO_2, SnO_2) etching, and are used to require a high density plasma.

The Plasma-Therm 790 Reactive Ion Etcher is used to remove the TiO_2 and SnO_2 residual layers on the top of AAO after ALD deposition. RIE Plasma-Therm 790 is appropriate for various RIE processing on silicon wafers up to 200 mm diameter. Four gas sources are available for the etching processes: oxygen, nitrogen, argon and CF_4.

The RIE of TiO_2 and SnO_2 are optimised using a reactive gas mixture of CF_4, Ar and O_2, in proportion 32:8:6 sccm. The TiO_2 deposited at low temperature is amorphous and its etching is achieved with 50 W, 60 mTorr. In these conditions, the etching rate is determined at 5 nm/min. The SnO_2 film, which is already crystalline after the deposition, requires a more powerful plasma to achieve a similar etching rate (Figure 2-14). Therefore, SnO_2 etching conditions are optimal at 200 W and 60 mTorr.

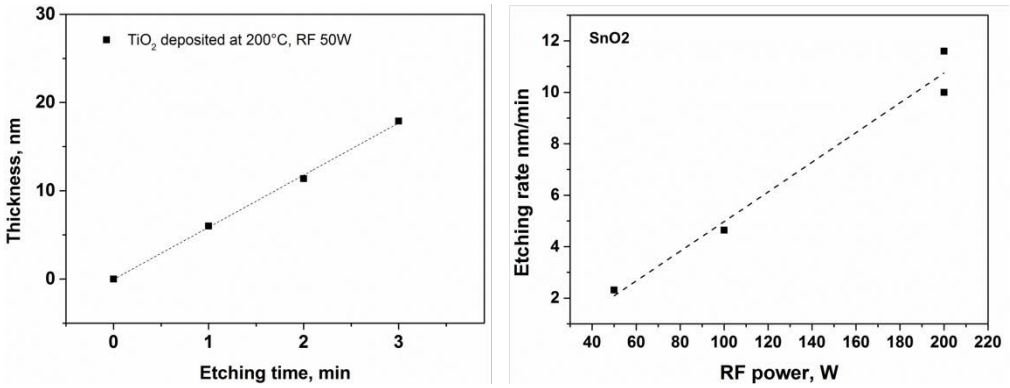

Figure 2-14 Reaction ion etching rate for TiO_2 (a) and SnO_2 (b) films.

The SEM pictures of samples after RIE treatment show very homogeneous etching of the residual metal-oxide films that were deposited on top of the membrane (Figure 2-15). The removal of this residual film allows to access to the alumina matrix for the further wet-etching step.

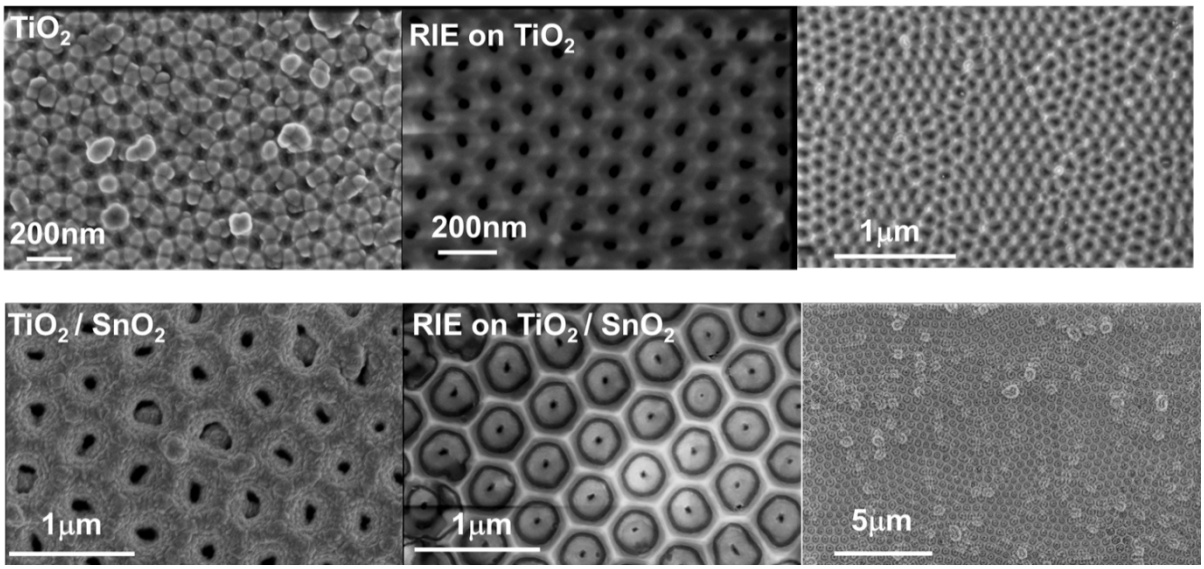

Figure 2-15 SEM images on TiO_2 and TiO_2/SnO_2 after applied RIE.

Wet- etching

The wet-etching setup is performed by fixing samples in the sample holder and placed them in a beaker with an etching agent. The sample holder maintains the sample parallel to the stirring rotation and keeps the distance between the sample surface and the magnetic stirring ~2 cm.

The accurate wet etching of the alumina matrix is still a technology challenge to achieve. In the literature, the wet-etching step is generally not well-assessed it consists of a complete alumina removal (over-etching), as it is presented on Figure 2-13 (I). Therefore, the goal of the wet-etching development presented in this section is to achieve an accurate etching of alumina on the partially removed matrix and to preserve the rest of the matrix to hold the periodic structures that prevents their aggregation.

The alumina is known to be soluble in acid and basic medium. The first etching tests are realised using aqueous solution of NaOH (4wt%). The SEM pictures of the samples after 5-20 min of etching at room temperature show a highly aggressive etching with the creation of numerous defects in the matrix. Another etching agent being also often used in the literature is the phosphoric acid (H_3PO_4). The use of various H_3PO_4 concentrations (1 to 5 M) demonstrates a significant improvement on the etching control. Moreover, the etching rate in the case of H_3PO_4 at ambient conditions is very slow. The main problems that are faced during the wet-etching optimisation are the non-homogeneity of the porous alumina, the presence of some areas where the etching rate is more important, and local mechanical defects as cracks leading to multidirectional etching. Local isotropic etching is extremely undesirable

in the case of long-time wet-etching processes. The non-uniform etching creates local defects (Figure 2-16 a) that propagate to the rest of the matrix leading to either the creation of a large number of defects, or premature over-etching (Figure 2-16 b, c).

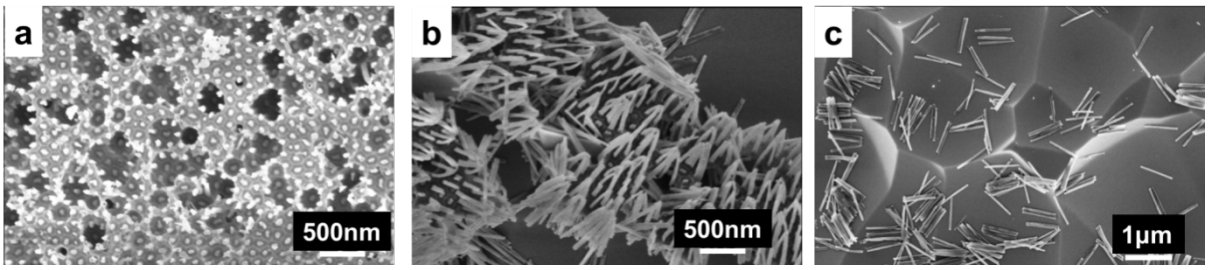

Figure 2-16 AAO matrix defects; (a) non-homogeneous etching alumina matrix, (b) propagating of matrix defects leading to the over-etching (c).

The annealing of porous substrates prior to the ALD deposition improves the matrix quality and significantly reduces the number of local non-homogeneities. However, the presence of small mechanical defects, such as cracks is still difficult to prevent. To solve this issue, we propose to apply concentrated H_3PO_4 (85%) mainly because of its high viscosity. The surface tension improves the etching homogeneity, even in the presence of local cracks. The viscous solution could not easily penetrate into a crack, which ensures unidirectional etching. Finally, the optimisation of the wet-etching of AAO allows to get a good control during this fabrication step. The nanostructures are developed by applying 15-20 h of H_3PO_4 etching. The alumina etching rate is determined at ~20 nm/h for membranes with pores diameter of 40 nm and 40 nm/h for membranes with pores of 180 nm.

The EDX analysis realised on nanostructures after the wet-etching reveal an important phosphorus contamination. The oxygen plasma at high power is able to remove the phosphorous surface contamination.

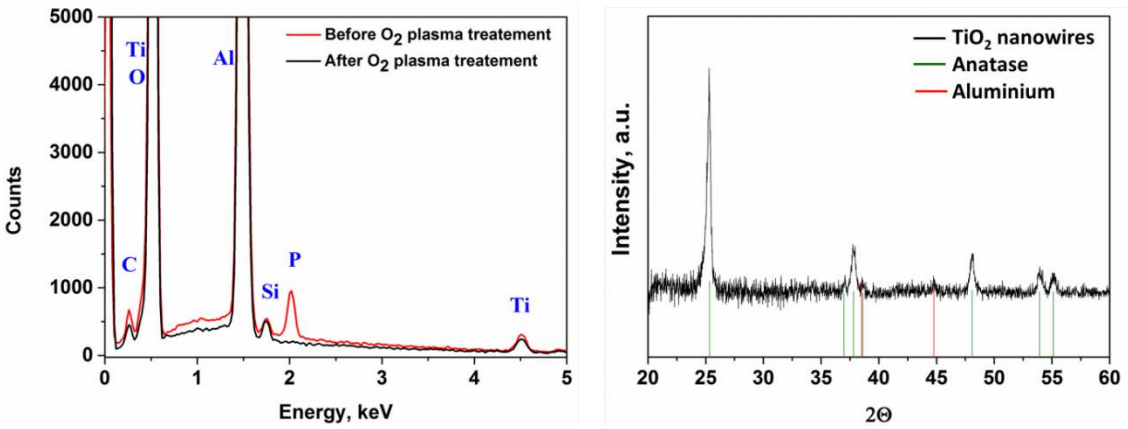

Figure 2-17 EDX spectra on TiO_2 nanowires (S70) before and after O_2 plasma treatment (left), XRD diffractogrames on TiO_2 nanowires after annealing at 600°C.

The EDX spectra realised on the nanowires after the H_3PO_4 etching show an important surface contamination by phosphor. We use an oxygen plasma treatment to get rid of this contamination (Figure 2-17). Additional annealing step at 600°C for 2 h in ambient air may be used to improve the crystalline quality of samples.

According to the SEM characterisations, arrays of periodic metal-oxide nanowires (TiO_2) with length of 350-450 nm, diameter of 40 nm and heterostructures (TiO_2/SnO_2) with length of 600 nm and diameter of 180 nm demonstrated a low number of matrix defects, and a high uniformity at large scale. Thus, the final fabrication protocol consists of following steps:

1. AAO annealing at 450°C on air
2. Metal-oxide films deposition by ALD
3. Reactive ion etching
4. Wet-etching in H_3PO_4 (85%) – stirring at room temperature for 15-16h
5. Rinsing in DI water
6. Oxygen plasma 200 W, 20 mTorr for 5 min
7. Annealing at 600°C for 2 h at ambient air

2.3 Photocatalytic test setup

A number of standard molecules are accepted by the scientific community to characterise the photocatalytic degradation at the research stage (ISO 10678 (2010)). Such organic molecules are often colorant, for which the degradation rate can easily be visualized and monitored by UV-Vis spectrometry (methylen blue, rhodamine B, methyl orange), as well as some organic acids that have a specific absorption in the UV-Visible range (e.g. salicylic acid). The degradation of real pollutants such as xenobiotic or herbicides requires a monitoring by chromatographic methods (LC/MS). The degradation of methylene blue (MB) generally undergoes several steps of bond breaking. A typical example of MB degradation determined by LC/MS is represented on Figure 2-18 [13].

Rhodamine B (RhB) is another standard molecule used in photocatalytic degradation. RhB being a more complex molecule than MB, it undergoes desethylating as preferential bonds breaking ($+N–(C_2H_5)$) that can be followed by chromatographic methods (Figure 2-19) [128].

Salicylic acid (SA) is another widely used target molecule for the laboratory scale photocatalytic tests [129]–[132]. The SA is a monohydroxybenzoic acid (o-hydroxybenzoic acid, o-HBA) also known as aspirin, and its degradation occurs via oxidation. Oturan et al. [133] demonstrated the sequential hydroxylation of the aromatic ring, though the formation of the intermediate states as di-, tri-, tet-and p-HBA. The LC/MS characterisations of intermediate compounds formed during the photocatalytic degradation of the SA were realised by Mukherjee et al. [131]. Initially, aspirin hydrolysed in water forms salicylic and acetic acids; their further oxidation follows the schematic presented on Figure 2-20.

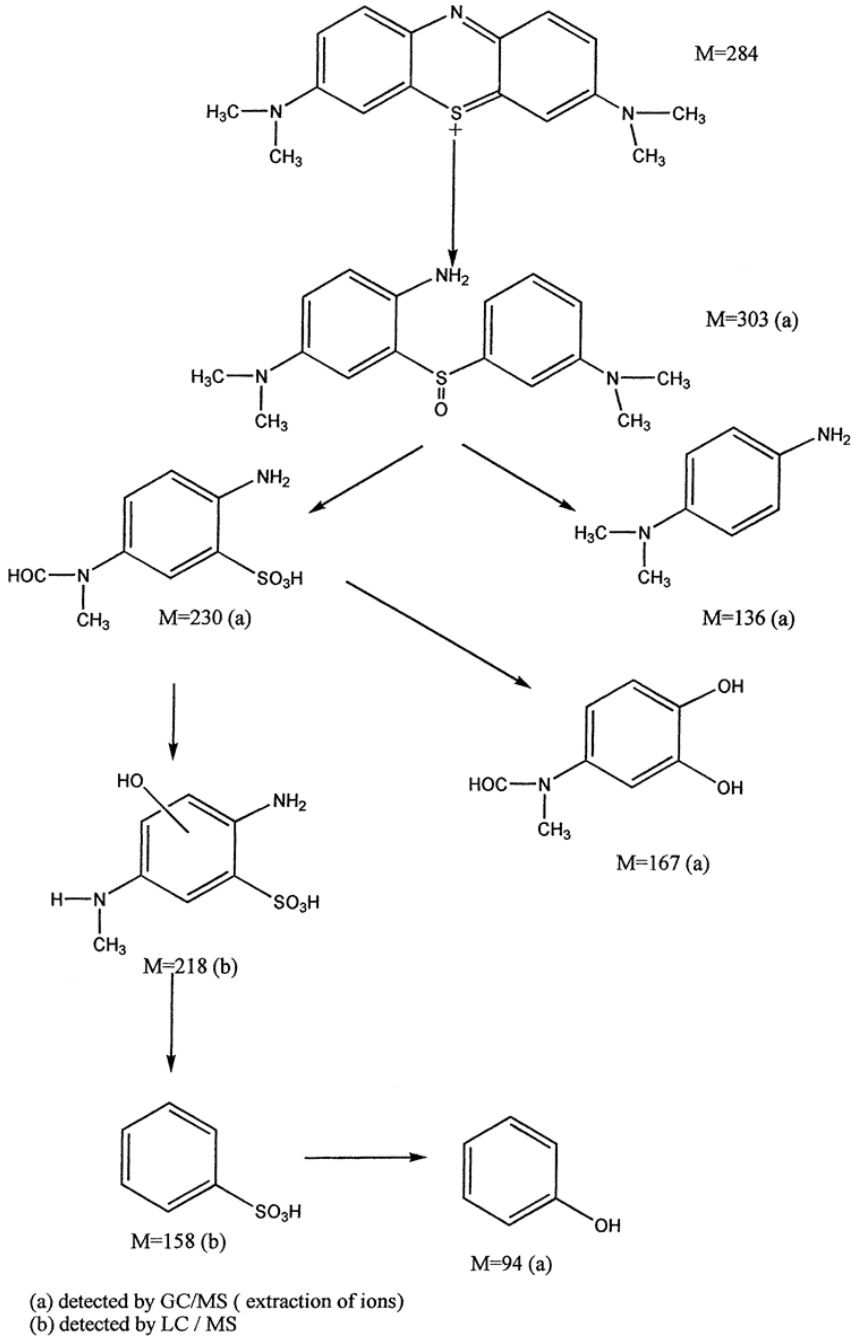

Figure 2-18 Possible pathway of methylene blue photocatalytic degradation [13].

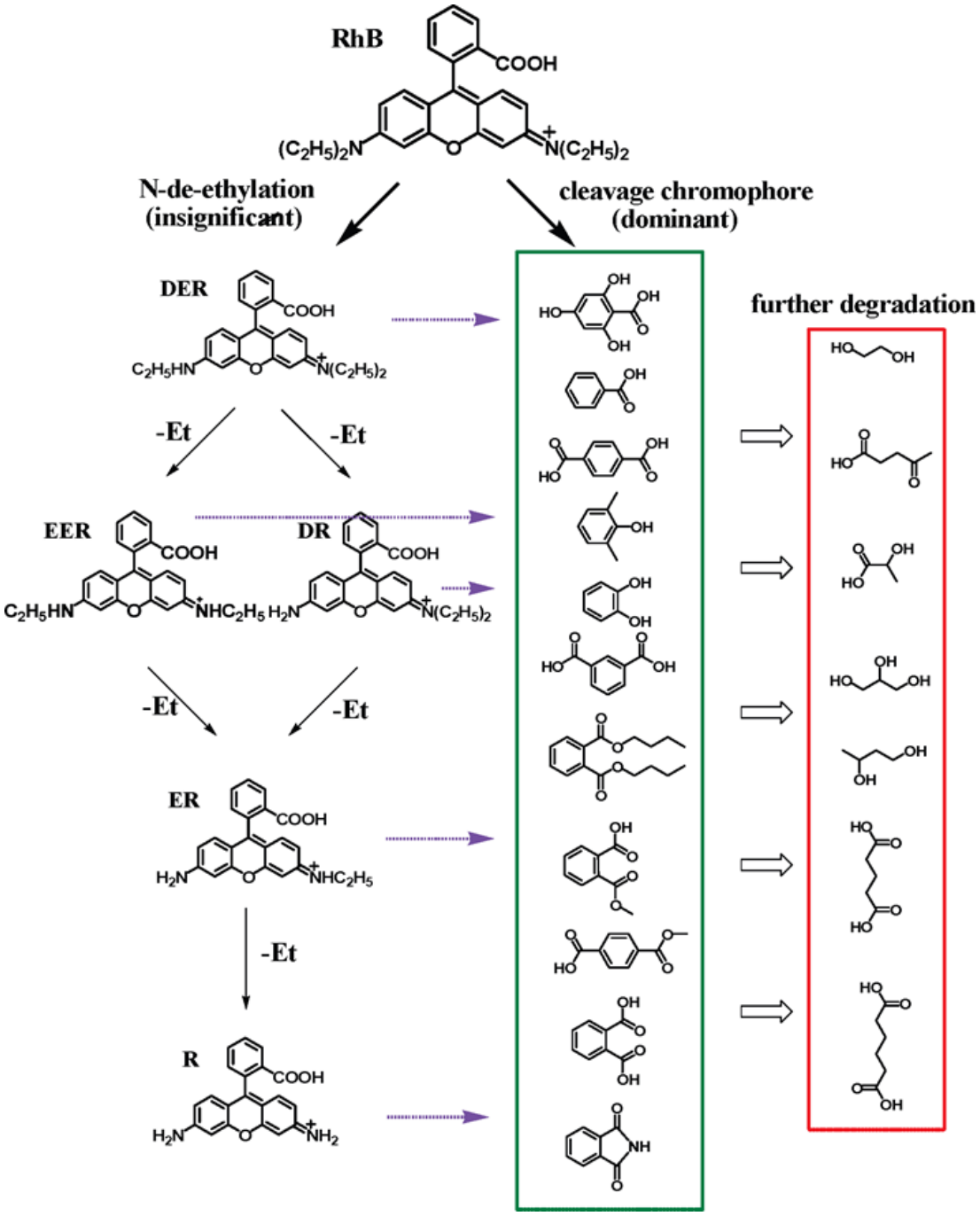

Figure 2-19 Possible pathway of Rhodamine B photocatalytic degradation [128].

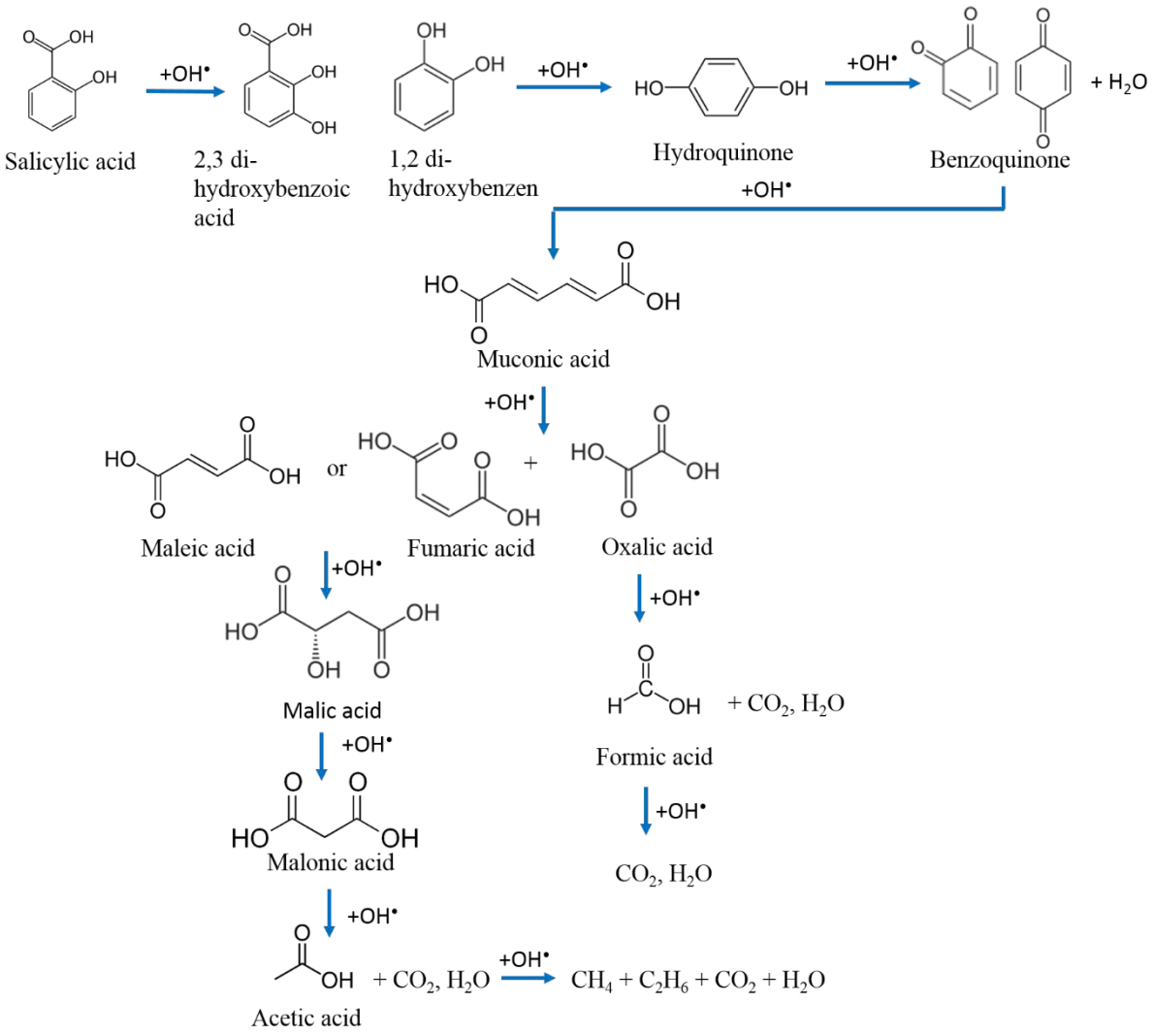

Figure 2-20 Possible pathway of salicylic acid degradation [130], [131].

The photocatalytic tests are performed using close reactors – quartz cuvettes (standard four polished windows, 10 mm light path Hellma® fluorescence cuvettes). The use of closed reactors avoids several problems that often occur when using open reactors for photocatalytic measurements. In open reactors, such as culture multiwell plates, various uncertainty factors due to the evaporation of water from the aqueous solution of pollutants, which involves the increase of their concentration, occur. At the same time, the volume change decreases the optical light path through the solution, which leads to an unreliable determination of the absorption peak intensity. The use of closed reactors a quartz cuvette, significantly reduces the evaporation problem and the optical light path is still constant.

Samples being pre-cut to a standard size of 0.9×35 mm are placed along of the side of cuvette. Cuvettes are filled with 4 mL of pollutants solution, closed with a plastic lid and sealed by Teflon-tape. The simplicity of this approach allows several samples to be measured at the

same time, limited only by the number of available cuvettes. One cuvette of the set was dedicated as the control to test the pollutant solution photodegradation without a device.

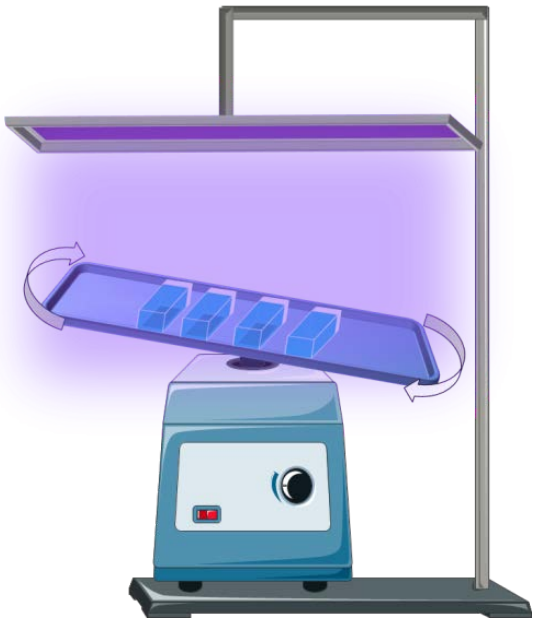

Figure 2-21 Schematic of photocatalytic test setup.

The photocatalytic degradation tests are carried out on the MB (RhB, SA) solutions with a concentration of 5 mg/L using a weakly powered lamp (UV lamp at 365 nm (8 W) and visible irradiation range using lamp 400 - 700 nm (8 W). The pollutant adsorption-desorption phenomenon on the samples surface is controlled by the MB concentration measurement in time without irradiation (tests in the dark). It corresponds to the negative time scale (-60 min up to 0 min) on the photocatalytic degradation plots. After the last measurements in the dark realised at 0 min, the irradiation is switched on and the positive time scale corresponds to the photocatalytic degradation measurements under irradiation. The UV-Vis spectra are acquired every 30 - 60 min to follow the degradation kinetics. The degradation rate is controlled by measuring the pollutant absorption peak intensity. The principal absorption peak for methylen blue (MB) is at 666 nm, for Rhodamine B (RhB) at 554 nm and for alicylic acid (SA) at 298 nm. To ensure a homogenous degradation, the cuvettes are placed on the rotary stirring plate (Figure 2-21). The photocatalytic degradation rate is determined according to the first order of the reaction kinetic. The obtained photocatalytic degradation constants are normalized by the sample surface area, and not by the specific surface area of the sample.

2.4 Characterisation Techniques, Substrates and Precursors

Physicochemical properties of fabricated samples are investigated using a large spectrum of characterisation methods providing information about morphology, chemistry and crystalline quality of samples. Table 2-1 provides an overview of the characterisation methods that are used along this work. The detailed working principles of these methods are reported in the Appendix 3. The typical substrates are used in this work are Si (100) and commercial AAO. The details regarding both substrates and their surface preparation are given in Appendix 4. The summary on the used precursors is given in Appendix 5.

Table 2-1. Summary on used characterisation methods.

Information	Characterisation techniques
Morphology and microstructure	• Scanning Electron Microscopy (SEM) • Atomic Force Microscopy (AFM) • Transmission Electron Microscopy (TEM)
Crystallography	• X-ray diffraction (XRD) • Electron backscatter diffraction (EBSD)
Chemical composition	• X-ray Photoelectron spectroscopy (XPS) • Energy dispersive X-ray spectroscopy (EDX) • Secondary ion mass spectrometry (SIMS)
Surface energy	• Kelvin Probe Force microscopy (KPFM) • Contact angle
Optical properties	• UV-VIS spectroscopy • Photoluminescence • Ellipsometry

2.5 Conclusion

This chapter presented the nanostructure fabrication methods and the thin film deposition process used in this work. The optimised fabrication process flow of the periodic nanowires via AAO template assisted approach is the core achievement reported in this chapter. Moreover, a presentation of fabrication approaches for other building blocks required for the photocatalytic device assembly such as plasmonic nanoparticles were highlighted.

3 Synthesis of Nanomaterials

3.1 Fabrication of nanoparticles via the block-copolymer method

To reach the typical size of nanoparticles we targeted (10-20 nm), we use and develop the direct block copolymer (BCP) self-assembly into reversed micelles. The possibility to obtain different micelles morphologies such as spheres [134]–[136], parallel or perpendicular cylinders [137]–[139], or lamellae [140]–[142] offers various kinds of polymer patterns. The block copolymer domains form a kind of polymeric template that tailors size and spacing down to sub-10nm scale[143]. The simplicity of this method and its large scale production makes it very popular and competitive vis-à-vis more complicated and expensive lithographical techniques.

The principle of the BCP self-assembly method is based on the reversed micelles formation due to the selective solubility of one copolymers block in an appropriated solvent. The partly-dissolved copolymers block forms a “corona”, whereas the block incompatible with the solvent forms the micelles “core”, and together consists of a micelle. The micelles solution can be used itself for the colloidal nanoparticles fabrication [144] [145] [146], either be deposited on a substrate by spin-coating and form a hexagonally ordered BCP template. The spherical arrangement of block copolymer domains allows a large scale production of hexagonally ordered self-assembled metal, metal-oxides, and complex nanoparticles.

The precursors infiltration on pre-deposited micelle template can be realised using two different approaches: liquid or vapour phase impregnation. The vapour phase impregnation is generally used for the metal-oxide nanoparticles formation such as TiO_2. Using the CVD technique, Li and co-workers [147] formed TiO_2 nanoparticles through the exposure of $TiCl_4$. The micellar film was immersed in water before the exposure of precursor. The authors supposed that immersion promotes water trapping by the poly-vinylpyridine PVP micro-domains of micelles. Krishnamoorthy and co-workers [127] as well as Yin and co-workers [148] used ALD as an exposure tool for the sequential infiltration of $TiCl_4$ and water to form TiO_2 nanoparticles. The liquid phase impregnation is more appropriate for the fabrication of noble metal nanoparticles. The precursors of these metals are often solid metal salts soluble in a polar solvent. In both modes of precursor loading, the pyridyl groups play a key role in the mechanism of the nanoparticles formation [140], [148], [149]. The diffusion of the precursor inside the micelles is driven by the chemical contrast between the micelle core and corona. It allows considering the micelle as a confined chemical reactor.

3.1.1 Fabrication of self-assembled TiO_2 nanoparticles

Ordered arrays of block copolymer reversed micelles with a hexagonal organization are obtained by spin-coating, as is illustrated in Figure 4-1.

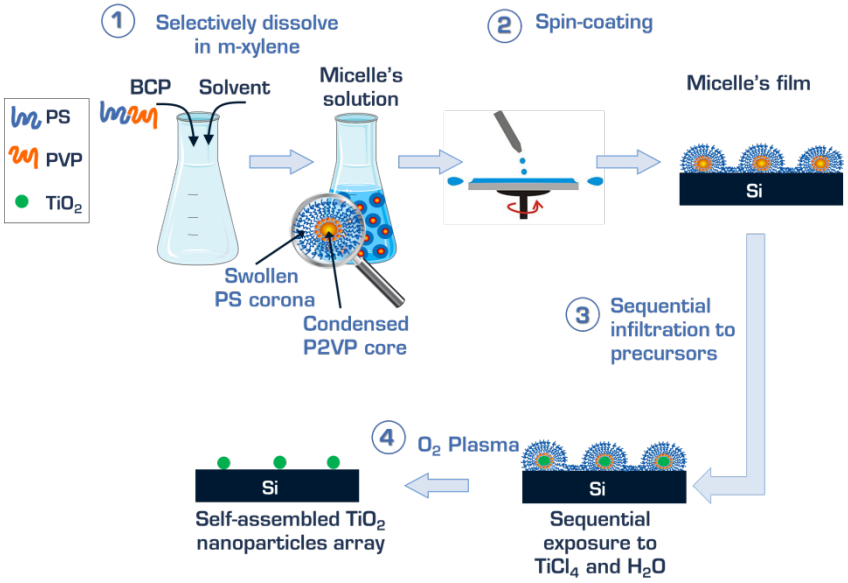

Figure 3-1. Illustration of steps involved in the formation of titania nanoparticles guided by BCP templates.

The growth of well-assembled TiO_2 nanoparticles is carried out using sequential vapour infiltration (SVI) two modes as detailed in Section 2.2.1.

The SEM pictures on samples after exposure in mode I show a significant increase in micelle size as a function of precursor exposure (given by the number SVI cycles). Swelling of the micelle is observed even after a relatively low number of SVI cycles (Figure 3-2A), as expected due to the formation and growth of titania within the micelles core. After a low number of $TiCl_4$ and water SVI cycles (mode I) and stripping of the polymer template by O_2 plasma, the samples exhibits an array of self-assembled nanoparticles. However, for samples that exposed to a greater number of SVI cycles (more than 50 cycles), no change in the micelles size after O_2 plasma treatment was observed. This finding could indicate that the polymer is covered by titanium dioxide shell and is therefore inaccessible to the oxygen plasma. Exposure of the micelles film to a low number of cycles in mode I forms confined nanoparticles inside the micelles (in-growth). An increase of SVI cycles leads to an over-growth through the micelles corona and ultimately forms a TiO_2 shell around the micelle via further classical ALD growth. The periodicity of micelles (center-to-center distance) limits the space for the shells formation. A similar growth regime after exposure to $TiCl_4$ and H_2O was investigated by Yin and co-workers [148]. According to the authors, the PVP-micelles core, which contains pyridyl groups, was saturated by metal-organic complexes that formed

after a few SVI cycles. Then, further deposition from $TiCl_4$ and H_2O continued to grow on top of the preformed and polymer-encapsulated nanoparticles, which led to the micelles size extension [148].

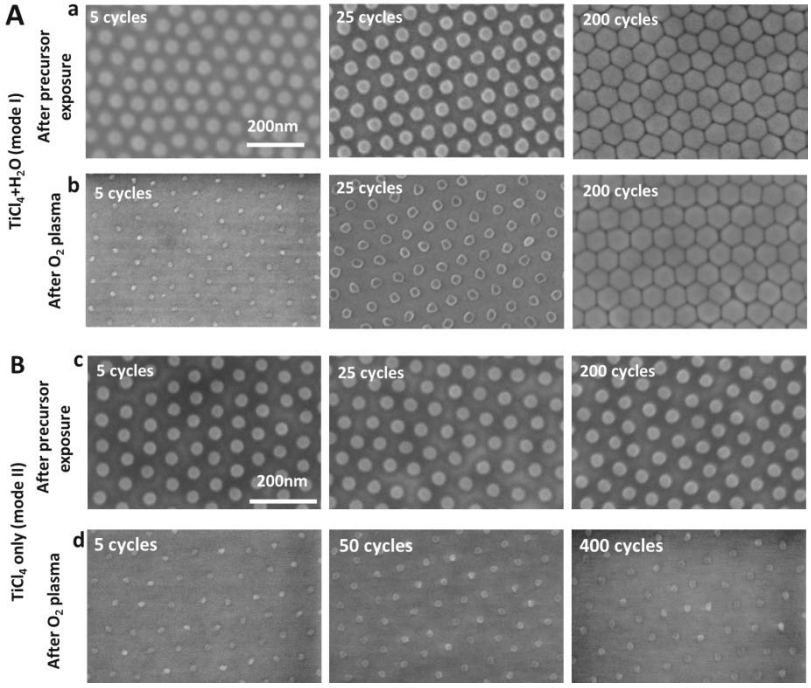

Figure 3-2. Micellar film after SVI of $TiCl_4$ + H_2O (mode I-(A)) (a) and after O_2 plasma treatment (b), and micellar film after SVI of $TiCl_4$ (mode II (B)) (c) and after O_2 plasma treatment (d).

The samples fabricated by exposure to a different number of $TiCl_4$ pulses in mode II show that the micelles diameter do not change (according to SEM), even after exposure to a high number of SVI cycles. The O_2 plasma treatment removed the BCP micelles on all samples, and the developed arrays show significantly smaller nanoparticles than obtained with mode I; however, the nanoparticles do show the size increasing with the number of SVI, eventually reaching saturation at a diameter less than the initial micelle (Figure 3-2B). This observation could indicate that the growth of TiO_2 is limited by one or several parameters, such as the micelles core size, accessibility to pyridyl groups, and quantity of water trapped during formation of the micellar film. Comparisons of the micelles size after exposure to different modes and the nanostructures obtained after oxygen plasma treatment are illustrated in Figure 3-3.

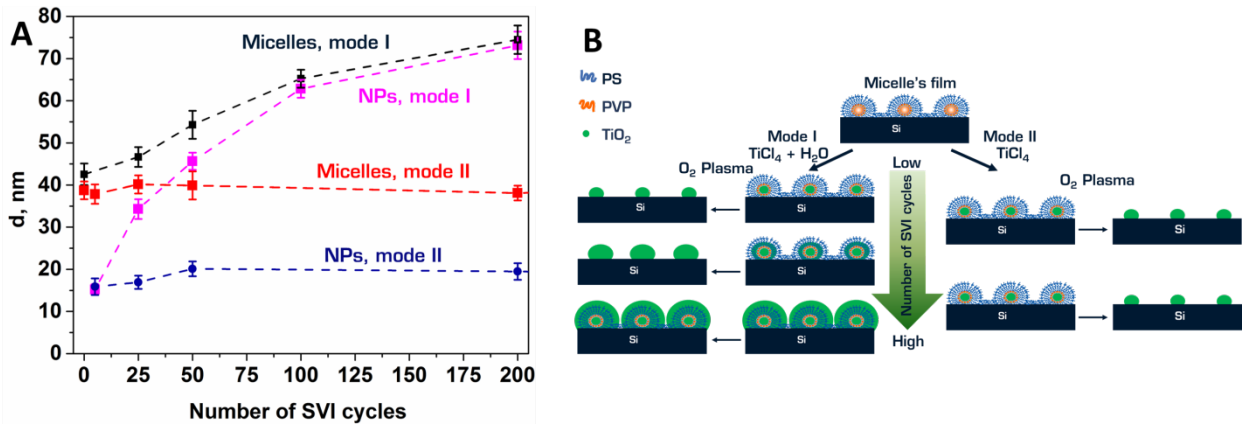

Figure 3-3. (A) Micelles size modification after two exposure modes and nanoparticles (NPs) size after O_2 plasma treatment. (B) Schematic illustration of difference between mode I and II.

The behaviour of growth mode I is in accordance with what has been reported in earlier publications [127],[150]. In mode II the quantity of water trapped within the micelle serves as a growth-limiter, or the determinant for the upper limit for the nanoparticle sizes. In the mode I, a continuous supply of water during each SVI cycle enables the continuous growth of titania, the nanoparticles size is determined only by the number of SVI cycles. However, the complete confinement of nanoparticles into the template, as observed in exposure mode II, has not been shown in literature. The growth of titania in mode II could be explained only by the presence of moisture trapped within the micelle core, which is expected to have resulted from condensation of moisture, during the micelle film formation on the substrate, by an extent determined by the relative humidity of the environment. This motivated further investigations to gain a deeper understanding of the chemical functionality of the PVP core upon exposure to the precursors.

Chemical analysis of micelle films

A chemical characterization on the nanoparticle formation within the core is investigated by performing XPS before and after exposure to $TiCl_4$ (in mode II) prior to oxygen plasma treatment. The intent is to obtain insight into chemical modifications of the functional groups in PVP upon exposure to $TiCl_4$. The influence of ambient air on the samples exposed to $TiCl_4$ is explored by comparing samples that are exposed to the precursor and then measured by XPS after a short transfer (few hours) into vacuum and after storage in vacuum, or after 2 weeks in the ambient environment. There is no difference in the XPS results between the samples examined immediately after exposure and the samples stored under vacuum.

However, the samples left in the ambient environment after precursor exposure exhibits a difference in their chemical compositions.

The XPS spectra presented on Figure 3-4 corresponds to the spectra acquired on the BCP micellar film as deposited (A) and aged for 2 weeks (B). The spectra C and D correspond to the micellar film: (C) just after the exposure to $TiCl_4$ and (D) after 2 weeks of aging.

Binding energies in the XPS spectra are corrected for samples containing titanium (Figure 3-4, spectra C and D) by placing the Ti $2p_{3/2}$ peak at 458.8 eV and applying a rigid shift to the remaining peaks. The Ti 2p spectra for Ti in $TiCl_4$ and TiO_2 are known to be in close proximity [151],[152], [153]. After this energy correction, the main peaks of nitrogen (N 1s) and oxygen (O 1s) are found at 399.0 eV and 531.8 eV, respectively. A rigid shift in binding energy is also applied to spectra of BCP films without exposure to $TiCl_4$ (Figure 3-4, spectra A and B) to have the main N 1s contributions at 399.0 eV. The energy shift is found to be 0.9 eV for spectra A and B and 0.75 eV for spectra C and D. For a comparison of intensities, the spectra in C are normalized relative to the spectra in D using the Ti $2p_{3/2}$ peak.

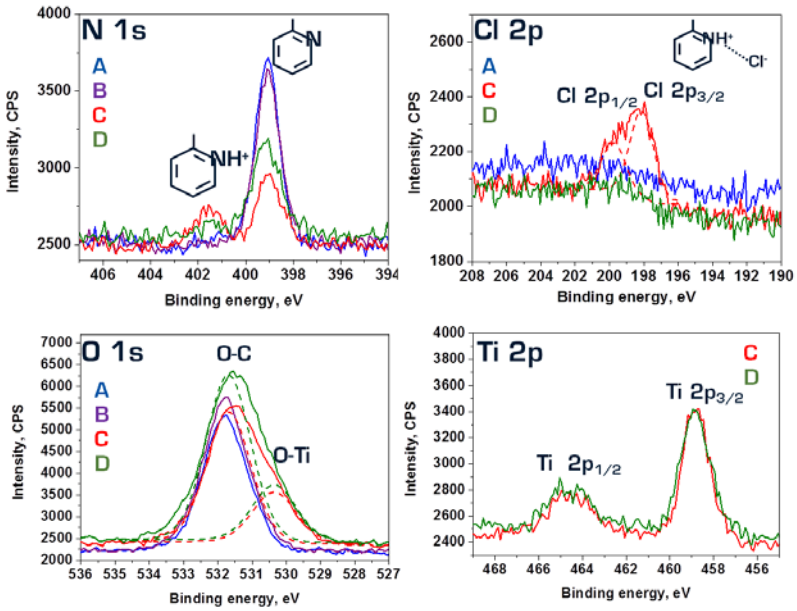

Figure 3-4. The XPS N 1s, Cl 2p, O 1s, and Ti 2p: (A) BCP micellar film, (B) BCP micellar film aged for 2 weeks, (C) BCP micellar film just after exposure to $TiCl_4$, and (D) BCP micellar film exposed to $TiCl_4$ aged for 2 weeks.

The XPS spectra presented in Figure 3-4 highlights a strong chemical state modification of the P2VP structure upon exposure to $TiCl_4$. The nitrogen of the pyridyl groups (P2VP) showed partial protonation, as observed from the appearance of a new peak (401.4 eV) in the N 1s spectra just after exposure to $TiCl_4$. The peak corresponding to the unprotonated nitrogen is found at 399.0 eV. Protonation of the nitrogen is expected to result from the presence of hydrochloric acid that formed during the hydrolysis of $TiCl_4$, which is initiated by moisture

within the micelle films. The potential to trap moisture within the reverse micelles and the influence of environmental humidity have been discussed in literature [154],[155] Krishnamoorthy and co-workers [154] related the influence of moisture content (defined by the relative humidity) on the height of the micelle. They reasoned that the moisture content induced an increase in the surface tension at the PS-PVP interface. Kim et al.[155] showed that the relative humidity level also played a crucial role in the self-assembly of polystyrene-b-poly(ethylene oxide) (PS-b-PEO) microdomains.

The chemical modifications in the micelle structure are also confirmed by changes in the O 1s spectrum. The micellar film before exposure shows oxygen signals from O-Si and O-C bonds at 531.7 eV. After exposure to $TiCl_4$, the O 1s spectrum broadened by exhibiting a shoulder at 530.4 eV that corresponds to the formation of oxygen-metal bonds (O–Ti). The formation of TiO_2 could only be explained by hydrolysis of $TiCl_4$, which is initiated by moisture trapped within the micelle core. The concentration ratios [O]/[Ti] for spectra C and D (Figure 3-4) are close to 2, which suggests the formation of TiO_2 after exposure to $TiCl_4$ (Table 3-1).

Table 3-1. Quantitative XPS analysis of sample exposed to 25 cycles in mode II, just after exposure and after two weeks ageing.

	Concentration, at. %	
	BCP film after exposure to $TiCl_4$	**BCP film after exposure to $TiCl_4$, aged for 2 weeks**
$[NH^+]$	0.6	0.1
$[Cl^-]$	0.8	0.2
[O-Ti] in [O]	2.0	2.1
[Ti]	1.1	0.9
[O]/[Ti]	1.8	2.3
$[NH^+]/[Cl^-]$	0.8	0.5

The possible SVI synthesis of metal-oxide structures without adding water was shown by Biswas et al. [156], [157] investigating interaction of poly(methyl methacrylate) (PMMA) with infiltrated vapors of trimethylaluminium (TMA). The presence of carbonyl and ester functional groups of PMMA enables TMA incorporation through the formation of Al-O coordination bonds. Similarly, one could envisage $TiCl_4$ incorporation into PVP via formation of Ti-N bonds as postulated by Yin and co-workers based on FTIR measurements that showed additional stretching band at 1637 cm^{-1} upon exposure to $TiCl_4$ and H_2O [148]. However, our

XPS measurements on the reverse micelle films upon exposure to $TiCl_4$ show that the peak positions of N 1s and Ti 2p do not correspond with Ti-N bond formation (for reference, Ti $2p_{3/2}$ for Ti-N bond should appear at 454-455 eV, as against 458.8 in our case). The position of N 1s peak at 401.4 eV indicates protonation of the pyridyl group of the PVP domains. This is in agreement with the observations by Zhou et al., who attribute N 1s peak at 401.3 eV to the protonation of PVP films by polystyrene sulfonic acid [158]. Further, the FT-IR observations by Zhou et al. attribute the appearance of peak at 1634 cm^{-1} to an increase in the rigidity of pyridinium ring due to intermolecular interactions. These observations contradict conclusions drawn by Yin et al. towards Ti-N bond formation based on the same peak. Further, it is very hard to exclude presence of residual moisture in polymeric films under normal conditions of sample preparation, and therefore it would not be possible to exclude protonation of the PVP in Yin et al.'s investigations. Additionally, in the mode-II experiments, we observe a threshold exposure beyond which the incorporation of $TiCl_4$ is found to saturate, which can be attributed to the limited quantity of residual water present in the PVP core. Such saturation cannot be explained if the precursor incorporation are to occur via complex formation. Thus, the hypothesis of the weak complex PVP-TiCl formation is supported neither by our experimental evidence nor by literature. We therefore conclude that the trapped residual water present within the PVP cores of the reverse micelles determine the incorporation of the precursor, by promoting the hydrolysis of $TiCl_4$. The XPS characterization performed on the micelle films exposed to $TiCl_4$ after ageing for a duration of two weeks in ambient air shows an unexpected reconstruction of the initial state of the block-copolymer micelles. This is observed from the decrease of the peak at 401.4 eV, associated with the protonated nitrogen (NH^+), and a decrease in the Cl 2p peaks. The O-Ti bonds contribution to the O 1s peak shows a slight increase (spectrum D) and could be explained by completing the hydrolysis of $TiCl_4$. Additionally, carbon contamination (C–O) from the ambient air is also noted (peak at 531.7 eV). The observations suggested the deprotonation of the protonated pyridyl units, and a loss of HCl upon ageing. Indeed, the atomic concentrations of N (in NH^+) and Cl before and after ageing decreases (Table 3-1), although the detected quantitative values are close to the detection limit of XPS. The HCl formed upon hydrolysis of $TiCl_4$ should remain trapped in the micelles due to protonation of the pyridine moieties to form positively charged pyridinium chloride. The TiO_2 formed encounters a low pH environment (due to acidity within the core) and can be expected to acquire a positive surface charge (the isoelectric point of TiO_2 is 5.8). The unfavourable repulsive interactions between a positively charged TiO_2 and a positively charged pyridinium chloride may drive the release

of the HCl. The slow kinetics of the process may explain the decrease in HCl upon ageing for several days. A summary of the XPS observation is presented in Figure 3-5.

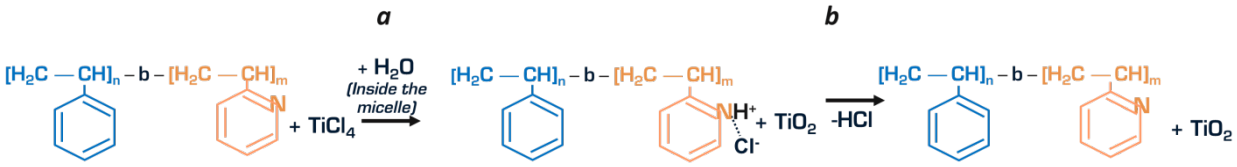

Figure 3-5. Chemical reaction mechanism on samples exposed to $TiCl_4$ in mode II based on observations from XPS; (a) after exposure, (b) after 2 weeks of aging.

Based on the XPS experiments, it is clear that a certain amount of moisture is consistently present within the micelles, which participates in the hydrolysis of the $TiCl_4$ and results in the formation of TiO_2 nanoparticles. The precursor loading mode (mode II) takes advantage of the moisture which is internally present in the micelles, and not externally supplied as in mode I. This mode further possesses the specific advantage of saturating the nanoparticle growth that is confined within the core of the reverse micelles, which significantly widens the process window when precise control of nanoparticle size is mandatory.

Microstructure of nanoarrays

Understanding the structural evolution within the block-copolymer feature is necessary to provide clarity about the growth of TiO_2 at multiple stages of exposure in mode I. Structural characterization of the nanostructures is performed by TEM and SIMS depth profiling on samples prepared after different levels of exposure in mode I.

The inability of oxygen plasma treatment to reduce the micelles size after a certain number of ALD exposures in mode I as it is shown on Figure 3-2A(b) is based on the possibility of titania shell growth on the polystyrene surface but on only OH-functionalised surface. In our case, there is no specific functionality that could drive a direct growth of TiO_2 on the PS corona. However, residual moisture within polystyrene contributing to the formation of tiny amounts of TiO_2 on the PS corona cannot be excluded. We believe the primary growth of titania on the PS corona is caused by an in-growth of the titania following an initial deposition within the hydrophilic PVP core.

TEM characterization of a sample after ALD exposure in mode I (200 cycles) confirmed the shell formation (Figure 3-6). The STEM-HAADF (scanning transmission electron microscopy - high-angle annular dark-field imaging) mode of imaging allows differentiating between regions with heavy elements (in our case, Ti) and elements of lower Z. This enables

qualitative descriptions about the chemical composition and porosity of the structures. We note that the denser area of micelles on the interface of micelle and substrate could be attributed to the core and that the less dense area on top of the micelle could be the corona. The micelles corona may not exhibit an equal thickness along the micelles core, with a greater thickness of the corona on top of the micelle compared with its borders (Figure 3-6c). The presence of a 5 nm residual polystyrene layer between the micelles could be clearly observed (Figure 3-6 b,c).

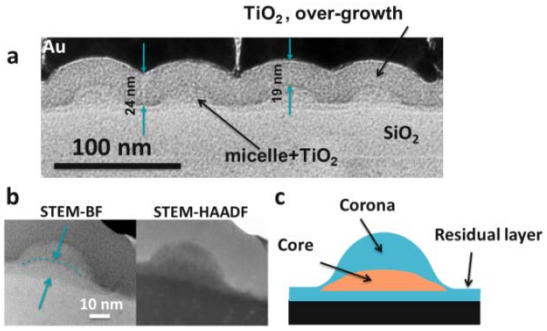

Figure 3-6. TEM image of sample after exposure to 200 cycles in mode I: overall view (a), detail of the structure of a micelle (b), and schematic representation of the micelles internal structure (c).

However, the information obtained by TEM micrographs is not sufficient to draw a conclusion about the titanium dioxide distribution throughout the micelle. We use dynamic SIMS, which allows the depth-profiling of the distribution of the elements across the micellar features. SIMS profiles are performed on the micellar film before and after exposure (Figure 3-7) to 25, 75, 200 and 400 ALD cycles in mode I.

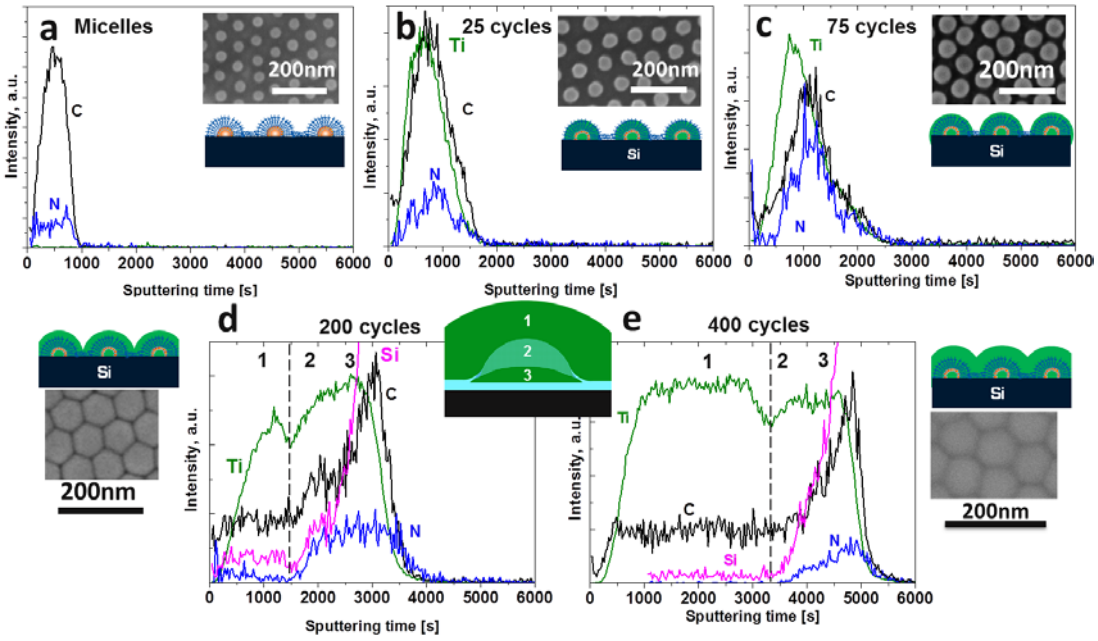

Figure 3-7. SIMS profiles of the micellar film without exposure (a), the micellar film after exposure to 25 (b), 75 (c), 200 (d) and 400 cycles (e) in mode I ($TiCl_4$+H_2O).

The micelles film without any exposure to the precursors reveals the presence of carbon and nitrogen in the film as expected for the BCP system. However, the SIMS analysis of the micellar film shows a nitrogen signal appearing at the same time as carbon, which is unexpected because the nitrogen signals correspond to the core and should appear later. The simultaneous appearance of nitrogen and carbon signals may be explained by the asymmetric shape of micelle features; a thinner corona at the border that may be sputtered away quicker, thereby exposing the nitrogen functionality underneath (Figure 3-6c). The similar distribution profiles of N and C are also observed for the samples following exposure to 25 and 75 cycles of $TiCl_4$ and H_2O (mode I). According to the results in Figure 3-3A, the sample after 25 cycles of exposure resulted in nanoparticles that are smaller than the initial micelles size. The SIMS profile obtained for this sample shows the presence of titanium that appeared to be on the surface of the film as well, given that an observable titanium signal appears earlier than did the nitrogen and carbon signals. The presence of titanium on the surface increases with the number of cycles and may be an indicator of in-growth through the polystyrene corona. This is supported by the fact that the profile of the sample exposed to 400 cycles of only $TiCl_4$ (mode II) did not show a similar behavior. In this case, the titanium appeared together with C and N and not earlier, as observed for the sample after 25 cycles exposure in mode I (Figure 3-8).

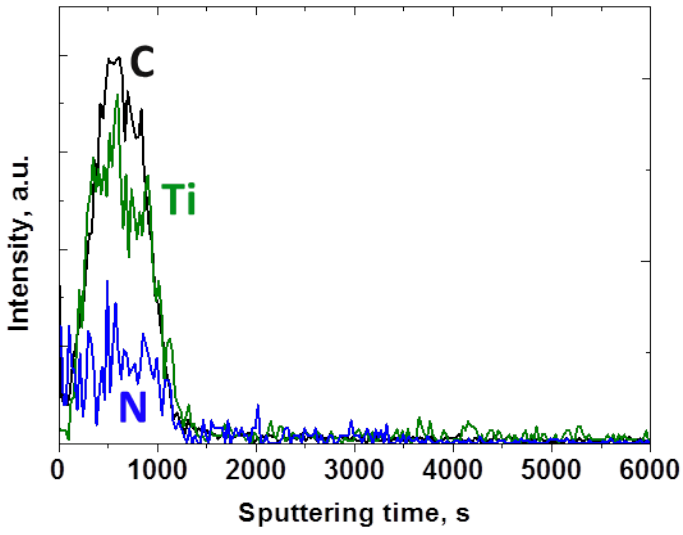

Figure 3-8 SIMS profile of samples exposed to 400 cycles in mode II (without water).

The presence of a small amount of titania on the polystyrene do not exclude the possibility of successfully removing the underlying polymer during the O_2 plasma exposure, resulting in a smaller nanoparticle (Figure 3-7B). A continuous in-growth during the exposure in mode I

results in the over-growth of a conformal TiO_2 layer, which encapsulates the BCP micelles and prevents etching.

The sample exposed to 200 cycles of mode I (TEM data in Figure 3-6) is also investigated by SIMS for C, N, Ti and Si. Following the titanium profile, three distinct areas could be observed. The first area, which began at the surface, corresponds to the "titania shell" that formed on top of the micelle film (zone 1, Figure 3-7D). In zone 1, the carbon levels observed on the micelle films exposed to the different number of SVI are similar to the carbon levels observed on planar TiO_2 films deposited on silicon substrates (C contamination). Zone 1 is followed by a prominent reduction in the Ti signal. This origin of this signal loss is not clear because it could be caused by either (i) the presence of a thin layer with lower Ti and higher O content than neighboring layers or (ii) a SIMS artifact at the interface between two different layers, a TiO_2 shell/micelle (Figure 3-9). This signal decreasing is followed by zone 2, where the signals of Si and C increased again and is indicative of sputtering the micelles. Increasing of the Ti signal in this zone would suggest the presence of TiO_2 in the corona likely caused by in-growth through the PS, and originating from the PVP core. We note that zones 2 and 3 show an initial increase in the Ti peak, followed by a plateau. The plateau could indicate the titania presence within the PVP core, as indicated by the concomitant presence of nitrogen. The elements' distribution for the sample exposed to 400 cycles in mode I, has a similar appearance to the profile from 200 cycles. We note that the titanium profile in the first zone is more extended and corresponded to a thicker layer deposited on the top of the micellar layer; the reduction of the Ti signal at the TiO_2 shell/micelle interface is reproducible.

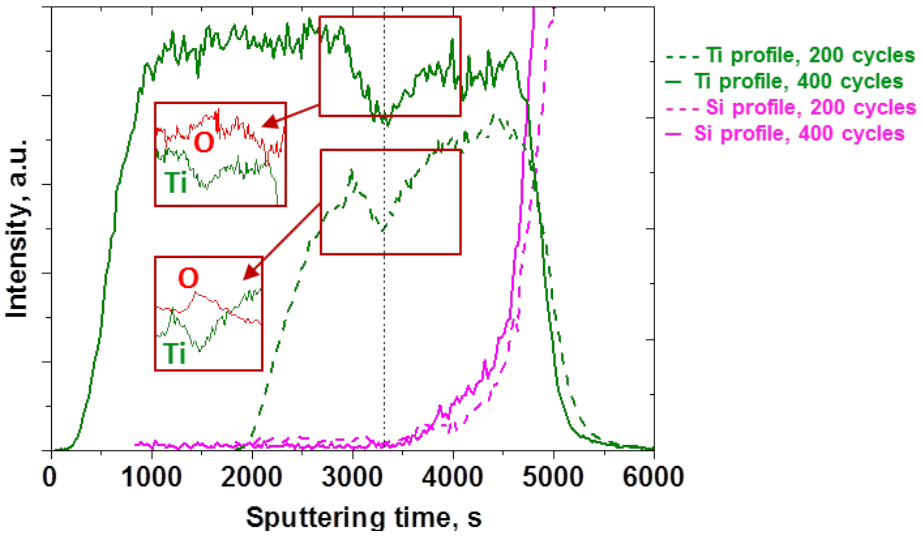

Figure 3-9 SIMS profiles of Ti Si and O for samples after exposure to 200 and 400 cycles in mode I.

After precursor exposures, the carbon distributions of all samples showed a significant increase at the micelle/substrate interface that is due to the residual polystyrene layer. This observation, in addition to an increase in sputtering time with increasing numbers of SVI cycles, could be a sign of the polymer cross-linking.

It is shown that the precursor loading mode determined the nanoparticles growth rate. The inclusion of water pulses enabled significant growth that is not defined by the micellar core dimensions. Exposure to $TiCl_4$ without water pulses confined the reaction to the micelles core, which could lead to the fine-tuning of nanoparticle dimensions. To our knowledge, this is the first time that TiO_2 nanoparticle synthesis did not require any specific exposure to water during the SVI synthesis. However, it underlines the importance of control over humidity to ensure reproducibility in the size of deposited features.

Therefore for further experiments the nanoparticles are formed using 50 cycles of $TiCl_4$ exposure. The nanoparticles seeds are used for further tentative selective MOCVD growth of TiO_2 nanowires.

3.1.2 Fabrication of plasmonic nanoparticles.

Similarly to the TiO_2 nanoparticle fabrication, gold nanoparticles are also fabricated using the BCP method. Well-ordered micelles arrays are exposed to an aqueous solution of the gold precursor. A variation in the exposure time from 10 min to 24 h is tested in order to reach the precursor saturation within the micelles. The saturation is already reached after 10 min of immersion and further exposure has no impact on the nanoparticles size. The liquid infiltration approach addresses limitations imposed by the micelles core parameters. When the cores PVP functionalities are saturated by the precursor, no further precursor incorporation could be achieved. The size and spacing of formed nanoparicles are controlled by SEM and AFM measurements, correspond to 8 nm and 15 nm for two used BCP systems 40.5-b-41 and 102-b-97 respectively (Figure 3-10).

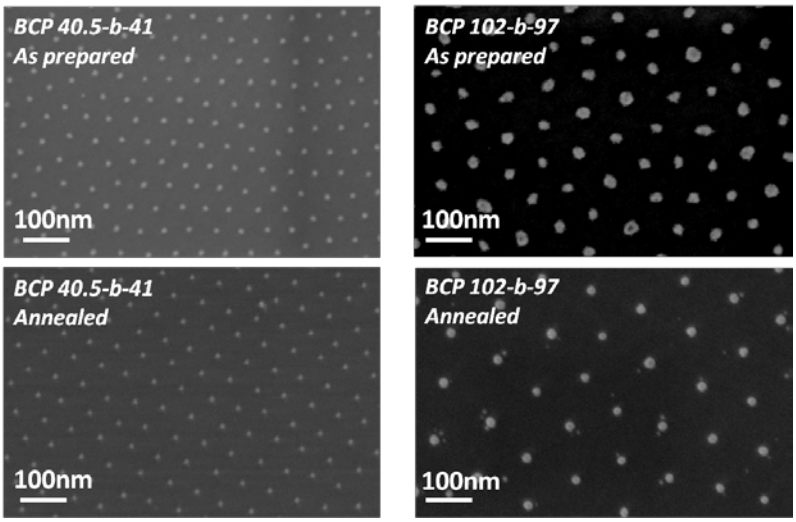

Figure 3-10 SEM images of gold nanoparticle (as prepared and annealed) obtained by PS-b-PVP systems: 40.5-b-41 (left) 102-b-97 (right).

Gold in three different oxidative states are evidenced by the XPS analysis of nanoparticles after O_2 plasma, before and after annealing (Figure 3-11). The XPS spectrum of Au 4 $f_{7/2}$ before annealing shows the non-reacted chloride ($HAuCl_4$) with binding energy at 87 eV, oxidised gold at 85 eV and small amount of metallic gold (Au^0) at 84 eV. In order to promote the reduction of the oxidized and non-reacted gold precursors to the metallic state an annealing of nanoparticles is performed at 500°C in ambient air atmosphere for 1 h. After annealing the amount of oxidized and non-reacted gold precursor contribution is reduced. However, oxidised gold remains significant after 1h of annealing.

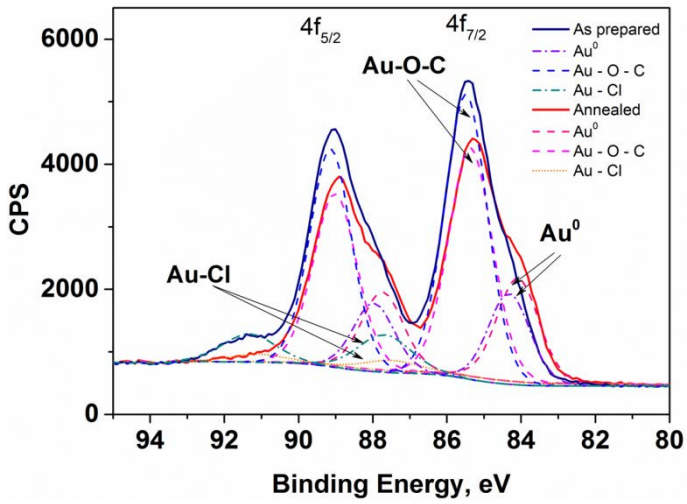

Figure 3-11 HR-XPS of Au 4f on gold nanoparticles as prepared and after annealing.

The SEM pictures of samples after annealing show the smoothing of the nanoparticles shape which becomes more spherical and also exhibits more contrast on the SEM images (Figure 3-10).

UV-Vis spectra performed on the nanoparticles deposited on the glass substrates and annealed, demonstrate a SPR peak at 525 nm for both BCP systems showing that the SPR wavelength does not significantly depend on the nanoparticles size and spacing within the range 8-15 nm size and 70-100 nm spacing (Figure 3-12). As expected the absorbance is lower for smaller gold nanoparticles, since the light to nanoparticles interaction is 36% lower in this case.

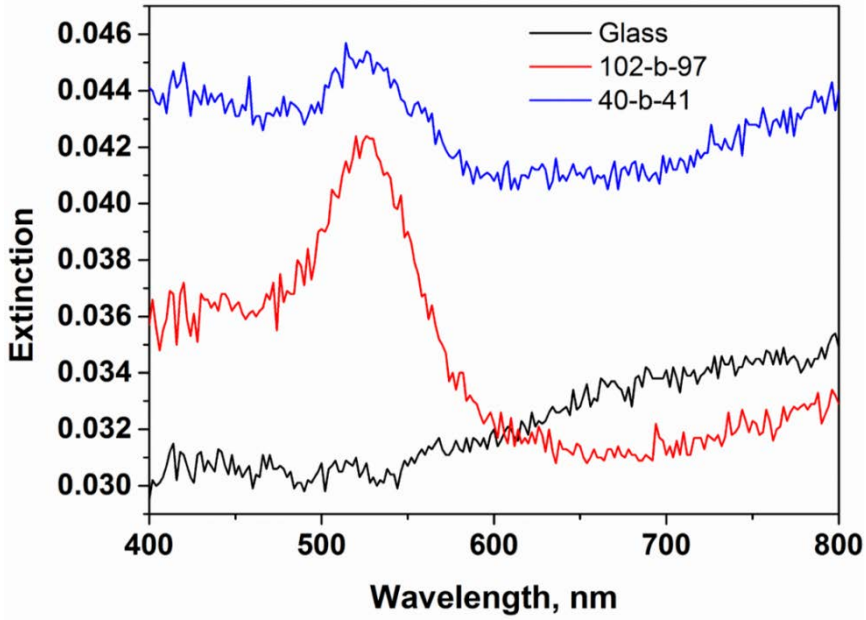

Figure 3-12 UV-Vis spectra on Au nanoparticles for PS-b-PVP systems: 40.5-b-41 (left) 102-b-97 (right).

3.1.3 Summary

The development of the BCP self-assembly approach for the fabrication of periodically well-organised metal-oxides and metallic nanoparticles is demonstrated in this Section. The TiO_2 nanoparticles are successfully formed. The detailed investigation on the BCP micelles exposure to the $TiCl_4$ precursor allows getting new insights on the metal-oxide nanoparticles formation mechanism that offers better size control and reproducibility.

3.2 Fabrication of well aligned TiO_2 nanowires

This section presents the investigations realised on TiO_2 synthesis by MOCVD, and ALD as the key deposition techniques selected for the development of the periodic TiO_2 nanowires

3.2.1 TiO_2 nanowires growth by MOCVD

The main challenge of this study is the selective growth of metal oxide nanowires that can be privileged either the precursors decomposition on the TiO_2 nanoparticles seeds, or the growth initiation on the TiO_2 nanoparticles, acting as pre-formed nuclei. It was shown that the temperature of thermal decomposition of TTIP could be lowered by pre-coating substrate with TiO_2 [104], [159]. The optimisation of growth parameters is realised on Si substrates with thermal oxide layer (50 nm) and similar substrates with seeds of self-assembled TiO_2 nanoparticles.

The influence of the temperature and pressure on films morphology is deeply investigated.

3.2.1.1 *Optimisation of TiO_2 nanowires growth*

Effect of the growth temperature

According to the MOCVD growth principle, at high temperature the substrate contributes in the formation of highly energetic adatoms (**ad**sorbed **at**oms) which are able to migrate at the samples surface and result in the columnar morphology.

The variation of the temperature in the range of 250 -750°C without using any oxidative gas and at low pressure (0.94 mbar) results in different morphologies (Figure 3-13). We observe that the thermal decomposition of the precursor seems to happen at susceptor temperature higher than 350°C. For susceptor temperature between 350°C to 450°C the growth leads to the compact and homogeneous thin film. At 400°C the growth rate is ~ 0.7 nm/min, while at 450°C the growth rate is 3 times higher and film morphology becomes faceted. For the susceptor temperature around 500°C, an intermediate growth regime between faceted grains and columnar grains is evidenced. Beyond 550°C, a columnar growth regime is fully established, whereas the growth rate is decreased from 3.3 to 2.5 nm/min with the susceptor temperature.

In this process conditions, we do not achieve any selective growth of TiO_2 over the TiO_2 nanoparticle seeds.

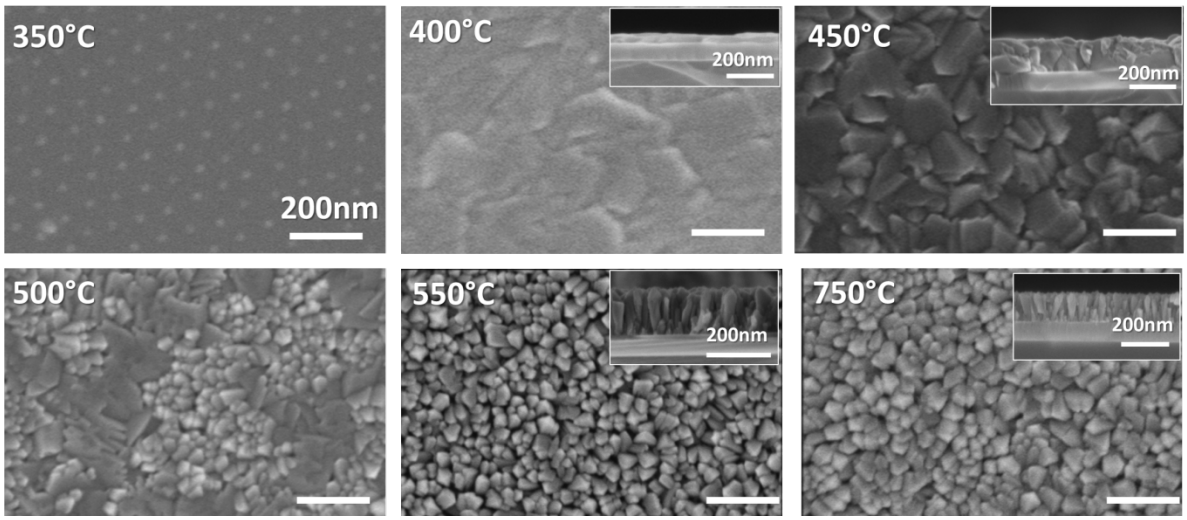

Figure 3-13 SEM images of TiO_2 grown by MOCVD at process pressure 0.94 mbar in the temperature range 350°C -750°C.

Effect of the injection rate

As we can observe on Figure 3-14, the increase of precursor injection rate while keeping all other parameters constant (0.94 mbar, 550°C and 5mmol TTIP) results in significantly larger and higher columns. The columnar growth with "fishbone" structures occur in samples with higher injection rate. The higher precursor injection rate results in faster growth rate (reaching 10.4 nm/min). The formation of the fishbone morphology seems to start from a compact columnar film as it obtained with low injection rate. Further precursor supply leads to the widening of the column by the side facets formation ("bones").

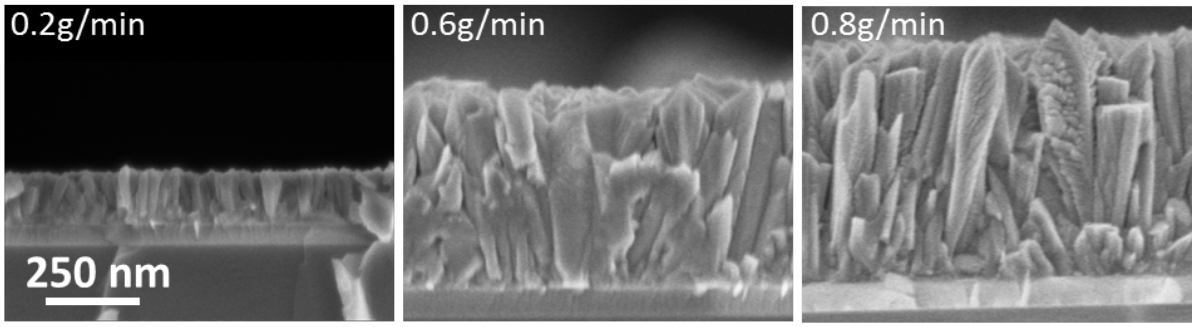

Figure 3-14 SEM cross-sectional images of TiO_2 films grown at low pressure (0.94 mbar), 550°C and molar fraction 5mmol/L.

Effect of the growth pressure

The process pressure was varied between 0.94 mbar to 20 mbar for different susceptor temperatures. The injection rate is kept constant at 0.2 g/min. The increasing of the pressure, results in decreasing of the temperature threshold allowing the growth of nanocolumns. Nanocolumns are obtained for susceptor temperature down to 330°C when the process

pressure is increased to 15 mbar. The morphology as a function of the susceptor temperature and the reactor pressure is summarised on Figure 3-15.

Two distinguished films morphology are reported i.e. homogeneous thin films, usually obtained in a low temperature regime, and nanocolumnar thin films being obtained for high temperature. In the pressure range 10-20 mbar, the threshold temperature between the two grown morphology is almost constant (~330-350°C). For lower pressure the threshold temperature uses to smoothly increase until 550°C.

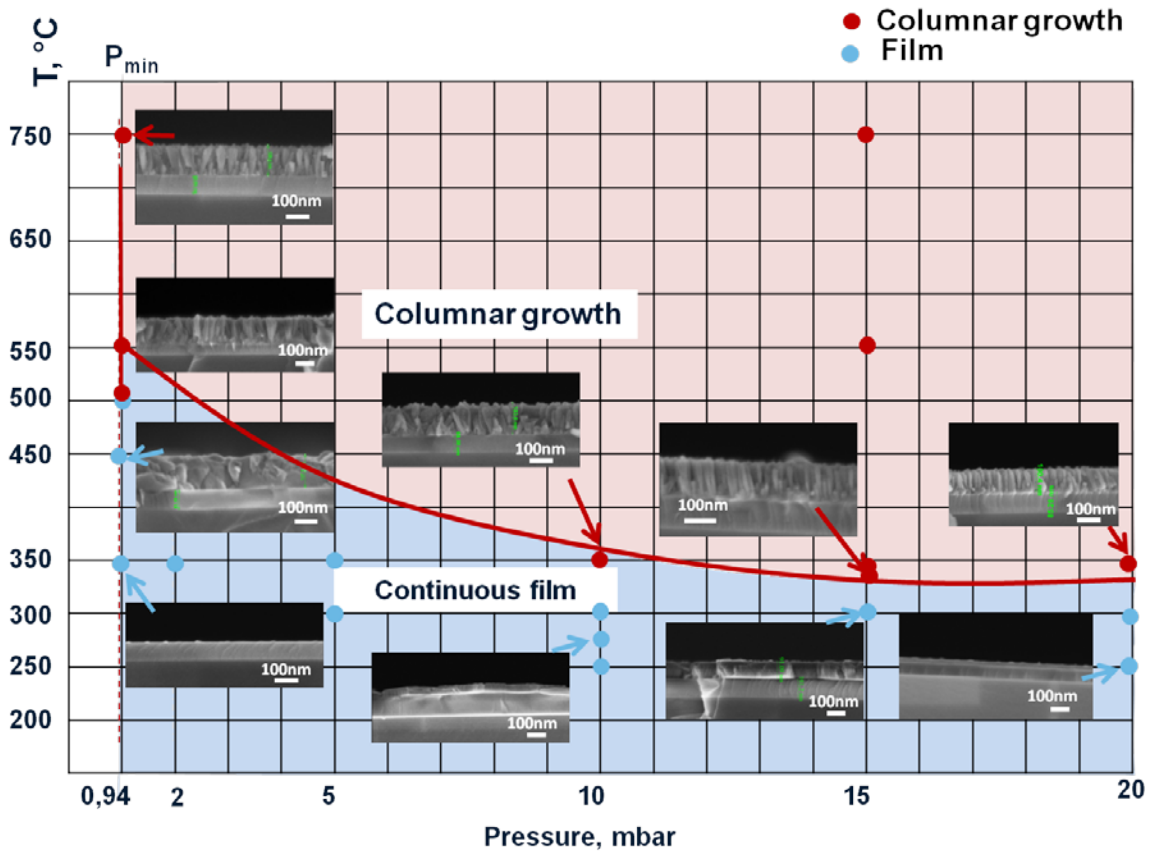

Figure 3-15 Morphology of TiO_2 films grown by MOCVD as function of temperature and pressure.

Nevertheless, one of the important drawback of the high pressure regime (>15 mbar) is the promotion of parasitic gas-phase reactions.

Typically the TiO_2 film growth by pyrolysis of TTIP follows the Equation 3-1:

$$[TTIP]_{gas} \rightarrow [TiO_2]_{film} + [\text{by-products}]_{gas} \qquad (3\text{-}1)$$

The formed by-products depend on the temperature and pressure conditions. According to Fictoire et al. [160] at high temperatures (650-800 K) the formed by-products contain propene and water in a gas phase (Equation 3-2). At lower temperature (<650 K) the reaction follows Equation 3-3 where the formed TiO_2 is not able to act as an alcohol dehydration catalyst.

$$Ti(OC_3H_7)_4 \rightarrow TiO_2 + 4C_3H_6 + 2\ H_2O, \quad (3\text{-}2)$$

$$Ti(OC_3H7)_4 \rightarrow TiO_2 + 2\ C_3H_6 + 2\ C_3H_7OH. \quad (3\text{-}3)$$

In generally, the kinetic of the growth rate depends on the growth temperature, according to the Arrhenius low:

$$k = k_0\, e^{-\frac{E_a}{RT}} \quad (3\text{-}4)$$

Where k is the constant of the heterogeneous reaction, k_0 is the pre-exponential factor, E_a is the activation energy and R is the universal gas constant.

The growth rate versus temperature is plotted for 15 mbar process pressure on Figure 3-16. Three growth regimes are distinguished. For lower pressure (0.94 mbar) these regimes are also present but in lesser extent. At low temperature (regime 1), the growth rate increases exponentially with the growth temperature. In this regime the growth rate is defined by the kinetic of heterogeneous reaction (kinetic regime).

$$\text{Slope} = -\frac{E_a}{R} \quad (3\text{-}5)$$

The temperature window of the kinetic regime varies with pressure and is shifted to the higher temperatures at lower pressure, while the estimated activation energies are very similar for both process pressures as 24 and 26 kJ/mol. These values are lower than shown in the literature. Sarantopoulos reported the activation energy value at 47 - 93 kJ/mol [102].

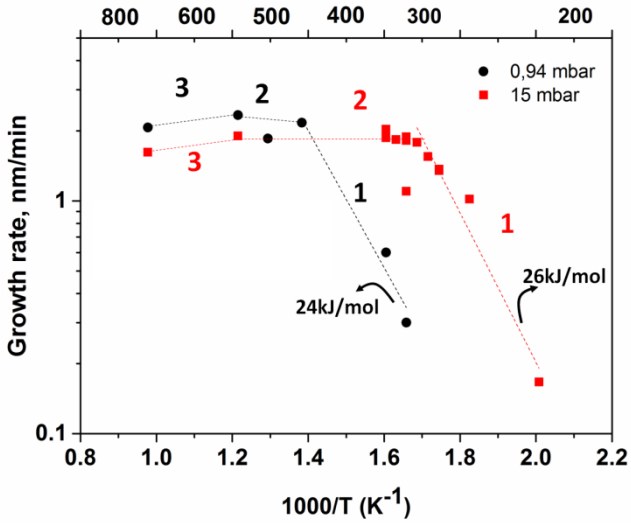

Figure 3-16 Arrhenius plot for TiO_2 growth rate in pressure conditions 0.94 and 15 mbar and precursor concentration 5mmol/L.

In the second regime (2) the growth rate does not anymore increase so significant with the temperature. The influence of the mass transport of reagents to the surface through the boundary layer seems to become predominant [161]. Further increase of the temperature promotes the parasitic gas-phase reaction or reaction with reactor walls that reduces the

growth rate (regime 3). We notice that there is no significant difference on the film morphology between substrates with or without TiO_2 nanoparticle seeds (Figure 3-15). Moreover, the variation of the temperature and pressure conditions do not allow to reach the selective growth of TiO_2. The underlying growth mechanisms are discussed in the next paragraph.

Growth mechanism

The MOCVD equipment configuration ensured the transformation of the liquid precursors into the vapour phase. Therefore, we consider the vapour phase growth mechanisms. In general, the vapour phase growth mechanism consists of four main steps after the adsorption of growth species: migration, nucleation, crystal growth and grain growth. After the adsorption of growth species on the substrate surface, crystal can differently grow depending on the surface energies of the substrate γ_{sub}, the growing crystal γ_c and the interface energy between the two, γ_i. Three growth modes are usually discussed: Frank van der Merwe, Volmer–Weber, and Stranski–Krastanov growth modes. When $\gamma_c + \gamma_i \leq \gamma_{sub}$, the minimization of surface energy pushes the deposited material to cover the substrate surface completely, thus resulting in layer-by-layer or Frank-van der Merwe growth. When $\gamma_c + \gamma_i \geq \gamma_{sub}$, the total energy is minimized by agglomerating adsorbed species towards nucleated three-dimensional islands (Volmer-Weber growth). The third growth mode starts by covering the substrate surface with few monolayers prior to promoting the growth of islands (Stranski-Krastanov growth). The surface energies involved in the growth process play a critical role in determining the growth mode. The growth of nanostructure such as nanowires often relies on the Volmer-Weber growth [162]. Therefore, the use of self-organized TiO_2 nanocrystals on Si-surface was believed to selectively promote this growth mode. However, the crystal from a nucleus is driven by the supersaturation [163], which can be defined as the difference between the supply phase (μ_a) and condensed phase (μ_s) (Equation 3-6).

$$\Delta\mu = \mu_a - \mu_s \tag{3-6}$$

For the gas phase deposition, the supersaturation could be expressed by the total reactor pressure (P) and precursor partial pressure (P_v) dependence (3-7):

$$\Delta\mu = \mu_a - \mu_s = RTln\frac{p}{p_v} \tag{3-7}$$

The nucleation of islands induces a corresponding change in the Gibbs free energy per nucleus which is a balance between supersaturation and surface energy. In the absence of active nucleation sites with negligible wetting of the substrate and sufficient surface diffusion

to ensure equilibrium, the free energy change can be written as Equation 3-8, where V_{mc} is the molar volume of the nucleus, r is the radius of the nucleus and A_c the specific area.

$$\Delta G = -(\mu_a - \mu_s)\frac{V}{V_{mc}} + \gamma_c A_c \quad (3\text{-}8)$$

This becomes with Equation 3-9:

$$\Delta G = -RT\ln\left(\frac{P}{P_v}\right)\frac{\frac{4}{3}\pi r^3}{V_{mc}} + \gamma_c 4\pi r^2 \quad (3\text{-}9)$$

$$r^* = r\left(\left(\frac{\Delta G}{dt}\right) = 0\right) = \frac{2\gamma_c}{[\frac{RT}{V_{mc}}\ln\left(\frac{P}{P_v}\right)]} \quad (3\text{-}10)$$

When ΔG for a given radius r is positive, the growth is suppressed since the dissociation of the nucleus is more energetically favourable. According to Equation (3-9), the change in free energy ΔG reaches its maximum for a critical nucleus size r^* (Equation 3-10), above which the nucleus are stable. The critical nucleus size depends on P/P_v and temperature. Our experimental results effectively show that beyond pressure and temperature thresholds, the preferential growth of nanocolumns is achieved. When considering the growth nanocolumns in our various P/Pv and temperature conditions, the smallest dimensions at the feet of the nanocolumns are typically ranging from 12 to 18 nm (Figure 3-17). In a first approximation, this may be related to the critical nucleus size r^* to be reached for promoting the growth of nanostructures.

In the case of self-assembled TiO_2 nanoparticles, the size of TiO_2 seeds falls into the same range of dimensions or is even below this critical size. Therefore, TiO_2 nanoparticles do not substantially modify the surface energy of the substrates and may tend to dissolve prior to the columnar growth, in the used pressure and temperature conditions. The use of larger TiO_2 nanoparticles may be needed to demonstrate the selective growth of well-organized nanowires. This would request further development of the block-copolymer structures and of the sequential vapour infiltration processes. It is beyond the scope of the current thesis work.

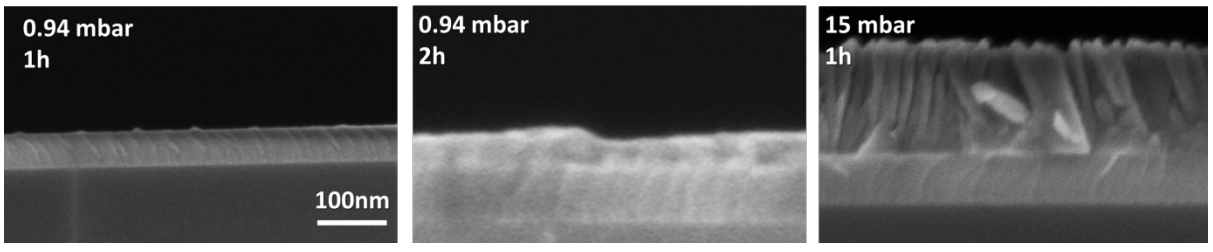

Figure 3-17 Influence of pressure P/Pv ratio on the TiO_2 growth at 350°C at 0.94 mbar and 15 mbar.

3.2.1.2 *Characterisation of TiO_2 films grown by MOCVD*

For the investigation of the physicochemical properties of MOCVD films we selected four characteristic samples having different morphologies as continuous granular films or nanocolumnar films. The selected samples were grown with following experimental conditions.

Table 3-2. Growth conditions on TiO_2 films by MOCVD.

Sample	Growth temperature; °C	Process pressure, mbar	Precursor injection rate
A	550	0.94	0.2
B	550	0.94	0.8
C	300	10	0.2
D	350	10	0.2

The XRD realised on samples grown at pressure conditions (10 mbar) and temperatures 300 and 350°C show pure anatase phase with similar texturated orientation (Figure 3-18). While the intensity of XRD peaks is slightly higher for the higher deposition temperature (columnar morphology).

The chemical composition of samples (measured by the XPS) shows the stoechiometric TiO_2 in both cases. The carbon contamination is only on the surface.

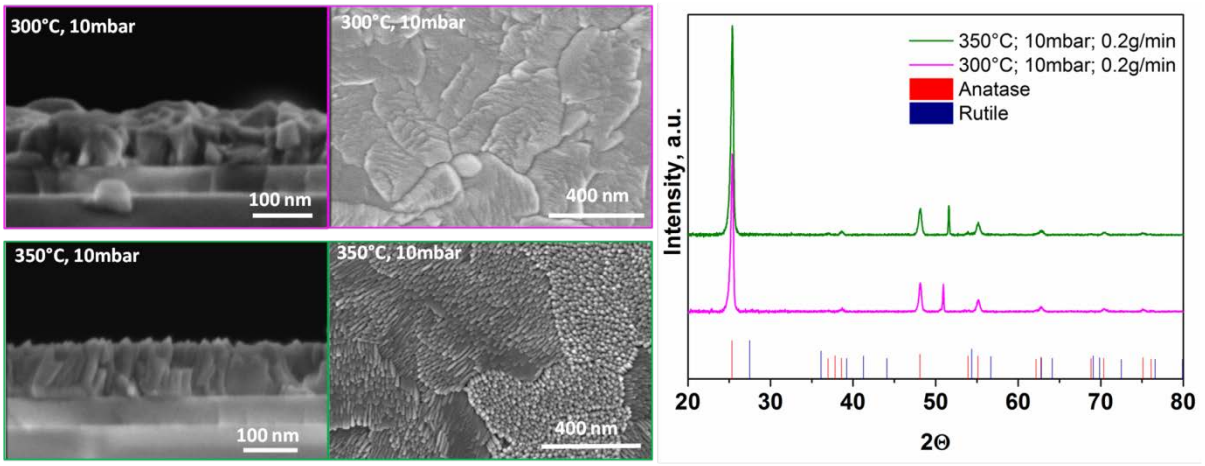

Figure 3-18 Cross-sectional, top view SEM images with associated XRD data for TiO_2 grown at 10mbar at 300°C and 350°C.

The deposition at low-pressure conditions (0.94 mbar) at 550°C forms columnar films (Figure 3-15). In this pressure and temperature conditions, the precursor injection rate has been changed from 0.2 to 0.8 g/min. At low injection rate (0.2 g/min) a compact columnar growth is formed, while for 0.8 g/min injection rate, a fishbone type morphology with wider columns

is obtained. Similar fishbone morphology was reported in the literature by Chen and co-workers [97]. The authors evidenced the major orientations being (220) and (112) by TEM measurements. As illustrated by the schematic of the fishbone nanocolumns, presented on Figure 3-19, the orientation (112) corresponds to the “bones” orientation within the column and (220) to the "backbone".

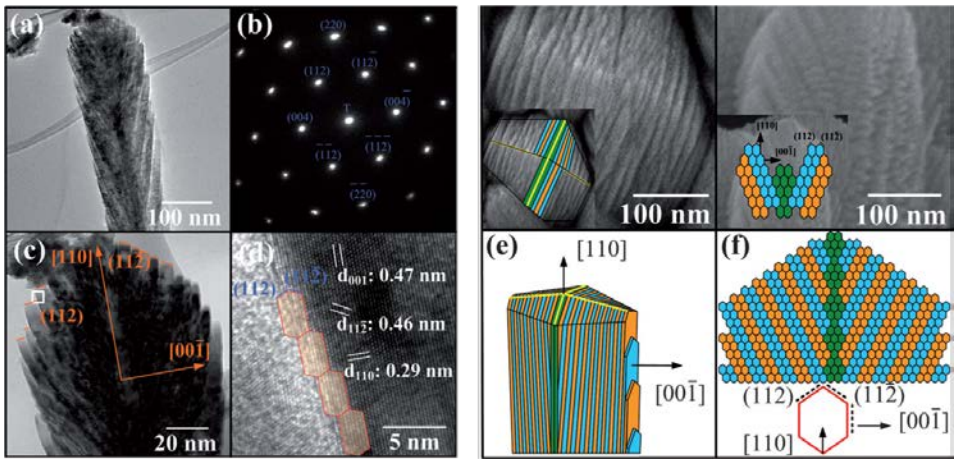

Figure 3-19 (a) –(d)TEM image of TiO_2 nanocrystals, (e) and (f) The schematic diagrams of the growth behavior of TiO_2 nanocrystals. Adopted from ref. [97].

In our case, the XRD measurements confirm the anatase phase with predominant (112) and (211) crystalline orientations for the highest injection rate (Figure 3-20). Considering that the XRD measurements are performed with the grazing incidence mode and that the nanocolumns orientations are randomly distributed around the vertical axis, the XRD spectrum collects most of the diffraction planes. The "backbone" (220) orientation is still detected in agreement with Chen et al. [97].

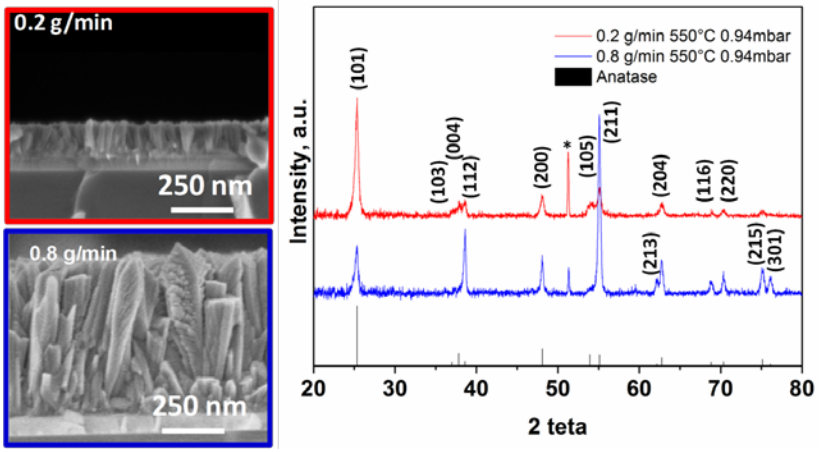

Figure 3-20 SEM cross-sectional images and associated XRD data for TiO_2 grown at 0.94 mbar, 550°C, precursors injection rate 0.2 g/min and 0.8g/min. (*sign is related to the substrat peak).

The XPS spectra acquired on the surface (Figure 3-21) shows that for both films the carbon contamination is related to C-C and C-O bonding, evidenced respectively by the C 1s binding

energies at 285 eV and 288 eV. XPS analyses within the film do not show any carbon contamination when the 0.8 g/min injection rate is used. The use of a lower injection rate (0.2 g/min) induces carbon contamination corresponding to C-Ti bonding in our case (C 1s at 281 eV).

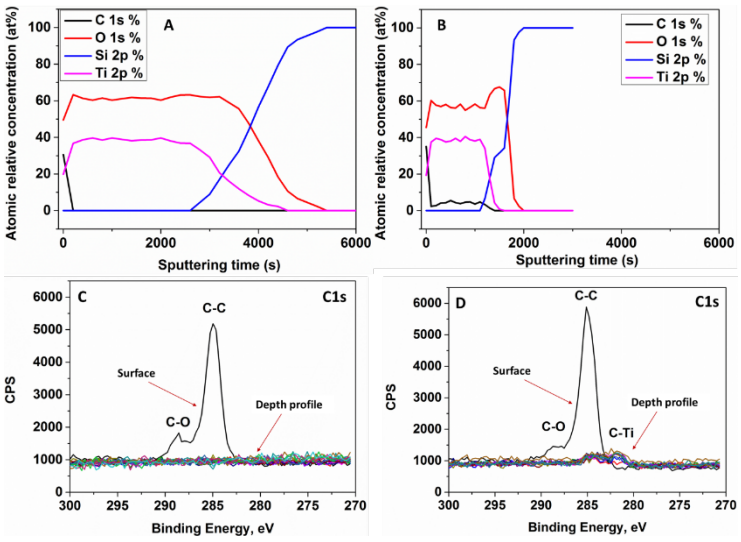

Figure 3-21 XPS depth profile for samples grown at 550°C and low pressure with high injection rate a (A) and low injection rate (B); HR-XPS spectra of C 1s on surface (sputtering time 0 and in the film) for high injection rate a (C) and low injection rate (D).

3.2.1.3 Summary

The TiO_2 films grown by MOCVD are shown in this section. The interplay of the growth temperature, pressure and injection rate on the film morphology is discussed. The selective growth of TiO_2 nanowires over the TiO_2 seed nanoparticles is not achieved.

3.3 Metal-oxide films deposition by ALD

The template-assisted approach of the fabrication of periodic nanostructures is the preferred alternative to the lack of selective MOCVD growth from self-assembled TiO_2 nanoparticle seeds. The template-assisted approach is based on the film deposition into the porous space of anodised alumina membranes (AAO). The membrane fabrication is realised according to the description presented in Section 2.2.2. The parameters of the membranes are defined as a pore diameter of 40 nm and a pore length of 1-2 µm. Such low pore dimensions require a very conformal thin-film deposition; therefore the ALD method was privileged. The developments of conformal TiO_2 and SnO_2 films with low roughness will be principally addressed in this section. The metal-oxides films are initially developed on the flat surfaces, the optimised conditions are then transferred on to porous templates.

3.3.1 Titanium oxide deposition by ALD

It is known that the major problem of TiO_2 ALD synthesis from $TiCl_4$ and water is the important roughness of the crystalline films [164]. Therefore it is mandatory to optimize the process growth in order to get the best trade-off between the film quality (that would trigger the photocatalytic properties) and its roughness that needs to be compatible with a 40 nm pore diameter. To this end, investigations on ALD parameters such as temperature, purge time, substrate influence are performed.

Influence of deposition temperature

Earlier research on TiO_2 ALD deposition from $TiCl_4$ and H_2O determined typical deposition temperatures in a range of 200 - 400°C [108], [164], [165]. However, the high reactivity of the precursor also enables film formation at lower temperatures (down to room temperature) [166][167].

The investigations performed in this work cover a broad temperature range, from room temperature to 400°C using $TiCl_4$ and deionised water as precursors.

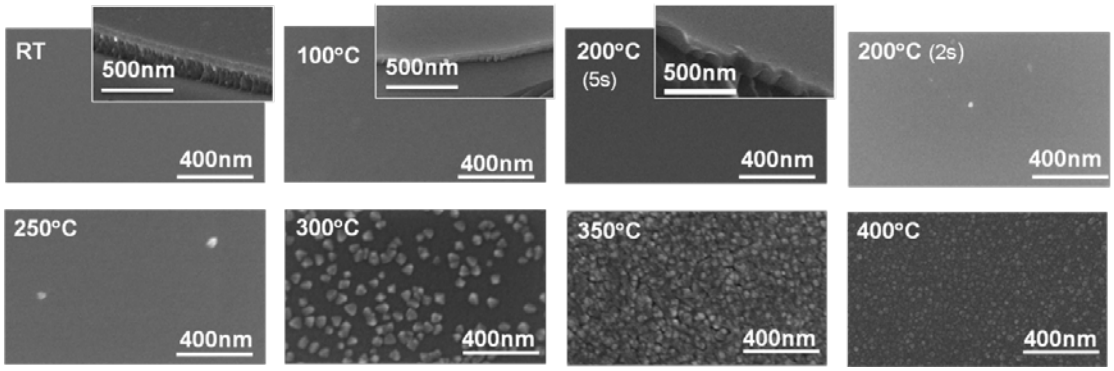

Figure 3-22 SEM images of TiO_2 films deposited in temperature range of RT-400°C.

Table 3-3 Summary on the thickness and roughness of TiO_2 films (as deposited).

Growth temperature, °C	Roughness, RMS, nm (from AFM)
RT	0.77
100	0.68
200 (purge 5s)	0.75
200 (purge 2s)	1.70
250	3.13
300	7.64
350	16.98
400	5.64

Thin films of ~25-40 nm are obtained using standard conditions provided by the ALD equipment supplier: precursors pulse 0.2 s and purge time 2 s for both precursors (for temperature range 200-400°C). In the low temperature range (20°C (RT) -200°C) depositions of thicker films (~100 nm) are obtained with longer purge time as 5 s and 30 s. The SEM and AFM measurement (Figure 3-22 and Table 3-3) show that the roughness of films increases with the deposition temperature. Samples grown in the low temperature range (RT-200°C) show a smooth and highly conformal films, while films obtained at 350°C show the highest RMS value (16.98 nm). It is worth noting that the roughness decreases suddenly for the films deposited at 400°C. These results until 350°C are in agreement with the literature [115], [168]. Therefore, from the morphological point of view, for further deposition into porous substrate, the low temperature range (RT-200°C) is privileged. However, for better understanding of the morphology variation, the growth mechanisms have to be discussed. We also noted the formation of random nanoparticles for the deposition at 200°C and purge time 2 s, similarly reported by Luka et al. [169]. Such nanoparticles formation may unfortunately cause an inhomogeneous deposition into the porous space. The increase of the purge time to 5 and 30 s has solved this problem.

The XRD analysis demonstrates that films synthesised at a temperature below 300°C do not show any crystalline structure, therefore diffractograms for films deposited at RT and 100°C are not presented. The anatase crystalline phase is detected for the depositions beyond 300°C and the increase of deposition temperature up to 400°C logically improves the film crystallinity (Figure 3-23).

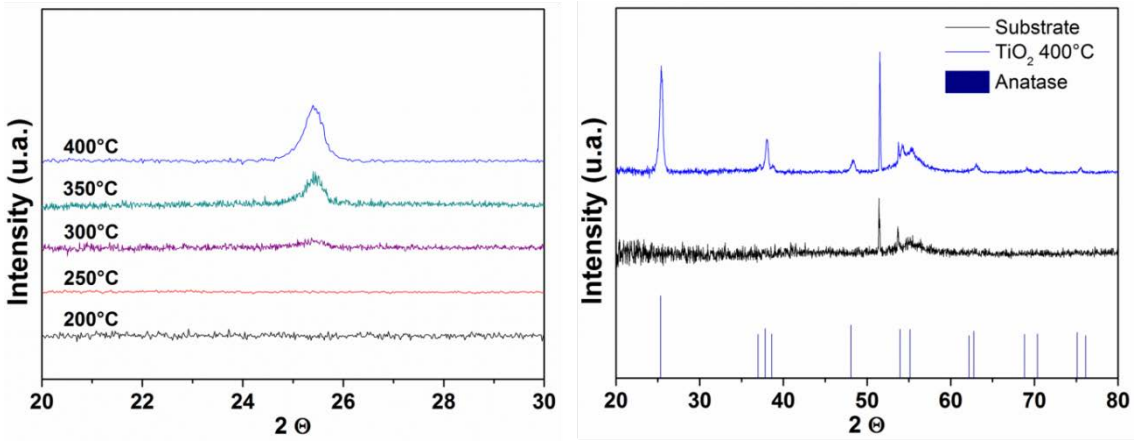

Figure 3-23 XRD TiO_2 anatase (101) peak evolution as a function growth of temperature (200-400°C) (left), 20-80° diffractogram of the TiO_2 film synthesised at 400°C (right).

Growth rate and mechanism

The growth rate (growth per cycle, GPC) in whole temperature range (RT-400°C) represented on Figure 3-24 for TiO_2 films.

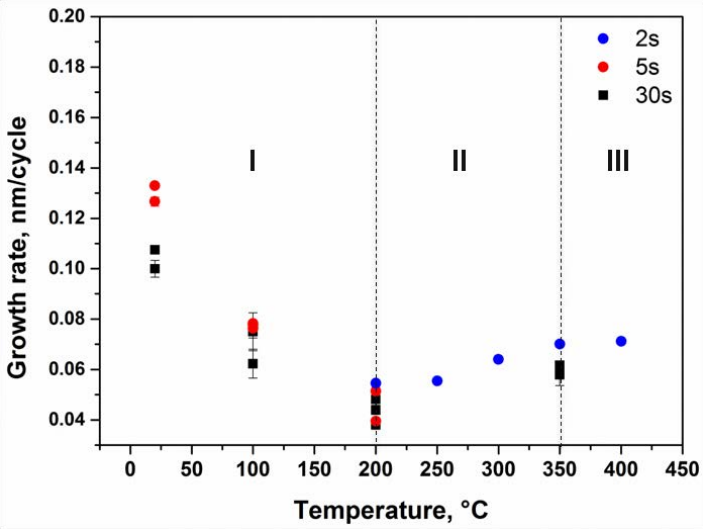

Figure 3-24 Growth rate of ALD TiO_2 films deposited at RT-400°C.

Three growth regimes can be distinguished: (i) low temperature regime (RT-200°C) where the growth rate decreases with the temperature increase that corresponds to the ALD condensation regime; (ii) intermediate regime (200°C-350°C) demonstrate a growth rate increase followed by the standard ALD plateau (iii) at high temperature regime (>350°C). Similar trends were also reported by Leem and co-workers [170].

It is generally established that the surface reaction with the metal-oxide precursor mainly involves the OH functional groups. [165], [167], [170]–[172]. Therefore, the typical TiO_2 growth reaction follows Equations 3-10, 3-11 and is schematically represented on Figure 3-25.

$$\text{[Pulse } TiCl_4\text{]:} \quad x(-OH)_x + TiCl_4 \rightarrow (-O-)_xTiCl_{4-x} + xHCl \ (x=1, 2) \qquad (3\text{-}10)$$

$$\text{[Pulse } H_2O\text{]:} \quad (-O-)_xTiCl_{4-x} + (4 - x)H_2O \rightarrow (-O-)_xTi(OH)_{4-x} + (4-x)HCl \qquad (3\text{-}11)$$

Nevertheless, the surface chemistry is highly dependent on the temperature. At low temperatures (<300°C), the isolated hydroxyl groups OH and H-bonded OH groups are dominate on the surface of substrates such as SiO_2 or Al_2O_3 [167]. The increase of temperature (>300°C) may lead to the dehydroxilation and the formation of oxygen bridges (Equation 3-12) [170]. At high temperature, the oxygen bridge terminated surface promotes

also the direct $TiCl_4$ chemisorption according to IIa-IIb reaction paths showed on Figure 3-25 and used to improve the film quality because of the lack of HCl by-product.

$$Ti(–OH)–O–Ti(OH) \rightarrow Ti(-O-)_2Ti + H_2O \qquad (3\text{-}12)$$

The GPC increase in the intermediate regime can be related to the temperature dependent surface functionalities and also the important role of the HCl by-product on the growth mechanisms. This latter feature is specifically discussed in the next paragraph.

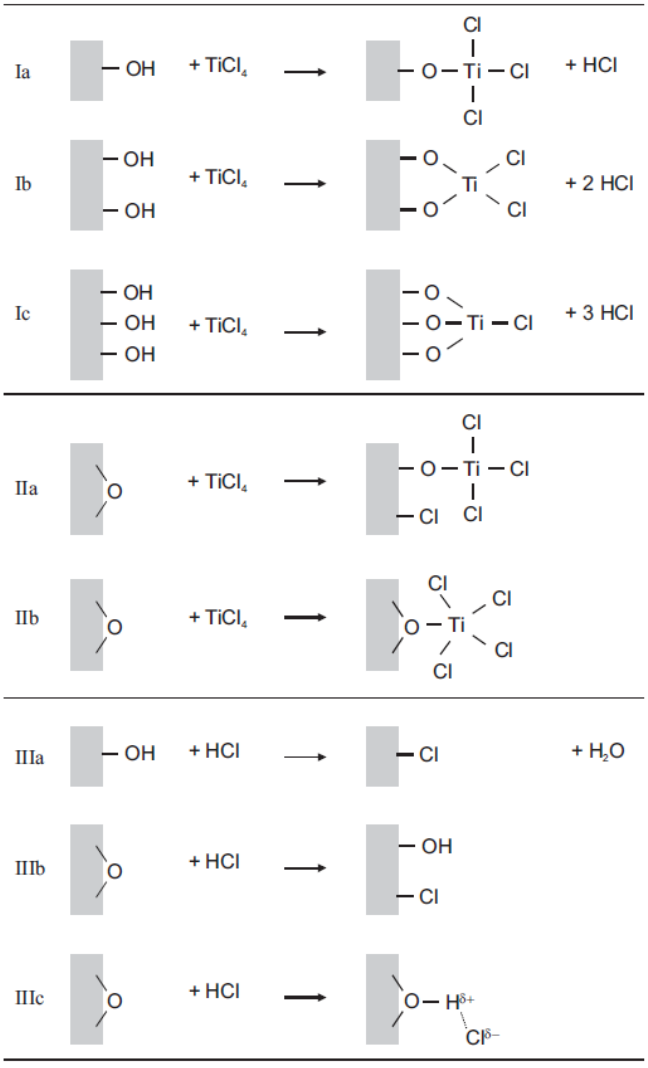

Figure 3-25 Possible paths of $TiCl_4$ chemisorption on oxide surfaces [171], [173].

Role of HCl

In the literature, the role of HCl on the TiO_2 growth mechanism was fully established by Leem and co-workers [170]. The authors showed that in the temperature range 150-300°C, the volontary addition of the HCl after the $TiCl_4$ pulse significantly lowers the growth rate. For the high temperature range (>300°C), the additional HCl increased the growth rate. The

authors postulated that at lower temperatures (150-300°C), the surface reaction occurs via OH-groups and forms intermediate or non-stable products, according to the reactions 3-10, 3-11. HCl may induce the reversible reaction and promote the desorption of $TiCl_{4-x}$ or $Ti(OH)_2Cl_2$ volatile compounds. The overall reaction being partially reversible, the growth rate of TiO_2 is lowered. Beyond 300°C, the oxygen bridge terminated surfaces are induced and promote the TiCl4 adsorption as previously described without any release of HCl. The oxygen bridges are mainly triggering the TiO_2 growth reaction according to Equation 3-13

$$Ti(\text{-}O\text{-})_2Ti + TiCl_4 \rightarrow Ti(Cl)\text{-}O\text{-}Ti(OTiCl_3) \qquad (3\text{-}13)$$

This investigation highlights that the mono- (Figure 3-25 Ia) or bifunctional (Figure 3-25 Ib) adsorption of $TiCl_4$ on hydroxyl groups is reversible under HCl atmosphere, while dissociative adsorption on oxygen bridges is irreversible [170]. Interestingly, while HCl was added at the end of the ALD cycle (after water pulse), it significantly decreases the growth rate for the whole studied temperature range (150 - 400°C). When oxygen bridges are exposed to HCl (Equation 3-14 and the schematic IIIb-IIIc represented on Figure 3-25). TiO_2 surfaces are functionalised with -OH, -Cl, =OHCl. That retards the growth of TiO_2. This fundamental investigation highlights the predominant role of HCl on the TiO_2 growth mechanism. The time of residence of HCl in our ALD processes is strongly dependent on the purge time.

$$Ti(\text{-}O\text{-})_2Ti + HCl \rightarrow Ti(Cl)\text{-}O\text{-}Ti(OH) \qquad (3\text{-}14)$$

Therefore, further investigations require the optimisation of purge time using the quartz crystal microbalance (QCM). The QCM being integrated into the reactor lid cannot be used at deposition temperature above 250°C. Henceforth, we focus on low temperature TiO_2 deposition regime: at RT, 100 and 200°C, so more as these regimes conduct to the low surface roughness of TiO_2 films.

Influence of purge time

The importance of the purge time is logically more significant in the low temperature regime, where the excess of precursors and by-products desorption is not assisted by heat.

The QCM measurements realised first at 200°C using pulse time 0.2 s and purge time 2, 5, 30 s for both precursors (Figure 3-26). The pulse of $TiCl_4$ induces the mass increase following stabilisation during the purge. The addition of a water pulse enables the surface reaction and

the mass drop due to the release of HCl by-product (Figure 3-26B). The completed mass stabilisation was not achieved in the case of a 2 s purge time. The increase of the purge time up to 5 (Figure 3-26C) and 30 s (Figure 3-26D) improved the mass stabilisation. However, for a purge time of 30 s after the $TiCl_4$ pulse, an anomalous mass drop after 12-15 s of purge time is observed (Figure 3-26D). To further study the "relaxation" time after the pulse of each precursor, an exaggerated purge of 600 s is applied (Figure 3-26E). This study shows that after the $TiCl_4$ pulse the mass signal decreases continuously during the first 5-8 s of purging, but then the mass re-increases significantly without any visible stabilisation. The water pulse promotes a slow mass decrease within the first 10 s of purging, then the sensor signal increases again. Such QCM behaviour of mass increases within the long purge time is intriguing. It may be associated to the re-adsorption of volatile species or surface reaction by-products from the reactor walls and re-deposits on the QCM surface [165]. Moreover, after the completed 50 cycles deposition with purge time 2 and 5 s, we notice that the mass sensor signal continues to decrease; that could be characteristic of the desorption of volatile compounds (Figure 3-26 A zoom). Aarik and co-workers [165] also pointed out on the continuous decrease of mass sensor signal during the purge time for depositions realised at 100°C. The authors have suggested the continuous dehydration of the surface after exposure to water pulse at low temperature, or desorption/decomposition of formed $Ti(OH)_xCl_{4-x}$ volatile species. [108], [165].

The QCM control on the mass evolution during the ALD deposition demonstrated that, at 200°C, the purge time after the water injection should be longer than 600 s.

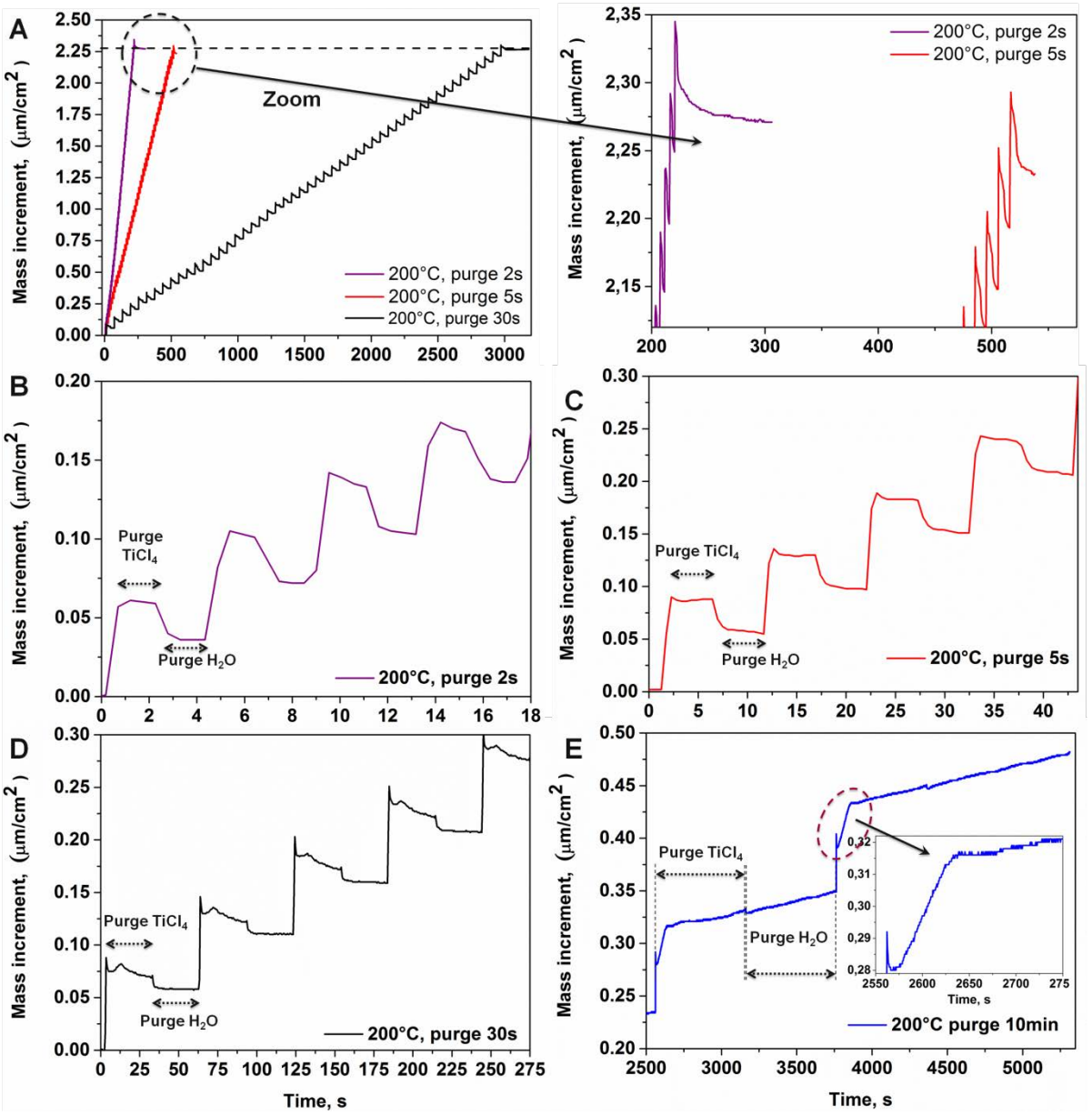

Figure 3-26 QCM as a function of deposition time recorded profile at 200°C using purge time of 2 s, 5 s, 30 s and 600 s for both precursors.

The decrease in the deposition temperature to 100°C does not significantly modify the mass sensor profiles compared to the previously recorded for 200°C. The study of the relaxation time at 100°C demonstrates that a purge time of 600 s is still not sufficient to stabilise the mass sensor signal after the pulse of $TiCl_4$, however after injection of water, the mass sensor signal stabilisation is interestingly achieved after a purge time of 30 s of purge (Figure 3-27C).

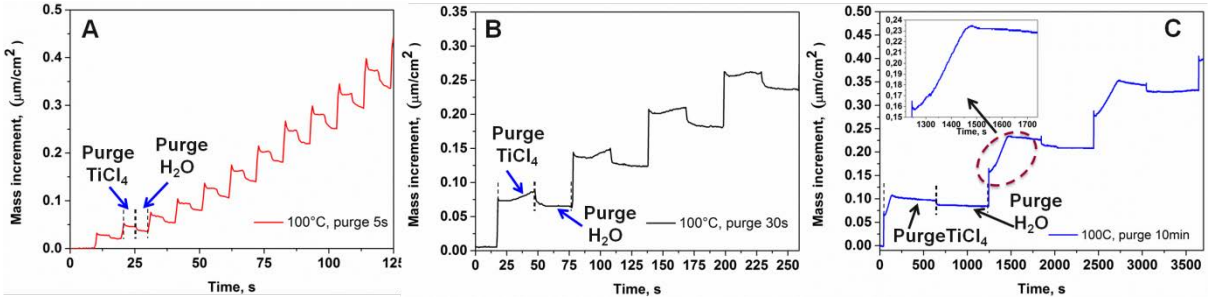

Figure 3-27 QCM as a function of deposition time as a recorded profile at 100°C using purge time of 5 s, 30 s and 600 s (10 min) for both precursors.

The mass change, as recorded by QCM, for depositions realised at room temperature is significantly different from previously discussed QCM profiles recorded for thin-films grown at 100 and 200°C (Figure 3-28). An anomalous behaviour is noted while the water pulse is supplied. Instead of the mass decrease due to the HCl release, the mass sensor show a mass increase and then a continuous decrease of the mass increment without stabilisation, even after 30 min of purge (Figure 3-28). The mass increment per cycle is strongly dependent on the purge time. The mass increments per cycle of ~ 0.14, 0.06, and 0.02 µg/cm^2 is determined for depositions realised with 5, 30 and 1800 s purge time. The final mass increment, after 50 cycles, is twice larger for 5 s purge time than for 30 s purge time (Figure 3-28 inserted) at room temperature.

For high temperature (100 and 200°C), the final mass increment is not significantly different for the different purge time. This demonstrates that the unreacted precursors or by-product thus accumulate within the film at room temperature. At a low temperature, the surface is mainly functionalised by hydroxyl groups and H-bonded OH. Furthermore at temperatures below 100°C, the presence of molecularly absorbed water on the surface is inevitable. Thus, $TiCl_4$ molecules could react not only with functional groups but also with residual water. The reaction of $TiCl_4$ hydrolysis at room temperature generally leads to the formation of $TiOCl_2$, TiOCl, Ti_2O_3 and/or $Ti(OH)_xCl_{4-x}$ with generation of HCl [174]. All of these chemistries may be expected in our films.

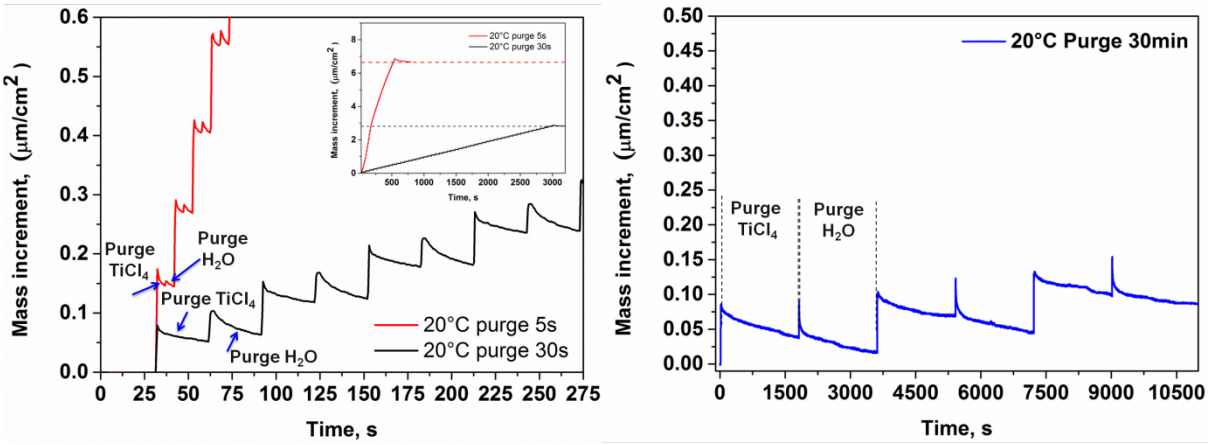

Figure 3-28 QCM as a function of deposition time as a recorded profile at 20°C using purge time of 5 s, 30 s and 1800 s (30 min) for both precursors.

Several theoretical studies have reported that the first half-reaction of $TiCl_4$ and H_2O is endothermic and thus the desorption of HCl is hampered [175][170][176]. That is in line with our hypothesis about an accumulative growth mechanism at room temperature.

Nevertheless, it is important to consider the slow film growth rate (~6 Å/ cycle for purge 30 s) for which a further increase in the purge time (to reach the ideal ALD regime) will lead to an unreasonably long deposition time (dozens of hours), for the considered TiO_2 thickness. Consequently, we focus on TiO_2 thin-films deposited with purge times of 5 s and 30 s and since ALD thin films grown at low temperature are amorphous, we use the post-deposition annealing for engineering the thin film crystallisation. The use of AAO membranes for further TiO_2 nanowires fabrication imposes the annealing temperature limit at 600°C.

Effect of post-deposition annealing

Post-deposition annealing of TiO_2 films grown at 200°C

The used ALD pulse/purge parameters are 0.2 s pulse / 5 s and 30 s nitrogen purge for both precursors and result in different thicknesses of 25, 50, 90 nm corresponding to 500, 1000, 2000 cycles. The TiO_2 films grown with the purge time 30s are much less crystallised than the films grown with 5 s purge time (Figure 3-29). The 25 nm and 50 nm samples after 500 and 1000 cycles respectively for both purge time show an enhanced crystallinity with the increase of the film thickness. Indeed, the typical crystallite size increases from 18 nm to 25 nm when the thickness is increased to 50 nm. The thickest sample grown with 30 s purge time exhibits a broadening of the (101) anatase peak, while any other diffraction plan are detected. The morphology of these particular samples is significantly smoother than the thinnest film.

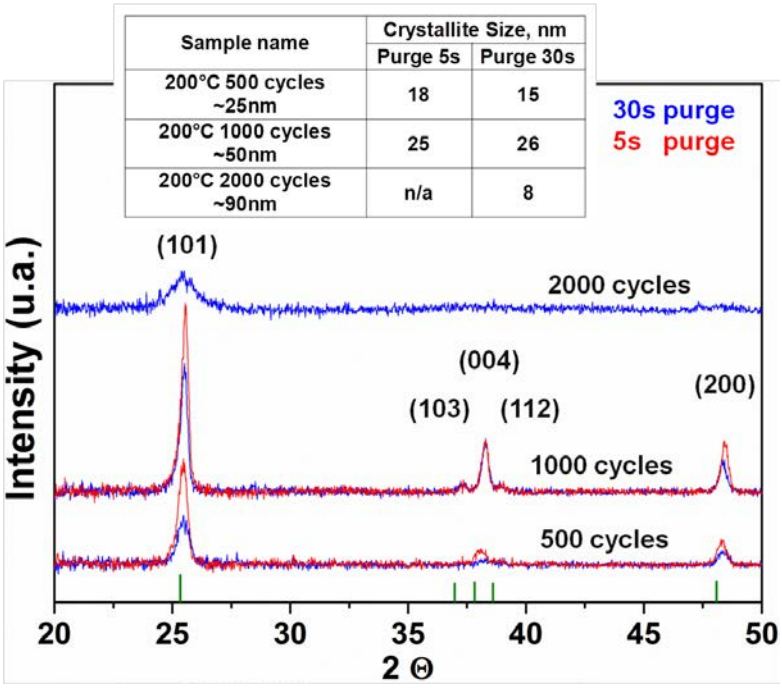

Figure 3-29 XRD of TiO_2 deposited at 200°C after annealing at 600°C.

The thick sample grown with long purge time (30 s) does not demonstrate any morphology change after annealing (Figure 3-29). The estimated crystallite sizes reduce significantly for 90 nm thick samples. These overall results tend to demonstrate that the thermal budget of annealing is not enough to properly recrystallise samples thicker than 50 nm. For 50 nm samples, the calculated lattice parameter from the position of the diffraction peak indicates the compressive stress: for 30 s purge time a=b=3.7521 Å, c=9.3937 Å and for 5 s purge time a=b=3.7612 Å, c=9.3937 Å vs. reference values being: a=b=3.7845 Å, c=9.514 Å.

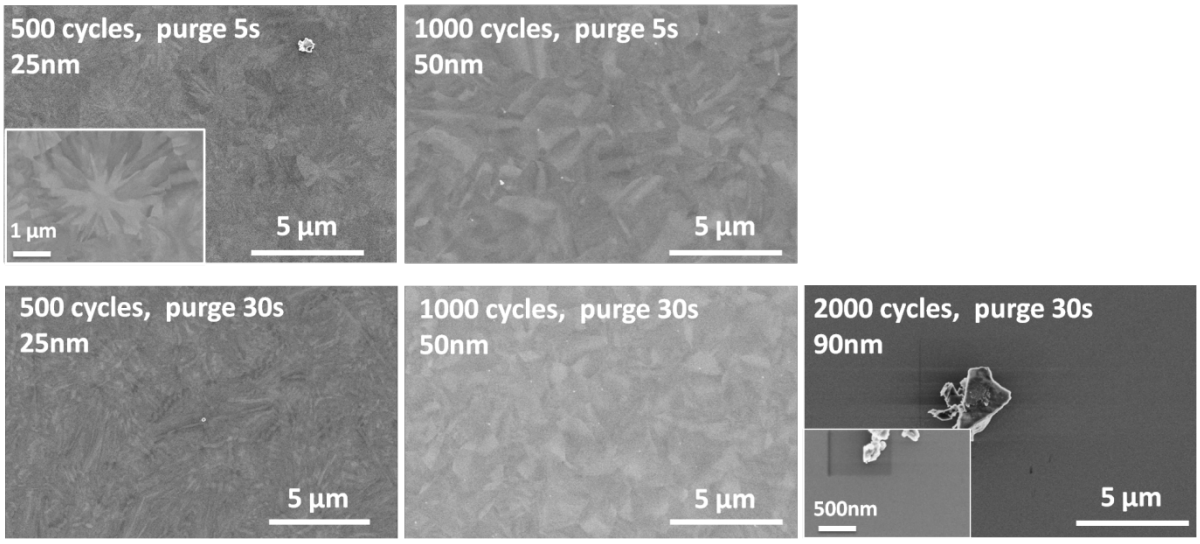

Figure 3-30 SEM images of TiO_2 films after annealing at 600°C. TiO_2 films were deposited at 200°C after 500, 1000 and 2000 cycles with purge time of 30 s and after 500, 1000 cycles with purge time of 5 s annealed.

The morphologies of 25 and 50 nm samples are very similar: they exhibit "hand-fan" - like domains (Figure 3-30). These results are compared with the ones obtained for TiO_2 films grown at 100°C.

Post-deposition annealing of TiO_2 films grown at 100°C

The ALD growth at deposition temperature of 100°C with two purge times 5, 30 s results in films with thicknesses of 25, 50 and 120 nm (350, 700, 1650 cycles). The obtained amorphous samples were also annealed at 600°C in ambient air. No significant thickness variation is observed according to the purge time.

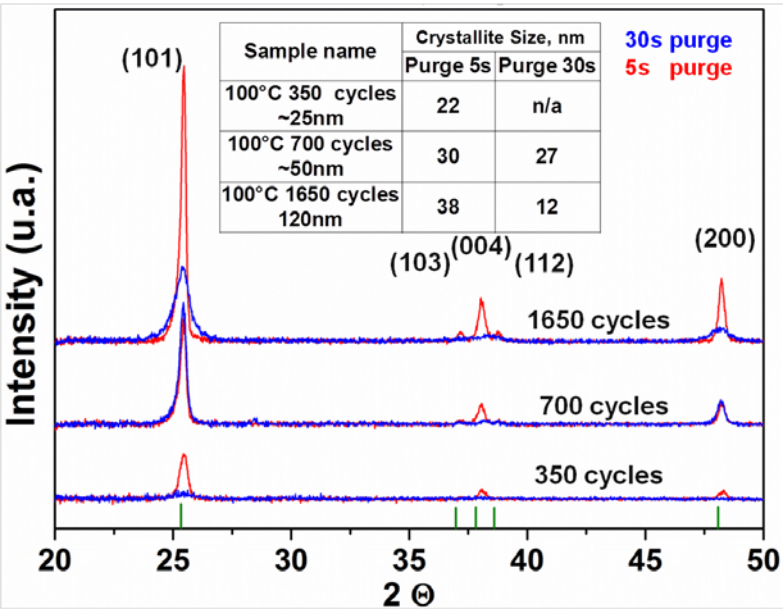

Figure 3-31 XRD of TiO_2 deposited at 100°C after annealing at 600°C.

However, the purge time of the deposition process does noticeably impact the thin-films crystallinity after the post-deposition annealing (Figure 3-31). All samples demonstrate the presence of anatase phase. For samples grown with a purge time of 5 s, the peak intensity increases monotonously with the sample thickness while samples grown with a purge time of 30 s show an anomalous crystallisation behaviour. Indeed, the thinnest film grown with 30 s purge time seems to be poorly crystallised after annealing at 600°C. At intermediate thickness of 50 nm in both depositions (5 and 30 s), the anatase peak intensity corresponding to the (101) and (200) orientations appear with similar intensity. While the peak corresponding to the (004) orientation was not detected in case of longer purge time deposition (30 s). The increase of the film thickness to 120 nm makes this purge time influence even more remarkable. The film deposited with longer purge time forms smallest crystallite size (12 nm), while the deposition with (5 s) of the purge time leads to the formation of larger crystallites

(38 nm). The calculated lattice parameters from the obtained XRD peak positions for short purge regime demonstrate a compressive stress compare to the TiO_2 anatase reference (a=b=3.7660 Å, c=9.4460 Å vs. reference: a=b=3.7845 Å, c=9.514 Å). These results highlight that the recrystallisation behaviour is significantly dependent on the purge time used for the growth of the amorphous thin film. From SEM observations on Figure 3-32, thin films deposited with 5 s purge time demonstrate a large grain morphology being significantly changed according to the film thickness. The 25 nm thin film shows an unusual "hand fan"-like crystallisation with contrasted stripes going from the centre of grain to the border of it. Such morphology corresponds to the one that is formed by an explosive crystallisation [180]. The explosive crystallisation of amorphous or liquid materials is an autocatalysed process that occurs when the applied heat induces a release of the latent heat that makes this crystallisation very fast as "explosive". The explosive crystallisation was noted in the literature for amorphous silica and germanium films [177] [178] or amorphous silica films with ion implantation [179]. Pore and co-workers [180] demonstrated the explosive crystallisation in mixed amorphous oxides Ti-Nb-O and Ti-Ta-O deposited by ALD. Nevertheless, for our knowledge, such morphology has never been reported for TiO_2 ALD films.

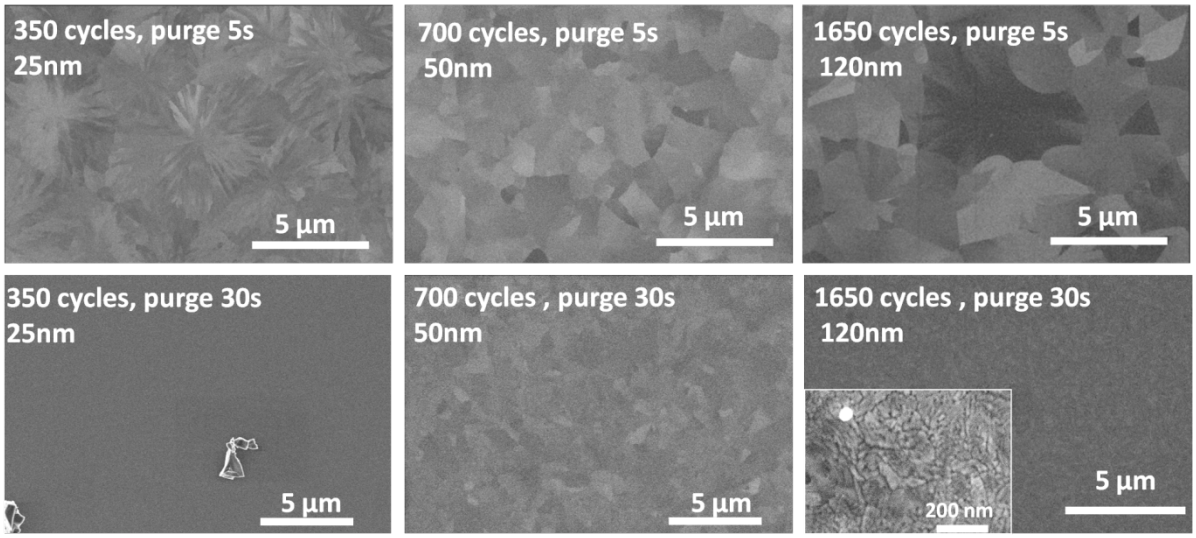

Figure 3-32 SEM images of TiO_2 films deposited at 100°C after 350, 700 and 1650 cycles with purge time of 5 s and 30 s annealed at 600°C.

The EBSD characterisations are realised on similar samples (35 nm and 70 nm); both samples are from different deposition batches with 30 s purge time; the 35 nm sample is annealed at 500°C for 1 h while the 70 nm sample is annealed at 450°C for 2 h (Figure 3-33).

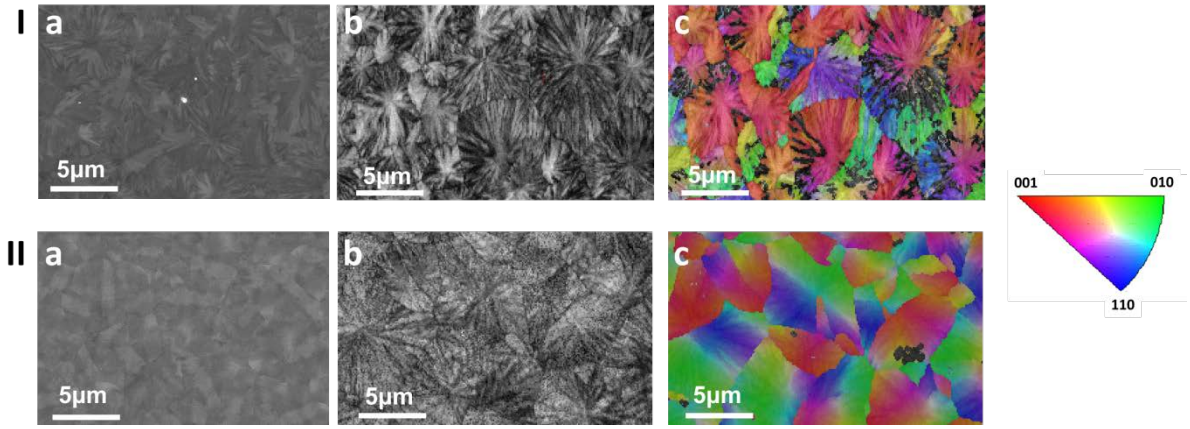

Figure 3-33 SEM (a) and band contrast (b) and EBSD (c) images for TiO_2 samples of thickness 35 nm (I) and 70 nm (II).

The EBSD map and associated pole figures (pole figures are not presented) further confirm anatase grains with a main (001) orientation. It is known that anatase (001) facets have high surface energy. The EBSD analysis also demonstrates an important disorientation (<8°) within the same grain. This morphology type should present an important strain. Indeed, lattice parameters calculated from the XRD peak positions for this sample (data are not presented) are lower than reference values, which also indicates compressive stress ($\Delta a=b=0.0234$ Å, $\Delta c=0.08$ Å). Thus, crystallisation is likely to start from a nucleus and propagate laterally. EBSD band contrast images also demonstrate that the brighter stripes correspond to the better electron diffraction patterns, which indicate better crystallisation. It was also found that within the large "hand fan"-like domains, the crystallographic orientation changes and may include smaller grains. The increase of the thickness leads to a more homogeneous grain distribution, where the stripes are less marked. The crystal disorientation <5° is still present within the domain.

Post-deposition annealing of room temperature TiO_2 films

In the literature, the TiO_2 films deposited at RT are investigated to a much lesser extent than films grown at temperature above 80°C and such depositions are mainly realised on polymer substrates. Our study investigates a new regime of TiO_2 thin-films deposited by ALD at RT, and crystallised with post-deposition annealing.

The non-ideal regime of ALD depositions at RT using 5 s and 30 s purge time results in conformal films. A thickness variation is found versus the number of cycles (160, 320 and 965) grown with two purge time. It is worth noticing that the samples thickness was reduced by 10-25% after annealing. Table 3-4 summarises the thickness values of as deposited and annealed films.

Table 3-4 RT TiO_2 film thicknesses as deposited and after annealing.

Number of ALD cycles	Purge 5s		Purge 30s	
	Thickness, as deposited, nm	Thickness, after annealing, nm	Thickness, as deposited, nm	Thickness, after annealing, nm
160 cycles	21	16	15	12
320 cycles	41	33	32	27
965 cycles	220	173	103	93

The film crystallinity is analysed by XRD in the 0.5°grazing incidence configuration, which provides the information about all crystallographic orientations of the film (Figure 3-34). The obtained diffractograms evidence anatase phase in all samples annealed at 600°C for 2 h; the intensity of the detected peaks usually increases with the film thickness. According to these XRD data, we note a slight increase in the peak intensity for samples grown the shortest purge time (5 s). Taking into account the QCM and GPC data, which show a more important mass increment for the depositions with shorter purge time, such XRD intensity difference can be attributed to the small variation of the film thickness.

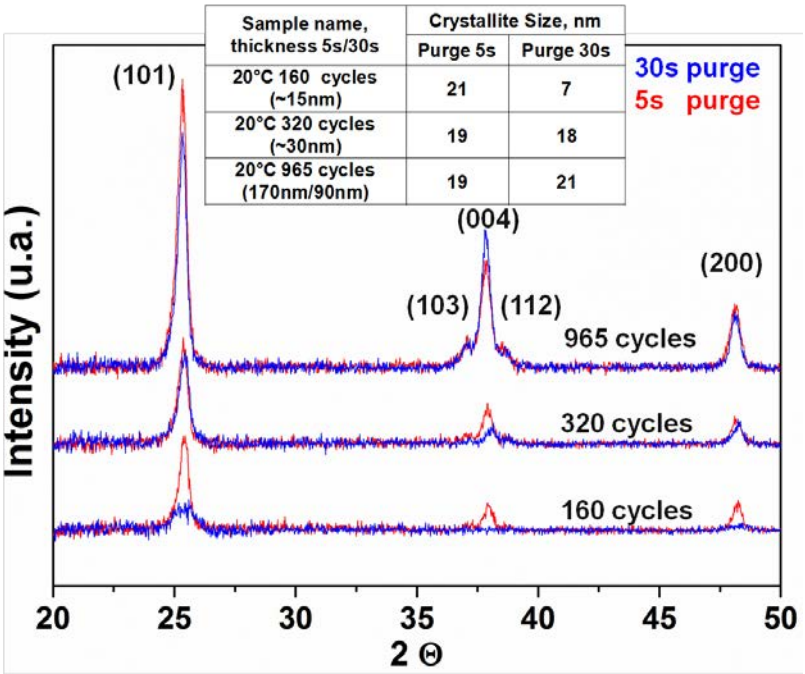

Figure 3-34 XRD of the TiO_2 deposited at room temperature after annealing at 600°C.

The SEM and AFM pictures show that the morphology of the samples undergoes a significant modification after annealing (Figure 3-35, Figure 3-36). The 15 nm thin-films fabricated with

purge time 30 s with a low number of ALD cycles (160 cycles) do not show any particular change in the morphology compared to the amorphous one. When the film thickness is increased to 90 nm, the post-deposition annealing induces a porous structure. When the purge time is 5 s, the porous structure is formed even at low film thickness (~i.e. 15 nm). Such kind of structure is likely to be formed by degassing some of volatile compounds from the amorphous film since films are thermally shrunk during annealing. A priori, the longer purge time ensures better evacuation of reaction by-products during the growth process. However, the thick samples deposited with purge time 30 s are likely to also undergo a certain accumulation of by-products into the film, which is releasing during the annealing and leads to porous structure.

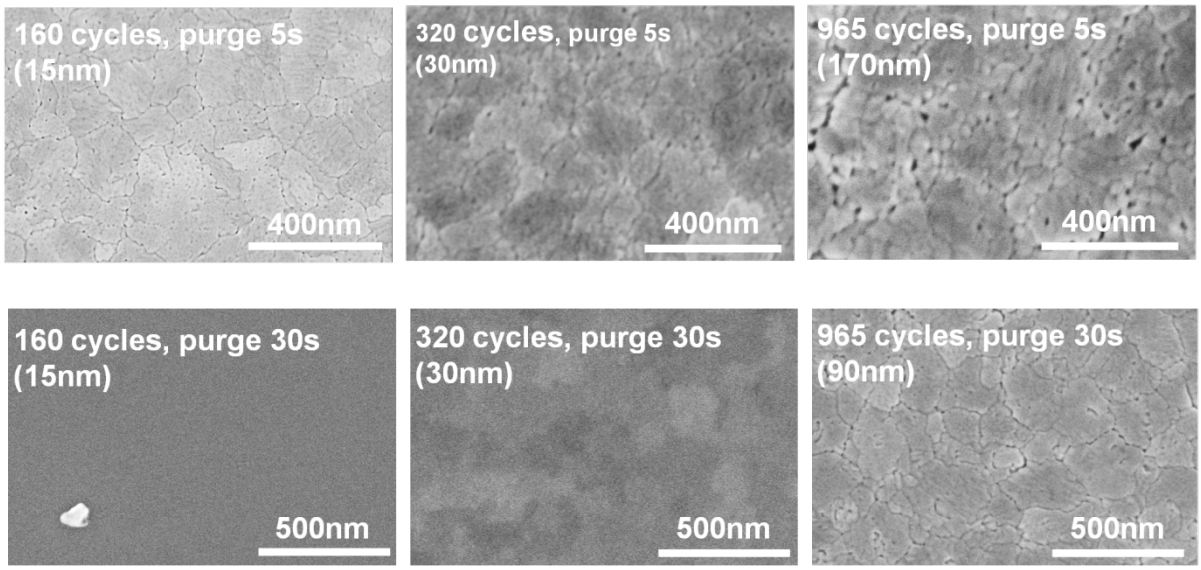

Figure 3-35 SEM images of annealed TiO_2 films deposited at RT after 160, 320 and 965 cycles with purge time 5 s and 30 s.

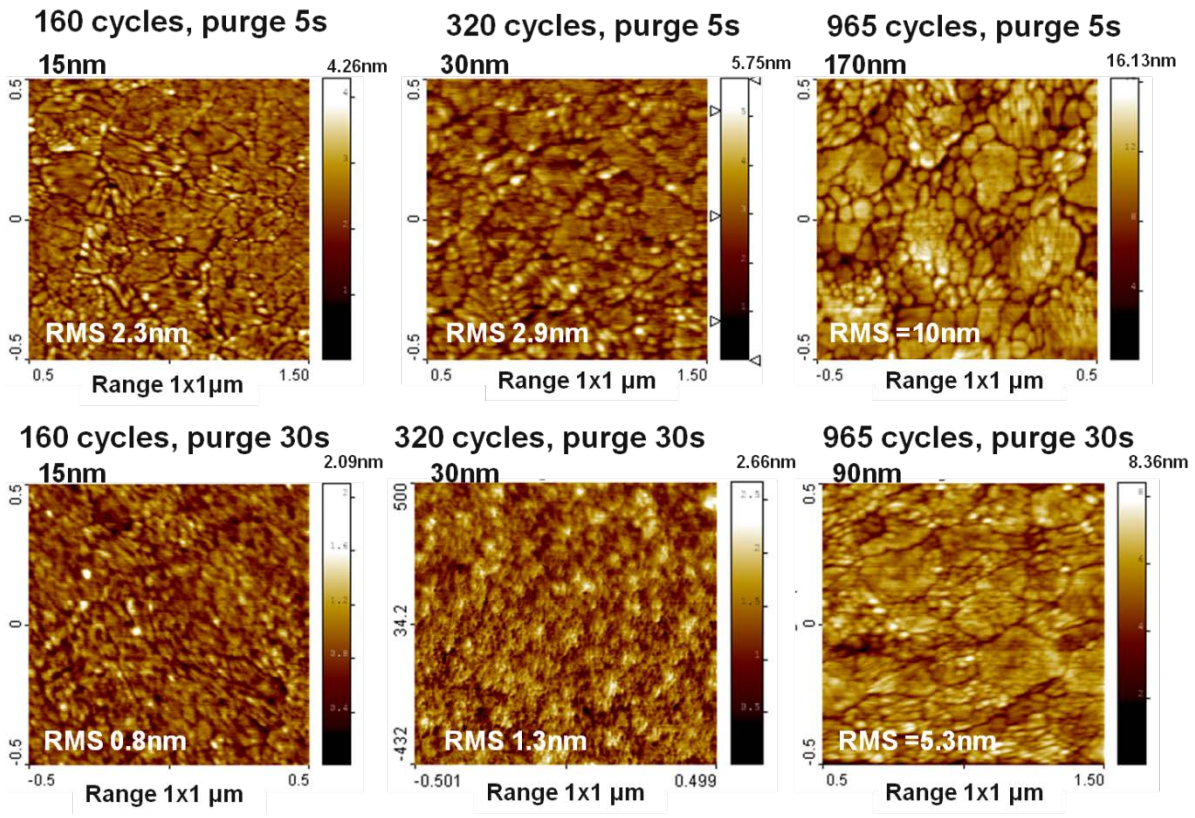

Figure 3-36 AFM topography images of annealed TiO_2 films deposited at RT after 160, 320 and 965 cycles with purge time 5s and 30 s.

The by-products desorption upon annealing is further corroborated by the important mass increment per cycle at RT, indicating the lack of desorption of by-products and therefore their preferential accumulation into the film. The chemical characterisation of the films is achieved by performing an XPS analysis on the amorphous and annealed films. The XPS spectra are calibrated by placing the main Ti $2p_{3/2}$ peak at 458.8 eV and applying a constant shift of the remaining peaks.

The O 1s peak of the amorphous samples is found to be asymmetric and a shift of 0.3 eV of the peak position is observed after the annealing (Figure 3-37). Such a shift of O 1s was also noticed by Park and Shin [181] on TiO_2 powders treated by HCl. However, this shift, equivalent to 0.75 eV was found for both Ti $2p_{3/2}$ and O 1s peaks and was attributed to a charge effect due to the TiO_2 protonation. Moreover the binding energy difference (ΔE) between Ti $2p_{3/2}$ and O 1s for bare TiO_2 and HCl-treated TiO_2 was the same at 71.25 eV [181]. In our samples, this binding energy gap ΔE (Ti $2p_{3/2}$,O 1s) is found at 71.5 eV and 71.2 eV on amorphous and annealed films, respectively. The Ti $2p_{3/2}$ peak on the surface demonstrates that in all samples, titanium seems to be in Ti^{4+} coordination.

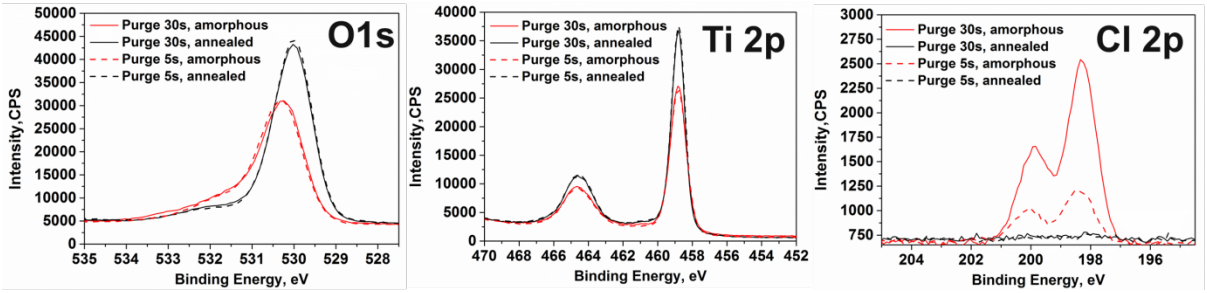

Figure 3-37 XPS on Ti 2p, O 1s and Cl 2p spectra on amorphous and annealed samples, grown in short (5 s) and long (30 s) purge time regimes at RT.

The quantitative data for the samples before and after annealing on the surface and in the volume are summarised in Table 3-5. The relative concentrations of the titanium-bonded oxygen (O-Ti) on the surface are calculated by subtracting the possible oxygen-carbon (C-O, C=O, and O-C=O) and SiO_2 contributions from the total oxygen O 1s signal, determined from the C 1s and Si 2p fitted peaks, respectively. The in-depth profiles with the absence of carbon in the films allows us to define the (O-Ti) concentration by subtracting the SiO_2 contribution from the total oxygen O 1s contribution. Thus, the relative concentration ratio [(O-Ti)/Ti] on the surface and in the volume is found close to 2 and do not change after the thermal treatment. The presence of chlorine is detected only in the amorphous samples fabricated in both deposition processes. Therefore, the annealing of amorphous samples ensures the complete removal of chlorine and further confirms the release of trapped Cl-based by-products upon annealing (Figure 3-37).

The depth profiles of the amorphous samples grown with long purge show the homogeneous distribution of chlorine in the volume (Figure 3-38). While for samples grown with short purge time, the presence of chlorine is lower on the surface but increases in the volume from 2 to 6%.

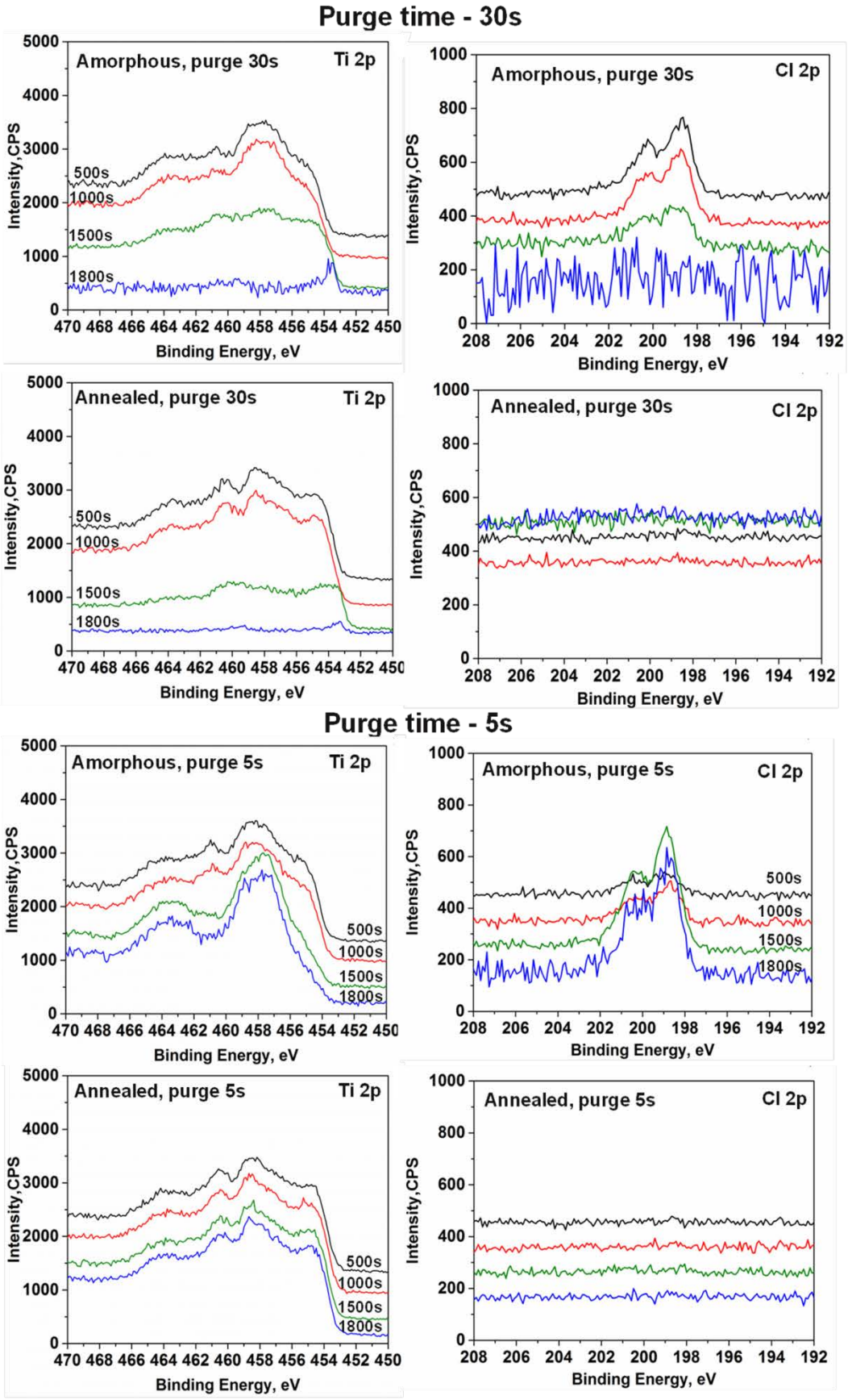

Figure 3-38 In depth XPS Ti 2p and Cl 2p spectra on amorphous and annealed samples, grown in short (5 s) and long (30 s) purge time regimes at RT.

The Ti 2p peaks in the depth profile are used to be modified by the Ar beam sputtering [182]. In TiO_2, the Ti 2p peak shape changes due to the reduction of Ti^{4+} under the Ar beam into Ti^{4+}, Ti^{3+}, Ti^{2+}. Moreover, the typical relative concentration ratio [O/Ti] in a reduced TiO_2 standard reference is in the range 1.3-1.6 [182]–[185] due to the preferential sputtering of the oxygen atoms. Interestingly, in our case the analysed samples demonstrate an almost constant [O/Ti] concentration ratio close to 2.

The depth profile of the amorphous sample grown in the short purge-time process demonstrates that after a sputtering of 1500 s and 1800 s , the Ti 2p peak shape changes from a broad peak due to the contributions of Ti^{4+}, Ti^{3+}, Ti^{2+} to a sharper peak with a predominant contribution at 457.8 eV (Figure 3-38). This behaviour differs from the usual sputtered profile of TiO_2 layers and another titanium-based phase is therefore expected within the film. The increase of chlorine concentration in the film volume is noticed and both signatures (Ti peak energy and Cl profile) tend to indicate TiO_xCl_y compounds. In agreement with Gu and Tripp's model, the film is likely composed of TiO_x, TiO_xCl_y or $Ti(OH)_xCl_{4-x}$ compounds where the relative concentration [(O-Ti)/Ti] is preserved at 1.9.

Table 3-5 Elemental composition on the surface of samples deposited at RT after 965 cycles, purge time of 5 and 30 s, before and after annealing, at.%.

		Ti	**O**	**Cl**	**C**	**Si**	**Calculated (O-Ti)**	**[(O-Ti)/Ti]**
20°C 965 cycles, purge 30 s, amorphous	**Surface**	**21**	*51*	**4**	*22*	*1*	**42**	**2.0**
	Volume	**34**	*63*	**4**	*0*	*0*	**63**	**1.9**
20°C 965 cycles, purge 30 s, Annealed	**Surface**	**26**	*56*	**0**	*11*	*3*	**50**	**1.9**
	Volume	**36**	*65*	**0**	*0*	*0*	**65**	**1.8**
20°C 965 cycles, purge 5 s, amorphous	**Surface**	**23**	*53*	**1**	*21*	*1*	**43**	**1.9**
	Volume	**31**	*62*	**2→6**	*0*	*0*	**62**	**2**
20°C 965 cycles, purge 5 s, Annealed	**Surface**	**27**	*60*	**0**	*11*	*2*	**52**	**1.9**
	Volume	**35**	*65*	**0**	*0*	*0*	**65**	**1.9**

Table 3-6 The O 1s concentration within the films and (O-Ti) and (-OH) relative component concentrations from the total oxygen contribution (O 1s is 100%).

		O 1s	***(O-Ti)***	***(-OH)***	***(H_2O)****
20°C 965 cycles, purge 30 s, amorphous	**Surface**	***51***	*72*	*24*	*0*
	Volume	***63***	*72*	*25*	*4*
20°C 965 cycles, purge 30 s, Annealed	**Surface**	***56***	*85*	***15***	*0*
	Volume	***65***	*70*	***26***	*5*
20°C 965 cycles, purge 5 s, amorphous	**Surface**	***53***	*76*	*24*	*0*
	Volume	***62***	*72*	*22*	*3*
20°C 965 cycles, purge 5 s, Annealed	**Surface**	***60***	*87*	***13***	*0*
	Volume	***65***	*70*	***25***	*4*

* H_2O is detected only in the depth profile and is related to the characterisation technique artefact.

The fine decomposition of the O 1s peak highlights hydroxyl groups in the amorphous sample, which are significantly reduced on the surface after annealing. The decomposition of the O 1s peaks on the surface and in volume underlines that annealed films are more hydroxylated in the volume compared to the surface (Table 3-6). This tends to indicate Ti-OH coordination within the volume corresponding to Ti^{3+} oxidation state.

For the thickness range ≥90 nm, amorphous and annealed samples grown at 100, 200°C are measured via XPS. The titanium-bonded oxygen (Ti–O) contribution is determined with the same approach by excluding the related carbon – and silicon – bonded oxygen as it was done for the XPS analysis of samples grown at RT (Figure 3-37). The concentration values for the TiO_2 samples deposited in three temperature regimes are summarised in Table 4-7. The relative concentration ratio [(O–Ti)/Ti] on the surface decreases with an increase in the deposition temperature. Indeed, at 200°C for both amorphous and annealed samples this concentration is 1.1, whereas in the film volume this ratio is still close to 2. Such a high degree of under-stoichiometry is likely to be compensated by the important hydroxyl contribution of 40% on the surface and 34% in the volume.

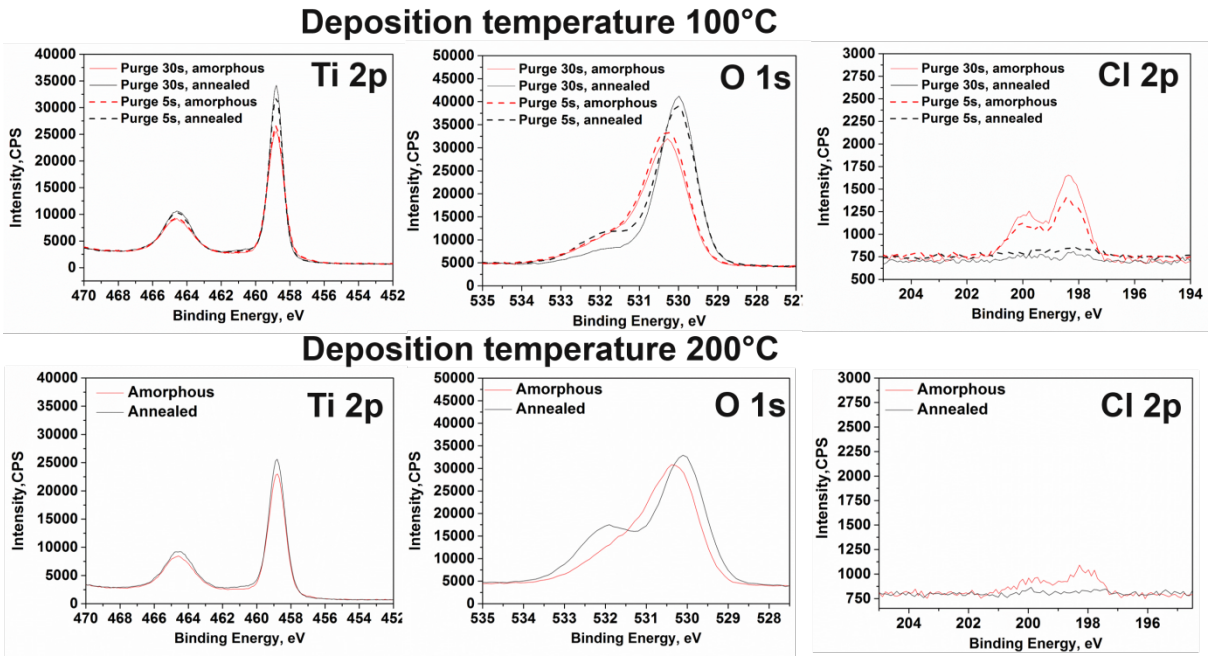

Figure 3-39 Ti 2p, O 1s and Cl 2p XPS spectra on amorphous and annealed samples, grown at 100 and 200°C.

A characteristic feature of all TiO_2 samples deposited by ALD using $TiCl_4$ and water as precursors is in the O 1s peak shift of 0.3eV after the annealing. Park and Shin [181] attributed this O 1s shift to the oxygen protonation in the acidic medium that promotes the TiO_2 hydroxilation, for instance in the case of TiO_2 treated by HCl.

However, the important concentration of hydroxyl groups may induce a charge effect, which results in the spectra shift [181]. Moreover, in our XPS quantification, the sample grown at 200°C demonstrates the highest hydroxyl concentration on the surface and in the volume after the post-deposition annealing without any significant change in the O 1s peak shift as it is measured for other samples. Therefore, we may consider that the high concentration of the OH groups (from 23 to 26%) in all annealed films significantly modified the atomic arrangement of our hydroxylated TiO_2 leading to slight shift of the O 1s binding energy. This is in a rather good agreement with Chen et al. results which correlate O 1s peak shift with disordered TiO_2 nanocrystals [186]. In the case of the thick TiO_2 amorphous film (~100 nm), one shall note a low concentration of chlorine compound 1.1%at. for 100°C deposition and 0.5%at. for 200°C, which is close to the detection limits of the XPS measurements, while the surface stoichiometry shows an important oxygen deficiency TiO_{2-x}.

The TiO_2 deposition in the classical ALD low-temperature window as 100 -200°C shows that in our conditions the short purge time leads to the better crystallization (XRD results). This contradicts to the well-established ALD assumption that a larger purge time should improve

by-products removal. In the case of the short purge time the deposition follows a non-ideal ALD regime. That is confirmed by QCM and the small amount of chlorine ~1.1% present in the amorphous film deposited at 100°C. Therefore, we suggest that the chlorine presence within amorphous films improve their crystallization during the post-annealing. We may also suggest that the small amount of the non-reacted precursor incorporated in the film or some intermediate reaction products release a latent heat under the annealing conditions and thus governs the explosive auto-catalysed crystallization.

3.3.1.1 Summary

The investigations of the TiO_2 films grown by ALD using $TiCl_4$ and water in the broad temperature range RT - 400°C demonstrate the strong dependence of the films morphology, chemistry and crystallinity versus the deposition temperature and the purge times. The temperature-dependant growth mechanisms are discussed and correlated with the growth rate data, where the important role of HCl is confirmed. The generally established drawback of using the halide Ti precursors is turned into an advantage; at low deposition temperatures, the non-ideal condensation regime is studied. The lowest film roughness makes these regimes a candidate for further deposition into porous membranes. Moreover, the investigations of the film growth at room temperature show that HCl is present in the amorphous film, degasses during annealing, which allows the formation of oxygen-deficient and highly-porous films. Interestingly, the recent studies [181], [187] have shown the beneficial influence of hydrochloric acid treatment on the enhancement of TiO_2 properties (photocurrent density and carriers life time) and discloses the benefits of hydrogenated TiO_2. Such chemistries are obtained in our cases.

Table 3-7 Summary table of relative concentration [O]/[Ti] and [Cl]/[Ti] , O 1s and (O-Ti) (-OH) and (H_2O) contribution within O 1s peak, on the surface and in the volume for all TiO_2 films deposited at RT, 100°C and 200°C.

		As deposited		**Annealed**	
		Surface	**Volume**	**Surface**	**Volume**
RT, purge 5s	**[O-Ti]/[Ti]**	**1.9**	**2**	**1.9**	**1.9**
	[Cl]/[Ti]	0	0→0.2	0	0
	O 1s	53	62	60	65
	O-Ti	76	72	87	70
	OH	24	22	**13**	**25**
	H_2O	0	3	0	4
RT, purge 30s	**[O-Ti]/[Ti]**	**2**	**1.9**	**1.9**	**1.8**
	[Cl]/[Ti]	0.2	0.1	0	0
	O 1s	51	63	56	65
	O-Ti	72	72	85	70
	OH	24	25	**15**	**26**
	H_2O	0	4	0	5
100°C, purge 5s	**[O-Ti]/[Ti]**	**1.5**	**1.9**	**1.6**	**1.8**
	[Cl]/[Ti]	0.1	0	0	0
	O 1s	53	65	57	64
	O-Ti	73	72	73	72
	OH	27	24	**27**	**24**
	H_2O	0	4	0	4
100°C, purge 30s	**[O-Ti]/[Ti]**	**1.6**	**1.9**	**1.9**	**1.8**
	[Cl]/[Ti]	0.1	0	0	0
	O 1s	51	65	57	64
	O-Ti	74	75	85	74
	OH	26	23	**15**	**23**
	H_2O	0	2	0	3
200°C, purge 30s	**[O-Ti]/[Ti]**	**1.1**	**1.9**	**1.1**	**1.8**
	[Cl]/[Ti]	0	0	0	0
	O 1s	53	65	58	65
	O-Ti	60	78	60	74
	OH	34	20	**40**	**23**
	H_2O	0	2	0	3

3.3.2 TiO_2 deposition into porous membranes

The previously discussed correlation of the films roughness dependence on the deposition temperature suggests that for deposition on porous membranes the low temperature regimes (lower than 200°C) are the most appropriate. Therefore, the TiO_2 depositions into porous membranes are performed at RT, 100 and 200°C with the 30 s purge time.

The periodic nanowires fabrication follows the protocol developed during this thesis and presented in the Section 2.2.2. The deposition at room temperature is very homogenous into pores, however the use of amorphous film leads to the systematic over-etching and the loss of nanowires during the H_3PO_4 wet-etching.

Depositions performed at 100 and 200°C forms also smooth and dense TiO_2 films which enabled the development of TiO_2 nanowires as seen on Figure 3-40. The nanowire dimensions are measured by SEM - tilted images with the angular correction, showing nanowires diameter around of 40 nm, length of 350 nm and spacing of ~70-80 nm (S70).

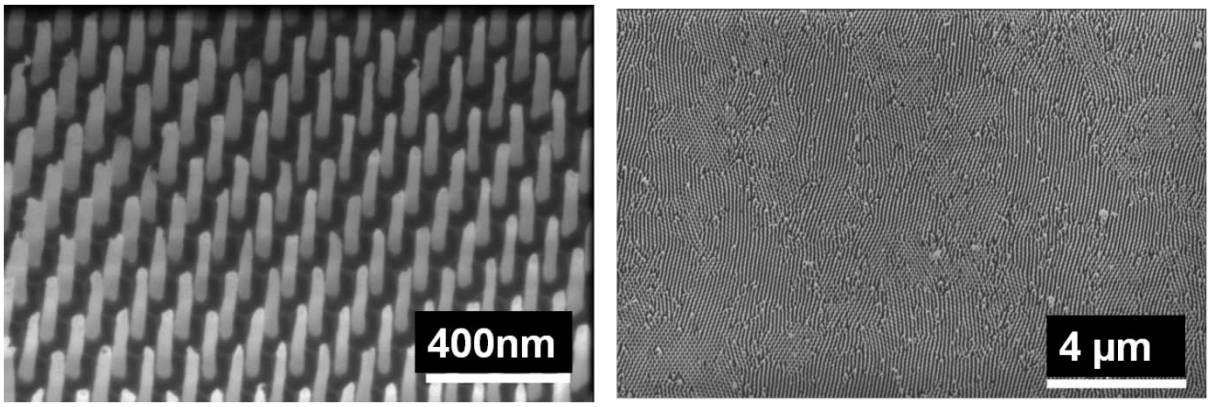

Figure 3-40 SEM images of periodic free standing TiO_2 nanowires (S70).

The diameters and spacing of the nanowires are determined by the pores diameter and their spacing in the AAO membrane. It is possible to tune the pore diameter and spacing by initially using AAO membranes with large pore sizes (200 nm), and adjusting the required pore diameters by subsequent ALD deposition of alumina. Following the already established nanowires fabrication protocol, TiO_2 nanowires that have 40 nm diameter, 500 nm spacing and 600 nm length are thus developed (S500). The wet-etching rate of the anodised alumina is found slightly faster than the alumina deposited by ALD, which justified the formation of the "nano-flasks" with the bottom widening due to the less-etched ALD deposited alumina (Figure 3-41).

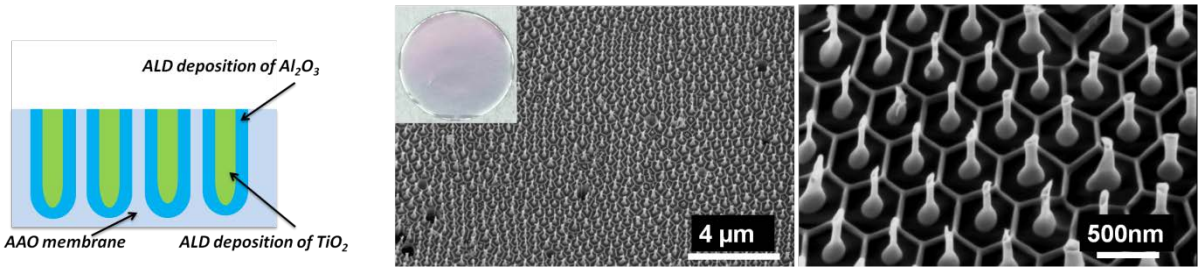

Figure 3-41 Tailoring of TiO_2 nanowires diameter and spacing (S500).

3.3.3 Tin oxide deposition by ALD

Similarly to TiO_2, the growth of smooth tin oxide films is required in order to perform deposition into porous membranes. Indeed, the fabrication of periodic tin oxide nanowires covered by TiO_2 form a semiconductor-semiconductor heterostructures that shall promote the photo-generated carrier separation towards the active surface in order to enhance the photocatalytic activity.

The optimisation of SnO_2 thin-films ALD is performed using a halide tin precursor - $SnCl_4$. Various approaches reported the use of different oxidative precursors such as H_2O, H_2O_2, O_2 and O_3 to oxidize $SnCl_4$, in our case we use H_2O. The main difficulty of SnO_2 ALD compared to the TiO_2 one is that $SnCl_4$ is not sufficiently reactive at low deposition temperatures (<250°C).

According to the literature, the typical deposition temperature range is 200-400°C, and depends on the oxidative precursor. In the case of using water as the oxidative precursor the surface reaction between follows the equations 3-16 and 3-17 [188]:

$$SnCl_4 + 2H_2O = SnO_2 + 4HCl \quad (3\text{-}15)$$

$$[\text{Pulse } SnCl_4]: \quad (-OH)_{(surface)} + SnCl_4 \rightarrow (-O)SnCl_{3(surface)}) + HCl \quad (3\text{-}16)$$

$$[\text{Pulse } H_2O]: \quad (-O)SnCl_{3(surface)} + H_2O \rightarrow (-O)SnOH_{(surface)+} HCl \quad (3\text{-}17)$$

In this work, the SnO_2 deposition is studied in the temperature range 200-400°C on Si (100) substrates and commercially available AAO Anodisk^{TM} with 0.2 µm pore diameter. ALD deposition parameters are set at 0.25 s pulse time and 30 s purge time for both precursors similarly to the TiO_2 deposition study. The films thickness is determined by ellipsometry and is in relatively good agreement with the cross-sectional SEM measurements presented below. Based on the ellipsometry measurements, the growth rate was determined for each

temperature. The growth rate of SnO_2 is very low at 200°C and increases exponentially with the deposition temperature until 350°C (Figure 3-42).

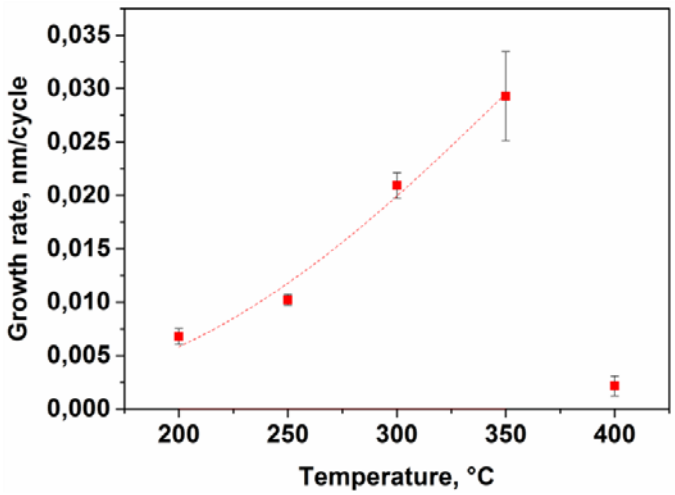

Figure 3-42 Growth rate of SnO_2 as function of deposition temperature.

The maximum growth rate is obtained at 350°C while at 400°C the growth rate is suddenly droped down to 0.002nm/cycle. The decrease of the growth rate with the temperature was also reported in the literature, however in much lesser extent [188][189]. The authors reported on the lower growth rate beyond 400°C and relate it with the temperature induced surface dehydroxylation or surface passivation with chlorine.

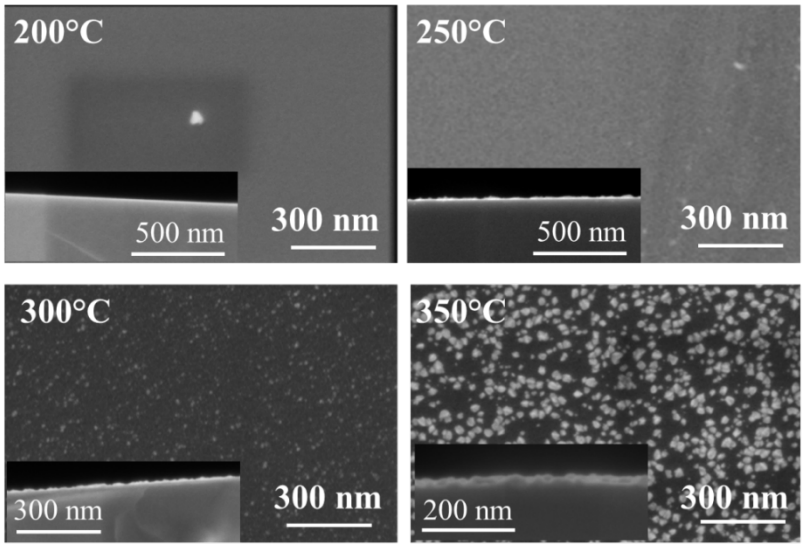

Figure 3-43 SEM images of SnO_2 films deposited on Si(100) in the temperature range 200-350°C.

Figure 3-43 shows the SEM pictures of the grown SnO_2 thin-films on Si substrates. The films morphology changes from a smooth-thin layer to rough layers corresponding to the nucleation and growth of SnO_2 islands distributed over the substrate. The final goal of the SnO_2 deposition optimisation is to achieve of smooth and conformal coatings that are compatible

with the porous alumina template, further development of SnO_2 deposition process is carried out on commercially available Wathmann Anodisk^{TM} AAO membranes.

The depositions of SnO_2 on porous substrates are realised simultaneously with flat Si substrates. From a general perspective (growth rate, morphology etc.), the growth behaviour of SnO_2 thin-films into porous substrates is comparable to the ones detailed previously on flat surfaces (Figure 3-44). With the former ALD process parameters, the low growth rate and the growth of discontinuous islands impairs the growth of continuous thin-films in a reasonable time. Therefore, ALD process parameters are then set as 0.25 s pulse ($SnCl_4$ and H_2O) and reduced purge time (5 and 10 s).

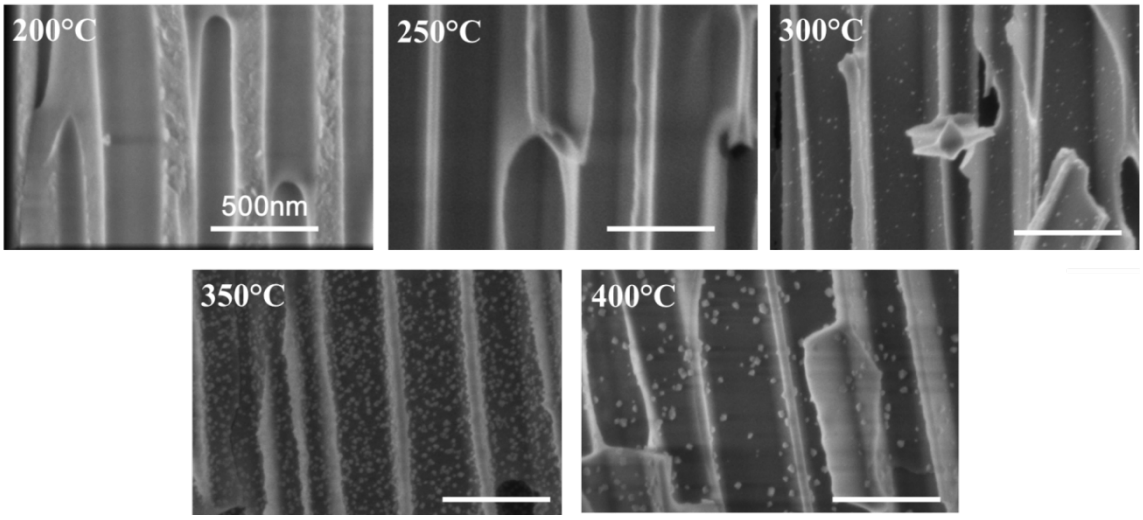

Figure 3-44 SEM images of 500 cycles SnO_2 films deposited on AAO in the temperature range of 200-400°C.

Influence of the purge time

The growth rate still determined by ellipsometry on Si substrates is lower than the ones measured in previous conditions with 30 s purge time and the growth rate monotonously increases with the purge time increases (Figure 3-45). This trend is confirmed by SEM cross-sectional control on AAO membranes. This is contradicting to the expected trends in the standard ALD regime for which usually stable or decreased growth rate is measured for longer purge time [190][109].

Taking into account HCl as a reaction by-product, it may react with the SnO_2 deposited layer as etching agent. Lu and co-workers [191] suggest that the HCl etching is the main reason of high film roughness. Gueoruiev et al. [192] demonstrated the SnO_2 etching by hydroiodic acid (HI). Thus by analogy the reaction 3-18 can be reversed under high temperature:

$$SnO_2 + 4HCl = SnCl_4 + 2H_2O \qquad (3\text{-}18)$$

The long purge time improves the evacuation (desorption or degassing) of HCl rather than it is in case of shorter purge times, when HCl could be retained within the film or reactor and enable the etching reaction [49]. However, the important number of cycles required for the deposition could not be determined when using such a long 30 s purging time. For this reason, the 5 s purge time is set for further studies.

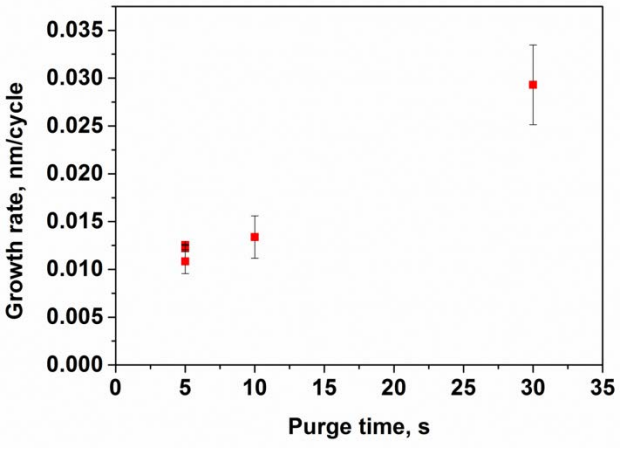

Figure 3-45 Influence of purge time on SnO_2 growth rate on Si substrates at 350°C.

For these conditions (350°C, 0.25 s pulse time, 5 s purge time), the film thickness is calibrated depending on the number of cycles (500, 1000 and 3000 cycles) (Figure 3-46). The film thickness controlled on Si substrate increases linearly with the number of cycles; after 3000 cycles, a 37 nm film is deposited.

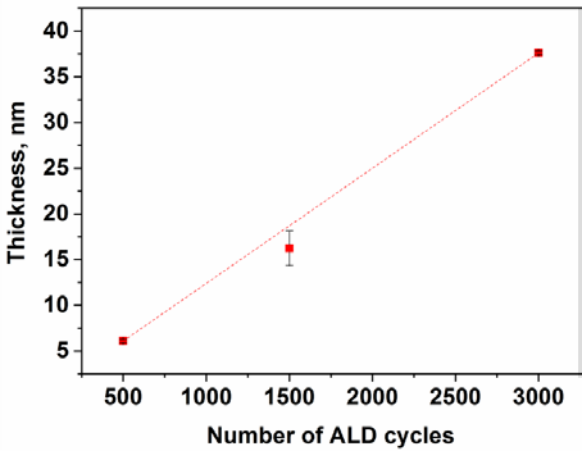

Figure 3-46 Thickness dependency of the ALD number of cycles.

The morphology in AAO films follows the growth of small clusters to nanoparticles to granular discontinuous film (Figure 3-47). Such kind of morphologies is not suitable for the conformal coating into porous channels of 40 nm. Therefore, the fabrication of SnO_2

nanowires with these process parameters is restricted to porous templates with larger channel diameter of 180-200 nm.

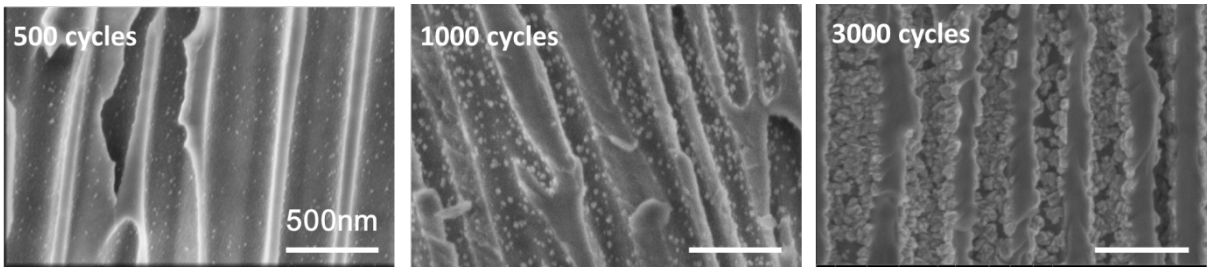

Figure 3-47 SEM images of SnO_2 films deposited on AAO at 350°C using 5 s as purge time and 500, 1000 and 3000 cycles.

Engineering of thin-film morphology

The important roughness of the SnO_2 film may be explained by a combination of factors such as HCl etching, poor surface hydroxylation under high temperatures or surface passivation by chlorine. The low number of absorbed sites on the surface initiates the growth of nanoparticles. The continuous growth expends these nanoparticles into the film grains. It is mandatory to improve the precursors adsorption to initially grow conformal monolayer. Therefore, the modification of the surface energy and the surface chemistry are likely to improve homogeneous chemisorption of precursors. To this end, we study the deposition of SnO_2 on three different surfaces chemistries: Si/Al_2O_3 (Al_2O_3 deposited by ALD), Si/TiO_2 and bare Si (100). ALD depositions are realised using the previously determined conditions 350°C, 0.25 s pulse/5 s purge for both precursors, with 500 and 1000 cycles.

Interestingly, samples, after 500 cycles depositions, show very different film morphologies (Figure 3-48). The growth onto Si/Al_2O_3 substrates leads to small clusters with a relatively low density. While the growth onto Si substrates and into commercial AAO membranes leads to similar growth results (Figure 3-43 and Figure 3-44), the growth of SnO_2 over ALD grown Al_2O_3 is significantly reduced. This highlights that beyond the materials chemistry (being almost identical for the commercial membrane and ALD Al_2O_3), the surface termination and the surface preparation play a significant role in the growth of SnO_2 thin-films in ALD processes over different Al_2O_3 surfaces. This is beyond the scope of this thesis to clarify the rationales in the case of commercial alumina and the one grown with ALD.

In a first approximation, we estimate that the surface energy is related to the water contact angle (WCA) (Table 3-8). We observe that the ALD alumina coating shows the important hydrophobicity compare to the Si-substrate. It could explain the notable growth difference by

the lower concentration of OH-functionalities on alumina surface, especially at high temperature, which induces the lower SnO_2 growth.

Table 3-8 Water contact angle values for different substrates.

Surface	WCA
Si (100)	26 ± 3.0°
Si/Al_2O_3	76 ± 4.5°
Si/TiO_2 (anatase)	45 ± 2.6°

The TiO_2 ALD coating studied previously in Section 3.3.1 demonstrates an intermediate WCA value between Si and Si/Al_2O_3 surfaces. Very interestingly, the SnO_2 deposition onto substrate with a 35 nm buffer layer of TiO_2-anatase leads to an almost continuous thin-film of SnO_2 having a grain morphology similar to the one observed for the TiO_2 buffer layer. One of the possible reasons of the SnO_2 growth enhancement on the TiO_2 anatase buffer layer is the ability of TiO_2 to retain the adsorbed water, which is difficult to rid of. Pak and co-workers [173] in the earlier 70th demonstrated that Ti-atoms serve as the adsorption centres for molecular water, which is hold on the surface at a temperature up to 180°C. The authors showed that after thermal treatment at 350°C for 4h, ~ 74% of Ti-atoms on the surface desorbed the coordinated water molecules. However this dehydroxylation was found to be reversible by the exposure of water vapour at lower temperatures.

Therefore it is possible that OH functionalities of TiO_2 are more stable at 350°C that on other surfaces and ensure the formation of continuous monolayer. It is worth noticing the SnO_2 morphology varies from particles to continuous film according to the TiO_2 grains.

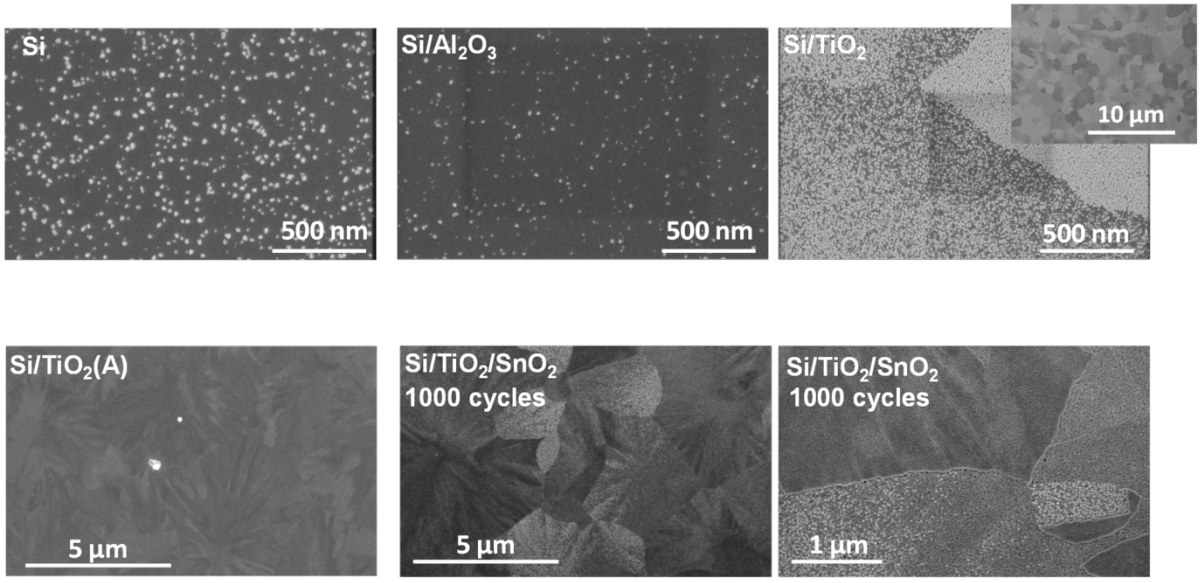

Figure 3-48 Top range: SEM micrographs of SnO_2 deposition on Si, Si/Al_2O_3, Si/TiO_2 after 500 ALD cycles and bottom range: TiO_2 buffer layer before and after the deposition of 1000 cycles.

In this study, SnO_2 deposition is realised on anatase-TiO_2 film grown by ALD at 100°C and annealed, as it is previously discussed in Section 3.3.1. 35 nm TiO_2 film consists of large grains having different crystalline orientations. Therefore, the corresponding local surface energy varies according to this crystalline orientation (Table 3-9) [16][25] [193].

Table 3-9 TiO_2 surface energy according to crystalline orientation.

TiO_2 crystalline orientation	**Surface energy γ, J/m^2**
(111)	1.61
(110)	1.09
(001)	0.90
(100)	0.53
(101)	0.44

The SnO_2 thin-film is very smooth when grown on certain grain orientations, its growth mimics the grain shapes of the TiO_2 under-layer. This growth behaviour of SnO_2 is mainly obtained over the whole TiO_2 surface. However, on other few grains, having probably different crystalline orientation, rough deposition of highly-dense SnO_2 nanoparticles is obtained.

The KPFM measurements realised on the TiO_2 film confirm the surface potential variation between the formed grains (Figure 3-49). Unfortunately the KPFM data have only indicative character and does not allow determining the exact crystalline orientation of each grain.

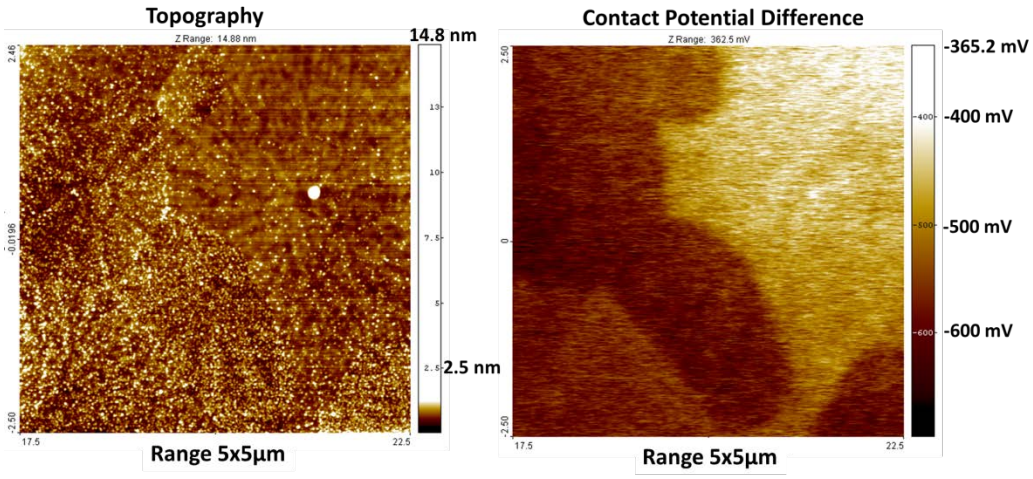

Figure 3-49 TiO_2 film surface topography (left) and contact potential difference measurements (right) on the same area.

The EBSD characterisation of TiO_2 buffer layer reveals the presence of important amount of high surface energy orientation as (001). According to the EBSD map we estimate the percentage of this orientation as ~47% of the whole map area. In the same way we estimate the percentage of smooth area of SnO_2 film from the SEM image (Figure 3-50) which is

~50% of the image area. That allows us suppose that (001) facets are responsible for the smooth SnO_2 growth.

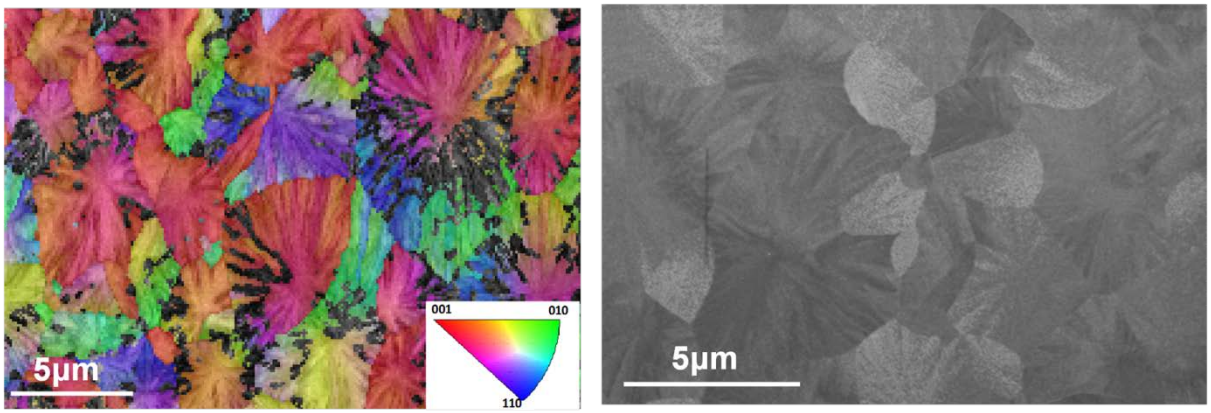

Figure 3-50 EBSD map; SEM image of SnO_2 film deposited on Si/TiO_2 substrate and surface energy values corresponding to different orientations.

The (001) facets are usually difficult to obtain because of their high surface energy. This is mainly due to the atomic coordination of Ti and O. The (001) orientation is characterised by a high density of undercoordinated Ti atoms and the Ti–O–Ti bond angle is very large (Figure 3-51). Such arrangement distabilises the 2p states of the surface oxygen atoms and makes them very reactive [194]. Numerous theoretical and experimental studies demonstrate that the (001) promote the dissociative adsorption of various precursors (water, methanol etc.) while on the low energy orientation (101) these molecules are adsorbed without dissociation (Figure 3-51) [195][194].

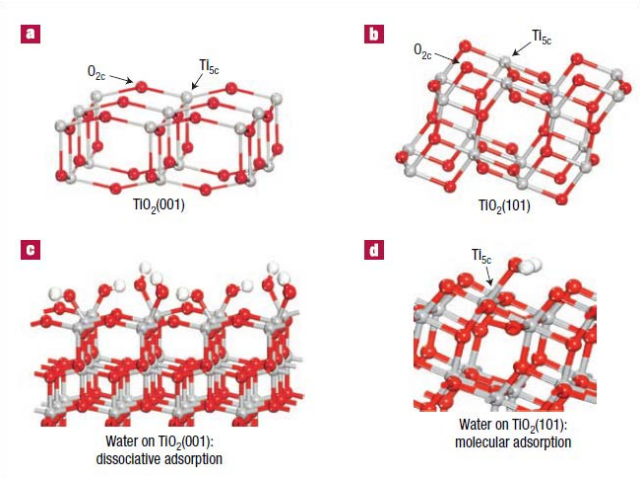

Figure 3-51 The atomic structure of anatase TiO_2 (001) and (101) surfaces and their water-adsorption behaviour. Adopted from reference [194].

TEM investigations are currently on-going to accurately determine the interplay between the crystalline orientation of the TiO_2 under-layer and the growth behaviour of SnO_2.

The crystallographic structure of films deposited with and without TiO_2 buffer layer is controlled by XRD. The diffractograms (Figure 3-52) show SnO_2 in cassiterite phases for both samples.

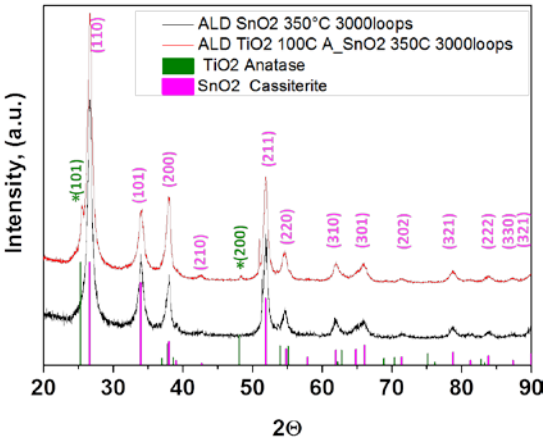

Figure 3-52 XRD on SnO_2 grown with and without TiO_2 buffer layer on Si (100) substrate after 3000 ALD cycles.

3.3.4 SnO_2 Deposition into porous membranes

The optimisation of the SnO_2 smooth layer deposition using TiO_2 anatase buffer layer is applied in first in commercially available Anodisk^{TM} porous membranes with 200 nm pores diameter. The 20 nm of TiO_2 buffer layer is deposited by ALD at 200°C and annealed at 450°C in air and is followed by SnO_2 ALD deposition (3000 cycles at 350°C). The SEM observations show the significant improvement of the SnO_2 thin-films morphology into the membrane when a TiO_2 layer is used (Figure 3-53b). A homogeneous, continuous and conformal closely-packed SnO_2 thin-films is grown all along the membrane pores. This is a significant breakthrough in the field of growing continuous and conformal SnO_2 thin-film by ALD.

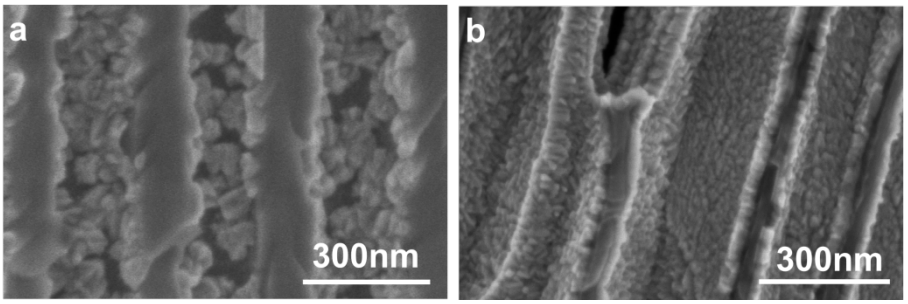

Figure 3-53 SnO_2 deposition after 3000 ALD cycles on (a) AAO AnodiskTM and (b) AAO with TiO_2 buffer layer.

A similar deposition process is applied on membranes having 2 µm pores length and well distributed 180 nm pores diameters. SEM pictures highlight the top-view pores architecture after each process step (as-received, after TiO_2 deposition, after SnO_2 deposition - Figure 3-54).

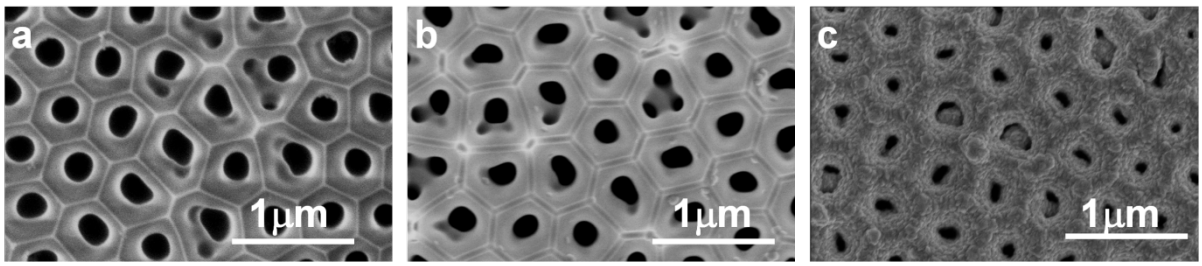

Figure 3-54 Deposition into porous template steps: (a) AAO without deposition, (b) deposition 20 nm of TiO_2, (c) SnO_2 deposition.

This finding allows the direct fabrication of TiO_2/SnO_2 heterostructures using the template-assisted approach and opens new architectural engineering of complex heterostructured nanowires or nanotubes with a broad range of dimensions (size, length, spacing etc.). Similarly to the TiO_2 periodic nanowires fabrication, the heterostrucured periodic nanowires are fabricated according to the protocol developed in Section 2.2.2 and presented on Figure 3-55.

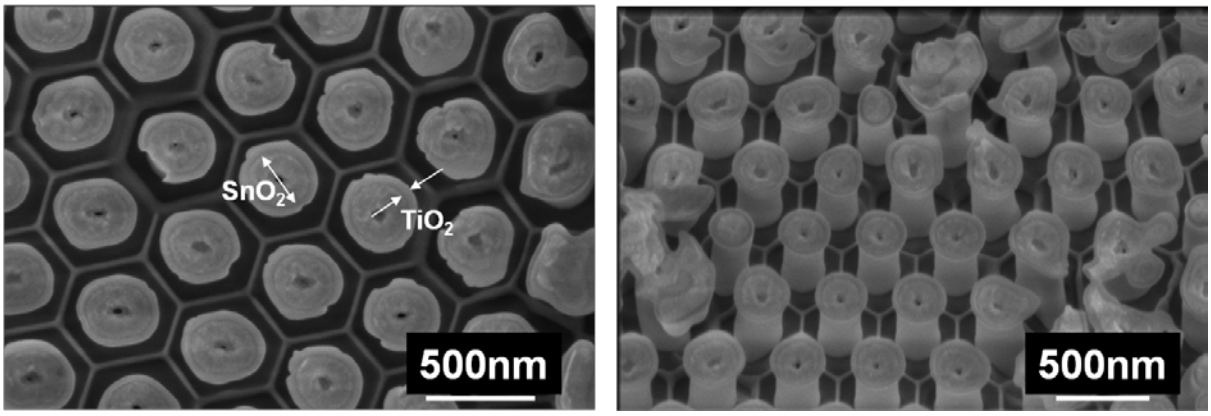

Figure 3-55 SEM images of fabricated TiO_2/SnO_2 periodic heterostructures. Top-view (left) and tilted 20°(right).

3.3.5 Summary

This section presents the development and characterisation of ALD grown TiO_2 and SnO_2 thin-films compatible with nanoscale pore size alumina templates. The depositions of TiO_2 at 100 and 200°C after the post-deposition annealing form original “hand-fan” like crystallised thin films. Moreover, the films deposited at room temperature after post-deposition annealing formed a unique and highly porous morphology. The obtained films roughness is compatible

with AAO templates, therefore the development of TiO_2 periodic nanowires is performed according to the nanofabrication protocol being optimized and detailed in Section 2.2.2. The TiO_2 deposition at low temperature (<200°C) using short purge time leads to the non-ideal ALD regime and thus possible accumulation of the by-products within the film. We showed that samples grown in the non-ideal ALD regime have better crystallinity after the post-deposition annealing. Moreover, the presence of HCl in the film enables its hydroxilation/hydrogenation and forms disordered TiO_2 nanocrystals. The high surface roughness of ALD grown SnO_2 thin-films even at a relatively high temperature window (350°C) is a significant limitation of the usual SnO_2 ALD processes.

The original use of TiO_2 (anatase) buffer layer improves the $SnCl_4$ chemisorption for the first monolayers formation and enables the growth of smooth cassiterite thin films via ALD process based on $TiCl_4$ and water. That is successfully implemented in the AAO template assisted approach for the fabrication of well-organised SnO_2/TiO_2 crystallized heterostructures.

4 Photocatalytic Test on TiO_2 Films and Nanostructures

One of the main objectives of this thesis is the development of photocatalytic titanium dioxide films and nanostructures by relying on improved and tailored material properties to overcome the main drawbacks of raw TiO_2, which are the photo-response being limited to the UV range and the fast recombination of the photo-generated carriers.

In previous chapters, the fabrication aspects of TiO_2 films, nanowires and heterostructures with SnO_2 were investigated, discussed and optimised. Their respective photocatalytic activity/performance is studied in this chapter.

On the laboratory scale, photocatalytic degradation tests use organic dye molecules as the pollutant models, such as methylene blue (MB), rhodamine B (RhB) and salicylic acid (SA).

4.1 Photocatalytic degradation tests on TiO_2 deposited by MOCVD

The first approach of nanowires fabrication from self-assembled TiO_2 nanoparticles by MOCVD did not lead to the expected nanowires architecture. The samples grown by MOCVD show two distinct morphologies: granular or columnar films. Photocatalytic tests are performed on representative samples with respect to their morphological and crystalline features (Table 4-1).

According to the XRD characterisation, the samples that we investigate have an anatase-TiO_2 phase. The samples grown with a high precursor injection rate have a greater thickness (~600 nm) but also a preferential growth orientation (211) that is contrary to the most common (101) orientation (Diffractograms presented in the Section 3.2.1).

Table 4-1. Summary on MOCVD samples used for the photocatalytic tests.

Growth temperature, °C	**Process pressure, mbar**	**Precursor injection rate, g/min**	**Crystalline phase**	**Morphology**	**Contamination**
550	0.94	0.2	Anatase	Columnar film	carbon
550	0.94	0.8	Anatase	Columnar film	-
300	10	0.2	Anatase	Granular film	-
350	10	0.2	Anatase	Columnar film	-

The highest photocatalytic degradation rates are found in the sample grown at a pressure of 10 mbar and a temperature of 300°C and at a low pressure of 0.94 mbar, and at 550°C with a high rate of precursor injection. A reference baseline is reported to validate the absence of the photolysis of the pollutant (light blue curve, Figure 4-1).

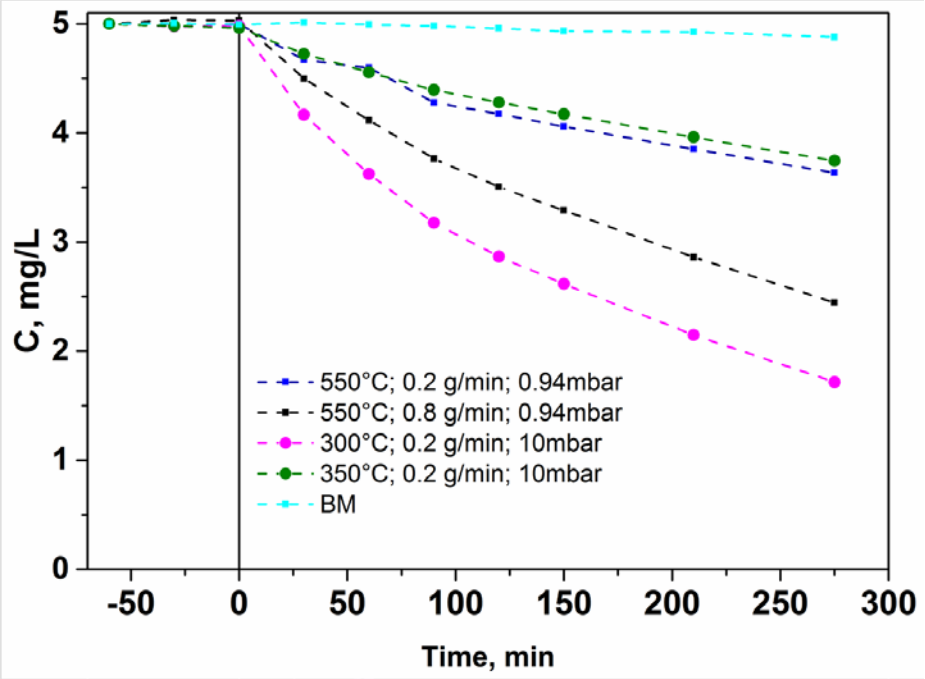

Figure 4-1 Photocatalytic degradation on TiO2 films deposited by MOCVD.

Photocatalytic performance is usually discussed based on the photocatalytic degradation rate. The photocatalytic degradation rate (r) of a molecule with concentration [C] towards reaction products is usually written by differential law:

$$r = -\frac{d[C]}{dt} = k[C]^n \qquad (4\text{-}1)$$

where k is the degradation rate constant and n is the reaction order that can be 0, 1, 2 or 3 [196].

Considering that the photocatalytic degradation follows the first reaction order, the concentration at the time t [C] is as follows:

$$[C] = [C_0]e^{-kt} \qquad (4\text{-}2)$$

or

$$\ln\left(\frac{C}{C_0}\right) = -kt \qquad (4\text{-}3)$$

where C is the concentration of the molecule at the moment t, and C_0 is its initial concentration. Then the plot of the values $Ln(C_0/C)$ versus the degradation time, for the first order of the reaction kinetic, should respond to a linear fit, with a slope corresponding to the reaction constant k_r (Figure 4-2). This is indeed the case for our samples grown via MOCVD.

..

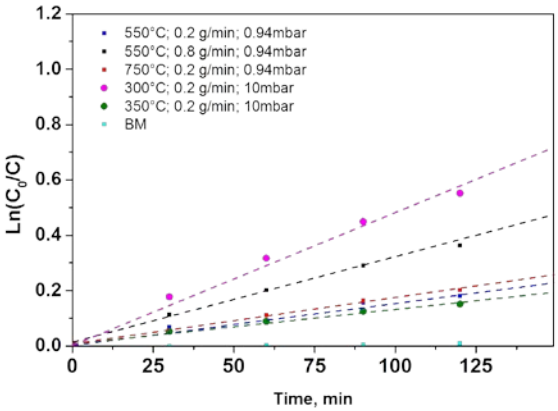

Sample	Photocatalytic degradation constant, k_r x10^{-3}, min^{-1}	Photocatalytic degradation constant normalised by surface unit, k_r x10^{-4}, $min^{-1}cm^{-2}$
550°C; 0.2g/min; 0.94mbar	1.3	4.3
550°C; 0.8g/min; 0.94mbar	2.8	9.2
750°C; 0.2g/min; 0.94mbar	1.5	5.6
300°C; 0.2g/min; 10mbar	4.1	14.4
350°C; 0.2g/min; 10mbar	1.1	4.0

Figure 4-2 Plot Ln(C_0/C) versus reaction time for the TiO_2 samples grown by MOCVD and reaction constant values kr for given samples.

The increase of the precursor injection rate from 0.2 to 0.8 g/min at 550°C results in a thicker film with “fish-bone” nano-columns instead of a standard columnar growth at a low precursor injection rate (Figure 3-20). Predominant (211) and (112) crystalline orientations are noted for the film grown with the higher injection rate, compared to the (101) orientation for the thinner film.

For the first approximation, we can suppose that thicker film (~600 nm vs. 130 nm) can induce a difference in the photocatalytic degradation constants. Moreover, the sample grown with a higher injection rate is characterized by high energy anatase facets that may preferentially modify the MB adsorption. Therefore, all of these factors can synergistically improve the photocatalytic degradation rate. A significant difference in the photocatalytic activity is noted for samples grown at 10 mbar at 300 and 350°C, respectively. The normalised degradation constant is almost divided by 4 when the deposition temperature is increased by 50°C, despite an improved crystallinity at higher temperature. As shown in Section 3.2.1, both films show similar stoichiometry, but the change in the deposition temperature leads to a morphology transition between a granular film (300°C) to a columnar film at 350°C.

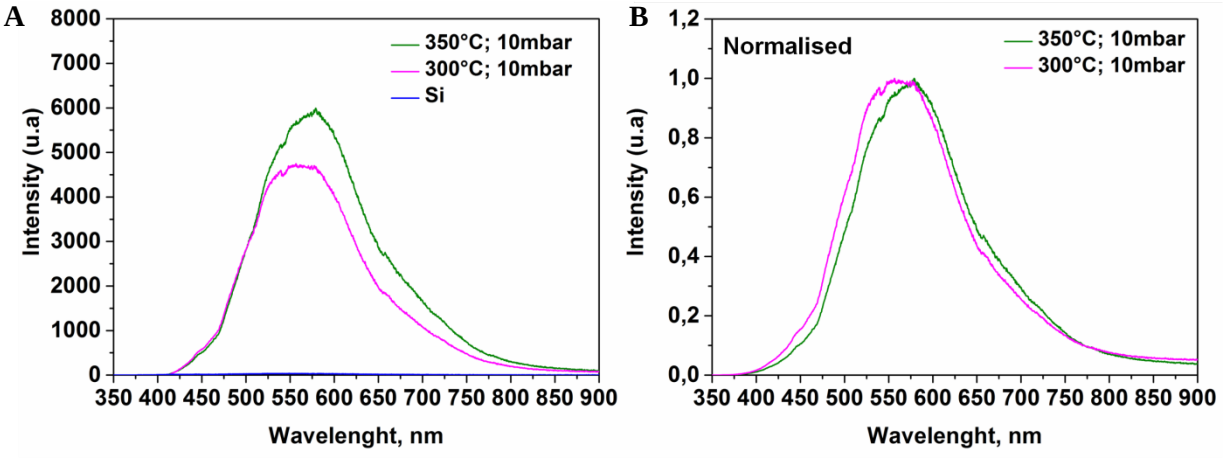

Figure 4-3 PL spectra of MOCVD TiO_2 films grown at 300°C and 350°C, 10 mbar.

The PL spectra of samples grown at 300°C at 10 mbar show higher intensity than the sample grown at 350°C, that is logically due to the slightly thicker film and better TiO_2 crystallisation. The normalised spectra show a slight shift to the green band (~525 nm) which may be associated to oxygen vacancies [197]. Two kinks at 540 nm and 656 nm are attributed to the known measurement artefacts due to the change in the filter network to cover a broad spectral range (idem for further PL measurements).

Therefore, the greater photocatalytic activity can be explained by the presence of the oxygen vacancies which may promote the photo-generated carrier separation. The respective morphologies may also have an important impact on the carriers lifetime.

4.2 Photocatalytic degradation tests on TiO_2 deposited by ALD

Physical and chemical properties of the TiO_2 films grown by ALD are previously discussed in Section 3.3.1. The TiO_2 films morphology, crystallinity and chemical composition show very significant features according to the ALD process parameters.

The first investigations on the photocatalytic activity of TiO_2 films grown in low-temperature ALD regimes, are also performed using the MB solution. In that case, any adsorption-desorption mechanism of MB on the sample surface is checked by controlling the MB concentration in a dark environment for 24 h on samples showing mesoporous morphology (as samples grown at RT). These measurements do not show any significant change of the MB concentration. Therefore, any detected variation of the MB concentration when photocatalytic tests are performed is strictly due to a chemical degradation of the molecule.

The TiO_2 films deposited at the higher temperatures of 100 and 200°C show a photocatalytic activity that varies with the growth conditions of films (Figure 4-4).

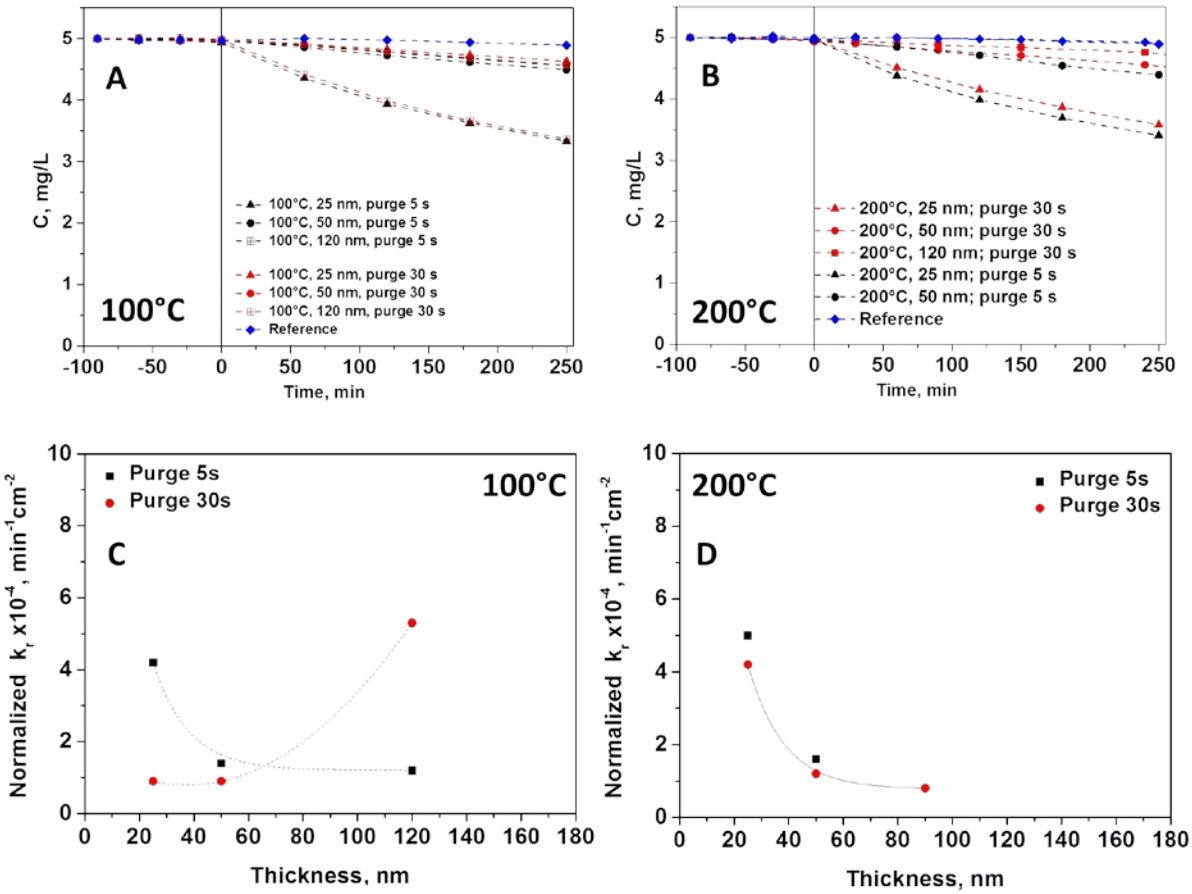

Figure 4-4 Photocatalytic degradation plots of BM on TiO_2 films grown on Si(100) at 100°C (A) and 200°C (B). Normalised photocatalytic degradation constant as function of the film thickness for both purge time regimes (5s, 30s) at 100°C (C) and 200°C (D).

In the case of samples deposited at 100°C, the evolution of the photocatalytic activity vs. the film thickness has opposite behaviours for the studied purge time (Figure 4-4 C). In the case of 5 s purge time, the photocatalytic degradation constant monotonously decreases with the thickness. For the depositions with 30 s purge time, the normalised photocatalytic degradation constant increases for films thicker than 60 nm.

The photocatalytic degradation rate on the TiO_2 films deposited at 200°C is very low (almost no activity) for the thickest film (90 nm). The highest efficiency is obtained for the thinnest film (25 nm), while the purge time does not seem to significantly impact the photocatalytic performance for ALD films grown at 200°C (Figure 4-4 D).

The photoluminescence of the films grown at 100°C and 200°C is presented in Figure 4-5, demonstrating a broad luminescence profile. For the films grown at 100°C with 30 s purge time, the PL intensity increases monotonously on the film thickness. In a first approximation, the photo-generation of carriers is enhanced due to higher absolute absorbance; therefore the

radiative recombination of excitons is enhanced. In that case, the trend of PL may be correlated to the normalised photocatalytic constant. For shorter purge time, PL responses are more intriguing since thicker and thinnest films show almost the same PL peak intensity while films with intermediate thickness show high photoluminescence. Thinnest films have almost the same PL peak wavelength while the PL peak wavelength for the thickest film is shifted towards shorter energy with a significant shoulder profile around ~700 nm.

At 200°C deposition temperature, the thickest film (90 nm) has a very low PL intensity. The normalised PL spectra for two temperatures regimes have a very similar shape with the intensity maximum at ~585 nm. A shoulder at ~700 nm is noted for the thick films deposited at 100°C (red curve) and for all samples deposited at 200°C.

For these samples, there is no clear correlation between PL signatures and photocatalytic efficiencies; however, PL profiles bring additional insights regarding the exciton recombination on structural/point defects with energy levels within the materials band gap. Therefore, we use mainly PL results to probe photo-active defects in the materials band gap and to correlate these features with the physical-chemical analysis of materials.

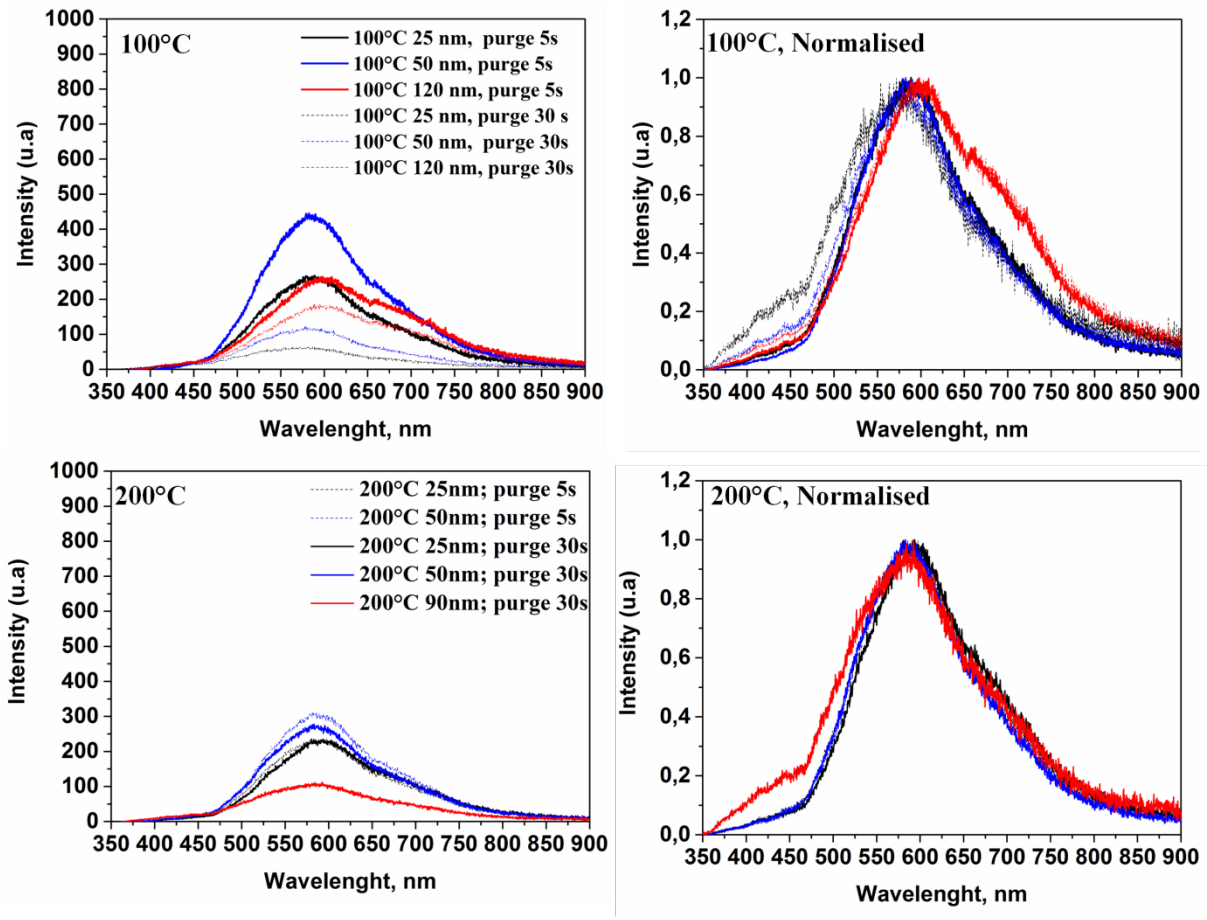

Figure 4-5 PL spectra of TiO_2 films deposited at 100°C and 200°C.

The photocatalytic performance of a materials system depends on many parameters: light absorption, efficiency of photo-generation of carriers, excitons lifetime, carriers mean free path, surface energy, carriers traps, band gap energies etc.

The films morphology plays a significant role in terms of active surface interacting with the pollutant molecules. The film morphology plays also a crucial role on the carriers path and their lifetime and the photo-generated carriers recombination is higher on smaller grain polycrystalline films than highly crystallized films. Concerning the polycrystalline structures, the crystallites size and the grains boundary modify significantly the photo-generation of carriers, their path and lifetime. As it is generally assumed, the grains/crystallites boundary is a carriers recombination site [198]. That is in line with our observations for the thick TiO_2 film deposited at 200°C. According to the XRD data, this sample forms the smallest crystallite of size ~8 nm (Figure 3-29), which likely promotes a fast recombination of the photo-generated carriers.

It is also generally assumed that the Ti^{4+}–OH sites participate to the carriers recombination. These sites located at the surface may trap electrons and result in the Ti^{3+}–OH , which at their turn attract holes and leads to the recombination of carrier [15]. These assumptions are coherent with the photocatalytic test results on the same thick sample deposited at 200°C. As it was mentioned previously in Section 3.3, the samples grown at 200°C exhibit the highest OH concentration on the surface (40%) with almost no photocatalytic activity. At lower deposition temperature (100°C) the 120 nm thick film also shows the smallest crystallite size (as 12 nm) across the 100°C deposition series. While the OH concentration on the surface (15%) is significantly lower as for 200°C deposition. In this case, the increase of the crystallites size and the reduction of the hydroxyl concentration tend to improve the photocatalytic efficiency.

The investigation of room temperature-deposited TiO_2 films with short and long purge time (5s and 30 s) is performed under conditions identical to those used for the 100 and 200°C depositions. The RT TiO_2 films deposited after 160, 320 and 965 cycles and annealed have thickness of 15 nm, 30 nm and 170/90 nm, respectively. Only for the high number of ALD cycles, the thickness is significantly different according to the process purge time: 170 nm for 5 s purge time and 90 nm for 30 s purge time. The RT deposition is also performed on two different substrate architectures, i.e., Si wafers with native and thermally grown SiO_2 films (Si, Si/SiO_2). The photocatalytic degradation results are shown in Figure 4-6 A and Figure 4-7.

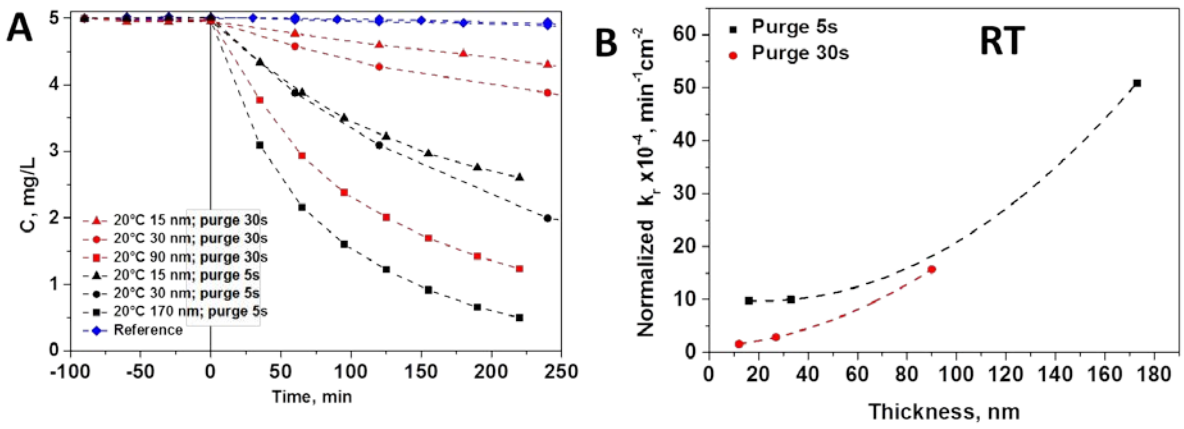

Figure 4-6 Photocatalytic degradation tendencies of MB on TiO_2 films grown on Si(100) wafers with native silicon oxide (UV-range) (A); Normalised photocatalytic degradation constant plot as the function of film thickness for both purge time regimes (5s, 30s) (B).

The TiO_2 films deposited at room temperature have a much higher photocatalytic activity compared to the films grown at 100 and 200°C (i.e., 10 times higher (Figure 4-4). In the best case, MB is fully degraded in almost 4 h in our experimental conditions.

The photocatalytic activity of RT TiO_2 thin-films increases monotonously with the films thickness. The films grown with the shortest purge time (5 s), have a significantly higher photocatalytic activity than films grown with the longest purge time (30 s), when the number of cycles, determining the thickness, is kept constant. The comparative plot of photocatalytic degradation constant versus the film thickness for two purge time is presented in Figure 4-6B. In the first approximation, this improvement of the degradation rate for the short purge time can be related to the film thickness. It was shown in Section 3.3.1 that the GPC is higher for the 5 s purge time at RT. This difference is especially notable for the thick films deposited after 965 cycles. However, for thinner films deposited after 160 and 320 cycles, the thickness difference is minor (~4-6 nm), while the photocatalytic degradation rate is still ×6 and ×4 for 15 and 30 nm thick films, respectively. 15 and 30 nm thick films have smoother morphology for 30s purge time, while the use of 5 s purge time leads to very porous thin-films. This induces a significant increase of the specific active area that contributes to improve significantly the photocatalytic performance.

The growth of mesoporous TiO_2 thin-films via RT ALD and the post-annealing of substrates with a thermal SiO_2 layer of ~50 nm induces a significant improvement of the photocatalytic degradation rate in the case of the 170 nm films (965 cycles), when compared to the thin-films grown with the same deposition process on bare-Si wafers. A comparative plot of the $Ln(C_0/C)$ for the thick samples deposited on Si and Si/SiO_2 with the two purge time (Figure

4-7) highlights a slight increase of the reaction kinetic constant from $15.7 \cdot 10^{-4}$ to $19 \cdot 10^{-4}$ for Si and Si/SiO_2 substrates respectively when the purge time is 30 s. In the case of 170 nm TiO_2 films grown with 5 s purge time, the reaction kinetic constant is increased from $50.9 \cdot 10^{-4}$ to $57 \cdot 10^{-4}$, when Si/SiO_2 substrates are used instead of bare Si-wafers. These unexpected results highlights that beyond the growth process parameters, the substrate chemistry (native oxide vs. thermally grown oxide) plays a significant role in the functional property of RT ALD grown photocatalytic TiO_2. For the depositions at higher temperatures (100°C and 200°C), the substrate effect is not observed.

The photocatalytic degradation constants have been determined, and the constants normalised by the sample surface area for samples grown at RT 100 and 200°C are summarised in Table 4-2.

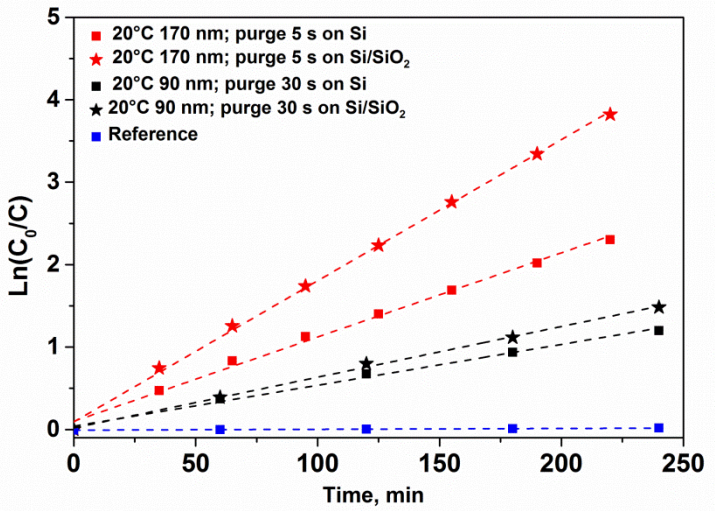

Figure 4-7 Plot $Ln(C_0/C)$ versus reaction time for the RT deposited TiO_2 films after 965 cycles on Si and Si/SiO_2.

The normalized values per surface area of the degradation constant are significantly higher than values reported for pure TiO_2 mesoporous films in the literature. For instance, the degradation constant obtained using similar photocatalytic test conditions on hierarchically ordered macro-mesoporous TiO_2 films is $20.5 \cdot 10^{-4}$ $min^{-1}cm^{-2}$ as demonstrated by Du et co-workers [199] while our degradation constant is almost twice higher. However, the irradiation levels being different during the photocatalytic test experiments, a direct comparison of the performances is still puzzled.

Table 4-2 Photocatalytic degradation constants k_r of TiO_2 films deposited at RT, 100°C and 200°C.

TiO_2 films deposition regimes		**Photocatalytic degradation constant, $\times 10^{-3} min^{-1}$**			**Photocatalytic degradation constant, normalised by surface unit, $\times 10^{-4}$ min^{-1} cm^{-2}**		
		On Si(100)	**On Si/SiO_2**	**on Quartz**	**On Si(100)**	**On Si/SiO_2**	**on Quartz**
RT 160cycles	**Purge 5 s**	3.1	3.4	-	9.8	11.0	-
	Purge 30 s	0.5	0.8	-	1.6	2.6	-
RT 320cycles	**Purge 5 s**	3.5	3.4	-	10.0	10.6	-
	Purge 30 s	1	0.3	-	2.9	0.9	-
RT 965cycles	**Purge 5 s**	10.5	17.2	3.9	50.9	57.6	19.9
	Purge 30 s	4.7	5.7	2.2	15.7	19	9.2
100°C 350cycles	**Purge 5 s**	1.70	-	-	4.2	-	-
	Purge 30 s	0.30	-	-	0.9	-	-
100°C 700cycles	**Purge 5 s**	0.40	-	-	1.4	-	-
	Purge 30 s	0.30	-	-	0.9	-	-
100°C 1650cycles	**Purge 5 s**	0.40	-	-	1.2	-	-
	Purge 30 s	1.70	-	-	5.3	-	-
200°C 500cycles	**Purge 5 s**	1.6	-	-	5	-	-
	Purge 30 s	1.4	-	-	4.2	-	-
200°C 1000cycles	**Purge 5 s**	0.5	-	-	1.6	-	-
	Purge 30 s	0.4	-	-	1.2	-	-
200°C 2000cycles	**Purge 30s**	0.2	-	-	0.8	-	-

The photoluminescence measurements carried out on the most remarkable samples (in terms of photocatalytic performance) of RT TiO_2 films are presented in Figure 4-8A that shows the spectrum as-recorded, while Figure 4-8B shows the spectrum normalised to the maximum intensity of the main PL peak. Compared to the previously discussed PL of 100°C and 200°C TiO_2 as recorded, the PL intensity of the RT TiO_2 films is 10 times higher.

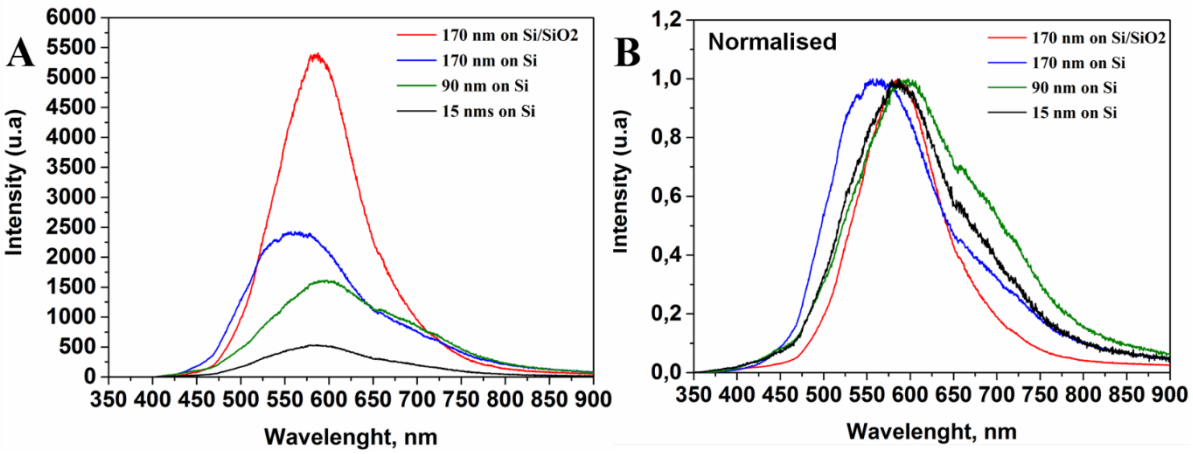

Figure 4-8 PL spectra of RT TiO_2 films.

The PL peak intensity of RT TiO_2 films/Si substrate increases monotonously with the film thickness and the peak wavelength is blue-shifted for the thickest film. For the same thickness (170 nm), the PL intensity is significantly exalted when thermally oxidized Si substrate is used. This may due to the better intrinsic opto-electronic properties of the films grown over SiO_2, as already noticed via the photocatalytic measurements.

All samples grown on Si have a broad PL response with specific contributions in the range ~500-525 nm (2.48-2.36 eV), ~585 nm (2.11 eV) and ~700 nm (1.77 eV). The TiO_2 grown on Si/SiO_2 (170 nm, 5 s) have a sharper peak with significantly lower contribution in the deep red band.

As a signature of the photo-generation of carriers and their radiative recombination, PL profiles provide specific information related to the localised electronic states associated with defects by the emission of light at sub-bang gap levels. [200]. McHale and Knorr demonstrated that the anatase TiO_2 PL spectra include the superposition of two types of radiative recombination: one of the mobile electrons from the conduction band and shallow traps (Type 1 PL), and another one from trapped electrons on defects to valence band holes (Type 2 PL) [200]:

Type 1: $e^-_{CB} + h^+_{tr} \rightarrow \nu h_{green}$

Type 2: $h^+_{VB} + e_{tr}^- \rightarrow \nu h_{red}$

Recently, Jin et al. [197] evidenced a correlation between the presence of red (600 nm) and green (515 nm) PL bands with characteristic defects of amorphous and annealed TiO_2 films grown by ALD (Figure 4-13A). The green band is claimed to be due to oxygen vacancies, while the red band indicates under-coordinated Ti^{3+} ions. These reported results agree with

some of our PL profile features, underlining point-defects and chemical doping of our thin-films.

A very important degradation rate, which is much higher than any reported in the literature for the raw TiO_2 films, is achieved under UV light on RT synthesised TiO_2 films. Therefore, these films are preferably chosen to evaluate, in a first phase, the fabrication of photocatalytic devices (TiO_2 thin film decorated with a well-organised assembly of plasmonic nanoparticles) to enhance the photocatalytic degradation under UV light by promoting the charge trapping and increasing their lifetime and also by tentatively shifting the light absorption into the visible range.

4.3 TiO_2 films assembly with gold nanoparticles

The assembly of the TiO_2 films with well-organised gold nanoparticles is carried out using the nanoparticles self-assembly method described in Sections 2.2.1 and 3.1.2.

The nanoparticles are deposited on the efficient TiO_2 mesoporous thin films that lead to the best photocatalytic efficiency in the UV range (Figure 4-6A). A film grown at RT with 965 cycles – 90 nm - on Si/SiO_2 (with 30 s purge). The thin film is patterned with 8 nm gold nanoparticles using two process-flow. The deposition of gold nanoparticles is performed on TiO_2 film that is already annealed (process flow 1) or on amorphous TiO_2 film (process flow 2). In the latter case, gold nanoparticles undergo the final recrystallization annealing process at 600°C.

The SEM images of the fabricated samples show a significant disorganisation of the formed nanoparticles, in both cases. This does not correspond to the previous optimisation tests with the results shown in Figure 4-9. The random organization of gold nanoparticles is still under investigation but it may be due to the higher nanoparticles annealing temperature (600°C) compare to 500°C that was used for the process development. The increased annealing temperature is required to mimic the thermal budget of process flow (1). Such a high temperature may lead to the partial surface melting of the gold nanoparticles [201] and thus their reorganisation.

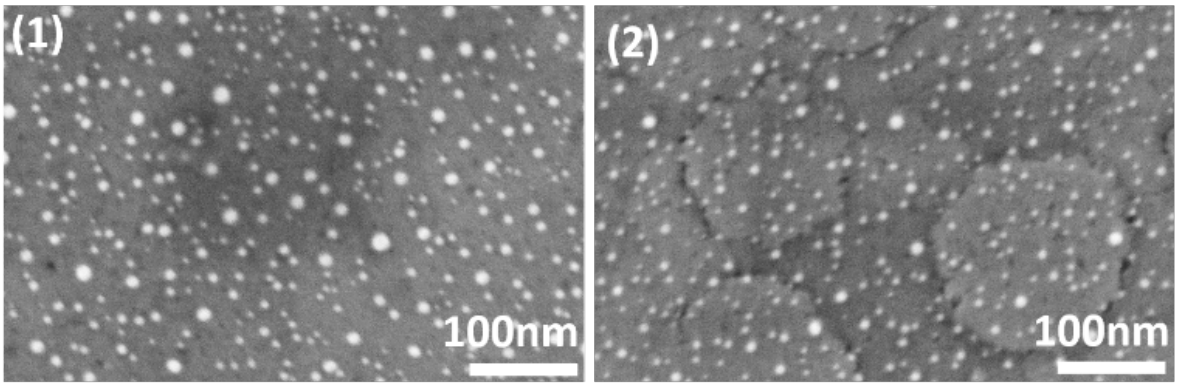

Figure 4-9 SEM images of annealed Au nanoparticles deposited on already annealed TiO_2 (1) and on amorphous TiO_2 (2).

The photocatalytic degradation of the MB solution on these samples is first carried out in the UV range (Figure 4-10-a). The photocatalytic degradation plot does not evidence a significant overall improvement in the photocatalytic activity due to the coupling of metallic nanoparticles on the TiO_2 surface. However, we observe an improvement in the photocatalytic efficiency for the sample (2) during the first 100 min. For this sample, the amorphous TiO_2 films are assembled with the nanoparticles and then annealed. Such an assembly could improve the TiO_2/Au interface for trapping the photo-generated carriers in TiO_2. The metallic nanoparticles tend to efficiently increase the electrons lifetime. However, after 100 min the photocatalytic degradation rate is decreased. We may envisage that the surface of the gold nanoparticles is saturated or passivated by the degradation by-products of the photocatalytic reaction. The degradation rate becomes almost similar to the one measured for sample (1) where the nanoparticles seem to be inactive. Moreover, the sample (1) demonstrates a lower degradation rate than the reference TiO_2 film without nanoparticles, probably due to the specific surface area of TiO_2 being reduced by the nanoparticles.

This inefficiency may be attributed to several features: non-metallic contact due to the non-metallic gold phase or carbon contamination at the interface between TiO_2 films and nanoparticles. The latter hypothesis may be supported by the TEM characterisation of the micelle films presented in Section 3.1.1. Indeed, we showed that the BCP micelle monolayer forms a ~5 nm residual layer of partially dissolved polystyrene chains. Usually, the activation mechanism of wide bandgap semiconductor materials by plasmonic nanoparticles in the visible range assumes that a Schottky barrier that enables the direct electron injection into the conduction band of the semiconductor. Because the Schottky barrier requires an ideal metal-semiconductor interface, we may question the parasitic carbon contamination of the surface when the BCP self-assembly approach for the plasmonic nanoparticle fabrication is used.

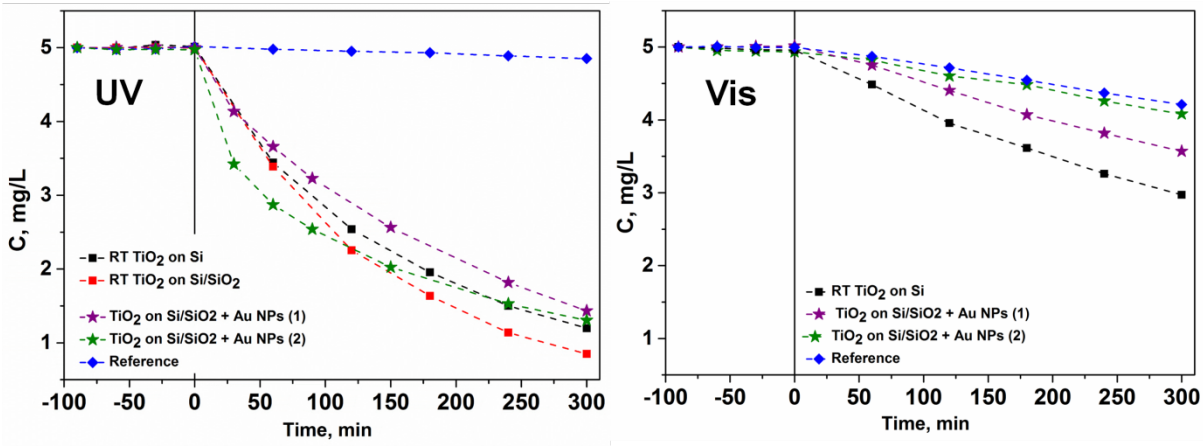

Figure 4-10 Photocatalytic degradation plots on RT TiO_2 films with and without assembled gold nanoparticles.

Photocatalytic tests in the visible range are performed after the UV tests. Surprisingly, the devices based on gold nanoparticles deposited on the annealed TiO_2 film degrade the photocatalytic performance of mesoporous TiO_2 thin films in the visible range, regardless of the integration process-flow of the gold nanoparticles. Even more surprisingly, a significant photocatalytic degradation of MB in the visible range is observed for bare TiO_2 and relies on the intrinsic properties of the mesoporous TiO_2 thin films, without the use of plasmonic nanoparticles.

The degradation constants and the degradation constants normalised by the sample surface area are summarised in Table 4-3.

The measurements under visible light irradiation underline the astonishing intrinsic properties of the mesoporous TiO_2 thin films grown at RT via ALD and then annealed. Such behaviour has been found for the first time, to our knowledge, and our investigations are thus focused on this thin film.

Table 4-3 Photocatalytic degradation constants k_r RT TiO_2 films with and without assembled gold nanoparticles.

	UV (365 nm)		**Visible (400-700 nm)**	
Sample	**Photocatalytic degradation constant, $k_r x10^{-3}$ min^{-1}**	**Photocatalytic degradation constant normalised by surface unit k_r $x10^{-4}$ $min^{-1}cm^{-2}$**	**Photocatalytic degradation constant, k_r $x10^{-3}$ min^{-1}**	**Photocatalytic degradation constant normalised by surface unit k_r $x10^{-4}$ $min^{-1}cm^{-2}$**
RT TiO_2 on Si	4.7	15.7	1.72	5.7
RT TiO_2 on Si/SiO_2	5.9	21.4	-	-
RT TiO_2 on Si/SiO_2+Au NPs (1)	4.04	14.7	1.16	4.2
RT TiO_2 on Si/SiO2+Au NPs (2)	4.04	15.9	0.64	2.5
BM	0.09	-	0.58	-

4.4 Visible light degradation on the TiO_2 films

The photocatalytic activity of the room temperature-deposited TiO_2 films with various thickness and grown with both purge time is tested under the visible range irradiation. The obtained degradation curves, presented on the Figure 4-11 confirm the activity of the films in the visible range whatever the used growth process, substrate and thickness.

Similar to the degradation results obtained in the UV range, the best performing mesoporous thin film is grown on thermally oxidised Si substrates. As previously noted for the results in the UV range, the photocatalytic degradation is enhanced with the film thickness, with a degradation rate constant reaching $57.6 \cdot 10^{-4}$ for the 170 nm thick film grown with 5 s purge time. In the visible range, the photocatalytic degradation constant normalised by the sample surface area versus film thickness is higher in the case of films deposited on Si with a 30 s purge time (Figure 4-11). For the short purge time (5 s), thin films lower than 30 nm are not active in the visible range when grown on the Si substrate. Only thicker film (170 nm) shows a degradation when the 5 s purge time process is used to elaborate the mesoporous TiO_2. However, the deposition of a thick film of 170 nm on the oxidised substrate (Si/SiO_2) with 5 s purge time shows the maximum photocatalytic degradation values at $8.0 \cdot 10^{-4}$ $min^{-1}cm^{-2}$.

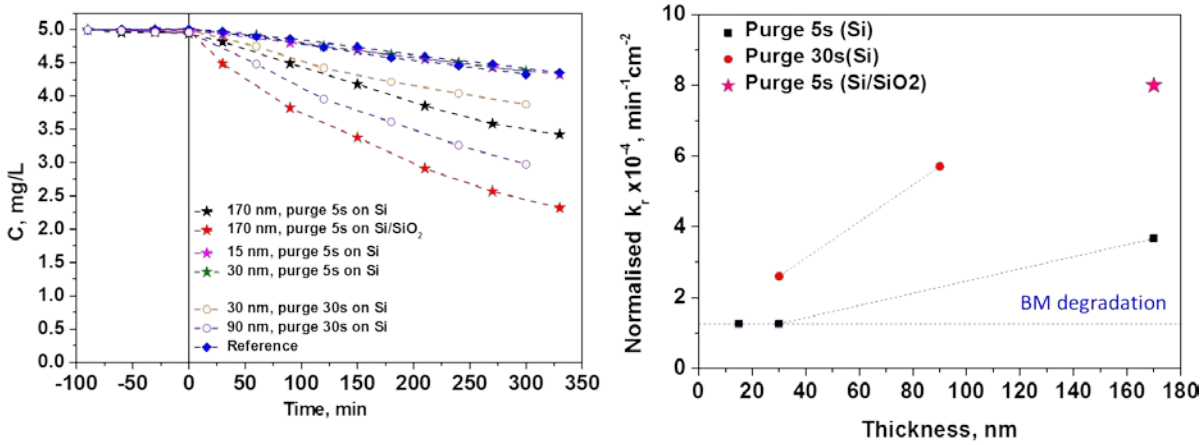

Figure 4-11 Photocatalytic degradation of MB solution on the RT deposited TiO_2 films under visible light (left), Photocatalytic degradation constant normalised by the sample surface area as the function of the film thickness for both purge time regimes (5 s, 30 s) (right).

The interplay between physical and chemical properties of room temperature ALD TiO_2 films and their photocatalytic performance in both UV and visible ranges is discussed hereafter.

The use of the RT process condition significantly modifies the TiO_2 thin film chemistry and morphology. First of all, an amorphous thin-film of Ti_xO_y is grown and traps unreacted precursors, reaction by-products, and complex $Ti\text{-}O_x\text{-}H_y\text{-}Cl_z$ chemistries typically characterised as-grown thin films.

The post-deposition annealing of the amorphous films enables the thermal oxidation of the film under ambient air conditions, promotes degassing of the chlorine compounds and leads to a mesoporous hydrogenated-Ti_xO_y thin film. The degassing of a chlorine compound (typically HCl or Cl_2) may induce oxygen vacancies in the film volume and Ti^{3+}. The chemical characterisation of the films before and after annealing by the XPS analysis (Section 3.3.1) does not show any change in the Ti 2p spectra. O 1s peak is systematically shifted towards high binding energy (+0.3 eV) when amorphous films are annealed (Figure 4-12A). O 1s shoulder at 532 eV is attributed to the hydroxylation of TiO_2 (Ti-OH) [186] [202] [203].

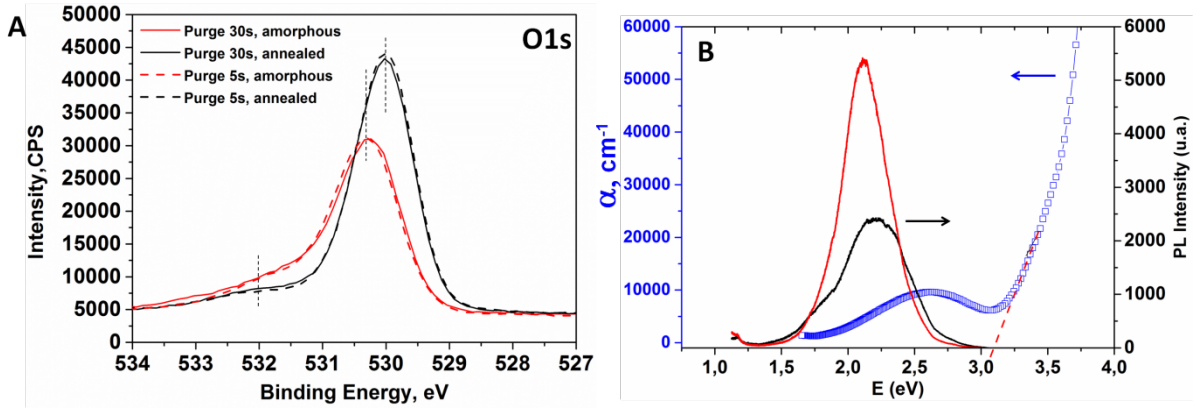

Figure 4-12 (A) XPS O 1s spectra of amorphous and annealed TiO_2 RT, (B) Comparison plot of the absorption coefficient(left axis) and PL spectra (right axis): TiO_2 RT 170 nm deposited on Si/SiO_2 (red curve) on Si (black curve).

Similar results were reported by Chen and co-workers for highly hydrogenated black TiO_2 [186] and by Wang and co-workers on hydrogen-treated rutile nanowires [203]. Chen et al. noted two O 1s peak contributions at 530 to 530.9 eV without Ti 2p spectral modification, and Wang et al. report these peak positions at 530.4 and 532 eV, respectively. The authors postulated that hydroxylation of TiO_2 by hydrogen treatment induces a significant disorder of the crystalline structure i.e. oxygen vacancies, hydroxylation of the dangling bonds and Ti-OH [186]. These structural defects may have a significant impact on the electronic properties via inter bang gap energetic levels. The theoretical predictions realised by Chen et al. predicts that disordered hydrogenated-TiO_2 crystals induce mid-gap electronic states at 1.8 eV and high-energy states at 3 eV, leading to a band gap narrowing.

In our case, PL profiles (Figure 4-8, Figure 4-12,) evidence defects contributing to the radiative recombination of carriers at ~500-525 nm (2.48-2.36 eV), ~585 nm (2.11 eV) and ~700 nm (1.77 eV). Therefore, we propose inter band gap recombination states at 0.72-0.84 eV corresponding to oxygen vacancies in agreement with Wang at al. [203] 1.09 eV which may either be allocated to oxygen vacancies [203] or Ti^{3+} states [197] and 1.43 eV below the conduction band may be attributed to the H-TiO_2 mid-gap states (Figure 4-13B).

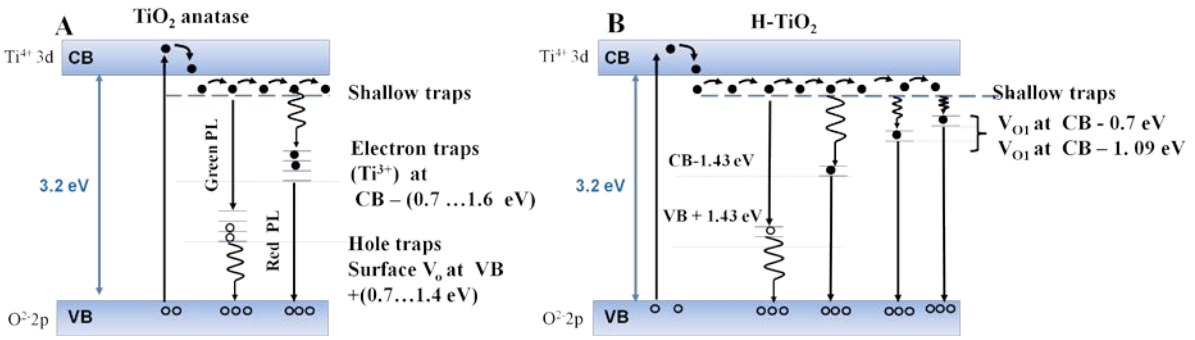

Figure 4-13 Models for photoluminescence from electronic reansition of trop states (A) for anatase [197] and (B) for hydrogenetaed TiO_2 [203].

The RT TiO_2 samples (965 cycles, 5s) deposited on quartz substrates are characterized by UV-Vis spectroscopy (Figure 4-12). The optical band gap remains close to usual TiO_2 values (~3.1 eV) however an additional absorption band is noted between 2 and 3 eV (413-620 nm). This corresponds to the light absorption in the visible range. PL peaks are also reported for comparison and evidences a lower radiative energy of excitons than the peak energy of the visible absorption. The atypical stoichiometry and morphology of RT thin-films induces multiple energy levels within the TiO_2 band gap. At this stage, complementary experiments such time-resolved photoluminescence, absorption and luminescence vs. temperature shall be conducted to provide further insights regarding the energy levels of our “anomalous” TiO_2.

From these first results, we suggest that RT thin-films feature specific oxygen vacancies and Ti-OH coordination. RT ALD process leads to HCl or Ti-O_x-H_y-Cl_z in amorphous films. During annealing, the HCl degasing shall promote oxygen vacancies and Ti^{3+} while its thermals decomposition at 600°C into Cl_2 and H_2 leads to "in-situ" hydrogen treatment of TiO_2 occurs. Hydrogenation process has been shown recently to modify significantly the opto-electronic properties of TiO_2 due to a significant concentration of Ti-OH inducing disordered crystalline arrangement. Such features are shown to modify considerably the photocatalytic responses [181], [187]. In our case, we figure out that the astonishing photocatalytic efficiency is also correlated to the immense specific area (Figure 4-14) and the "in-situ" hydrogenation of TiO_2.

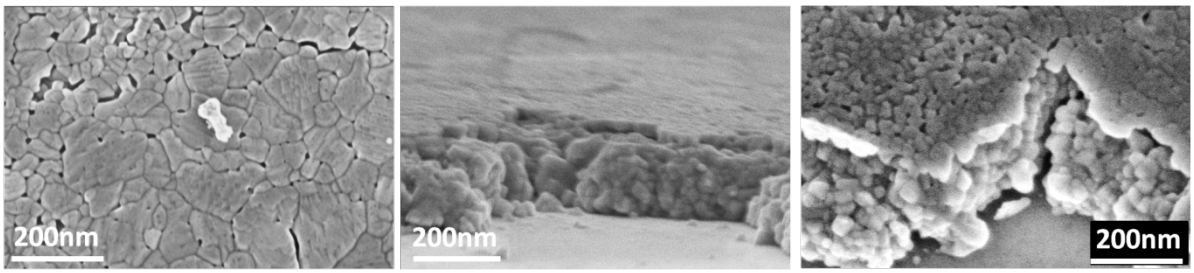

Figure 4-14 SEM images of RT TiO_2 film deposited after 965 cycles in short purge time regime; top-view and tilted image.

The samples having a very high surface area, the lack of simple adsorption of MB (i.e., without any degradation) within the sample should be checked. To this end the photocatalytic degradation is repeated 4 times on the same sample. Moreover, for one of the runs, the sample is held overnight in the MB solution. In that case, the change in the MB concentration is almost insignificant. The photocatalytic degradation rate is unchanged even after 4 runs, highlighting the very high stability and efficacy of our samples that show unchanged photocatalytic performance over time. After four hours, the MB is fully degraded, regardless of the number of experiments performed with the same sample. This remarkable photocatalytic efficiency competes with the very best material solution provided today (Figure 4-15).

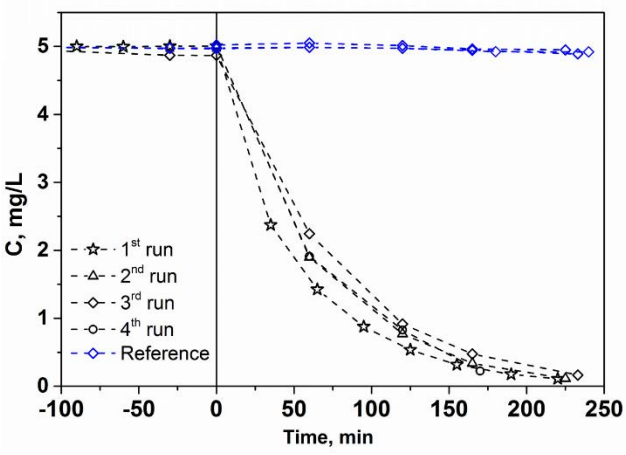

Figure 4-15 Repeatability of the MB photocatalytic degradation in UV range repeated 4 times.

The MB affinity to the TiO_2 surface facilitates its degradation [204]. An efficient photocatalytic system shall degrade multiple molecule chemistries. Therefore, our mesoporous TiO_2 is also exposed to other target molecules such as rhodamine B (RhB) and salicylic acid (SA) at the same time as MB. The photocatalytic tests are performed using MB, RhB, and SA solutions with an equivalent concentration of 5 mg/L under UV and visible irradiation (Figure 4-16). The molar concentration for MB, RhB, and SA corresponds to 15, 10 and 36 µmol/L, respectively. The degradation rate in the UV range is almost identical for the three target molecules. In our case, the photocatalytic degradation under UV light is not dependent on the molecular affinity towards our photocatalyst surface. This feature is of very high interest for depolluting water typically characterised by a mixture of pollutant molecules having significantly different chemical features such as steric volume, polarity, and chemical termination. For instance, when considering emerging photocatalysts such as the Bi_2WO_6 nanosheet with a positively charged surface, the MB and RhB were found to have higher adsorption, while neutrally-charged molecule like SA are hardly adsorbed (and thus degraded) on such a surface [205]. In our case, a slight increase in the degradation constant on SA is measured when compared to the two other molecules.

When visible light irradiation is used, the degradation rate for the same tested pollutants is different. The degradation constant of MB is the highest, but the “natural” degradation of MB under visible light must be considered, as evidenced by the significant photodegradation of the reference solution. The SA and RhB molecules are highly stable under visible light, as proven by the concentration plateau of the reference solution. The photocatalytic degradation under visible light is even more efficient for neutral molecules such as SA compared to BM and RhB, showing that our mesoporous TiO_2 material is particularly efficient. The

photocatalytic degradation rate for different molecules was formerly explained by better adsorption due to the charge difference between the surface and the molecule. However, our results in the UV range contradict this assumption, showing an identical degradation rate for all molecules. The lower activity in the visible range may be due to the lower carrier density and thus lower radical concentration. Therefore, in the visible range, the degradation occurs according to the stability of the molecules.

For better insights into the different degradation mechanisms of the target molecules, a chromatographic control of the degradation by-product must be further achieved.

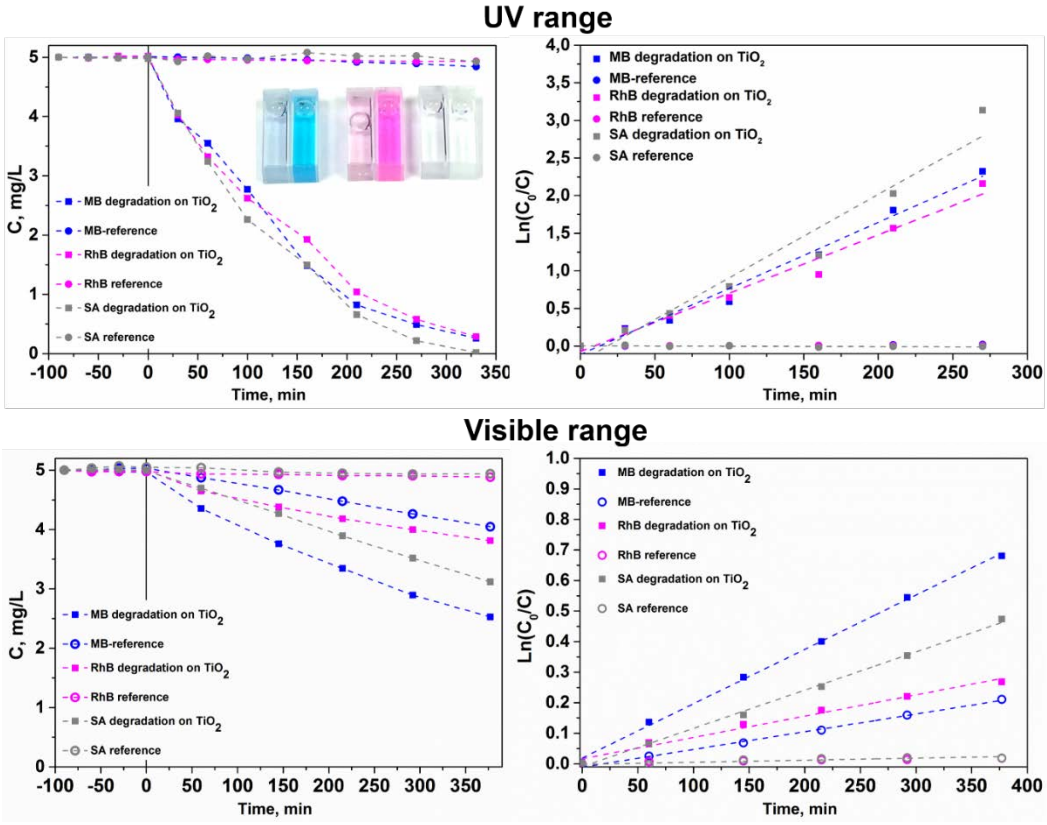

Figure 4-16 Photocatalytic degradation of MB, RhB and SA on RT TiO_2 films in the UV and visible ranges.

Table 4-4 Photocatalytic degradation constants on RT TiO_2 normalised by the sample surface area, ($min^{-1}cm^{-2}$), and photolysis constants of the reference solutions.

	k_r, normalised by the sample surface area, $min^{-1}cm^{-2}$			
	UV range		**Visible range**	
Target molecule	**On TiO_2**	**Reference**	**On TiO_2**	**Reference**
BM	$3.8 \cdot 10^{-3}$	$9 \cdot 10^{-5}$	$1.7 \cdot 10^{-3}$	$5.8 \cdot 10^{-4}$
RhB	$3.1 \cdot 10^{-3}$	$4 \cdot 10^{-5}$	$0.6 \cdot 10^{-3}$	$4.3 \cdot 10^{-5}$
SA	$5.0 \cdot 10^{-3}$	$4 \cdot 10^{-5}$	$1.2 \cdot 10^{-3}$	$5.0 \cdot 10^{-5}$

4.5 Photocatalytic degradation on periodic TiO_2 nanowires

The periodically-organised TiO_2 nanowires are fabricated using the AAO template approach, as previously discussed in Sections 2.2.2 and 3.3.2. Three different temperature-dependent ALD process for TiO_2 growth (RT, 100 and 200°C) are used. The fabrication of nanowires using the RT TiO_2 deposition is not successful due to the porous structure of the grown film. Therefore, the nanowires are only formed at 100 and 200°C. The post-deposition annealing is then applied. The crystalline phases of the annealed nanowires are controlled by XRD and evidences the expected anatase phase only.

The photocatalytic degradation test in the UV range is performed on TiO_2 nanowires. The degradation rates of nanowires architecture is very close to the one measured for planar films (Figure 4-17) in spite of the increased specific area for nanowires (×3 specific area of planar films). The overall TiO_2 volumes of films and nanowires are equivalent. The architectural engineering of TiO_2 thin-films into nanowires does not bring any improvement in photocatalytic performance. The reduction of the material dimensions towards nanowires architecture is likely to increase the presence of microstructured defects, especially in the polycrystalline structures. Therefore, the lower "normalised" photocatalytic activity of nanowires is attributed to the short lifetime of photogenerated carriers, due to Shockley-Read-Hall recombination (trap-assisted recombination). Such kind of recombination processes is known to be promoted in objects with a predominant surface to volume ratio [206]. The confirmation of this hypothesis requires more detailed investigations on the microstructure level by TEM microscopy.

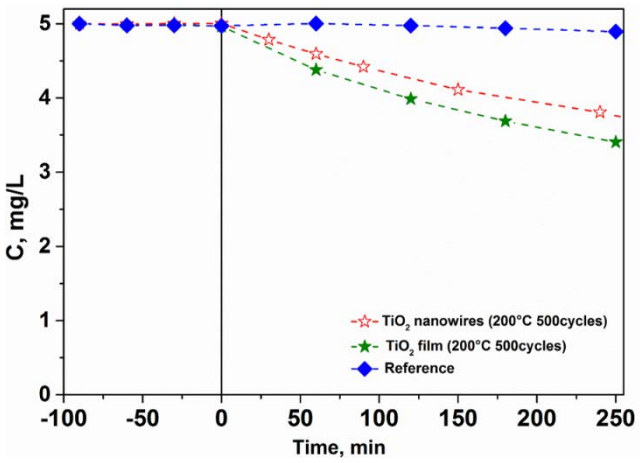

Figure 4-17 Photocatalytic degradation of MB solution on TiO_2 nanowires in the UV range.

Because nanowires based on ALD performed at 100°C or 200°C do not show any photocatylitic enhancement, an array of heterostructured nanowires based on core nanowires (grown with 200°C ALD process) coated with a conformal thin film deposition of 15 nm of RT TiO_2 are fabricated. TiO_2 nanowires grown using 200°C ALD into AAO having larger spacing, i.e. 500 nm (S500), do not show any photocatalytic activity. This array of nanowires is also conformally coated with RT 15 and 180 nm thick TiO_2 films (using 160 and 965 cycles, respectively). The RT TiO_2 coating of periodic TiO_2 nanowires demonstrates, in general, an improvement in the degradation rate with the RT film thickness (Figure 4-18 Table 5-5). Nanowires with spacing 70 and 500 nm after coating with 15 nm films show improvement of 10% of photocatalytic degradation rate. 170 nm thick film on periodic nanowires S500 demonstrates 37% improvement. However, these performances are far from the photocatalytic efficiency of planar films deposited on Si substrate. The nanostructures after coatings show a higher Water Contact Angle (WCA), typically 60°, while before coating highly hydrophilic surface (WCA of 15°) is measured. The thick coating of 170 nm also demonstrates an increase in the WCA to 30°. Compared to the nanostructures, the flat films show hydrophilic behaviour with a WCA of 15-20°.

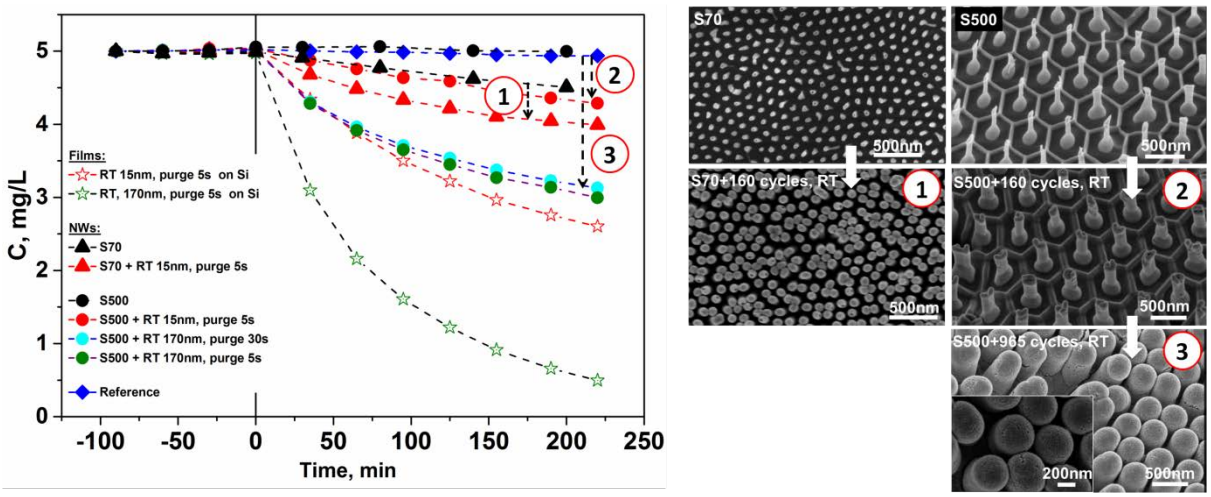

Figure 4-18 Photocatalytic degradation of MB solution on TiO_2 nanowires coated with 160 and 965 cycles of RT TiO_2 compare to the films deposited on silicon substrates (UV range).

Table 4-5 Photocatalytic degradation rate on TiO_2 nanowies as fabricated and coated with RT TiO_2.

Nanowires	**Degradation after 200 min, %**		
	As fabricated	**+ 15 nm**	**+ 170 nm**
S70	10	20	
S500	0.4	13	37
Film on Si		46	88

4.6 Degradation on TiO_2/SnO_2 nanowires

The periodically-organised TiO_2/SnO_2 heterostructures are also fabricated according to the description given in the Sections 2.2.2 and 3.3.3. The periodic heterostructures are fabricated with the following geometry: diameter 180 nm, length 600 nm and 125 nm of spacing between nanowires. The fabrication procedure already includes the annealing step of amorphous TiO_2, while the SnO_2 deposition realised at high temperature enables a direct formation of the cassiterite phase. The photocatalytic tests do not evidence any improvement in the degradation rate in that case. However, an attempt to improve the photocatalytic activity of the heterostructures is performed by annealing TiO_2 at 600°C in ambient air for 2 h. A slight improvement is observed, however, the degradation constant is still low. The degradation rate of the TiO_2/SnO_2 heterostructures is presented in Figure 4-19.

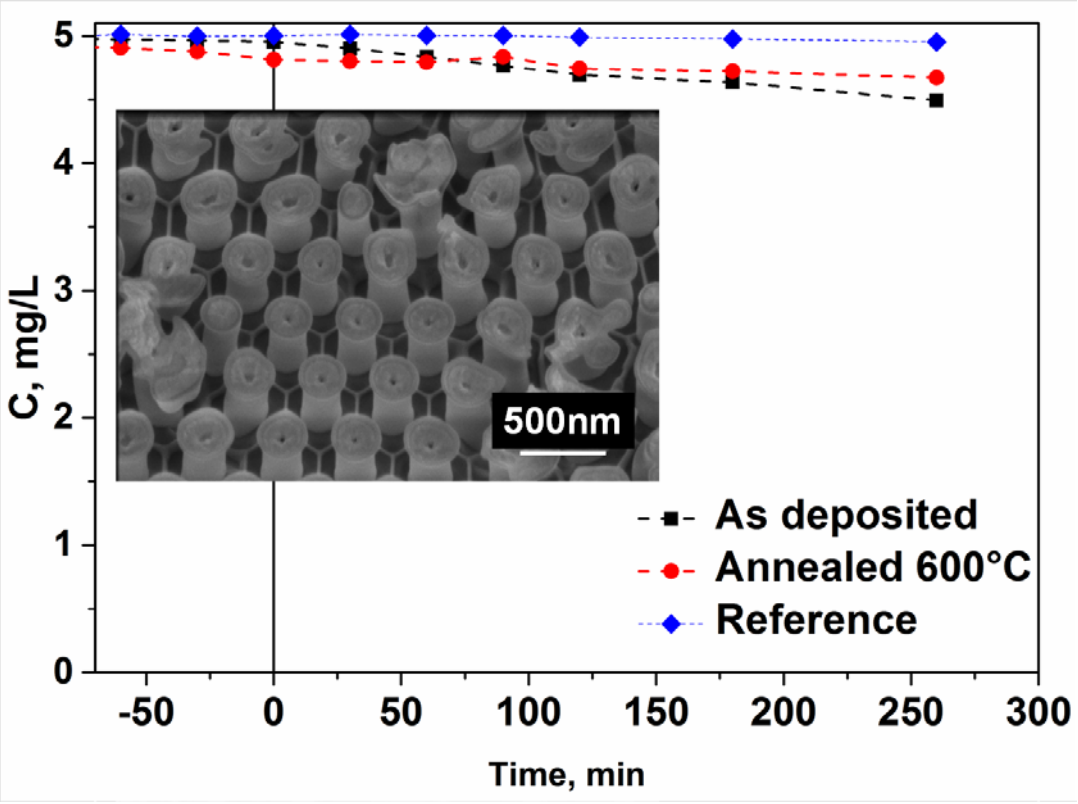

Figure 4-19 Photocatalytic degradation of MB solution on TiO_2/SnO_2 heterostructured nanowires.

Essentially, we find that the nanostructurisation with large pillars (200 nm in diameter) shows a significant hydrophobic behaviour, as measured by a water contact angle of 110°. Therefore, the insufficient wettability of our devices impairs the gain of any functional photocatalytic improvement, owing to this band gap engineering aimed at increasing the photogenerated carrier lifetime significantly.

Therefore, further investigations with smaller nanowires diameters and with optimized surface functionalization should be foreseen. In parallel, photocatalytic tests in the gas phase shall be envisaged to evaluate the functional properties of the heterostructures SnO_2/TiO_2 nanowires.

4.7 Summary

The photocatalytic degradation performances of the TiO_2-based photocatalytic devices are investigated using pollutant models such as methylene blue, rhodamine B and salicylic acid. The photocatalyst degradation efficiency of TiO_2 films deposited by MOCVD considerably depends on the films morphology and structural defects. The granular and continuous film is more efficient than narrow nano-columnar films. That is likely due to the carriers diffusion in larger grains while nanocolumns may enhance the recombination of carriers. Moreover at low temperature oxygen vacancies are evidenced by PL spectra and increase the photocatalytic activity.

The ALD TiO_2 film features, originally developed for the fabrication of TiO_2 nanowires via the AAO templated approach, are mostly dependent on the temperature and the purge time during the deposition. The deposition at room temperature leads to thin-films with the highest photocatalytic activity. The photocatalysis based on RT TiO_2 films is also intrinsically active under the visible range.

The plausible reasons may combine the presence of structural defects as oxygen vacancies (Ti^{3+}) and TiOH in the film volume. These defects are known to extend the photo-response of the TiO_2 from the UV to the visible range. However, further detailed investigations on these films are required to confirm this hypothesis.

In contrast to the RT TiO_2 films, their assembly with plasmonic gold nanoparticles show an improvement in the photocatalytic activity in the UV range for samples assembled with gold nanoparticles in amorphous state and then annealed together. That is likely due to the better metal/semiconductor contact. However this improvement is significantly reduced after 100 min of experiments indicative of nanoparticles saturation or passivation by the organic degradation products.

The development of the free-standing TiO_2 nanowires is a technological challenge that has been achieved in this thesis. However, because this development is new, it requires more detailed investigation of the physicochemical properties to identify the limiting problem. The RT TiO_2 coating applied to the nanowires improves their activity in the UV range. This

improvement is proportional to the coating thickness. The photocatalytic activity of the heterostructured nanowires SnO_2/TiO_2 could not be rigorously evaluated due to the high hydrophobitiy of this architecture.

5 Conclusion and perspectives

Climate Change was recently the front page topic of the global media due to the historic United Nations Climate Change Conference (COP 21). The international agreement establishes the objective to decrease the global average temperature to that of the pre-industrial era, which means decreasing the average global temperature by 1.5 - 2°C by the end of 21st century. Therefore, developing technologies towards efficient reductions of greenhouse gas emissions could be considered to be the major challenge of this century.

Despite the fact that the objective of this thesis is water remediation by photocatalytic materials, it is indirectly related to this global challenge. The efficient photocatalyst could be applied not only to the water treatment but also to solar electricity (photovoltaic) and hydrogen production as alternative energy sources.

This thesis was conducted in the framework of the VISICAT project (FNR Luxembourg), with the fixed objective being to improve the photo-response of well-known photocatalytic materials, which are usually only active in the UV range. The basic idea of this project is to assemble several approaches within one device to improve the photocatalytic properties. The major technological challenges were the fabrication of the periodically organised TiO_2 nanostructures, which may allow for more efficient light harvesting, and the assembly with plasmonic nanoparticles, which may extend the photoresponse into the visible range.

Two fabrication strategies were selected for these purposes. The first approach consisted of the selective growth of well-organised nanowires by pre-deposited seed nanoparticles. However, this approach was not succesful, but the investigation did allow the identification of key parameters that potentially could lead to the controlled growth of nanowires. Therefore, to complete this study, the effect of the seed nanoparticles size has to be examined in detail. The photocatalytic measurement on the MOCVD generated films highlighted the influence of the films morphology. Interestingly, higher photocatalytic efficiency was measured for compact thin film compare to columnar morphology; this contradicts the assumption that the nanostructures would improve the degradation efficiency due to the higher surface area. Therefore, in the application perspectives of such structures, it is necessary to find a trade-off between the crystallites grain size, the nanostructure size and the density of potential recombination sites.

The second approach for the fabrication of periodic TiO_2 nanowires was successfully implemented using an AAO template. An accurate control over the aspect ratio of freestanding TiO_2 nanowires was attained. The development of a protocol for the fabrication of such mechanically stable nanostructures is a significant technological achievement.

However, these nanostructures did not show the expected improvement of photocatalytic performances, likely due to the carrier recombination mechanisms on structural defects. Despite that fact, the development of the TiO_2 ALD films by the template-assisted approach reveals original results. At low deposition temperature, the purge time becomes crucial in determining the physicochemical properties of thin film after the further post-deposition annealing. The deposition of the TiO_2 films at room temperature leads to unusual and highly porous film morphology.

The photocatalytic measurements achieved on TiO_2 films deposited by ALD using the MB as the pollutant model show the very higher photocatalytic activity of the room temperature deposited TiO_2 films. 170 nm thick TiO_2 films deposited on Si/SiO_2 substrate attained the degradation constant of $57 \cdot 10^{-4}$ $min^{-1}cm^{-2}$. It is very difficult to compare the degradation constant values with the literature data due to the considerable differences in experimental conditions. Nevertheless, we can compare with results previously developed in the group: the photocatalytic degradation constant of ZnO high-temperature films was reported as $21 \cdot 10^{-4}$ $min^{-1}cm^{-2}$. Tested in UV range on various pollutant models such as rhodamine B and salicylic acid, molecules are efficiently degraded with identical kinetics being independent of the molecular nature.

Moreover, these photocatalytic samples were also significantly active in the visible range. The excellent photocatalytic activity of the RT deposited films in both illumination ranges is likely due to structural defects and hydrogenation induced by the HCl medium incorporated in the amorphous films and activated by the high-temperature annealing. The initial goal, being the improvement of photocatalytic properties by the assembly of TiO_2 with self-assembled plasmonic nanoparticles into a plasmonic device, was not fully achieved. We showed that the TiO_2 films assembled with gold nanoparticles improve the degradation rate but in a non-stable way. This improvement is likely reduced by the passivation of the gold surface by the degradation product. The underlying reasons for this behaviour are not yet clear, and a detailed investigation of the degradation products and their adsorption on the gold surface should be performed.

The smooth SnO_2 films deposited by ALD on complex surfaces as a porous template were also attained using a tin halide precursor. It was found that the anatase TiO_2 buffer layer enables better precursor chemisorption that leads to a highly conformal coating of SnO_2. This is another new technological achievement that, to the best of our knowledge, has not yet been

reported in the literature. This approach enables versatile TiO_2/SnO_2 heterostructure assembly that requires further optimisation and development.

References

[1] "http://ec.europa.eu/clima." .

[2] K. Honda and A. Fujishima, "Electrochemical Photolysis of Water at a Semiconductor Electrode," *Nature*, vol. 238, 1972.

[3] M. R. Hoffmann, S. T. Martin, W. Choi, and D. W. Bahnemannt, "Environmental Applications of Semiconductor Photocatalysis," *Chem. Rev.*, vol. 95, no. 1, pp. 69–96, 1995.

[4] A. N. Banerjee, "The design , fabrication , and photocatalytic utility of nanostructured semiconductors : focus on TiO 2 -based nanostructures," *Nanotechnol. Sci. Appl.*, vol. 4, pp. 35–65, 2011.

[5] M. L. Brongersma, Y. Cui, and S. Fan, "Light management for photovoltaics using high-index nanostructures," *Nat. Mater.*, vol. 13, no. 5, pp. 451–460, 2014.

[6] L. Cao, P. Fan, A. P. Vasudev, J. S. White, Z. Yu, W. Cai, J. a Schuller, S. Fan, and M. L. Brongersma, "Semiconductor nanowire optical antenna solar absorbers.," *Nano Lett.*, vol. 10, no. 2, pp. 439–445, 2010.

[7] K. Seo, M. Wober, P. Steinvurzel, E. Schonbrun, Y. Dan, T. Ellenbogen, and K. B. Crozier, "Multicolored vertical silicon nanowires," *Nano Lett.*, vol. 11, no. 4, pp. 1851–1856, 2011.

[8] M. Castellote and N. Bengtsson, "Applications of Titanium Dioxide Photocatalysis to Construction Materials," in *Application of Titanium Dioxide Photocatalysis to Construction Materials*, no. 1, Y. Ohama and D. Van Gemert, Eds. Springer Science+Business Media, 2011, pp. 1–5.

[9] M. J. Berr, P. Wagner, S. Fischbach, A. Vaneski, J. Schneider, A. S. Susha, A. L. Rogach, F. Jäckel, and J. Feldmann, "Hole scavenger redox potentials determine quantum efficiency and stability of Pt-decorated CdS nanorods for photocatalytic hydrogen generation," *Appl. Phys. Lett.*, vol. 100, no. 22, pp. 2014–2017, 2012.

[10] L. Zhou, H. Zhang, H. Sun, S. Liu, M. O. Tade, S. Wang, and W. Jin, "Recent advances in non-metal modification of graphitic carbon nitride for photocatalysis: A historic review," *Catal. Sci. Technol.*, 2016.

[11] K. Eufinger, D. Poelman, H. Poelman, R. De Gryse, and M. G.B., *TiO2 thin films for photocatalytic applications*, vol. 661, no. 2. 2008.

[12] G. R. Buettner, "The Pecking Order of Free Radicals and Antioxidants: Lipid Peroxidation, a-Tocopherol, and Ascorbate," *Archives of biochemistry and biophysics*, vol. 300, no. 2. pp. 535–543, 1993.

[13] A. Houas, H. Lachheb, M. Ksibi, E. Elaloui, C. Guillard, and J.-M. Herrmann, "Photocatalytic degradation pathway of methylene blue in water," *Appl. Catal. B Environ.*, vol. 31, no. 2, pp. 145–157, 2001.

[14] M. Batzill and U. Diebold, "The surface and materials science of tin oxide," *Prog. Surf. Sci.*, vol. 79, pp. 47–154, 2005.

[15] J. Schneider, M. Matsuoka, M. Takeuchi, J. Zhang, Y. Horiuchi, M. Anpo, and D. W. Bahnemann, "Understanding TiO 2 Photocatalysis : Mechanisms and Materials," *Chem. Rev.*, vol. 114, pp. 9919–9986, 2014.

[16] U. Diebold, "The surface science of titanium dioxide," *Surface Science Reports*, vol. 48, no. 5–8. pp. 53–229, 2003.

[17] H. Tang, "Electronic properties of anatase TiO2 investigated ba electrical and optical measurements on single crystals and thin films," Ecole Polytechnique fédérale de Lausanne, 1994.

[18] S. Springer, "Free Carriers in Nanocrystalline Titanium Dioxide Thin Films," 2004.

[19] R. Asahi, Y. Taga, W. Mannstadt, and A. J. Freeman, "Electronic and optical properties of anatase TiO2," vol. 61, no. 11, pp. 7459–7465, 2000.

[20] A. Iacomino, G. Cantele, D. Ninno, I. Marri, and S. Ossicini, "Structural, electronic, and surface properties of anatase TiO2 nanocrystals from first principles," *Phys. Rev. B*, vol. 78, no. 7, p. 075405, Aug. 2008.

[21] K. M. Reddy, S. V Manorama, and A. R. Reddy, "Bandgap studies on anatase titanium dioxide nanoparticles," vol. 78, pp. 239–245, 2002.

[22] T. Luttrell, S. Halpegamage, J. Tao, A. Kramer, E. Sutter, and M. Batzill, "Why is anatase a better photocatalyst than rutile?--Model studies on epitaxial TiO2 films.," *Sci. Rep.*, vol. 4, p. 4043, 2014.

[23] J. Zhang, P. Zhou, J. Liu, and J. Yu, “New understanding of the difference of photocatalytic activity among anatase, rutile and brookite TiO2,” *Phys. Chem. Chem. Phys.*, vol. 16, no. 38, pp. 20382–20386, 2014.

[24] A. Di Paola, M. Bellardita, and L. Palmisano, “Brookite, the Least Known TiO2 Photocatalyst,” *Catalysts*, vol. 3, no. 1, pp. 36–73, Jan. 2013.

[25] M. Lazzeri, A. Vittadini, and A. Selloni, “Structure and energetics of stoichiometric TiO2 anatase surfaces,” *Phys. Rev. B*, vol. 63, p. 155409, 2001.

[26] W.-J. Ong, L.-L. Tan, S.-P. Chai, S.-T. Yong, and A. R. Mohamed, “Highly reactive {001} facets of TiO2-based composites: synthesis, formation mechanism and characterization.,” *Nanoscale*, vol. 6, no. 4, pp. 1946–2008, Feb. 2014.

[27] S. Yamamoto, T. Sumita, and A. Miyashita, “Preparation of TiO 2 -anatase film on Si (001) substrate with TiN and SrTiO 3 as buffer layers,” *At. Energy*, vol. 13, pp. 2875–2881, 2001.

[28] X. Du, Y. Du, and S. M. George, “CO gas sensing by ultrathin tin oxide films grown by atomic layer deposition using transmission FTIR spectroscopy.,” *J. Phys. Chem. A*, vol. 112, no. 39, pp. 9211–9219, 2008.

[29] D. Choi and J.-S. Park, “Highly conductive SnO2 thin films deposited by atomic layer deposition using tetrakis-dimethyl-amine-tin precursor and ozone reactant,” *Surf. Coatings Technol.*, vol. 259, pp. 238–243, Nov. 2014.

[30] B. Liu and E. S. Aydil, “Growth of oriented single-crystalline rutile TiO(2) nanorods on transparent conducting substrates for dye-sensitized solar cells.,” *J. Am. Chem. Soc.*, vol. 131, no. 11, pp. 3985–90, Mar. 2009.

[31] Z. Nabi, A. Kellou, S. Méçabih, A. Khalfi, and N. Benosman, “Opto-electronic properties of rutile SnO2 and orthorhombic SnS and SnSe compounds,” *Mater. Sci. Eng. B Solid-State Mater. Adv. Technol.*, vol. 98, no. 2, pp. 104–115, 2003.

[32] J. Pan, H. Shen, L. Xiao, P. Born, and W. Mader, “SnO2 - TiO2 Core-Shell Nanowire Structures : Investigations on Solid State Reactivity and Photocatalytic Behavior,” pp. 17265–17269, 2011.

[33] C. Jin, H. Kim, K. Baek, H. W. Kim, and C. Lee, “Preparation, structure, and photoluminescence properties of Ga_2O_3/SnO_2 coaxial nanowires,” *Cryst. Res. Technol.*, vol. 45, no. 2, pp. 199–203, 2010.

[34] S. Kim, D.-H. Kim, and S.-H. Hong, “Epitaxial growth of orthorhombic SnO2 films on various YSZ substrates by plasma enhanced atomic layer deposition,” *J. Cryst. Growth*, vol. 348, no. 1, pp. 15–19, 2012.

[35] W.-S. Choi, “The Fabrication of Tin Oxide Films by Atomic Layer Deposition using Tetrakis(Ethylmethylamino) Tin Precursor,” *Trans. Electr. Electron. Mater.*, vol. 10, no. 6, pp. 200–202, Dec. 2009.

[36] H. Sefardjella, B. Boudjema, a. Kabir, and G. Schmerber, “Characterization of SnO2 obtained from the thermal oxidation of vacuum evaporated Sn thin films,” *J. Phys. Chem. Solids*, vol. 74, no. 12, pp. 1686–1689, 2013.

[37] A. Zaleska, “Doped-TiO2: A Review,” *Recent Patents Eng.*, vol. 2, no. 3, pp. 157–164, 2008.

[38] C. W. Dunnill and I. P. Parkin, “Nitrogen-doped TiO2 thin films: photocatalytic applications for healthcare environments.,” *Dalton Trans.*, vol. 40, no. 8, pp. 1635–1640, 2011.

[39] M. V. Dozzi and E. Selli, “Doping TiO2 with p-block elements: Effects on photocatalytic activity,” *J. Photochem. Photobiol. C Photochem. Rev.*, vol. 14, no. 1, pp. 13–28, 2013.

[40] C. Di Valentin, G. Pacchioni, A. Selloni, S. Livraghi, and E. Giamello, “Characterization of paramagnetic species in N-doped TiO 2 powders by EPR spectroscopy and DFT calculations,” *J. Phys. Chem. B*, vol. 109, no. 23, pp. 11414–11419, 2005.

[41] P. Carmichael, D. Hazafy, D. S. Bhachu, A. Mills, J. a Darr, and I. P. Parkin, “Atmospheric pressure chemical vapour deposition of boron doped titanium dioxide for photocatalytic water reduction and oxidation.,” *Phys. Chem. Chem. Phys.*, vol. 15, no. 39, pp. 16788–16794, 2013.

[42] W. Fang, M. Xing, and J. Zhang, “A new approach to prepare Ti3+ self-doped TiO2 via NaBH4 reduction and hydrochloric acid treatment,” *Appl. Catal. B Environ.*, vol. 160–161, no. 1, pp. 240–246, 2014.

[43] X. Liu, H. Xu, L. R. Grabstanowicz, S. Gao, Z. Lou, W. Wang, B. Huang, Y. Dai, and T. Xu, “Ti3+ self-doped TiO2-x anatase nanoparticles via oxidation of TiH2 in H2O2,” *Catal. Today*, vol. 225, pp. 80–89, 2014.

[44] F. Zuo, L. Wang, and P. Feng, “Self-doped Ti3+@TiO2 visible light photocatalyst: Influence of synthetic parameters on the H2 production activity,” *Int. J. Hydrogen Energy*, vol. 39, no. 2, pp. 711–717, 2014.

[45] J. Cai, Z. Huang, K. Lv, J. Sun, and K. Deng, “Ti powder-assisted synthesis of Ti3+ self-doped TiO2 nanosheets with enhanced visible-light photoactivity,” *RSC Adv.*, vol. 4, no. 38, p. 19588, 2014.

[46] R. Ren, Z. Wen, S. Cui, Y. Hou, X. Guo, and J. Chen, “Controllable Synthesis and Tunable Photocatalytic Properties of Ti3+-doped TiO2,” *Sci. Rep.*, vol. 5, no. April, p. 10714, 2015.

[47] A. Sasinska, T. Singh, S. Wang, S. Mathur, and R. Kraehnert, “Enhanced photocatalytic performance in atomic layer deposition grown TiO2 thin films via hydrogen plasma treatment,” *J. Vac. Sci. Technol. A Vacuum, Surfaces, Film.*, vol. 33, no. 1, p. 01A152, 2015.

[48] V. Rogé, “Etude, Fabrication et Caractérisation de nanostructures catalytiques de type ZnO/SnO2 intégrées à des membranes modèles pour la dépollution de l’eau,” Strasbourg University, 2015.

[49] V. Roge, A. Georgantzopoulou, K. Mehennaoui, I. Fechete, F. Garin, A. Dinia, A. C. Gutleb, and D. Lenoble, “Tailoring the optical properties of ZnO nano-layers and their e ff ect on in vitro biocompatibility,” *RSC Adv.*, vol. 5, pp. 97635–97647, 2015.

[50] C. Wang, X. Wang, B. Q. Xu, J. Zhao, B. Mai, P. Peng, G. Sheng, and J. Fu, “Enhanced photocatalytic performance of nanosized coupled ZnO/SnO2 photocatalysts for methyl orange degradation,” *J. Photochem. Photobiol. A Chem.*, vol. 168, no. 1–2, pp. 47–52, 2004.

[51] T. Uddin, Y. Nicolas, T. Toupance, L. Servant, M. M. Mu, H. Kleebe, J. Ziegler, and W. Jaegermann, “Nanostructured SnO 2 − ZnO Heterojunction Photocatalysts Showing Enhanced Photocatalytic Activity for the Degradation of Organic Dyes,” *Inorg. Chem.*, vol. 51, no. 14, pp. 7764–7773, 2012.

[52] W. Cun, Z. Jincai, W. Xinming, M. Bixian, S. Guoying, P. Ping’an, and F. Jiamo, “Preparation, characterization and photocatalytic activity of nano-sized ZnO/SnO2 coupled photocatalysts,” *Appl. Catal. B Environ.*, vol. 39, no. 3, pp. 269–279, 2002.

[53] X. Huang, L. Shang, S. Chen, J. Xia, X. Qi, X. Wang, T. Zhang, and X.-M. Meng, “Type-II ZnO nanorod–SnO2 nanoparticle heterostructures: characterization of structural, optical and photocatalytic properties,” *Nanoscale*, vol. 5, no. 9, p. 3828, 2013.

[54] Z. Liu, D. D. Sun, P. Guo, and J. O. Leckie, “An efficient bicomponent TiO2/SnO2 nanofiber photocatalyst fabricated by electrospinning with a side-by-side dual spinneret method,” *Nano Lett.*, vol. 7, no. 4, pp. 1081–1085, 2007.

[55] C. Wang, C. Shao, X. Zhang, and Y. Liu, “SnO2 nanostructures-tio2 nanofibers heterostructures: Controlled fabrication and high photocatalytic properties,” *Inorg. Chem.*, vol. 48, no. 15, pp. 7261–7268, 2009.

[56] V. R. De Mendonça, O. F. Lopes, R. P. Fregonesi, T. R. Giraldi, and C. Ribeiro, “TiO2-SnO2 heterostructures applied to dye photodegradation: The relationship between variables of synthesis and photocatalytic performance,” *Appl. Surf. Sci.*, vol. 298, pp. 182–191, 2014.

[57] J. F. Lei, L. B. Li, X. H. Shen, K. Du, J. Ni, C. J. Liu, and W. S. Li, “Fabrication of ordered ZnO/TiO2 heterostructures via a templating technique,” *Langmuir*, vol. 29, no. 45, pp. 13975–13981, 2013.

[58] J. Tian, L. Chen, Y. Yin, X. Wang, J. Dai, Z. Zhu, X. Liu, and P. Wu, “Photocatalyst of TiO2/ZnO nano composite film: Preparation, characterization, and photodegradation activity of methyl orange,” *Surf. Coatings Technol.*, vol. 204, no. 1–2, pp. 205–214, 2009.

[59] H. Ceylan, C. Ozgit-Akgun, T. S. Erkal, I. Donmez, R. Garifullin, A. B. Tekinay, H. Usta, N. Biyikli, and M. O. Guler, “Size-controlled conformal nanofabrication of biotemplated three-dimensional TiO_2 and ZnO nanonetworks.,” *Sci. Rep.*, vol. 3, p. 2306, 2013.

[60] T. J. Athauda, J. G. Neff, L. Sutherlin, U. Butt, and R. R. Ozer, “Systematic study of the structure-property relationships of branched hierarchical TiO2/ZnO nanostructures.,” *ACS Appl. Mater. Interfaces*, vol. 4, no. 12, pp. 6917–26, 2012.

[61] Z. Chen, J. Zhao, X. Yang, Q. Ye, K. Huang, C. Hou, Z. Zhao, J. You, and Y. Li, “Fabrication of TiO_2 /WO_3 Composite Nanofibers by Electrospinning and Photocatalystic Performance of the Resultant Fabrics,” *Ind. Eng. Chem. Res.*, vol. 55, no. 1, pp. 80–85, 2016.

[62] M. Basu, N. Garg, and A. K. Ganguli, “A type-II semiconductor (ZnO/CuS heterostructure) for visible light photocatalysis,” *J. Mater. Chem. A*, vol. 2, no. 20, p. 7517, 2014.

[63] L. Zhu, M. Hong, and G. Wei Ho, “Hierarchical Assembly of SnO2/ZnO Nanostructures for Enhanced Photocatalytic Performance,” *Sci. Rep.*, vol. 5, p. 11609, 2015.

[64] Z. W. Seh, S. Liu, M. Low, S.-Y. Zhang, Z. Liu, A. Mlayah, and M.-Y. Han, “Janus Au-TiO_2 Photocatalysts with Strong Localization of Plasmonic Near-Fields for Efficient Visible-Light Hydrogen Generation,” *Adv. Mater.*, vol. 24, no. 17, pp. 2310–2314, 2012.

[65] S. T. Kochuveedu, Y. H. Jang, and D. H. Kim, “A study on the mechanism for the interaction of light with noble metal-metal oxide semiconductor nanostructures for various photophysical applications.,” *Chem. Soc. Rev.*, vol. 42, no. 21, pp. 8467–93, Nov. 2013.

[66] M. R. Jones, K. D. Osberg, R. J. MacFarlane, M. R. Langille, and C. a. Mirkin, “Templated techniques for the synthesis and assembly of plasmonic nanostructures,” *Chem. Rev.*, vol. 111, no. 6, pp. 3736–3827, Jun. 2011.

[67] K. L. Kelly, E. Coronado, L. L. Zhao, and G. C. Schatz, “The Optical Properties of Metal Nanoparticles: The Influence of Size, Shape,

and Dielectric Environment," *J. Phys. Chem. B*, vol. 107, pp. 668–677, 2003.

[68] P. Christopher, H. Xin, and S. Linic, "Visible-light-enhanced catalytic oxidation reactions on plasmonic silver nanostructures," *Nat. Chem.*, vol. 3, no. 6, pp. 467–472, 2011.

[69] E. W. McFarland and J. Tang, "A photovoltaic device structure based on internal electron emission.," *Nature*, vol. 421, no. 6923, pp. 616–618, 2003.

[70] G. Zhao, H. Kozuka, and T. Yoko, "Sol—gel preparation and photoelectrochemical properties of TiO2 films containing Au and Ag metal particles," *Thin Solid Films*, vol. 277, no. 1–2, pp. 147–154, 1996.

[71] Y. Tian and T. Tatsuma, "Mechanisms and Applications of Plasmon-Induced Charge Separation at TiO2 Films Loaded with Gold Nanoparticles," *J. Am. Chem. Soc.*, vol. 127, no. 20, pp. 7632–7637, 2005.

[72] A. Furube, L. Du, K. Hara, R. Katoh, and M. Tachiya, "Ultrafast plasmon-induced electron transfer from gold nanodots into TiO2 nanoparticles," *J. Am. Chem. Soc.*, vol. 129, no. 48, pp. 14852–14853, 2007.

[73] Y. Fang, Y. Jiao, K. Xiong, R. Ogier, Z.-J. Yang, S. Gao, A. B. Dahlin, and M. Käll, "Plasmon Enhanced Internal Photoemission in Antenna-Spacer-Mirror Based Au/TiO $_2$ Nanostructures," *Nano Lett.*, p. 150506154242008, 2015.

[74] Y. He, P. Basnet, S. E. Hunyadi Murph, and Y. Zhao, "Ag Nanoparticle Embedded TiO2 Composite Nanorod Arrays Fabricated by Oblique Angle Deposition : Toward Plasmonic Photocatalysis," *ACS Appl. Mater. Interfaces*, vol. 5, pp. 11818–11827, 2013.

[75] F. Liu, E. J. Luber, L. A. Huck, B. C. Olsen, and J. M. Buriak, "Nanoscale plasmonic stamp lithography on silicon.," *ACS Nano*, vol. 9, no. 2, pp. 2184–93, 2015.

[76] J. Yan, K. W. Jacobsen, and K. S. Thygesen, "First-principles study of surface plasmons on Ag(111) and H/Ag(111)," *Phys. Rev. B*, vol. 84, no. November, p. 235430, 2011.

[77] S. Wang, A. Riedinger, H. Li, C. Fu, H. Liu, L. Li, T. Liu, L. Tan, M. J. Barthel, G. Pugliese, F. De Donato, M. Scotto D'Abbusco, X. Meng, L. Manna, H. Meng, and T. Pellegrino, "Plasmonic copper sulfide nanocrystals exhibiting near-infrared photothermal and photodynamic therapeutic effects.," *ACS Nano*, vol. 9, no. 2, pp. 1788–800, 2015.

[78] A. O. Govorov and H. H. Richardson, "Generating heat with metal nanoparticles," *Nano Today*, vol. 2, no. 1, pp. 30–38, 2007.

[79] D. a Boyd, L. Greengard, M. Brongersma, M. Y. El-Naggar, and D. G. Goodwin, "Plasmon-assisted chemical vapor deposition.," *Nano Lett.*, vol. 6, no. 11, pp. 2592–7, Nov. 2006.

[80] C. Fasciani, C. J. B. Alejo, M. Grenier, J. C. Netto-Ferreira, and J. C. Scaiano, "High-temperature organic reactions at room temperature using plasmon excitation: Decomposition of dicumyl peroxide," *Org. Lett.*, vol. 13, no. 2, pp. 204–207, 2011.

[81] Y. Zang, J. Yin, X. He, C. Yue, Z. Wu, J. Li, and J. Kang, "Plasmonic-enhanced self-cleaning activity on asymmetric Ag/ZnO surface-enhanced Raman scattering substrates under UV and visible light irradiation," *J. Mater. Chem. A*, vol. 2, no. 21, p. 7747, 2014.

[82] Z. Chen, L. Fang, W. Dong, F. Zheng, M. Shena, and J. Wang, "Inverse opal structured Ag/TiO2 plasmonic photocatalyst prepared by pulsed current deposition and its enhanced visible light photocatalytic activity," *J. Mater. Chem. A*, vol. 2, pp. 824–832, 2014.

[83] Z. Zhang, L. Zhang, M. N. Hedhili, H. Zhang, and P. Wang, "Plasmonic Gold Nanocrystals Coupled with Photonic Crystal Seamlessly on TiO2 Nanotube Photoelectrodes for E ffi cient Visible Light Photoelectrochemical Water Splitting," *Nano Lett.*, vol. 13, no. 1, pp. 14–20, 2013.

[84] E. Yablonovitch and G. D. Cody, "Intensity Enhancement in Textured Optical Sheets for Solar-Cells," *IEEE Trans. Electron Devices*, vol. 29, no. 2, pp. 300–305, 1982.

[85] R. B. Wehrspohn and U. Rau, Eds., *Photon Management in Solar Cells*. .

[86] J. N. Munday, D. M. Callahan, and H. a. Atwater, "Light trapping beyond the 4n2 limit in thin waveguides," *Appl. Phys. Lett.*, vol. 100, no. 12, p. 121121, 2012.

[87] Z. Yu, A. Raman, and S. Fan, "Fundamental limit of nanophotonic light trapping in solar cells.," *Proc. Natl. Acad. Sci. U. S. A.*, vol. 107, no. 41, pp. 17491–17496, 2010.

[88] B. P. Rand, J. Genoe, P. Heremans, and J. Poortmans, "Solar Cells Utilizing Small Molecular Weight Organic Semiconductors," *Prog. Photovolt Res. Appl.*, vol. 15, no. September 2010, pp. 659–676, 2007.

[89] D. M. Callahan, J. N. Munday, A. Atwater, and R. Khanna, "Solar Cell Light Trapping," *Nano Lett.*, vol. 12, pp. 214–218, 2012.

[90] S. F. Leung, Q. Zhang, F. Xiu, D. Yu, J. C. Ho, D. Li, and Z. Fan, "Light management with nanostructures for optoelectronic devices," *J. Phys. Chem. Lett.*, vol. 5, no. 8, pp. 1479–1495, 2014.

[91] M. Karg, T. A. F. König, M. Retsch, C. Stelling, P. M. Reichstein, T. Honold, M. Thelakkat, and A. Fery, “Colloidal self-assembly concepts for light management in photovoltaics,” *Mater. Today*, vol. 18, no. 4, pp. 185–205, 2015.

[92] F. Pastorelli, S. Bidault, J. Martorell, and N. Bonod, “Self-assembled plasmonic oligomers for organic photovoltaics,” *Adv. Opt. Mater.*, vol. 2, no. 2, pp. 171–175, 2014.

[93] S. Mozia, “Photocatalytic membrane reactors (PMRs) in water and wastewater treatment. A review,” *Sep. Purif. Technol.*, vol. 73, no. 2, pp. 71–91, 2010.

[94] V. Buscio, S. Brosillon, J. Mendret, M. Crespi, and C. Gutiérrez-Bouzán, “Photocatalytic Membrane Reactor for the Removal of C.I. Disperse Red 73,” *Materials (Basel).*, vol. 8, no. 6, pp. 3633–3647, 2015.

[95] D. E. Tsydenov, V. N. Parmon, and A. V. Vorontsov, “Toward the design of asymmetric photocatalytic membranes for hydrogen production: Preparation of TiO2-based membranes and their properties,” *Int. J. Hydrogen Energy*, vol. 37, no. 15, pp. 11046–11060, 2012.

[96] C. A. Chen, Y. M. Chen, A. Korotcov, Y. S. Huang, D. S. Tsai, and K. K. Tiong, “Growth and characterization of well-aligned densely-packed rutile TiO(2) nanocrystals on sapphire substrates via metal-organic chemical vapor deposition.,” *Nanotechnology*, vol. 19, no. 7, p. 075611, Feb. 2008.

[97] C.-A. Chen, Y.-M. Chen, Y.-S. Huang, D.-S. Tsai, K.-K. Tiong, and P.-C. Liao, “Synthesis and characterization of well-aligned anatase TiO2 nanocrystals on fused silica via metal–organic vapor deposition,” *CrystEngComm*, vol. 11, no. 11, p. 2313, 2009.

[98] F.-D. Duminica, F. Maury, and F. Senocq, “Atmospheric pressure MOCVD of TiO2 thin films using various reactive gas mixtures,” *Surf. Coatings Technol.*, vol. 188–189, pp. 255–259, Nov. 2004.

[99] C. Sarantopoulos, E. Puzenat, C. Guillard, J.-M. Herrmann, A. N. Gleizes, and F. Maury, “Microfibrous TiO2 supported photocatalysts prepared by metal-organic chemical vapor infiltration for indoor air and waste water purification,” *Appl. Catal. B Environ.*, vol. 91, no. 1–2, pp. 225–233, Sep. 2009.

[100] X. Zhang, M. Zhou, and L. Lei, “Preparation of anatase TiO2 supported on alumina by different metal organic chemical vapor deposition methods,” *Appl. Catal. A Gen.*, vol. 282, no. 1–2, pp. 285–293, Mar. 2005.

[101] J.-J. Wu and C.-C. Yu, “Aligned TiO 2 Nanorods and Nanowalls,” *J. Phys. Chem. B*, vol. 108, no. 11, pp. 108–110, 2004.

[102] C. Sarantopoulos, “Photocatalyseurs a base de TiO2 prepares par infiltration chimique en phase vapeur (CVI) sur supports microfibreux,” Institut National Polytechnique de Toulouse, 2007.

[103] C. Sarantopoulos, A. N. Gleizes, and F. Maury, “Chemical vapor infiltration of photocatalytically active TiO2 thin films on glass microfibers,” *Surf. Coatings Technol.*, vol. 201, no. 22–23, pp. 9354–9358, Sep. 2007.

[104] V. G. Courtecuisse, K. Chhor, J.-F. Bocquet, and C. Pommier, “Kinetics of the Titanium Isopropoxide Decomposition in Supercritical Isopropyl Alcohol,” *Ind. Eng. Res*, vol. 35, no. 1996, pp. 2539–2545, 1996.

[105] M. Reinke, Y. Kuzminykh, and P. Hoffmann, “Low temperature chemical vapor deposition using atomic layer deposition chemistry,” *Chem. Mater.*, vol. 27, no. 5, pp. 1604–1611, 2015.

[106] M. Reinke, Y. Kuzminykh, and P. Hoffmann, “Surface Reaction Kinetics of Titanium Isopropoxide and Water in Atomic Layer Deposition,” *J. Phys. Chem. C*, vol. 120, pp. 4337–4344, 2016.

[107] M. Ritala, M. Leskel, E. Nykfinen, P. Soininen, and L. Niinisto, “Growth of titanium dioxide thin films by atomic layer epitaxy,” *Thin Solid Films*, vol. 225, pp. 288–295, 1993.

[108] J. Aarik, A. Aidla, T. Uustare, and V. Sammelselg, “Morphology and structure of TiO2 thin films grown by atomic layer deposition,” *J. Cryst. Growth*, vol. 148, no. 3, pp. 268–275, 1995.

[109] M. Ritala and M. Leskela, *Chapter 2: Atomic Layer Deposition*, vol. 1. 2002.

[110] J. Shi and X. Wang, “Growth of Rutile Titanium Dioxide Nanowires by Pulsed Chemical Vapor Deposition,” *Cryst. Growth Des.*, vol. 11, no. 4, pp. 949–954, Apr. 2011.

[111] J. Shi and X. Wang, “Hierarchical TiO2–Si nanowire architecture with photoelectrochemical activity under visible light illumination,” *Energy Environ. Sci.*, vol. 5, no. 7, p. 7918, 2012.

[112] J. Shi, C. Sun, M. B. Starr, and X. Wang, “Growth of titanium dioxide nanorods in 3D-confined spaces.,” *Nano Lett.*, vol. 11, no. 2, pp. 624–31, Feb. 2011.

[113] X. Wang and J. Shi, “Evolution of titanium dioxide one-dimensional nanostructures from surface-reaction-limited pulsed chemical

vapor deposition," *J. Mater. Res.*, vol. 28, no. 03, pp. 270–279, Jan. 2013.

[114] Z. Li, C. Yao, F. Wang, Z. Cai, and X. Wang, "Cellulose nanofiber-templated three-dimension TiO\n 2\n hierarchical nanowire network for photoelectrochemical photoanode," *Nanotechnology*, vol. 25, no. 50, p. 504005, 2014.

[115] Y.-H. Chang, C.-M. Liu, H.-E. Cheng, and C. Chen, "Effect of geometric nanostructures on the absorption edges of 1-D and 2-D TiO2 fabricated by atomic layer deposition.," *ACS Appl. Mater. Interfaces*, vol. 5, no. 9, pp. 3549–55, May 2013.

[116] X. Meng, Y. Zhang, S. Sun, R. Li, and X. Sun, "Three growth modes and mechanisms for highly structure-tunable SnO2 nanotube arrays of template-directed atomic layer deposition," *J. Mater. Chem.*, vol. 21, no. 33, p. 12321, 2011.

[117] Z. Yao, C. Wang, Y. Li, and N.-Y. Kim, "AAO-assisted synthesis of highly ordered, large-scale TiO2 nanowire arrays via sputtering and atomic layer deposition," *Nanoscale Res. Lett.*, vol. 10, no. 1, p. 166, 2015.

[118] M. N. Mullings, C. Hägglund, and S. F. Bent, "Tin oxide atomic layer deposition from tetrakis(dimethylamino)tin and water," *J. Vac. Sci. Technol. A Vacuum, Surfaces, Film.*, vol. 31, no. 6, p. 061503, 2013.

[119] M. Wang, J. Bai, F. Le Formal, S. Moon, L. Cevey-ha, R. Humphry-baker, C. Gra, S. M. Zakeeruddin, and M. Gra, "Solid-State Dye-Sensitized Solar Cells using Ordered TiO 2 Nanorods on Transparent Conductive Oxide as Photoanodes," 2012.

[120] J. Wu, S. Lo, K. Song, B. K. Vijayan, W. Li, K. a. Gray, and V. P. Dravid, "Growth of rutile TiO2 nanorods on anatase TiO2 thin films on Si-based substrates," *J. Mater. Res.*, vol. 26, no. 13, pp. 1646–1652, Jun. 2011.

[121] H. Wang, Y. Bai, H. Zhang, Z. Zhang, J. Li, and L. Guo, "CdS Quantum Dots-Sensitized TiO 2 Nanorod Array on Transparent Conductive Glass Photoelectrodes," *J. Phys. Chem C*, vol. 114, pp. 16451–16455, 2010.

[122] X. Jia, W. He, X. Zhang, H. Zhao, Z. Li, and Y. Feng, "Microwave-assisted synthesis of anatase TiO(2) nanorods with mesopores.," *Nanotechnology*, vol. 18, no. 7, p. 075602, Feb. 2007.

[123] V. Tamilselvan, D. Yuvaraj, R. Rakesh Kumar, and K. Narasimha Rao, "Growth of rutile TiO2 nanorods on TiO2 seed layer deposited by electron beam evaporation," *Appl. Surf. Sci.*, vol. 258, no. 10, pp. 4283–4287, Mar. 2012.

[124] T. Nagata, D. J. Rogers, F. H. Teherani, Z. E. Horv, and Y. Wakayama, "Investigations into the Impact of the Template Layer on ZnO Nanowire Arrays Made Using Low Temperature Wet Chemical Growth," *Grystal Growth Des.*, vol. 11, pp. 2515–2519, 2011.

[125] S. Liu and K. Huang, "Straightforward fabrication of highly ordered TiO 2 nanowire arrays in AAM on aluminum substrate," *Sol. Energy Mater. Sol. Cells*, vol. 85, pp. 125–131, 2005.

[126] L. Shi, Y. Xu, and Q. Li, "Controlled fabrication of SnO(2) arrays of well-aligned nanotubes and nanowires.," *Nanoscale*, vol. 2, pp. 2104–2108, 2010.

[127] S. Krishnamoorthy, K. K. Manipaddy, and F. L. Yap, "Wafer-Level Self-Organized Copolymer Templates for Nanolithography with Sub-50 nm Feature and Spatial Resolutions," *Adv. Funct. Mater.*, vol. 21, no. 6, pp. 1102–1112, Mar. 2011.

[128] K. Yu, S. Yang, H. He, C. Sun, C. Gu, and Y. Ju, "Visible light-driven photocatalytic degradation of rhodamine B over NaBiO3: Pathways and mechanism," *J. Phys. Chem. A*, vol. 113, no. 37, pp. 10024–10032, 2009.

[129] O. Zahraa and M. Bouchy, "Photocatalytic degradation of salicylic acid on fixed TiO2 - kinetic studies," *Int. J. Photoenergy*, vol. 2, pp. 59–66, 2000.

[130] C. K. Scheck and F. H. Frimmel, "Degradation of phenol and salicylic acid by ultraviolet radiation/hydrogen peroxide/oxygen," *Water Res.*, vol. 29, no. 10, pp. 2346–2352, 1995.

[131] D. Mukherjee, A. Ray, and S. Barghi, "Mechanism of Acetyl Salicylic Acid (Aspirin) Degradation under Solar Light in Presence of a TiO2-Polymeric Film Photocatalyst," *Processes*, vol. 4, no. 2, p. 13, 2016.

[132] H. Wang, X. Liu, X. Liu, Q. Guan, P. Huo, and Y. Yan, "Enhancement of photocatalytic activity on salicylic acid by nonmetal-doped TiO 2 with solvothermal method," *Desalin. Water Treat.*, vol. 54, no. 9, pp. 2504–2515, 2015.

[133] M. A. Oturan and J. Pinson, "Polyhydroxylation of salicylic acid by electrochemically generated OH radicals," *New J. Chem.*, vol. 16, pp. 705–710, 1992.

[134] S. Krishnamoorthy, R. Pugin, J. Brugger, H. Heinzelmann, and C. Hinderling, "Nanopatterned Self-Assembled Monolayers by Using Diblock Copolymer Micelles as Nanometer-Scale Adsorption and Etch Masks," *Adv. Mater.*, vol. 20, no. 10, pp. 1962–1965, May 2008.

[135] S. Mossmer, J. P. Spatz, M. Moller, T. Aberle, J. Schmidt, and W. Burchard, "Solution Behavior of Poly(styrene)-," *Macromol. Rapid Commun.*, vol. 33, no. 13, pp. 4791–4798, 2000.

[136] R. Glass, M. M ller, and J. P. Spatz, “Block copolymer micelle nanolithography,” *Nanotechnology*, vol. 14, no. 10, pp. 1153–1160, Oct. 2003.

[137] F. Ferrarese Lupi, T. J. Giammaria, G. Seguini, M. Laus, E. Enrico, N. De Leo, L. Boarino, C. K. Ober, and M. Perego, “Thermally induced orientational flipping of cylindrical phase diblock copolymers,” *J. Mater. Chem. C*, vol. 2, no. 12, p. 2175, 2014.

[138] S. Park, J.-Y. Wang, B. Kim, W. Chen, and T. P. Russell, “Solvent-Induced Transition from Micelles in Solution to Cylindrical Microdomains in Diblock Copolymer Thin Films,” *Macromolecules*, vol. 40, no. 25, pp. 9059–9063, Dec. 2007.

[139] S. J. Ku, G. C. Jo, C. H. Bak, S. M. Kim, Y. R. Shin, K. H. Kim, S. H. Kwon, and J.-B. Kim, “Highly ordered freestanding titanium oxide nanotube arrays using Si-containing block copolymer lithography and atomic layer deposition.,” *Nanotechnology*, vol. 24, no. 8, p. 085301, Mar. 2013.

[140] J. Chai and J. M. Buriak, “Using Cylindrical Domains of Block Copolymers To Self-Assemble and Align,” *ACS Nano*, vol. 2, no. 3, pp. 489–501, 2008.

[141] N. a. Yufa, S. L. Fronk, S. J. Rosenthal, S. B. Darling, W. a. Lopes, and S. J. Sibener, “Self-assembled monolayer-modified block copolymers for chemical surface nanopatterning,” *Mater. Chem. Phys.*, vol. 125, no. 3, pp. 382–385, Feb. 2011.

[142] Q. Peng, Y.-C. Tseng, S. B. Darling, and J. W. Elam, “Nanoscopic patterned materials with tunable dimensions via atomic layer deposition on block copolymers.,” *Adv. Mater.*, vol. 22, no. 45, pp. 5129–33, Dec. 2010.

[143] W. J. Durand, G. Blachut, M. J. Maher, S. Sirard, S. Tein, M. C. Carlson, Y. Asano, S. X. Zhou, A. P. Lane, C. M. Bates, C. J. Ellison, and C. G. Willson, “Design of high-χ block copolymers for lithography,” *J. Polym. Sci. Part A Polym. Chem.*, vol. 53, no. 2, pp. 344–352, Jan. 2015.

[144] U. Wiedwald, L. Han, J. Biskupek, U. Kaiser, and P. Ziemann, “Preparation and characterization of supported magnetic nanoparticles prepared by reverse micelles.,” *Beilstein J. Nanotechnol.*, vol. 1, pp. 24–47, Jan. 2010.

[145] N. Li, X. Zhang, S. Yuan, X. Zhang, Y. Yuan, and X. Li, “(Hollow Ag−Au Nanoparticles)/TiO2 Composites for Improved Photocatalytic Activity Prepared from Block Copolymer-Stabilized Bimetallic Nanoparticles,” *Phys. Chem. Chem. Phys.*, pp. 12023–12030, 2015.

[146] H. Yu and A. Turak, “Nanoreactors or nanoscale stablizers : routes for solution processed indium tin oxide nanoparticles by reverse micelle,” *Can. J. Phys.*, vol. 5, no. October 2013, pp. 1–5, 2014.

[147] X. Li, K. Hang, A. Lau, D. H. Kim, and W. Knoll, “High-Density Arrays of Titania Nanoparticles Using Monolayer Micellar Films of Diblock Copolymers as Templates,” *Langmuir*, no. 25, pp. 5212–5217, 2005.

[148] J. Yin, Q. Xu, Z. Wang, X. Yao, and Y. Wang, “Highly ordered TiO2 nanostructures by sequential vapour infiltration of block copolymer micellar films in an atomic layer deposition reactor,” *J. Mater. Chem. C*, vol. 1, no. 5, pp. 1029–1036, 2013.

[149] M. Aizawa, J. M. Buriak, C. Tg, R. V May, V. Re, M. Recei, and V. July, “Block Copolymer Templated Chemistry for the Formation of Metallic Nanoparticle Arrays on Semiconductor Surfaces,” *Chem. Mater.*, vol. 19, no. 1, pp. 5090–5101, 2007.

[150] Q. Peng, Y. C. Tseng, S. B. Darling, and J. W. Elam, “A route to nanoscopic materials via sequential infiltration synthesis on block copolymer templates,” *ACS Nano*, vol. 5, no. 6, pp. 4600–4606, 2011.

[151] J. F. Moulder, W. F. Stickle, P. E. Sobol, and K. Bomben, *Handbook of Photoelectron Spectroscopy*. Perkin-Elmer: Eden Prairie, MN, 1992.

[152] B. Erdem, R. a Hunsicker, G. W. Simmons, E. D. Sudol, V. L. Dimonie, and M. S. El-aasser, “XPS and FTIR Surface Characterization of TiO2 Particles Used in Polymer Encapsulation,” *Langmuir*, vol. 17, no. 9, pp. 2664–2669, 2001.

[153] C. Mousty-Desbuquoit, J. Riga, and J. J. Verbist, “Solid state effects in the electronic structure of TiCl4 studied by XPS,” *J. Chem. Phys.*, vol. 79, no. 1, p. 26, 1983.

[154] S. Krishnamoorthy, R. Pugin, J. Brugger, H. Heinzelmann, and C. Hinderling, “Tuning the Dimensions and Periodicities of Nanostructures Starting from the Same Polystyrene-block-poly(2-vinylpyridine) Diblock Copolymer,” *Adv. Funct. Mater.*, vol. 16, no. 11, pp. 1469–1475, Jul. 2006.

[155] S. H. Kim, M. J. Misner, T. Xu, M. Kimura, and T. P. Russell, “Highly Oriented and Ordered Arrays from Block Copolymers via Solvent Evaporation,” *Adv. Mater.*, vol. 16, no. 3, pp. 226–231, Feb. 2004.

[156] M. Biswas, J. A. Libera, and S. B. Darling, “New Insight into the Mechanism of Sequential In fi ltration Synthesis from Infrared Spectroscopy,” *Chem. Mater.*, vol. 26, pp. 6135–6141, 2014.

[157] M. Biswas, J. A. Libera, S. B. Darling, and J. W. Elam, “Kinetics for the Sequential Infiltration Synthesis of Alumina in Poly(methyl methacrylate): An Infrared Spectroscopic Study,” *J. Phys. Chem. C*, vol. 119, no. 26, pp. 14585–14592, 2015.

[158] X. Zhou, S. H. Goh, S. Y. Lee, and K. L. Tan, “X-ray photoelectron spectroscopic studies of ionic interactions in poly(styrenesulfonic acid) / poly (vinylpyridine) complexes,” *Appl. Surf. Sci.*, vol. 126, pp. 141–147, 1998.

[159] H. Komiyama, T. Kanai, and H. Inoue, “PREPARATION OF POROUS, AMORPHOUS,AND ULTRAFINE TiO2 PARTICLES BY CHEMICAL VAPOR DEPOSITION,” *Chem. Lett. Chem. Soc. Japan*, no. C, pp. 1283–1286, 1984.

[160] C. P. Fictorie, J. F. Evans, and W. L. Gladfelter, “Kinetic and mechanistic study on the chemical vapor deposition of titanium dioxide thin films by in situ FT-IR using TTIP,” *Surf. Coat. Technol.*, vol. 171, no. 03, pp. 198–204, 2003.

[161] A. C. Jones and M. L. Hitchman, “Overview of Chemical Vapour Deposition,” in *Chemical Vapour Deposition: Precursors, Processes and Applications*, London: Royal Society of Chemistry, 2009, pp. 1–36.

[162] J. N. Lalena, D. a. Cleary, E. E. Carpenter, and N. F. Dean, *Inorganic Materials Synthesis and Fabrication*. WILEY VCH Verlag GmbH, 2008.

[163] H. Mehranpour, M. Askari, and M. S. Ghamsari, “Nucleation and Growth of TiO2 Nanoparticles,” in *Nanomaterials*, 2010.

[164] H.-E. Cheng and C.-C. Chen, “Morphological and Photoelectrochemical Properties of ALD TiO2 Films,” *J. Electrochem. Soc.*, vol. 155, no. 9, p. D604, 2008.

[165] J. Aarik, A. Aidla, H. Mandar, and T. Uustare, “Atomic layer deposition of titanium dioxide from TiCl4 and H2O: investigation of growth mechanism,” *Appl. Surf. Sci.*, vol. 172, pp. 148–158, 2001.

[166] L. K. Tan, M. A. S. Chong, and H. Gao, “Free-Standing Porous Anodic Alumina Templates for Atomic Layer Deposition of Highly Ordered TiO2 Nanotube Arrays on Various Substrates,” *J. Phys. Chem. C*, vol. 112, no. 1, pp. 69–73, 2008.

[167] W. Gu and C. P. Tripp, “Role of water in the atomic layer deposition of TiO2 on SiO2.,” *Langmuir*, vol. 21, no. 1, pp. 211–216, 2005.

[168] Y. Huang, G. Pandraud, and P. M. Sarro, “Characterization of low temperature deposited atomic layer deposition TiO2 for MEMS applications,” *J. Vac. Sci. Technol. A Vacuum, Surfaces, Film.*, vol. 31, no. September 2012, p. 01A148, 2013.

[169] G. Luka, B. S. Witkowski, L. Wachnicki, M. Andrzejczuk, M. Lewandowska, and M. Godlewski, “Kinetics of anatase phase formation in TiO2 films during atomic layer deposition and post-deposition annealing,” *CrystEngComm*, vol. 15, no. 46, p. 9949, 2013.

[170] J. Leem, I. Park, Y. Li, W. Zhou, Z. Jin, S. Shin, and Y. Min, “Role of HCl in Atomic Layer Deposition of TiO 2 Thin Films from Titanium Tetrachloride and Water,” vol. 35, no. 4, pp. 1195–1201, 2014.

[171] R. L. Puurunen, “Formation of Metal Oxide Particles in Atomic Layer Deposition During the Chemisorption of Metal Chlorides: A Review,” *Chem. Vap. Depos.*, vol. 11, no. 2, pp. 79–90, 2005.

[172] Y. M. Koshtyal, A. A. Malkov, and A. A. Malygin, “Temperature influence on the formation of titanium-oxide structures on finely porous silica,” *Russ. J. Gen. Chem.*, vol. 81, no. 1, pp. 41–48, Feb. 2011.

[173] V. N. Pak, Y. P. Kostikov, S. I. Koltsov, and V. B. Aleskovskiy, “Determination of coordination number of titanium atoms on a titaniumcontaining silica surface by measuring shifts in K(alfa1) X-ray lines,” *Kinet. i Katal.*, vol. 15, no. 5, p. 1358, 1974.

[174] P. V. Purohit, M. Rothschild, and D. J. Ehrlich, *Mechanisms of Reactions of Organometallic Compounds with Surfaces*, vol. 1. New York: Springer Science+Business Media, LLC, 1989.

[175] Z. Hu and C. H. Turner, “Initial Surface Reactions of TiO 2 Atomic Layer Deposition onto SiO 2 Surfaces : Density Functional Theory Calculations,” *J. Phys. Chem. B*, vol. 110, pp. 8337–8347, 2006.

[176] T.-H. Wang, A. M. Navarrete-López, S. Li, D. a Dixon, and J. L. Gole, “Hydrolysis of TiCl(4): initial steps in the production of TiO(2).,” *J. Phys. Chem. A*, vol. 114, no. 28, pp. 7561–70, Jul. 2010.

[177] T. Takamori, R. Messier, and R. Roy, “Phenomenology of the ‘explosive’ crystallization of sputtered non-crystalline germanium films,” *J. Mater. Sci.*, vol. 8, no. 12, pp. 1809–1816, 1973.

[178] H. D. Geiler, E. Glaser, G. G??tz, and M. Wagner, “Explosive crystallization in silicon,” *J. Appl. Phys.*, vol. 59, no. 9, pp. 3091–3099, 1986.

[179] L. N. Aleksandrov and F. L. Edelman, “Shock crystallization in amorphous films of dielectrics,” *Surf. Sci.*, vol. 86, no. C, pp. 222–229, 1979.

[180] V. Pore, M. Ritala, M. Leskelä, T. Saukkonen, and M. Järn, “Explosive crystallization in atomic layer deposited mixed titanium oxides,” *Cryst. Growth Des.*, vol. 9, no. 7, pp. 2974–2978, 2009.

[181] S. K. Park and H. Shin, “Effect of HCl and H2SO4 Treatment of TiO2 Powder on the Photosensitized Degradation of Aqueous

Rhodamine B Under Visible Light," *J. Nanosci. Nanotechnol.*, vol. 14, no. 10, pp. 8122–8128, 2014.

[182] S. Pétigny, H. Mostéfa-Sba, B. Domenichini, E. Lesniewska, A. Steinbrunn, and S. Bourgeois, "Superficial defects induced by argon and oxygen bombardments on (110) TiO2 surfaces," *Surf. Sci.*, vol. 410, no. 2–3, pp. 250–257, 1998.

[183] M. Iwaki, Y. Okabe, and K. Yabe, "Comparison between oxygen depth profiles in oxygen-implanted titanium measured by RBS and XPS combined with argon sputtering," *Nucl. Instruments Methods Phys. Res. Sect. B Beam Interact. with Mater. Atoms*, vol. 45, no. 1–4, pp. 212–215, 1990.

[184] V. S. Lusvardi, M. A. Barteau, J. G. Chen, J. Eng, B. Frühberger, and A. Teplyakov, "An NEXAFS investigation of the reduction and reoxidation of TiO2(001)," *Surf. Sci.*, vol. 397, no. 1–3, pp. 237–250, 1998.

[185] S. Hashimoto and A. Tanaka, "Alteration of Ti 2p XPS spectrum for titanium oxide by low-energy Ar ion bombardment," *Surf. Interface Anal.*, vol. 34, no. 1, pp. 262–265, 2002.

[186] X. Chen, L. Liu, P. Y. Yu, and S. S. Mao, "Increasing solar absorption for photocatalysis with black hydrogenated titanium dioxide nanocrystals.," *Science*, vol. 331, no. 6018, pp. 746–50, 2011.

[187] L. Song, P. Du, X. Shao, H. Cao, Q. Hui, and J. Xiong, "Effects of hydrochloric acid treatment of TiO2 nanoparticles/nanofibers bilayer film on the photovoltaic properties of dye-sensitized solar cells," *Mater. Res. Bull.*, vol. 48, no. 3, pp. 978–982, 2013.

[188] X. Du, Y. Du, and S. M. George, "In situ examination of tin oxide atomic layer deposition using quartz crystal microbalance and Fourier transform infrared techniques," *J. Vac. Sci. Technol. A Vacuum, Surfaces, Film.*, vol. 23, no. 4, p. 581, 2005.

[189] H.-E. Cheng, D.-C. Tian, and K.-C. Huang, "Properties of SnO2 Films Grown by Atomic Layer Deposition," *Procedia Eng.*, vol. 36, pp. 510–515, 2012.

[190] J. W. Elam, M. D. Groner, and S. M. George, "Viscous flow reactor with quartz crystal microbalance for thin film growth by atomic layer deposition," *Rev. Sci. Instrum.*, vol. 73, no. 8, p. 2981, 2002.

[191] J. Lu, J. Sundqvist, M. Ottosson, a Tarre, a Rosental, J. Aarik, and a Hårsta, "Microstructure characterisation of ALD-grown epitaxial SnO2 thin films," *J. Cryst. Growth*, vol. 260, no. 1–2, pp. 191–200, 2004.

[192] v. K. Gueoruiev, L. I. Popova, G. D. Beshkov, and N. A. Tomajova, "Wet Etching of Thin SnO2 Films," *Sensors Actuators A*, vol. 24, pp. 61–63, 1990.

[193] W. Chen, Q. Kuang, Q. Wang, and Z. Xie, "Engineering a high energy surface of anatase TiO_2 crystals towards enhanced performance for energy conversion and environmental applications," *RSC Adv.*, vol. 5, no. 26, pp. 20396–20409, 2015.

[194] A. Selloni, "Crystal growth: Anatase shows its reactive side.," *Nat. Mater.*, vol. 7, no. 8, pp. 613–615, 2008.

[195] X. Gong and A. Selloni, "Reactivity of Anatase TiO Nanoparticles : The Role of the Minority (001) Surface Reactivity of Anatase TiO 2 Nanoparticles : The Role of the Minority (001) Surface," *J. Phys. Chem. B*, no. 001, pp. 1–4, 2005.

[196] U. I. Gaya, *Heterogeneous photocatalysis using inorganic semiconductor solids*. Dordrecht: Springer Science+Business Media, 2014.

[197] C. Jin, B. Liu, Z. Lei, and J. Sun, "Structure and photoluminescence of the TiO2 films grown by atomic layer deposition using tetrakis-dimethylamino titanium and ozone," *Nanoscale Res. Lett.*, vol. 10, no. 1, 2015.

[198] U. I. Gaya, *Heterogeneous Photocatalysis Using Inorganic Semiconductor Solids*, vol. 1. Dordrecht: Springer Netherlands, 2014.

[199] J. Du, X. Lai, N. Yang, J. Zhai, D. Kisailus, F. Su, D. Wang, and L. Jiang, "Hierarchically ordered macro-mesoporous TiO2-graphene composite films: Improved mass transfer, reduced charge recombination, and their enhanced photocatalytic activities," *ACS Nano*, vol. 5, no. 1, pp. 590–596, 2011.

[200] J. L. McHale and F. J. Knorr, *Handbook of Luminescent Semiconductor Materials*. Taylor & Francis Group, LLC, 2012.

[201] M. Bechelany, X. Maeder, J. Riesterer, J. Hankache, D. Lerose, S. Christiansen, J. Michler, and L. Philippe, "Synthesis mechanisms of organized gold nanoparticles: Influence of annealing temperature and atmosphere," *Cryst. Growth Des.*, vol. 10, no. 2, pp. 587–596, 2010.

[202] E. McCafferty and J. P. Wightman, "Determination of the concentration of surface hydroxyl groups on metal oxide films by a quantitative XPS method," *Surf. Interface Anal.*, vol. 26, no. 8, pp. 549–564, 1998.

[203] G. Wang, H. Wang, Y. Ling, Y. Tang, X. Yang, R. C. Fitzmorris, C. Wang, J. Z. Zhang, and Y. Li, "Hydrogen-treated TiO2 nanowire arrays for photoelectrochemical water splitting," *Nano Lett.*, vol. 11, no. 7, pp. 3026–3033, 2011.

[204] T. S. Natarajan, H. C. Bajaj, and R. J. Tayade, "Preferential adsorption behavior of methylene blue dye onto surface hydroxyl group

enriched TiO2 nanotube and its photocatalytic regeneration," *J. Colloid Interface Sci.*, vol. 433, no. August 2016, pp. 104–114, 2014.

[205] Y. Zhou, Y. Zhang, M. Lin, J. Long, Z. Zhang, H. Lin, J. C.-S. C.-S. Wu, and X. Wang, "Monolayered Bi2WO6 nanosheets mimicking heterojunction interface with open surfaces for photocatalysis.," *Nat. Commun.*, vol. 6, p. 8340, 2015.

[206] W. F. Zhang, M. S. Zhang, Z. Yin, and Q. Chen, "Photoluminescence in anatase titanium dioxide nanocrystals," *Appl. Phys. B Lasers Opt.*, vol. 70, no. 2, pp. 261–265, Feb. 2000.

[207] M. Pazoki, N. Taghavinia, Y. Abdi, F. Tajabadi, G. Boschloo, and A. Hagfeldt, "CVD-grown TiO2 particles as light scattering structures in dye-sensitized solar cells," *RSC Adv.*, vol. 2, no. 32, p. 12278, 2012.

[208] H. Liu, Y. Zhang, R. Li, M. Cai, and X. Sun, "A facile route to synthesize titanium oxide nanowires via water-assisted chemical vapor deposition," *J. Nanoparticle Res.*, vol. 13, no. 1, pp. 385–391, Aug. 2010.

[209] H. Liu, Y. Zhang, R. Li, M. Cai, and X. Sun, "Synthesis and characterization of TiO2@C core-shell nanowires and nanowalls via chemical vapor deposition for potential large-scale production.," *J. Colloid Interface Sci.*, vol. 367, no. 1, pp. 115–9, Feb. 2012.

[210] J. M. Baik, M. H. Kim, C. Larson, X. Chen, S. Guo, A. M. Wodtke, and M. Moskovits, "High-yield TiO[sub 2] nanowire synthesis and single nanowire field-effect transistor fabrication," *Appl. Phys. Lett.*, vol. 92, no. 24, p. 242111, 2008.

[211] R. S. Dariani and Z. Nafari Qaleh, "Microstructure characterization of TiO2 nanowires fabricated by thermal evaporation process," *Thin Solid Films*, vol. 542, pp. 192–198, Sep. 2013.

[212] F. Zhuge, T. Yanagida, K. Nagashima, H. Yoshida, K. Masaki, X. Bo, K. Annop, M. Gang, H. Yong, R. Sakon, L. Xiaomin, S. Masaru, K. Shoichi, T. Seiji, and Tomoji Kawai, "Fundamental Strategy for Creating VLS Grown TiO2 Single Crystalline Nanowires," *J. Phys. Chem. C*, vol. 116, pp. 24367–24372, 2012.

[213] J.-Y. Ha, B. D. Sosnowchik, L. Lin, D. H. Kang, and A. V. Davydov, "Patterned Growth of TiO 2 Nanowires on Titanium Substrates," *Appl. Phys. Express*, vol. 4, no. 6, p. 065002, May 2011.

[214] J.-C. Lee, K.-S. Park, T.-G. Kim, H.-J. Choi, and Y.-M. Sung, "Controlled growth of high-quality TiO 2 nanowires on sapphire and silica," *Nanotechnology*, vol. 17, no. 17, pp. 4317–4321, Sep. 2006.

[215] K. Tai, K. Sun, B. Huang, and S. J. Dillon, "Catalyzed oxidation for nanowire growth.," *Nanotechnology*, vol. 25, no. 14, p. 145603, Apr. 2014.

[216] M. F. Chisholm, *Scanning Microscopy for Nanotechnology*. 2006.

[217] J. Mayer, L. a Giannuzzi, T. Kamino, and J. Michael, "TEM Sample Preparation and FIB-Induced Damage," *MRS Bull.*, vol. 32, no. 05, pp. 400–407, 2007.

[218] A. J. J. Schwartz, M. Kumar, B. L. L. Adams, and D. P. P. Field, *Electron Backscatter Diffraction in Materials Science*. 2009.

[219] T. Prohaska, J. Irrgeher, A. Zitek, and N. Jakubowski, Eds., *Secondary Ion Mass Spectrometry in Sector Field Mass Spectrometry for Elemental and Isotopic Analysis*. RSC Books, 2015.

[220] "www.cameca.com." .

[221] W. Melitz, J. Shen, A. C. Kummel, and S. Lee, "Kelvin probe force microscopy and its application," *Surf. Sci. Rep.*, vol. 66, no. 1, pp. 1–27, 2011.

[222] P. Eaton and P. West, Eds., *Atomic Force Microscopy*. OxfordScholarship Online, 2010.

[223] OwenTony, "Fundamentals of modern UV-visible spectroscopy," *Hewlett-Packard Co.*, pp. 38–61, 2000.

[224] R. Loudon, *The Raman effect in crystals*, vol. 13, no. 52. 1964.

[225] Y. Yuan and T. R. Lee, "Contact Angle and Wetting Properties," in *Surface science techniques*, vol. 51, no. 1, G. Bracco and B. Holst, Eds. Springer Series in Surface Sciences, 2013.

Appendices

Fabrication of TiO_2 nanowires by Chemical Vapour Deposition

The main principle of the CVD technique is the reaction between the vapour phase precursors and deposition of reaction products on a substrate. The reaction localisation can be tuned by the deposition conditions and occurs on the substrate or in the gas phase. Typically the high quality CVD coatings require the precursor reaction on the surface. Classical CVD is restrained by the choice of precursors to volatile inorganic compounds.

TiO_2 nanostructures synthesis by CVD generally uses volatile titanium halides such as $TiCl_4$, TiI_4 as titanium precursor and water and oxygen as oxidative gases. The deposition temperature is a key factor determining the morphology of coating. CVD deposition realised in a tubular reactor using $TiCl_4$, water and oxygen as precursors demonstrates a temperature dependent morphology [207]. The high temperature zone (in the centre of the tubular reactor) was heated at 250°C; in the lower temperature zones, the temperature was maintained at 230 and 210°C. TiO_2 spherical nanoparticles of 450 nm were obtained in the lowest temperature zone at 210°C. The increase of temperature up to 230°C shows the formation of nanowires with an average diameter of 150 nm and a length of 2 µm. In the highest temperature zone, a mesoporous film-like structure was obtained (Figure A-1).

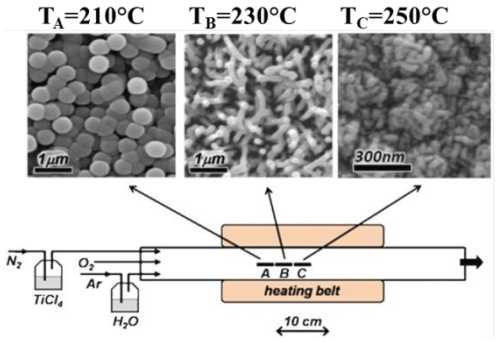

Figure A-1 Schematic CVD setup.

The classical TiO_2 CVD deposition results either in films deposition or in nanoparticles deposition. However, CVD modifications exist that are more appropriate for nanowires growth. It is worth noticing an approach based on the principle of the Vapour-Liquid-Solid (VLS) growth mechanism. It involves the use of a pre-deposited metal catalyst which forms an alloy with lower eutectic temperature, or also use some additive compounds which reduce the precursor melting point. For instance, the addition of carbon into titanium powder will lower the titanium melting point, thus the precursor can easily be transformed into vapour transported onto the substrate [208] [209]. The drawback of such nanowires growth method is

the inevitable carbon contamination. The deposition on metallic nanoparticles such as gold, nickel, copper, tin and bismuth [210]–[214] enables to form a liquid alloy with titanium. Because of alloy droplets formed on the substrate, the vapour of Ti-precursor is absorbed by the droplet up to supersaturation, which drives to the nanowires growth. The schematic of VLS mechanism is illustrated on Figure A-2. The growth temperature of TiO_2 nanowires by VLS approach depends on the formed alloy eutectic; but still be very high in the range 850-1050°C.

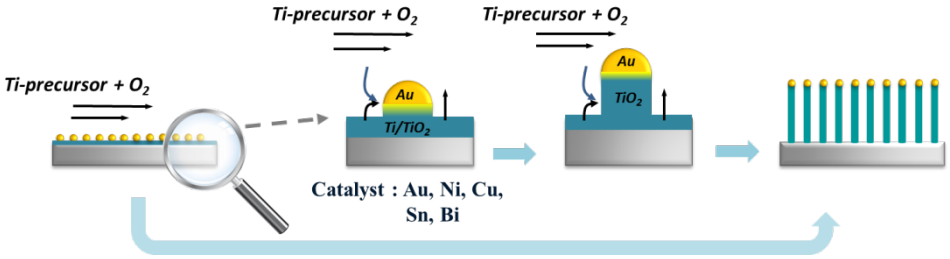

Figure A-2 Schematic illustration of VLS growth mechanism.

Zhuge and co-workers [212] studied VLS TiO_2 nanowires growth assisted by gold nanoparticles at 850°C. It was demonstrated that the catalyst nanoparticles size could determine the nanowires growth direction. The increase of catalyst diameter would allow the vertical nanowires growth. Another important growth parameter that authors pointed out is the control on the material flux. For this Ti target was ablated by ArF eximer laser. The laser energy vas optimised in order to control the material flux during the deposition. Moreover, for TiO_2, the nanowires growth takes place in the very narrow window of flux values; otherwise other morphologies will be grown. Tai and co-workers [215] also demonstrated the possibility of TiO_2 and ZnO nanowires growth using cupper catalytic particles. The growth was carried out by thermal oxidation of titanium layer with catalyst nanoparticles at 600°C.

Besides relatively high temperature, another drawback of the VLS synthesis is the presence of the catalyst nanoparticles on the top or bottom of nanowires, which are difficult to be eliminated.

Microwave synthesis

A commercial microwave reactor Monowave 300 from the Anton Parr Company was used for the hydrothermal synthesis tests on the substrates with catalytic seeds of well-organized TiO_2 nanoparticles. (Figure A-3).

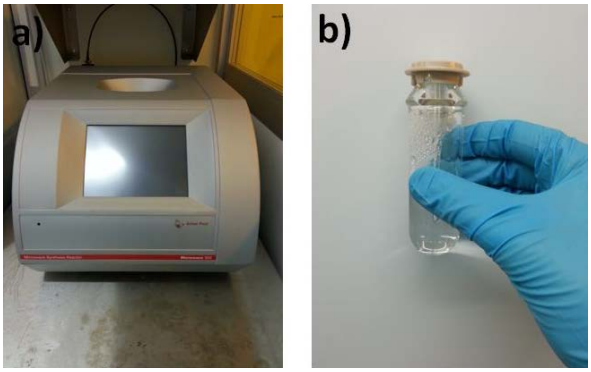

Figure A-3 Monowave 300 de chez Anton Parr (a), glass vial of 30 ml (b).

The Monowave 300 reactor has a microwave source of 2.6 GHz and a maximum power of 850W. The reactor configuration enables the concentration of the electromagnetic waves in the reaction zone that significantly enhances the heating efficiency and thus the reaction kinetics. The typical temperature rump is 9°C/s. Hydrothermal synthesis can be realised in glass vials of volume 1, 10 and 30 ml (Figure A-3 b). These vials allow working at hydrothermal synthesis conditions, which means high pressure and temperature. Monowave 300 is limited to 300°C and 30 Bar. A ruby detector, introduced into the reaction medium through the quartz capillar enables a direct measurement of the solution temperature. Additionally, an infra-red detector is used for controlling the solution temperature through the glass vial. The pressure is controlled by a non-invasive sensor, located in the swivelling cover of the reactor. A pneumatic system sealed the reaction vial. When the pressure increases during the reaction, a hydraulic piston translates the deformation of the silicon cover into a reaction pressure. If the pressure meets the set limit, the experiment will be aborted immediately and the system will cool slowly, releasing the pressure from the vial. The microwave synthesis is a significantly faster nanostructure synthesis than the conventional hydrothermal approach. However, the major drawback of this method is the vials volume limited to 30 mL. Therefore, in this work, the microwave synthesis was used only as a proof of concept for the nanowires synthesis from the TiO_2 nanoparticle seeds.

Characterisation techniques

The present work deals with the development of nanostructures with a specific morphology of periodic arrangement. For this reason, morphology characterisation tools are used, such as Scanning Electron Microscopy (SEM), Transmission Electron Microscopy (TEM) and Atomic Force Microscopy (AFM). The functional quality of nanostructures and films was studied by the physicochemical techniques such as X-ray diffraction (XRD), X-ray photoelectron spectroscopy (XPS) etc.

Scanning electron microscopy

Working principle

Scanning Electron Microscopy is a powerful visualization tool with a lateral resolution down to the nanoscale, which is based on the interaction of an electron beam with a material. The electron-matter interaction can be classified in two types: (i) elastic interaction, when no energy is transferred to the sample and (ii) inelastic interaction, when of energy is transferred from the incident electron to the sample. Depending on the amount of energy, different signals can be specifically detected such as secondary electrons, X-rays, Auger, plasmons, phonons, etc. The case of inelastic interaction is mainly used in the SEM approach. According to the type of signal, different information about morphology and/or chemistry can be collected.

SEM generally consists of an electron beam, a complex system of electromagnetic lenses to focus the electron beam, and the detection of the electrons reemitted by the sample surface (Figure A-4).

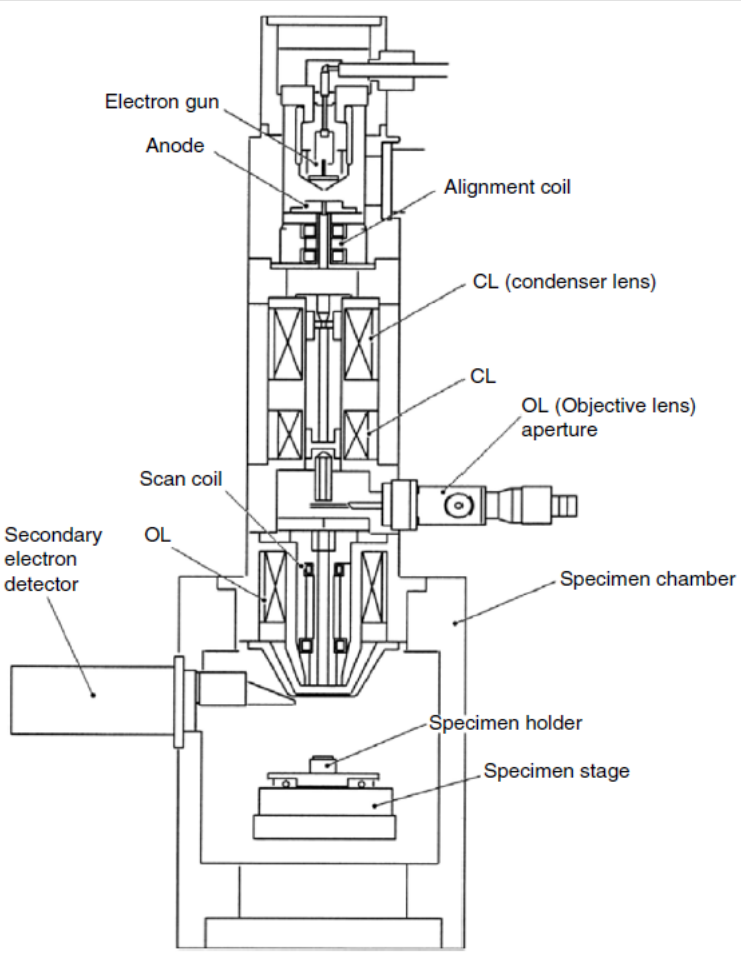

Figure A-4 Schematic standard Scanning Electron Microscope configuration [216].

The electron beam results from a heated filament at high current. The electrons emitted from the filament are accelerated by the electrical field produced by the potential difference between the gun and the anode. A complex system of electrostatic lens maintains the focalisation of the beam. Once the electron beam is focused on the sample, secondary or backscattered electrons are emitted and different kinds of detectors collect the signal. It is then possible to access to imaging and further analyses. The most commonly used detectors are secondary electrons (SE) detectors and backscattered electrons (BSE) detectors. The SE are the low energy electrons emitted from the sample, due to an inelastic interaction with the beam. The BSE are the highly energetic electrons reflected or backscattered on the sample, due to an elastic interaction.

Equipment and experimental conditions

In this work, all SEM measurements were performed on a dual beam Helios NanolabTM 650 -SEM from FEI Company (USA). This microscope allows working at low tension without a

significant impact on the resolution, which reduces the risk of sample damage. Typically, SEM images were performed on the structures at 2 kV tension, with a beam current of 25 pA and a working distance of 4 mm. The -SEM is coupled with Energy Dispersive X-ray Spectroscopy (EDX, Xmax 50 mm², Oxford Instrument), which gives elemental information. The Helios NanolabTM 650 is also equipped with an OmniProbe micromanipulator that enables TEM samples preparation following a standard procedure of lamella preparation [217].

Results interpretation

Depending on the detector used and also on the working parameters of the beam current, the SEM can provide information not only on the samples topography, but also on chemical contrast. In this work, the SEM images were mainly performed for the topographical study operating in SE mode.

Electron backscatter diffraction

Working principle

Electron backscatter diffraction (EBSD) is a particular SEM configuration that allows acquiring information about the crystallographic microstructure of samples. The main difference from the classical SEM is the detector. The EBSD camera offers simultaneously information about grain size, grain boundary character, grain orientation, texture, and phase identity of the sample. The EBSD detector consists of a phosphor screen and a charge-coupled device (CCD) camera sensitive at low beam intensity. The phosphor screen converts the diffracted electrons into light, which is collected by the low light CCD [216].

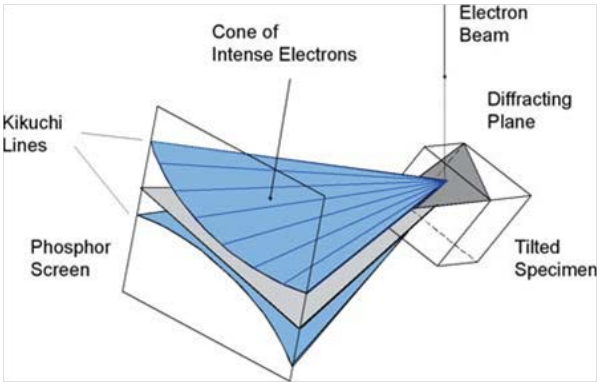

Figure A-5 Schematic of the diffracting cones with respect to the reflecting plane, the specimen, and the phosphor screen [218].

Equipment and experimental conditions

A SEM from Zeiss Company coupled with EBSD camera from Brüker was used for the TiO_2 films characterisation. Samples were characterised without any specific surface preparation. EBSD analyses were performed with beam tension at 10kV in the in-lens mode, (sample tilted at 70°C). The in-lens detector is located inside the electron column of the microscope and allows obtaining better contrast at low voltage.

Results interpretation

The electron diffraction patterns collected on CCD represent the Kikuchi lines, characteristic of each crystallographic orientation, as defined by the crystal lattice parameters and its orientation [218].

The interpretation of the diffraction pattern was carried out by a dedicated software, which fitted the obtained EBSD patterns with that ones reported in the library. Thus, the grains orientation was determined, taking into account the known crystalline phase parameters and working distance. The EBSD analyses depth was ~20nm.

Transmission Electron Microscopy

Working principle

Transmission electron microscopy is based on electron transmission through the material, and offers an excellent resolution for sample microstructure visualization up to 0.1 nm. In order to achieve such resolution, highly energetic electrons from e-beam are transmitted through the thin sample, which requires a specific preparation. The sample thickness allowing the electrons transmission should not exceed 100 nm. Typically, he electron beam of the TEM is accelerated at high voltage 80-300 kV and focused on the sample by the system of electromagnetic lenses (Figure A-6). Compared to the SEM, the sample (specimen) is placed in an intermediate position inside the column. The electron beam is transmitted through the specimen and the signal is collected either on phosphor screen or by CCD. Two main modes of TEM operation can be underlined: (i) imaging with ultra-high resolution (about a few Angström) and (ii) diffraction mode. The diffraction pattern represents the crystal in the reciprocal (Fourier) space. TEM can be also coupled with EDX in order to provide elemental analysis and mapping at the nanometer-scale.

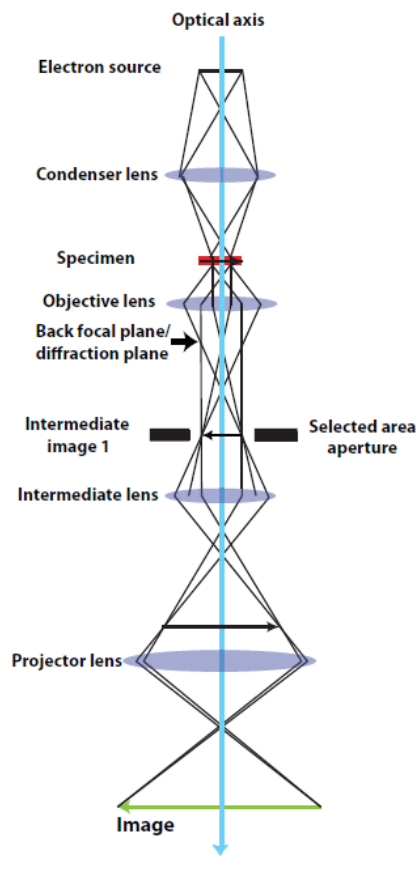

Figure A-6 Schematic illustration of a Transmission Electron Microscope.

Equipment and experimental conditions

TEM was performed on Jeol 2100F, operated at 200 kV. The samples for TEM were prepared by FIB-SEM, following a standard procedure of lamella preparation using gold and platinum protective layers. The images were recorded in scanning transmission electron microscopy high-angle annular dark-field (STEM-HAADF) and bright field (BF) modes.

Results interpretation

The TEM images show the microstructure of the sample with a high resolution. In BF mode, the transmitted beam is used to form an image. In this mode, the elements with higher atomic number Z appear darker than lighter ones on the image. The dark field (DF) mode uses a diffracted beam where the objects that participate in “reflection” appear as bright objects on dark background.

X-ray diffraction

Working principle

X-ray diffraction (XRD) is the classical method for crystal structure characterisation. The method is based on the X-ray diffraction on the crystalline lattice (atomic plane). The X-ray diffraction provides crystalline phase identification, and also information about the lattice parameters, crystallites size, and crystals orientation. The crystalline material consists of the periodic atomic planes –plane lattice with determined interplanar distance (d) (Figure A-7).

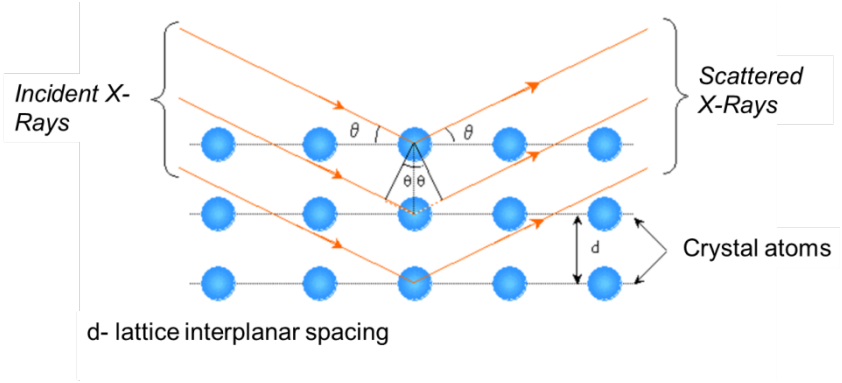

Figure A-7 Schematic of XRD principle.

While the crystalline material is irradiated with a monochromatic parallel X-rays, they are diffracted according to the lattice interplanar distance-d. The XRD follows the Bragg's theory: the incident X-ray with wavelength λ is refracted only on the lattice planes placed under certain angles to the beam (Bragg's angles - Θ). These angles can be determined by the Bragg's law (Equation 1).

$$\sin\Theta = \frac{n\lambda}{2d_{hkl}} \qquad (1)$$

where λ : X-Ray wavelength, d : lattice interplanar distance, Θ : incident angle of X-Rays, n : integer.

The diffracted X-rays are detected and transformed into the diffractogramme of the analysed sample.

The crystallites size can be determined according to the Scherrer equation:

$$\beta(2\theta) = \frac{k\alpha}{L\cos\theta} \qquad (2)$$

where α is wavelength (Å), L is FWHM (radians) corrected for instrument broadening, θ is Bragg angle, C is a Scherrer constant (0.94)

Equipment and experimental conditions

A diffractometer D8 Discover from Bruker with copper X-ray source at $K\alpha_{1-2}$ was used for XRD characterisations. The XRD measurements on thin films were carried out in grazing incidence mode with an angle of incidence of 0.5° (or at 0.5°). The crystallite size was estimated without taking into account the peaks broadening due to the instrumental error using $k\alpha_1$ and $k\alpha_2$ together.

Results interpretation

The sample characterisation by XRD allows determining if the material is amorphous or crystalline, as only crystalline materials can provide the diffraction peaks. By measuring the angles corresponding to the peaks, the lattice distance can be determined according to the Bragg's law (Equation 1).

Currently, the XRD pattern of the majority of crystalline materials known can be found in the Powder Diffraction File (PDF) or Joint Committee on Powder Diffraction Standards (JCPDS) data-bases.

The TiO_2 crystalline modifications as anatase, rutile or brookite can be identified by the XRD analysis. The anatase and rutile represent the tetragonal structure; therefore the lattice parameters can be determined according to the Equation 3.

$$\frac{1}{d^2} = \frac{h^2 + k^2}{a^2} + \frac{l^2}{c^2} \qquad (3)$$

Where d- interplanar spacing; a, c – lattice parameters, h, k, l –Miller indices.

X-ray photoelectron spectroscopy

Working principle

X-ray photoelectron spectroscopy is a surface characterisation technique with a sampling depth of 10-12 nm providing qualitative and quantitative information about elemental

composition of materials and chemical state on the present elements. This characterisation method is based on the interaction of X-ray photons with electrons of the atoms composing the samples to be analysed. This interaction generates electrons (called photoelectrons) characteristic of the atoms present in the matter. The kinetic energy of electrons and the number of detected electrons will be characteristic of the chemical state and of the concentration of the atoms present in the material.

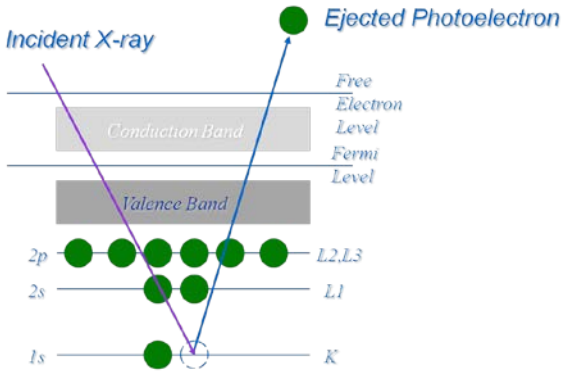

Figure A-8 Principle of XPS photoelectron emission.

Equipment and experimental conditions

XPS measurements were carried out on an Axis Ultra DLD, from Kratos Analytical Ltd., using an X-ray source (Al Kα monochromated, E=1486.6 eV) at 150 W, a pass energy of 20 eV for narrow spectra, and a step size of 0.1 eV. The analyzed area was 300 µm × 700 µm for surface analysis and 10 µm in diameter for depth profiles.

Since the sampling depth of XPS is only around 12 nm, an argon beam enables to sputter the surface is required in order to allow a depth profile analyses

Results interpretation

The photo-electrons are collected by an analyser, measuring their kinetic energy, which produce the spectrum of deduced binding energy versus intensity based on the following relation:

$$h\nu = E_b + E_k + \Phi_s, \qquad (4)$$

E_k - kinetic energy of photoelectron (eV), E_b - binding energy of photoelectron (eV), $h\nu$ - energy of incident X-ray (eV), Φ_s - spectrometer work function (known constant)

Therefore the spectrum consists of peaks corresponding to the characteristic energies of the orbitals of each element present in the analysed volume. Typically all spectra are calibrated on the C 1s peak position (285 eV) to correct the energy shift related to the charge effect. Any shift in binding energy is due to the modification of the atom chemical state either by a change of oxidative state or change of coordination with other elements.

Secondary ion mass spectrometry

Working principle

D-Secondary ion mass spectrometry (D-SIMS) is a surface analysis technique allowing analysis of any kind of solid material. A solid sample is sputtered with a primary ion beam of a few kiloelectronvolts energy. A part of particles emitted called secondary ions is analysed in a spectrometer according to their ratio mass/charge. SIMS analysis provides information about elemental and isotopic material composition via depth profiling or imaging. [219]

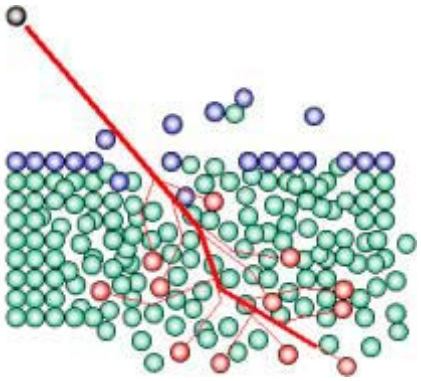

Figure A-9 Schematic of SIMS collision cascade [220].

Equipment and experimental conditions

A CAMECA SC-Ultra instrument was principally used for the characterization of self-organised TiO_2 nanoparticles, in order to conclude on the growth mechanisms. SIMS depth profiles were optimized for depth resolution using a Cs^+ primary ion beam with energy of 1 keV. The analysed area was limited to a circle that was centred in the scanned area and was 33 µm in diameter, ultimately encompassing ~10^4 micelles. The different elements of interest were analysed as MCs_x^+ clusters (M= C, Si, Ti, N, O and Cl; x=1 or 2) to circumvent matrix effects.

Results interpretation

The SIMS data acquired in our study provide information about sample chemical composition evolution versus sputtering time (i.e depth).

Atomic Force Microscopy and Kelvin Probe Force Microscopy

Working principle

Atomic Force Microscopy is a powerful topography visualisation tool based on the interaction between the sharp tip and sample surface.

The interaction between the probe and surface can have different origins and provides the information, not only about sample topography, but also about functionalities such as conductivity, surface energy, etc.

The sharped probe (tip) is positioned in such proximity to the surface that it is able to interact with the force field associated to the surface (Figure A-10). The deflection of the cantilever during the scan enables reconstructing the sample topography (Figure A-10).

Three operational AFM modes can be distinguished:

- Contact mode.
- Tapping mode (intermediate)
- Non-contact mode

In contact mode the tip touches the surface the repulsive force “tip-surface” deflect the cantilever. In tapping and non-contact mode the tip oscillates at frequencies close to its resonance one. In this condition the changes in the surface-tip distance in taping mode will change the oscillation amplitude, and the resonance frequency in case of non-contact mode. These amplitude and resonance frequency changes are used for the topography images reconstruction [221].

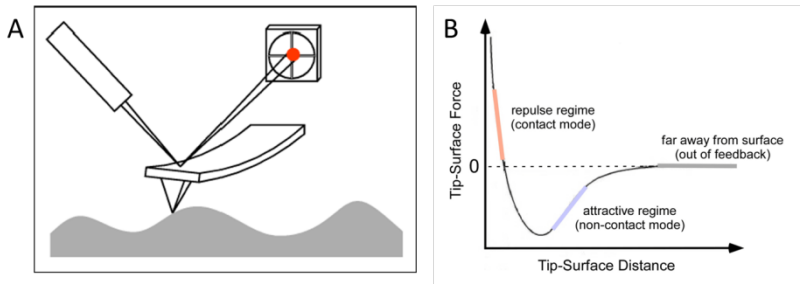

Figure A-10 (A) - basic block diagram of an AFM; (B) - schematic of cantilever displacement measurement, C - Atomic interaction at different tip-sample distances [222].

Kelvin Probe Force Microscopy

Kelvin Probe Force Microscopy (KPFM) or surface potential microscopy is one of the AFM variations, which enables measurement of Contact Potential Difference (CPD) between a reference surface (tip) and surface to analyse, which equals the work function difference of the two materials (Equation 5):

$$V_{CPD} = \frac{\phi_{tip} - \phi_{sample}}{-e} \qquad (5)$$

Where ϕ_{tip}, and ϕ_{sample} are the corresponding work function, e – electronic charge.

When the tip approaches the surface at a distance d, an electric force is generated between the sample and the tip, due to the difference of the Fermi level (Figure A-11a). While the electrical contact occurs, the Fermi levels will align through electron current flow (Figure A-11 b). However, the vacuum levels are not aligned anymore and V_{CPD} is formed between the sample and tip. An electrical force acts on the contact area can be nullified by application of the external potential V_{DC} equal to V_{CPD} with opposite direction (Figure A-11c).

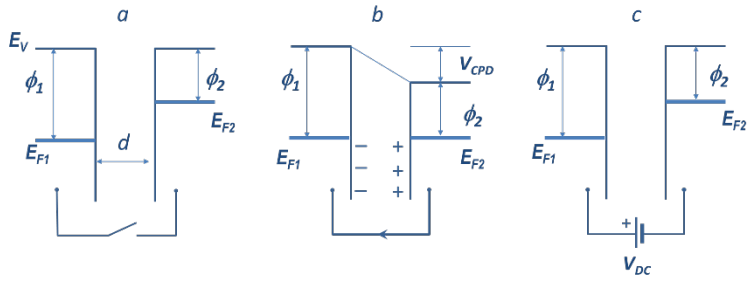

Figure A-11 Energy and charge diagram illustrating Kelvin probe technique principle; ϕ_1 corresponds to the tip work function and ϕ_2 to the sample work function [221].

The work function of the sample can be found according to Equation 5, as the tip work function is a known parameter and the applied V_{DC} to nullify the electrical force of V_{CPD} is the difference between surface- and tip- work functions.

Equipment and experimental conditions

Topography and CPD measurements were carried out with a commercial AFM (Innova, Bruker Inc.). The CPD was acquired by an amplitude modulation kelvin probe force microscopy (AM-KPFM) in one pass, under nitrogen flushing to limit the humidity fluctuations. The topography is obtained by maintaining the amplitude of the first resonance frequency f_0 constant (tapping mode). An AC bias (f_1=23 KHz and 2V amplitude) is applied on the tip to generate the electrostatic force. The detected amplitude of this force at f_1 is nullified by a DC bias applied to the tip and controlled by a feedback loop. The scan rate used was 0.1 Hz.

The tips used for CPD measurements are an ATEC-EFM from Nanosensors. They were coated with PtIr with a typical resonance frequency at 70 KHz. The topography measurements were performed in tapping mode using Micromasch HQ NSC15 tips.

Results interpretation

The samples roughness was determined from topography scans by the images post treatment in the software SPIP version 4.6. The Root Mean Square (RMS) parameter Sq, is defined following Equation 6:

$$S_q = \sqrt{\frac{1}{MN}\sum_{k=0}^{M-1}\sum_{i=0}^{N-1}[z(x_k, y_i)]^2} \qquad (6)$$

UV-Visible spectroscopy

Working principle

The UV-Visible spectroscopy is based on the interaction of the electromagnetic wavelength with matter. This interaction can result in various processes such as reflection, scattering, absorbance, fluorescence/phosphorescence (absorption and reemission), and photochemical reaction (absorbance and bond breaking). The UV-Vis absorbance spectra have a particular interest. Light is a form of energy and its absorption by matter causes the energy of molecules or atoms to increase. The UV-Visible light absorption measurements are important

characterisation tools for light sensitive materials such as photocatalytic metal-oxides, plasmonic nanostructures, and dye photocatalytic degradation.

Equipment and experimental conditions

UV-vis measurements were carried out on an UV-visible spectrometer TECAN Infinite M1000Pro from the TECAN Company.The spectrometer is equipped with a monochromator that allows to select the working wavelength in the UV-Infra red range. The TECAN detection limits are in the range 250-1000 nm.

The photocatalytic degradation measurements on methylene blue dye were followed by the absorption peak intensity at 666 nm and complete spectra acquisition in the UV-Vis range 500-700 nm.

The characterisation of plasmonic nanoparticles in solution or deposited on glass were run by spectra acquisition in the range 400 – 750 nm.

Results interpretation

The wavelength of light absorbed is the energy that is required to move an electron from a lower energy level to a higher energy level [223]. The TiO_2 films deposited on quartz substrates allow determining the value of optical band gap by a tangent to the spectrum slope.

The UV-Vis absorption peak on the plasmonic nanoparticles corresponds to the surface plasmon resonance peak. It means that the light wavelength coincides in frequency with electron oscillation on the surface of plasmonic nanostructures, which causes the resonance effect.

The application of the UV-Vis spectroscopy in the photocatalytic tests enables the precise control of the dye concentration change during the photocatalytic degradation.

Raman spectroscopy

Working principle

Raman spectroscopy is used to investigate vibrational modes in crystals which are their fingerprints. The electromagnetic radiation of frequency ν_r induces a change of polarisation in the crystal that in turn modifies the frequency of the scattered Raman light. This phenomenon

is described by the susceptibility of the crystal which describes the polarisation degree $\vec{P}$ of dielectric materials in the electric field $\vec{E}$ through the following Equation 7:

$$\vec{P} = \varepsilon_0 \chi \vec{E} \qquad (7)$$

where χ is a symmetric second rank tensor.

In first-order Raman scattering, the momentum is conserved: the momentum of the scattered light (or scattered photons) is equal to the momentum of the incident light plus the momentum of the vibration (or phonon). Since the momentum of the photons is very small compared to dimensions of the unit-cell in the reciprocal space, only small wave-vectors (close to the Brillouin-zone center) phonons are seen in the first-order Raman scattering [224].

Usually a laser beam is used as an electromagnetic radiation and shined on the sample. The elastic scattering, or Rayleigh scattering, is filtered by the notch filter, edge pass filter or band pass filter, while the rest of the collected light passes onto the detector.

Equipment and experimental conditions

Raman spectra were acquired by a Renishaw inVia confocal Raman microscope that schematic is represented on Figure A-12. It consists of (1) several monochromatic light sources; (2) waveplates to polarize the incident and analyzed light; (3) a microscope to focus the light on the sample and collect the scattered light; (4) a movable stage to move the sample in-situ and perform maps; (5) dielectric “edge” filters to cut the Rayleigh part of the spectra; (6) a diffraction grating for dispersing the Raman scattered light: (7) a CCD camera for detecting this light.

The Raman spectra on TiO_2 films were carried out at incident wavelength of 532 nm and a laser power below 0.44 mW.

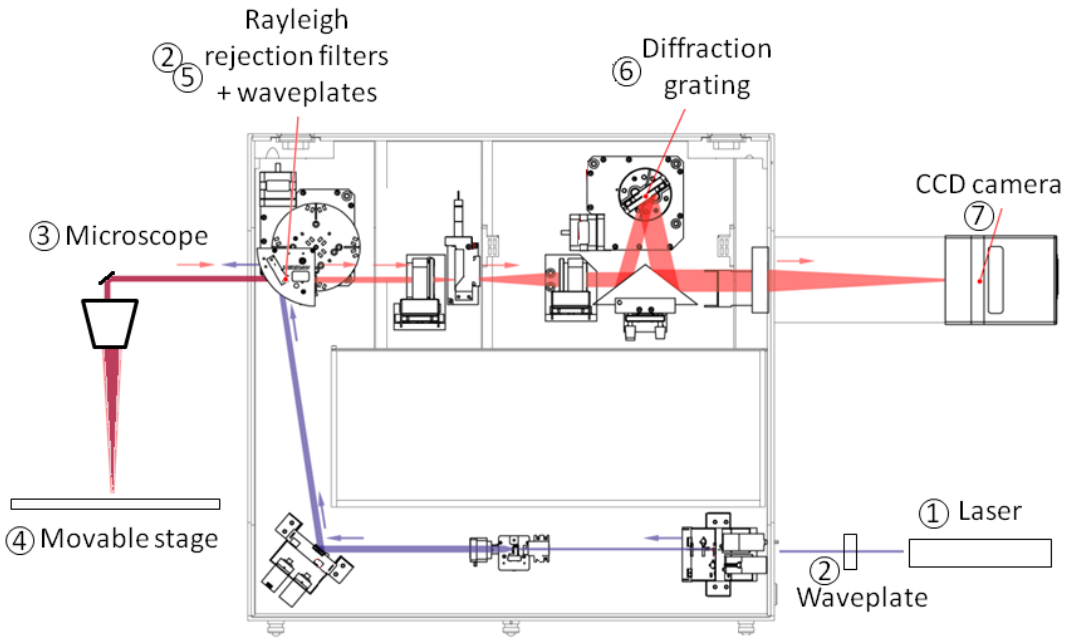

Figure A-12 Schematic of Renishaw inVia confocal Raman microscope. (The key components are highlighted. Adapted from Renishaw's documentation).

Result interpretation

The Raman spectra present the plot of the scattered light intensity (y-axis) versus light energy value (frequency, number of waves per cm, cm^{-1}) – (x-axis). For metal-oxides, the Raman spectroscopy is a fast mean to identify the presence of crystalline phase. A typical Raman spectrum for TiO_2 anatase demonstrates the presence of the following characteristic vibrational modes: 142 $cm^{-1}(E_g)$, 195 $cm^{-1}(E_g)$, 395 $cm^{-1}(B1_g)$, 514 $cm^{-1}(B1_g)$, 636 $cm^{-1}(E1_g)$.

Photoluminescence

Working principle

In general photoluminescence is the phenomenon of the light emission after absorption of photons (electromagnetic radiation).

For the semiconductor material the absorption of photons with energy higher than the band gap will induces the electrons and holes generation in the CB and VB respectively. Once the photogenerated carries recombine (phonon assisted recombination) the energy is emitted equivalent to the band gap energy level and collected by the spectrometer. Therefore the photoluminescence is the powerful mean to characterise the localised electronic states associated with defects by the emission of light at sub-bang gap levels [200].

Equipment and experimental conditions

The Raman spectrometer was used in the Photoluminescence mode (Renishaw inVia confocal Raman microscope is described previously on Figure A-12.

The PL spectra acquired using the near UV laser at 325 nm (7.8 mW) at room temperature in the range 350-1100 nm.

Result interpretation

The TiO_2 being a semiconductor with indirect band gap, under irradiation with energy at and above the band gap provide a weak emission up to the recombination of the conduction band electrons with valence band holes. In the literature, the PL in TiO_2 anatase is generally related to the self-trapped excitons. McHale and Knorr demonstrated that the anatase PL spectra represent the superposition on two types of radiative recombination: one of the mobile electrons, from the conduction band and shallow traps, with trapped holes (Type 1 PL), and other of trapped electrons with valence band holes (Type 2 PL) [200]:

Type 1: $e^-_{CB} + h^+_{tr} \rightarrow \nu h_{green}$ (8)

Type 2: $h^+_{BV} + e_{tr}^- \rightarrow \nu h_{red}$ (9)

Ellipsometry

Working principle

The thickness measurements of metal-oxide films deposited on Si-substrates were obtained by ellipsometry. This method is based on the measurement of change in light polarisation when it reflects or transmits from a material structure.

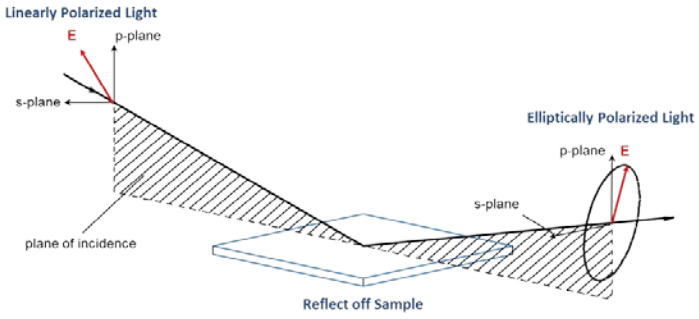

Figure A-13 Schematic principle of ellipsometry.

These measurements are highly sensitive to film thickness, roughness, and optical constants modification. The polarisation change is caused by the samples properties such as thickness or refractive index. The polarisation state of the incident light consists of surface (s) and plane (p) components. The s-component consists of the oscillation parallel to the surface and p-component parallel to the incident plane. Thus, the fundamental ellipsometry equation is resented bellow:

$$\rho = \frac{r_p}{r_s} = \tan(\Psi)e^{i\Delta} \qquad (10)$$

Where Ψ, Δ - Stokes parameters,

r_p, r_s - the intensity of the 's' and 'p' component after reflection

Equipment and experimental conditions

The thickness measurements were performed by an ellipsometer M2000 from the J.A. Woollam Co Company. The measurements were performed at 400 nm wavelength with incident angle of 75°.

Results interpretation

The ellipsometric data are analysed by the correspondence to the optical models which take into account the optical constants, and thickness parameters as well as the layer sequences.

In this work the TiO_2 and SnO_2 film thickness measurements followed the optical Cauchy model which better fits for the oxides transparent in the visible range.

Contact angle

Working principle

The formation of a drop of liquid on the solid surface can be characterised according to the contact angle which is determined by the interactions of three interfaces: the liquid phase of the droplet (L), the solid phase of the substrate (S), and the gas/vapour phase (G). Figure A-14 shows the equilibrium among the forces involved in the contact angle measurements. The contact angle allows determining a degree of hydrophilicity/ hydrophobicity of the substrate, which is surface energy depending parameter. It is generally established the surfaces with

contact angle (θ) lower than 90° the surface is hydrophilic, and hydrophobic if the θ >90°. Therefore, the samples wettability has to be taken into account for the photocatalytic measurements in aqueous middle [225].

The wettability by a water contact angle (WCA) is typically measured by deposition of the water drop on the sample surface. The camera records the drop profile image. The contact angles are measured by a tangent from two extreme contact points liquid-solid-air (Figure A-14).

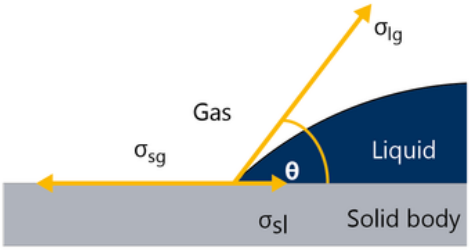

Figure A-14 Schematic of the contact angle measurements.

Equipment and experimental conditions

The WCA measurements were carried out on DSA16 Drop USB from Krüss. The DI water with MiliQ quality was used for the measurement. Drops of 2 µl were deposited on the sample by a micro-syringe. A digital camera recorded the photography of the drop on the surface. The WCA was determined from the recorded images by the tangent method on the interface between the drop and the surface. The angle θ between the solid surface and tangent is the contact angle (Figure A-14).

Results interpretation

The samples wettability can be determined according to the contact angles values: if θ ≤90° the surface wettability is high, in the opposite case if θ ≥90°, the surface wettability is low.

A relationship between the contact angle (θ), the surface tension of the liquid σ_l the interfacial tension σ_{sl} between liquid and solid and the surface free energy σ_s of the solid is given by the Young's equation (Equation 11):

$$\sigma_s = \sigma_{sl} + \sigma_l \cdot \cos\theta \qquad (11)$$

Substrates

Wafers

In this work, all film deposition processes are first developed on flat silicon wafers. Siegert Wafer, Germany provided silicon wafers. All depositions are carried out on one side mirror polished Si (100) wafers with p-type doping (boron). Prior to the deposition, the substrates are cleaned following standard cleaning procedures: sequential rinsing in acetone, ethanol, IPA in the ultrasonic bath and dried under nitrogen flow. Si (100) wafers with thermally grown 50 nm SiO_2 layer are used for the fabrication of TiO_2 self-assembled nanoparticles, MOCVD and ALD growths. In order to mimic alumina membranes chemistry, fused silica substrates from Siegert Wafer with Al_2O_3 buffer layer deposited by ALD are also used for further investigations of TiO_2 films deposition by ALD.

AAO Membranes

The ALD film deposition is first optimised using the commercial AAO membranes Anodisc from Whatman. The Anodisc membranes, 13mm in diameter with pores size 200nm are used without further cleaning. The commercial Smart Pore membranes (SmartMembranes Company, Germany) with pore diameter of 180 nm are ordered with tailored thickness parameters that are previously optimized as it was described in Section 2.2.2.

Summary of precursors

Table 1 Precursors for the block-copolymer method.

Precursor	Purity	N° CAS	Supplier, ref
Polystherene-b-poly(vinylpyridine) P10910B-P2VP Mn 40500-b-41000, Mw/Mn 1,1 P4925-P2VP Mn 102000-b-97000, Mw/Mn 1,12	As received	24980-54-9	Polymer Source, Inc. (Dorval, QC, Canada)
m-xylene	Anhydrous, >99%	108-38-3	Sigma Aldrich 296325
Gold(III) chloride trihydrate $HAuCl_3 \cdot 3H_2O$	>99.9%	16961-25-4	Sigma-Aldrich (Belgium) 520918
Chloroplatinic acid solution	8% in H2O	16941-12-1	Sigma-Aldrich (Belgium) 262587-10ML
Potassium tetrachloropalladate (II)	99.99%	10025-98-6	Sigma-Aldrich (Belgium) 379816-1G

Table 2 Precursors for the ALD method.

Precursor	Purity	N° CAS	Supplier, ref
$TiCl_4$	>99.995%	7550-45-0	Sigma-Aldrich (Belgium) 254312
$SnCl_4$	99.995%	7646-78-8	Sigma-Aldrich (Belgium) 217913
Trimethylaluminum (TMA)	97%	75-24-1	Sigma-Aldrich (Belgium) 257222

Table 3 Precursors for the MOCVD method.

Precursor	Purity	N° CAS	Supplier, ref
Titanium(IV) isopropoxide (TTIP)	>97%	546-68-9	Sigma-Aldrich (Belgium) 87560
Heptane	anhydrous	142-82-5	Sigma-Aldrich (Belgium) 592579

Table 4 Precursors for the AAO fabrication.

Precursor	Purity	N° CAS	Supplier, ref
Perchloric acid	70%	7601-90-3	Sigma-Aldrich (Belgium) 244252
Ethanol absolute	>99.8%	64-17-5	VWR BDH Prolabo 20821.32
Oxalic acid	>99%	6153-56-6	VWR 100495
Chrome oxide (VI)	>99%	1333-82-0	Sigma-Aldrich (Belgium) 27081
Ortho-phosphoric acid (H_3PO_4)	85% extra pure	7664-38-2	Merck 1.00563.1000

Olga ISHCHENKO

Elaboration de nanocomposites plasmoniques et étude des activités catalytiques spécifiques

Résumé

L'objective est d'améliorer l'activité photocatalytique de TiO_2 sous irradiations UV et Visible. Pour contourner les limites de TiO_2 intrinsèque nous envisageons une fabrication de nanocomposite plasmonique à base de nanofils de TiO_2 périodiquement organisés et assemblés avec des nanoparticules plasmoniques. Pour la fabrication des nanofils de TiO_2 mécaniquement stables, deux approches ont été réalisées. La première approche est basée sur la croissance sélective en phase vapeur, la deuxième approche consiste en l'utilisation d'un moule de membranes AAO et d'un dépôt de films conformes par ALD. En parallèle les films de TiO_2 déposés par ALD sont assemblés avec les nanoparticules plasmoniques d'or. Les différentes architectures de TiO_2 sont valorisées par des tests photocatalytiques (UV et Visible) sur les polluants modèles.

Une nouvelle approche de la fabrication des films mesoporeux d'H-TiO_2 avec efficacité photocatalytique à la fois sous irradiation UV et Visible est développée.

Mots-clés: TiO_2, TiO_2/SnO_2, AAO, Block copolymers, ALD, nanofils, nanoparticules plasmonique, H-TiO_2 mesoporeux, photocatalyse,

Résumé en anglais

The objective of this thesis is to improve the photo-response of well-known photocatalytic material such as TiO_2, which is usually only active in the UV range. The basic idea is to assemble several approaches within one device to improve the photocatalytic properties: fabrication of periodically-organised TiO_2 nanostructures and their assembly with plasmonic nanoparticles. Two fabrication strategies were investigated for these purposes. The first approach consists of selective vapour phase growth. The second approach implements the use of an AAO template. In parallel, TiO_2 films deposited by ALD and assembled with plasmonic gold nanoparticles are investigated. The photocatalytic measurements on various TiO_2 architectures were performed in both irradiation ranges UV and Vis.

A new fabrication approach of mesoporous H-TiO_2 films was developed giving promising results of photocatalytic efficiency improvement in both UV and Visible ranges.

Key words: TiO_2, TiO_2/SnO_2, AAO, Block copolymers, ALD, nanowires, nanostructures, mesoporous H-TiO_2, plasmonics, photocatalysis.